The Dissertation Committee for Gregory Ross Hays Certifies that this is the approved version of the following dissertation:

Development of Broad Spectrum Technologies for High Energy Chirped Pulse Amplification

Committee:

Todd Ditmire, Supervisor

Michael C. Downer

Manfred Fink

John W. Keto

Michael Becker

Development of Broad Spectrum Technologies for High Energy Chirped Pulse Amplification

by

Gregory Ross Hays, B.S.

Dissertation

Presented to the Faculty of the Graduate School of
The University of Texas at Austin
in Partial Fulfillment
of the Requirements
for the Degree of

Doctor of Philosophy

The University of Texas at Austin
August, 2007

Acknowledgements

Now that this long journey is nearing the end, I look back over the last seven years with a true sense of accomplishment. If I have learned one thing in my studies, it is that lasers require patience. They have also taught me voodoo incantations, unmentionable four-letter expletives, and the true reward of a cold beer after work. Lasers have taken me much further than I ever expected.

Foremost I must express genuine gratitude and love to my best friend and wife, Despina. She has been a pillar of support and a foot in the ass to keep me going. Her sage advice and constant encouragement has been a bottomless well. She has helped earn this degree as much as me. Being married to woman who understands the physics of what you are doing has amazing benefits.

If rectal motivation has two feet, the other foot belongs to my advisor, Todd Ditmire. His real passion for science and lasers overwhelmed me ten years ago. I had never met a scientist with such passion, and it truly rubbed off on me. His faith in me brought me to Texas and gave me two playrooms with unimaginable toys to play with. He has been a friend, confidant, and mentor in every way.

I owe a big debt of gratitude to the three gentlemen and founding members of the Fraternal Order and United Brotherhood of Giant Nerds who were there with me the entire time. Will, Gilliss and Aaron were more than friends and officemates. Will Grigsby single handedly pulled me through all of my core classes. The first semester he was number one on my speed dial. Aaron Edens was always willing to explain it to me one more time, and Gilliss Dyer always knew it could be done better. I have shared most of the best moments of graduate school with all of them, and will remember it fondly.

Another colleague of distinction is Bonggu Shim. He and I spent more late nights in the lab than I can remember. The man is a machine! With a steady supply of coffee and cigarettes, he can outrun the energizer rabbit.

I real bit of gratitude must also go to Sam Feldman and Daniel Herman. During the last year of my research, these to guys made it worthwhile. Together we learned that 24 hours straight in the lab is hard, but a lot of fun. Sam and Daniel were always willing to go back in there and try it again. With a little bit of German precision and a whole lot of Yankee sarcasm, anything is possible.

I would also like to thank Roger Bengston. In many ways Roger was a surrogate advisor and mentor. He helped me navigate the obstacles of graduate school with the least amount of frustration. With his constant questions of, "Is is done yet," and "are you getting paid overtime," he helped keep my eye on the prize.

Finally I would like to thank my parents, Bill and Rossanna Hays. My parents were never quite sure what I was doing in the lab, but they were 100% sure that I could get it done. They listened to every woe and sad story I had to tell. They also relished in every achievement that I made. My mother always told me I could do anything that I put my mind to, and my father taught me perseverance and the meaning of hard work.

In closing, I would like to express my gratitude to my brother, Scott Hays, who passed away from cancer in 2002. If ever there was a person that I idolized in my life, it was my big brother. He also learned from our parents and really demonstrated that you can do anything you set your mind to. I remember asking him when he entered graduate and medical school if he was daunted by the huge amount of work that lay ahead of him. His reply was simple, "Its not work, its fun."

Development of Broad Spectrum Technologies for High Energy Chirped Pulse Amplification

Publication No._____________

Gregory Ross Hays, Ph.D.

The University of Texas at Austin, 2007

Supervisor: Todd Ditmire

We have developed several broad-spectrum technologies for high-intensity chirped pulse amplification. We present the design and performance of two 20 TW laser systems. THOR is a Ti:sapphire, 10 Hz, ultra-fast laser that produces femtosecond pulses with a peak intensity of 18.4 TW. The laser operates near the bandwidth limit of the medium maintaining sufficient spectrum to produce 38 fs pulses. This equates to a near transform limited time-bandwidth product of 0.490. The second laser system was developed to study broad-spectrum pulse amplification in mixed Neodymium-doped laser glasses. Our efforts were to produce a multi-Joule laser with sufficient bandwidth to compress near 100 fs using mixed-glasses in the final amplifier. We present the GHOST laser with modeling and experimental analysis of the precise gain ratios between the mixed glasses. GHOST examines the bandwidth limit of the mixed-glass architecture in order to produce the broadest amplified spectrum with the shortest compressed pulsewidth. The laser has a total gain of 4×10^9 with a net gain of 260 from glass. The measured optimum gain ratio of 3.3 (G_{phos}/G_{sil}) produced 14.4 nm (FWHM) of bandwidth with a 103 fs pulsewidth. This constitutes a time-bandwidth product of 0.398. Additionally we have investigated two novel laser glasses in an effort to generate high energy (>1 kJ), broad spectrum pulses from a chirped-pulse amplification Nd:glass laser. Both glasses have significantly broader spectra (>38 nm FWHM) than currently available Nd:phosphate and Nd:silicate glasses. We present calculations for small signal pulse amplification to simulate spectral gain narrowing. The technique of spectral shaping using mixed-glass architecture with an optical parametric chirped-pulse amplification front-end is evaluated. Our modeling shows amplified pulses with energies exceeding 10 kJ with sufficient bandwidth to achieve 120 fs pulse widths are achievable with the use of the new laser glasses. With further development of current technologies, a laser system could be scaled to generate one exawatt in peak power. Finally we report controlled enhancement of optical third harmonic generation from hydrodynamically expanding clusters of noble gas atoms several hundred femtoseconds following ionization and heating by ultrashort pump pulses.

Table of Contents

1 Introduction

Since the invention of the laser in 1960 [1, 2], scientists have sought develop higher and more intense sources to study light interactions with matter. Early advances in laser technology produced the first observation of second harmonic generation (SFG) from laser light [3]. Soon thereafter a theory was developed [4, 5] and several nonlinear optical phenomena were observed; including third harmonic generation (THG), sum frequency generation (SFG) and difference frequency generation (DFG). Short pulse lasers have produced electric field strengths with large enough effects that are no longer sufficiently described by atomic perturbation theory. They have also bolstered the investigations into high field physics. Thirty years ago scientists were limited to study multi-photon ionization from laser interactions with materials. Today the development of intense lasers has enabled scientists to investigate many exotic realms of physics; including nonlinear optics, relativistic plasmas, x-ray generation, laboratory astrophysics, and fusion.

The motivation for this thesis is to investigate novel areas of laser design for the creation of high-energy ultrafast laser pulses with near transform limited pulse widths. The modeling, design, and construction of two state of the art laser systems will be presented. Additionally, experiments involving high field nonlinear optics on laser cluster interactions have also been investigated.

1.1 Short Pulse Laser Development

The earliest advancement in intense laser development came from the advent of Q-switching [6]. Q-switching a laser cavity permitted extremely high population inversions in the gain media thereby creating high gain. The cavity would create a short intense pulse on the order of the round-trip time of the laser oscillator. This generated the first nanosecond scale laser pulses with intensities of several hundreds of MW/cm^2. The next advancement came from the technology of mode-locking. Picosecond and ultimately femtosecond pulse were generated by phase locking the longitudinal modes of the laser. Here the pulse width is inversely related to the bandwidth of the laser emission.

As these technologies were developed, the fundamental limiting barrier was the high peak powers associated with the short pulse duration. When pulse intensities begin to exceed a few GW/cm^2, the laser pulse can undergo self-focusing due to the intensity dependent nonlinear index of refraction. This in turn deteriorates the beam quality and ultimately can damage the material in which the laser passes. Laser designers essentially have only two choices in their design to avoid self-focusing: either increase the beam diameter and demand larger amplifier mediums, or increase the pulse width, which lowers the peak intensity.

Large aperture gain mediums have been developed through the benefit of solid-state laser materials. These media generally have high saturation fluences in the ranges of 1 to 10 J/cm^2, thus enabling significant energy extraction from small diameter rods to large aperture disk amplifiers. However even with large aperture amplifiers, it becomes increasingly difficult to extract high energy as the pulse width is decreased. This is due to the inverse proportionality of the pulse width to the intensity. For example a 1-picosecond pulse propagated at a fluence of 1 J/cm^2 results in a peak intensity of 10^{12} W/cm^2. Not only is this well in excess of material damage thresholds, but also this is clearly in the realm of self-focusing and the nonlinear index of refraction. Further a 1 TW pulse would require a 36 cm beam diameter to reduce the intensity to 1 GW/cm^2.

In 1985 the revolutionary technique of chirped-pulse amplification (CPA) was first demonstrated [7]. In this approach a short pulse is generated and then stretched temporally several thousand times before amplification, thus reducing its intensity and circumventing the effects of high peak powers. Now sufficient high energy can be extracted from the amplifiers at a safe level of intensity. Following amplification, the temporal stretching factor is removed to reform the high intensity short laser pulse. This technique is accomplished by adding and later removing large amounts of chromatic dispersion to the laser pulse. This is well suited for short pulses since they inherently have large associated spectral bandwidths.

In early manifestations of CPA lasers, an optical fiber was used to stretch the pulse [8, 9] and a pair of diffraction gratings was used for compression [10]. The short pulse generated from a mode-locked oscillator was injected into a long fiber with positive group velocity dispersion to generate a frequency dependent phase. Therefore the pulse would emerge positively chirped and stretched in time because the red frequencies travel faster than the blue in the fiber. After amplification this frequency chirp was then removed using the negative dispersion of optical gratings.

In the late 1980s and early 1990's the material of Ti:sapphire [11] and subsequently the Kerr-lens mode-locked Ti:sapphire laser [12] made ultrafast (sub-100 fs) laser pulses widely accessible. In turn the ultrafast pulses had enormous amounts of bandwidth that required significant management of the spectral phase to produce an amplified transformed limited compressed pulse. Therefore the use of optical fibers were no longer a viable source for pulse stretching because of the inherent nonlinear phase accumulated over such long optical path lengths. This higher order phase was irremovable from the optical pulse and created large temporal modulations in the compressed pulse. Therefore a new scheme had to be devised to stretch and compress ultrafast optical pulses.

Martinez [13] showed that if a 1:1 imaging telescope was placed between two anti-parallel gratings positioned within the focal lengths of the telescope, a positive group velocity dispersion pulse compressor could be made. Ultimately it was this design that became the now common pulse stretcher. This is primarily attributed to the Treacy compressor being easier to align and having fewer optical elements generating less energy loss in the final amplified beam.

The combination of matched grating stretchers and compressors has led to an explosion of new technology in the realm of short pulse lasers in the last 15 years. Table-top terawatt laser systems have become increasing common and even commercial products [9, 14-16]. Further the pursuit of increasingly higher pulse intensities has developed higher and faster than one could have thought possible 25 years ago. In 1994 Perry and Mourou reported that the first petawatt lasers were immanent [17]. Just two years later Lawrence Livermore National Laboratory deployed such a system on one beam line of the NOVA laser [18]. Shortly there after a peak intensity of 10^{21} W/cm^2 was reported from a Ti:sapphire based laser system [19].

However current technologies have begun to push the boundaries and physical limitations of current laser materials. CPA has enabled the complete exploitation of the entire spectral contents of most laser mediums today. Fundamentally spectral gain narrowing has emerged as the chief opponent to increasingly short pulse laser development. To circumvent these effects, many groups have sought to develop hybrid lasers containing several laser mediums to reduce spectral gain narrowing [20, 21]. The Livermore Petawatt laser utilized hybrid technique of a Ti:sapphire front end to limit spectral gain narrowing and a Nd:glass back end to reach high energies (600 J). Another approach has been to utilize spectrally offset media to enhance the gain spectra of Nd:glass [22-24]. Here the shifted spectral lines of Nd:phosphate and Nd:silicate laser glass are used together to create a net larger amplification spectrum. Ultimately it is the Gaussian shaped emission and finite bandwidth of these gain narrowing media that squelch shorter pulses.

Recently the pairing of parametric amplification to CPA has spawned new research into the possibilities of the next generation high-energy short pulse laser, or even ultimately the first multi-petawatt laser. Optical parametric chirped-pulse amplification (OPCPA) is of keen interest to high energy broad band pulse amplification [25]. Because of the broadband phase matching conditions, parametric amplification creates a nearly uniform gain spectrum over a very large bandwidth. Further the gains are extremely high, exceeding 10^3 from a single pass in centimeter-scale length crystal. However reaching high energies (>1 J) is difficult due to the required highly formatted pump laser. Nonetheless a few groups have sought to incorporate OPCPA into hybrid laser designs in an effort to increase the amplified spectral bandwidth [26, 27].

Therefore the primary focus of this research will be to examine all of the above listed technologies in an effort to generate state-of-the-art high-energy short pulse lasers. Aspects of phase control and high gain amplification in various laser designs will be discussed. Conventional energy storage amplifiers and/or OPCPA in homogeneous and heterogeneous laser systems are also targeted for the investigation. In addition novel laser mediums for broad-spectrum amplification are included.

1.2 Short-pulse laser-cluster interactions

In recent years a great amount of research has focused on the irradiation of atomic clusters by intense laser pulses. These studies have lead to applications of x-ray generation [28], phase matching in high-harmonic generation (HHG) [29, 30], and even nuclear fusion [31]. Noble gas clusters have presented a rich field of physics due to their unique physical properties. If a gas jet is operated with sufficient high backing pressure, solid density clusters will form from cooling associated with rapid adiabatic expansion of the gas into vacuum [32]. Individual clusters form having near solid density even though the volume average density is low. Sizes can range up to 1000 Å containing 10^6 to 10^7 atoms per cluster from gases such as krypton and xenon.

When an intense laser pulse irradiates clusters, rapid local ionization occurs leaving a hot and dense plasma. Since individual clusters have near solid density, this will allow for collisional heating processes to dominate and allow for very efficient absorption of laser energy resulting in hot ion temperatures (multi-keV) [33]. However because of their large separation, they will behave independently. This eliminates rapid cooling thus allowing the cluster to stay hot for a relatively long period of time.

In 1996 Ditmire *et al* proposed the nano-plasma model [34] for laser-cluster interactions. Here the cluster is rapidly ionized in the early time evolution of the laser pulse. Subsequent heating and ionization is then dominated by plasma collisional processes in a uniformly expanding plasma sphere. This model requires that accumulated space charge from electrons that have freely streamed away be sufficient to confine the majority of the remaining electrons to the cluster nano-plasma. Subsequent application of this model was then able to explain the linear resonant laser absorption [35]. This effect arises when the electron density is three times that of the critical density in the spherical plasma ($N_e/N_{crit} \sim 3$).

The cluster focus of this dissertation is then to further investigate plasma resonances by examining the time evolution of the third order nonlinearity in a laser heated cluster plasma. Pump-probe experiments and analysis pertaining to third harmonic generation from an anharmonically driven cluster plasma will be presented.

1.3 Plan and Motivation for the Thesis

The generalized motivation for this work is to examine novel techniques and designs for high-energy short pulse laser systems consisting of various laser materials and pulse amplification methods. A majority of this work has been dedicated to experimental investigation and laser construction. However significant emphasis has been placed on numerical simulations to examine both pulse energetics and phase issues. In addition experimental work on third harmonic generation from laser-irradiated clusters is also presented.

The outline of this dissertation will be first to present in Chapter 2 generalized CPA laser design. Emphasis will be placed upon grating size and selection, stretcher and compressor designs, gain media, spectral gain narrowing, and final amplified pulse widths. Following this discussion, Chapter 3 presents a mid-level energy, 20 TW Ti:sapphire short pulse laser design. Aspects of design, development, and characterization will be studied in an effort to produce a bandwidth limited Joule-class 10 Hz laser. The system is designed and constructed to be a daily operational laser to be used for high intensity short-pulse laser-matter interactions.

Chapter 4 introduces two novel Nd-doped laser glasses, which could be used for ultra-broad band high-energy laser amplification. Both glasses have significantly broader spectra (>38 nm FWHM) than currently available Nd:phosphate and Nd:silicate glasses. Calculations for small signal pulse amplification to simulate spectral gain narrowing are presented. The technique of spectral shaping using mixed-glass architecture with an OPCPA front-end is considered. Modeling shows amplified pulses with energies over 1 kJ with sufficient bandwidth to achieve 150 fs pulse widths are achievable with the addition of the new laser glasses.

Chapter 5 will introduce the Glass-Hybrid Optical parametric chirped-pulse amplification Scaled Test bed (GHOST) laser. The GHOST laser is a novel 20 TW hybrid-laser system based upon the techniques of OPCPA and mixed Nd-doped laser glasses. This laser system serves the purpose of proof of concept and scale model of the Texas Petawatt Laser. The Texas Petawatt is a next generation high-energy ultrafast laser now being constructed at the University of Texas at Austin. Numerical simulations of energetics and phase modeling are presented in detail. Also the theory and application of OPCPA is investigated with emphasis on bandwidth-limited short pulse amplification. Further, the precise gain ratio and spectral shaping involved in using a mixed Nd:glass amplifier system for broad spectrum amplification is examined.

In Chapter 6 experiments on third harmonic generation (THG) from laser irradiated argon clusters are presented. In particular an examination of the time evolution of the third order nonlinear susceptibility ($\chi^{(3)}$) from a cluster micro-plasma is investigated. Emphasis on resonant enhancement of THG in conjunction with resonant absorption is discussed. Experimental results are shown in contrast to theory and numerical simulations. Finally Chapter 7 concludes the dissertation with a summary of results and discussing potential directions and future applications of this work.

2 High Energy Chirped-Pulse Amplification Laser Design

The concept and implementation of chirped-pulse amplification (CPA) [7] has revolutionized the development of high intensity lasers. Most intense lasers today utilize this technique to extend the final peak intensity well in excess of standard material damage thresholds. Current technology has matured to where short-pulse lasers are turnkey systems generating pulses as short as a few femtoseconds and/or with amplified energies up to several hundreds of Joules. Repetition rates range from single shot to many megahertz. Total gains routinely exceed 10^6 creating peak powers of over one terawatt.

There are two primary agendas in the use of CPA lasers today. One is to generate high energy densities by focusing the intense short pulse into a small area. Second is to do ultrafast illumination of short timescale events. Both motivations play major roles in the design of CPA lasers. A system can be designed specifically to do one or both of these applications. Therefore the experimental motivation will play a key role in their engineering design. There are many variables that must be considered when designing short pulse high-intensity laser systems. CPA demands rigorous phase and spectral control throughout the entire system, and both possess heavily interlaced aspects.

In this chapter to follow will be an outline and discussion of the critical elements that must be evaluated when designing a high-energy CPA laser. Elements of both spectral phase and amplitude will be presented. Emphasis will be placed on material and component selection, pulse stretchers and compressors, and finally amplification techniques. Each topic that is explored will be in a generic sense to provide general design considerations for intense laser architectures.

2.1 Chirped Pulse Amplification Schematic

Intense lasers are developed in one of two ways: either increase the total energy of the laser pulse, or decrease the pulse width.

$$Intensity = \frac{Energy}{Time \times Area} \tag{2.1.1}$$

Before the advent of CPA, high intensities were achieved by large energies from sizable amplifiers. In this case, energy would dictate size. Material damage thresholds could not tolerate peak intensities beyond a few GW/cm^2. Additionally optical constraints prevent focusing a beam down to less than a few microns. CPA seeks to exploit the inverse proportionality of the time scale of a pulse to its peak intensity.

Today most short pulse lasers utilize a generalized architecture in their design. It is relatively straightforward and is independent of the laser medium, size, and/or repetition rate (Figure 2.1). Pulses are generated in short pulse oscillator, usually a femtosecond class mode-locked oscillator, and then stretched in time using a matched pair of diffraction gratings earning a stretch factor of at least 10^3. The gratings are in an anti-parallel configuration in conjunction with a 1:1 imaging telescope between them [13]. The stretched pulse is then passed through and amplifier medium generating a gain of 10^6 or better at a significantly lower intensity to avoid material damage constraints. Subsequent to amplification, the now energetic pulse is recompressed using a second pair of diffraction gratings in parallel configuration [10]. Typically the gratings are separated by 1 to 2 meters to impart and later remove a large optical dispersion. The first demonstration of this design stretched a 85 fs pulse to 85 ps, and then back to 85 fs [36]. This constituted a stretching and compression factor of 1000.

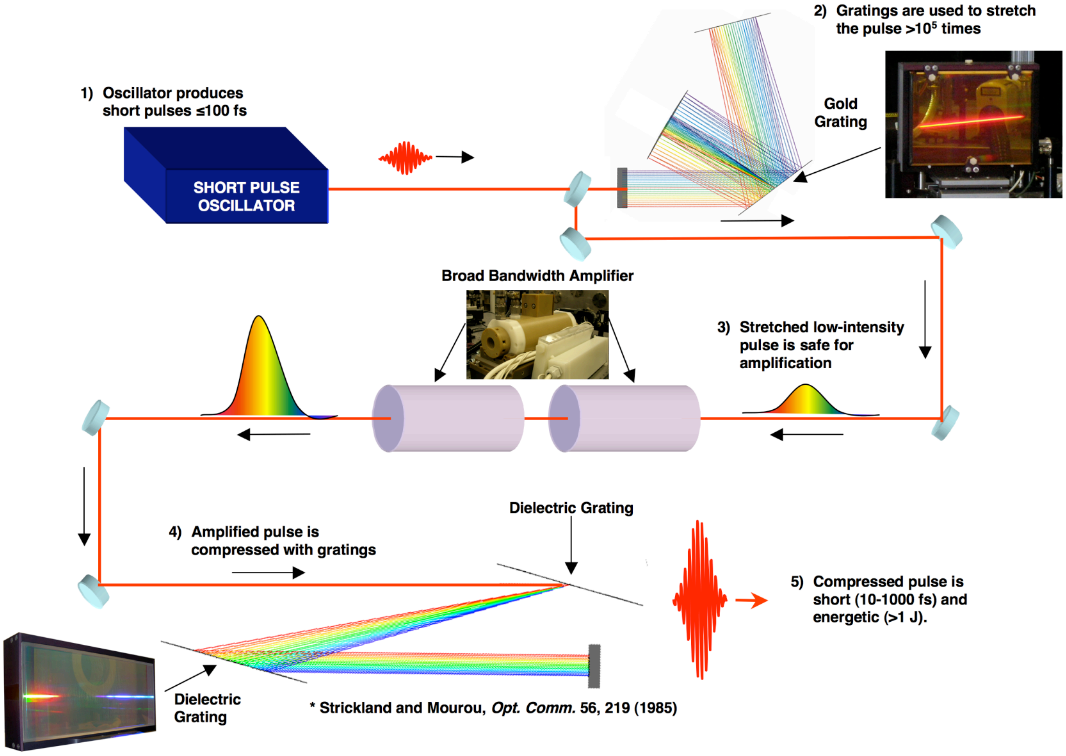

Figure 2.1: Chirped-pulse amplification generalized schematic for short-pulse laser design. An initial short pulse (<100 fs) is stretched by a factor of $>10^4$ using diffraction gratings. The stretched pulse is then amplified in laser amplifiers. Then the pulse is compressed back to near its original duration.

2.2 Spectral Phase and Amplitude

Chirped-pulse amplification as a whole is best understood when viewed from the aspect of frequency space. Each component from the stretcher, amplifiers, and compressor each influence the spectral and phase content of the pulse. Precise management of each optical element, including the optical path length through air, must be carefully balanced in each laser design. The degree of how much regulation is necessary is directly proportional to the amount of bandwidth being supported, and therefore is conjugate to the final pulse width. With shorter pulses comes more phase and spectral management. Several sources have produced in-depth review texts, dissertations and articles to both of these aspects [37-40].

A short-pulse oscillator generates a low energy mode-locked pulse that forms the input to the entire systems. First begin by assuming the initial electric field is described by a transform-limited pulse, which is immediately separable into a transverse term and a slowly varying amplitude centered at frequency ω_0 shown by:

$$E(r,t) = F(x,y)A(t)\left[\frac{1}{2}\left(e^{i\omega_0 t} + c.c.\right)\right]. \tag{2.2.1}$$

First the transverse term is assumed to have no immediate frequency dependence. However this is not true for the case of self-phase modulation, where time and space dependent phase is accumulated by the intensity dependent index of refraction. For now it can be ignored for simplicity. Further only the real component will be analyzed leaving the slowly varying amplitude and frequency components,

$$E(t) = A(t)e^{\mathrm{i}(\omega_0 t + \phi(t))}. \tag{2.2.2}$$

Since the pulse originates in the oscillator, the initial phase $\phi(t)$ is defined to be 0 from the transform limit. *A(t)* is the slowly varying amplitude which in many cases is approximated as a Gaussian-shaped profile,

$$A(t) = A_0 e^{-\left(2\ln 2t^2/\tau^2\right)}. \tag{2.2.3}$$

The electric field amplitude is given by A_0 and τ is the full width half maximum (FWHM) pulse width. Therefore a generalized model of the beginning pulse is defined by

$$E(t) = A(t) e^{i\omega_0 t} e^{i\phi(t)}. \tag{2.2.4}$$

Next the electric field spectrum is then defined by the Fourier transform ($\tilde{E}(\omega) = \Im[E(t)]$) of the electric field envelope:

$$\tilde{E}(\omega) = \int_{-\infty}^{\infty} E(t) e^{-i\omega t} dt = g(\omega) e^{i\eta(\omega)}. \tag{2.2.5}$$

Here $g(\omega)$ defines the spectral amplitude and $\eta(\omega)$ is the spectral phase. This is convenient since any material phase effects directly add in the exponential and spectral amplitude effects are multiplicative to the amplitude. Most effects from materials and amplification can be well understood with this formalism. However it does not account for gain saturation where the leading edge of the pulse experiences a higher gain than the trailing edge.

All propagation and pulse amplification can now easily be illustrated from the viewpoint of the spectral domain. The entire laser system operations can now be applied to equation 2.2.5 generating the amplified spectrum in the form of;

$$\tilde{E}'(\omega) = s(\omega) g(\omega) e^{i(\eta(\omega) + \sigma(\omega))}, \tag{2.2.6}$$

where the spectral amplitude is modified by the term $s(\omega)$ and the accumulated spectral phase is $\sigma(\omega)$. All amplitude effects, including attenuation and amplification, are accumulated in the $s(\omega)$ term. This can include diffraction efficiency from the gratings, spectral clipping from any component, and spectral shaping from the frequency dependent gain in various amplifiers. After ensuing operations of the stretcher, amplification, and compression, the final the output pulse is obtained through the inverse Fourier transform of $\tilde{E}'(\omega)$

$$E'(t) = \frac{1}{2\pi}\int_{-\infty}^{\infty} \tilde{E}'(\omega) e^{i\omega t} d\omega . \tag{2.2.7}$$

A properly designed CPA laser will have been designed where the compressor is able to nearly zero out the phase accumulated by the stretcher and material. In order to properly simulate the pulse through the laser, it is appropriate to include the phase functions from every component in the system. To accomplish this, the spectral phase is expanded in a Taylor series around its central frequency ω_0

$$\begin{gathered}\phi(\omega) = \phi(\omega_0) + \phi'(\omega_0)(\omega-\omega_0) + \frac{1}{2!}\phi''(\omega_0)(\omega-\omega_0)^2 \\ + \frac{1}{3!}\phi'''(\omega_0)(\omega-\omega_0)^3 + \mathrm{O}(\Delta\omega^4)\end{gathered} . \tag{2.2.8}$$

Here ϕ', ϕ'', and ϕ''' are the successive derivatives to the phase with respect to the frequency. The first derivative ϕ' is known as the group delay. The second derivative is called the group delay dispersion (GDD) or second order dispersion. All others are known as third order dispersion (TOD), fourth order dispersion (FOD), etc. The basic assumption is that the Taylor series is well behaved, *i.e.* each subsequent term produces a phase distortion that is significantly smaller than the previous term.

Each component in the system will contribute a specific phase to the pulse. The total phase is then the sum of the phases from each individual element. Treacy showed that the group delay by an optical element is defined by

$$T(\omega) = \frac{d\phi(\omega)}{d\omega} = \frac{l(\omega)}{c} \tag{2.2.9}$$

Physically this is exactly the path delay of light through an optical system of length l [41]. If equation 2.2.9 is Taylor expanded again around the central frequency ω_0,

$$\begin{aligned} T(\omega) &= \phi'(\omega_0)(\omega-\omega_0) + \phi''(\omega_0)(\omega-\omega_0)^2 \\ &+ \frac{1}{2}\phi'''(\omega_0)(\omega-\omega_0)^3 + \mathrm{O}(\Delta\omega^4) \end{aligned} \tag{2.2.10}$$

this will yield the various orders of dispersion. If the second derivative is non-zero, the pulse will then have quadratic phase or a linear frequency chirp. If other higher order terms are non-zero, the pulse will have cubic, quartic, and higher order phase terms. The basic assumption that the pulse is well behaved demands that second order dispersion is significantly larger than the TOD, which is larger than the FOD over the bandwidth of the pulse. Early laser systems only had to account for second order dispersion. However as the bandwidth is increased, higher order terms must be accounted for to achieve a near transform limit pulse after compression. The phase accumulated by a specific material can be calculated through empirical formulas of the index of refraction such as the

Sellmeier equations. Most materials are well documented and available from many sources [42, 43].

It is critical to control all of the phase elements in a system. This also includes the nonlinear phase introduced by the intensity-dependent index of refraction [44, 45]. For low intensities, the linear index of refraction is sufficient to calculate phase. However at higher intensities, the index of refraction becomes larger and is directly proportional to the pulse intensity

$$n_{tot} = n + n_2 I \tag{2.2.11}$$

where n is the linear index and n_2 is the nonlinear index of refraction with units of cm^2/W. It is critical to keep the total nonlinear phase to a minimum to avoid significant temporal pulse distortions upon recompression [46]. The standard measure of the nonlinear phase accumulated in a medium is call the B-integral and is defined as

$$B\left(t\right) = \frac{2\pi}{\lambda} \int_0^L n_2 I(z,t)dz \, , \tag{2.2.12}$$

where L is the length of the material. The total B summed over all components in the system should be ≤ 1 to achieve Fourier transform limited pulses. Nonlinear phase becomes increasingly important in high-intensity pulse amplifiers and components that have large n_2 values such as Faraday rotator glass and crystals.

2.3 Stretcher and Compressors

Original CPA lasers with narrow bandwidths utilized optical fibers to stretch pulses and grating pairs to compress [8, 9]. Positive group velocity dispersion (GVD) was imparted to the pulse in the optical fiber and negative GVD was added with the grating pair (Figure 2.2). The critical drawback was that the nonlinear chirp accumulated in the fiber could not be compensated. With the Martinez compressor design (Figure 2.3), positive GVD could be added using matched grating pairs with the addition of a relay imaging telescope [13]. Modern day CPA uses matched grating pairs in both stretchers and in the compressor. It should be noted that either design (Treacy or Martinez) can be used interchangeably as a stretcher or compressor. However the Treacy design is normally used as a compressor since it has the least number of optical elements.

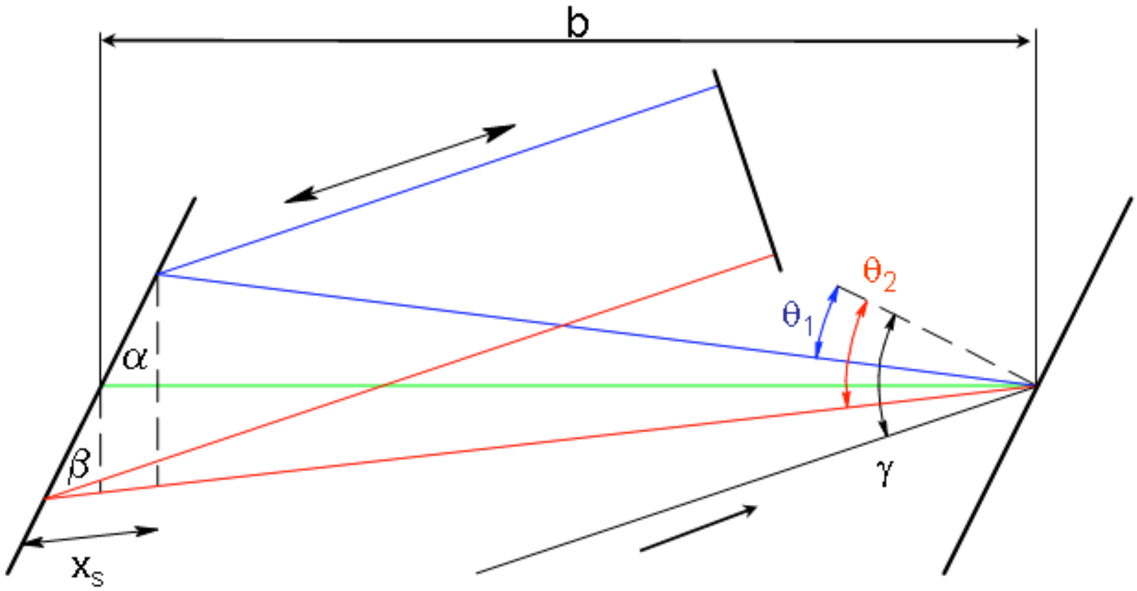

Figure 2.2: Optical layout of 2 grating pulse compressor.

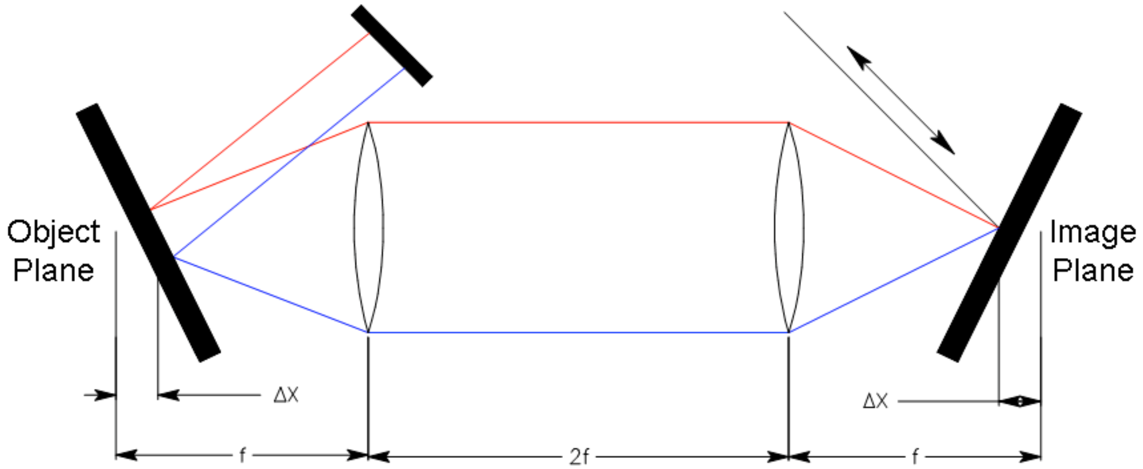

Figure 2.3: Optical Layout of 2 grating 2 lens pulse stretcher.

In the stretcher design (Figure 2.3), blue light travels a longer distance than the red creating a positive chirp. The chirp is then cancelled in the compressor when the blue rays travel a shorter distance than the red. Large stretching ratios over 10,000 have been demonstrated in many systems [20, 47, 48]. An effective stretched time delay Δτ (FWHM) for a grating separation of b in the compressor system can be estimated using the grating equation

$$d\left(\sin\theta_m - \sin\theta_i\right) = m\lambda, \tag{2.3.1}$$

density of the grating. The difference in the optical path length (x_s) between the red and where the incident angle is θ_i and the diffracted angle is θ_m. The diffracted order is chosen to be the m = -1 order closest to the Littrow mount, and d represents the ruling blue light is

$$\Delta\tau = \frac{x_s}{c}, \tag{2.3.2}$$

Here c is the speed of light in vacuum. Two approximations are made in this derivation. First, the green centerline of length b bisects the diffracted angle extremes with angle Δθ *($\Delta\theta = \Delta\theta_2 - \Delta\theta_1$).* This leaves two equal angles of *$\Delta\theta/2$* on either side of *b*. The path of the center frequency is also given by *b*, which is the grating spacing. The second approximation is that triangles α and β are right triangles with the grating surface as the hypotenuse. These approximations can be made due to the small bandwidth because $\Delta\lambda / \lambda \ll 1$. Therefore an expression of time delay for a grating separation of *b* is given by

$$\Delta\tau \approx \frac{4b}{c}\tan\left(\frac{\Delta\theta}{2}\right)\left[\frac{\sin\gamma}{\cos\theta_2} + \tan\theta_2\right]. \tag{2.3.3}$$

The incident angle is γ, and the diffracted angles of the blue and red are θ_1 and θ_2 respectively. For example, consider a beam of 800 nm light with a bandwidth of 33 nm FWHM. The grating angle is set to 56° for the incident beam with a ruling spacing of 1480 lines/mm. If *b* is 1 meter, this will produce a stretched pulse width of approximately 605 ps.

Switching attention to the stretcher design (Figure 3), a simple ray trace analysis shows that the grating spacing is

$$b_{eff} = 2f - 2\left(f - \Delta x\right) = 2\Delta x\,, \tag{2.3.4}$$

where f is the focal length of the lens and Δx is the distance the gratings are placed within the focal length of the lens. A further improvement on the Martinez stretcher has been the all reflective stretcher which eliminates the chromatic error from transmissive lenses [47, 49]. In these designs, the refractive lenses for the telescope are replaced with reflective spherical mirrors to remove chromatic aberrations. The Banks design eliminates spherical aberration from off-axis reflection at the spherical mirror by placing a reflective stripe mirror on the center of the grating (Figure 2.4). This allows the curved mirror to reflect on axis without spherical error.

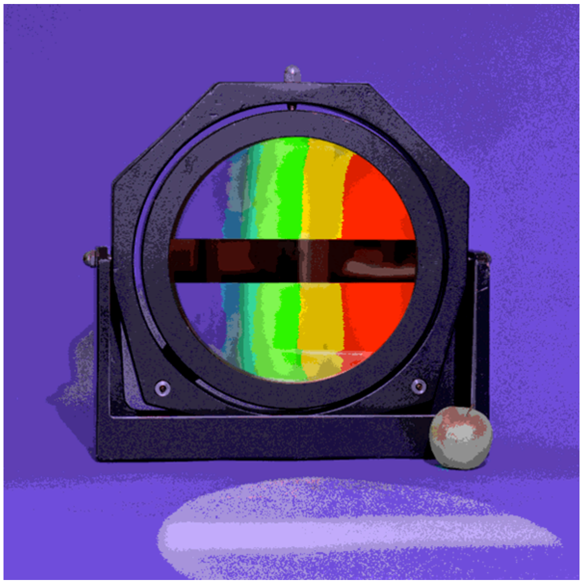

Figure 2.4: Picture of 40 cm diameter gold coated grating used in the Banks stretcher design. The ruling spacing is 1480 lines/mm. A 5 cm tall reflective stripe mirror is placed at the center of the grating. (photo courtesy of LLNL)

Historically the fundamental issues in developing high-energy short-pulse lasers have been overcoming gain narrowing in the laser medium and the development of large area high damage threshold diffraction gratings for pulse compression. However, recent developments in gain media have begun to narrow the issue to primarily grating size. To date, the largest area diffraction grating produced has been the 94 cm diameter gold reflective gratings used for the Livermore Petawatt [50]. The development of this laser was hinged upon the diffraction gratings used for final pulse compression. Diffraction gratings in excess of 50 cm in diameter are extremely costly and require significant procurement times. Further pulse compression gratings must be designed for maximum laser damage thresholds to reduce the size of the optics to the practical scale.

Laser engineers today frequently must start with the compressor when designing a high-energy CPA system. Usually the design parameters of final energy, bandwidth, and ultimately pulse width have been reasonably predicted. Gratings are usually the most critical elements with the lowest damage thresholds in the entire system.

Gratings used in high energy CPA are generally highly efficient planar reflection gratings. They are designed to diffract the first order (m = -1) nearly back along the incident direction (autocollumation or Littrow mount). Diffraction into this order must be efficient since at least 2 to 4 hits on the grating are typical to most compressors. If the singly incident diffraction efficiency is η, then the total transmission efficiency for the compressor is approximately η^4. If η is 80%, this corresponds to a transmission of only 41%. However if η is 95%, the transmission is dramatically increased to 81%.

The design of large diffraction gratings has made significant progress over the last decade. Early gratings made use of metal surfaces whose rulings were made by directly scribing lines into a metallic or dielectric substrate, or by coating a ruled replica of a master substrate with metal. However for high-energy applications where the grating diameters routinely exceed 20 cm, this was not deemed feasible. Therefore the technique of holographic laser interferometry and photolithography was developed to create the rulings. Here an interference pattern is created on a photoresponsive material by two intersecting single frequency coherent beams of light. By using large beam diameters, large uniform diffraction areas have been achieved (>> 300 cm^2) [51]. However, the substrate material is a metal surface. The conductivity of which results in energy absorption and heat deposition creating a relatively low damage threshold (~300 mJ/cm^2).

Recent advancements have been made by placing grating rulings directly into a dielectric substrate on top of a dielectric mirror coating [51]. Dielectric materials have damage thresholds that are significantly higher than those of metals. These gratings developed by Lawrence Livermore National Laboratory have demonstrated diffraction efficiencies up to 98% average over the entire area and with damage thresholds exceeding 1 J/cm^2. This constitutes to better than a factor of 3 improvement in damage threshold and an appreciable improvement in diffraction efficiency. At 98% the transmission efficiency from 4 grating hits improves to 92%.

2.4 Laser and Gain Media

Early developments in CPA were done using dye lasers. Dyes presented a broad bandwidth medium that could be used for mode locking a substantial bandwidth. However due to their low saturation fluences (~ 1 mJ/cm^2), they were not suitable for pulse amplification above 100 mJ. Further dye oscillators were not optimum for pulse generation since they were extremely sensitive to environmental conditions. Moreover they are unstable and difficult to use.

However broad-bandwidth solid-state laser media have lead to the largest advancements in pulse amplification for CPA. Solid-state media generally have high saturation fluences (≥ 1 J/cm^2) allowing for efficient energy storage and extraction. Further advantages are relatively long upper state lifetimes, broad bandwidths, and high damage thresholds. The potential of these materials has been readily exploited in the development of CPA laser.

There have been primarily two fronts in CPA development. First is to produce high energy (>10 J) sub-picosecond pulses from Nd:glass. The other has been production of modest energy (< 1 J) ultrashort pulses (< 50 fs) from a variety of host materials. This section will outline the primary laser media used in CPA lasers today. A discussion of both merits and demerits of several sources is presented.

2.4.1 Ti:sapphire

The most significant advancement in CPA short of optical compression has come from the medium of titanium doped sapphire (Ti:sapphire) [11]. It has single handedly lead the charge into the ultrafast realm. Ti:sapphire has become the most widely used tunable solid-state laser medium to date primarily due to its broad tuning range. Its unique energy-level structure eliminates the possibility of excited-state absorption of the laser radiation. This therefore allows for a broad emission spectrum, which is tunable from 700 to 1100 nm (Figure 2.5). Ti:sapphire also has a large absorption band located in the blue-green visible spectrum. This facilitates pumping from a variety of sources such as double Nd:YAG, Argon ion lasers, and copper vapor lasers.

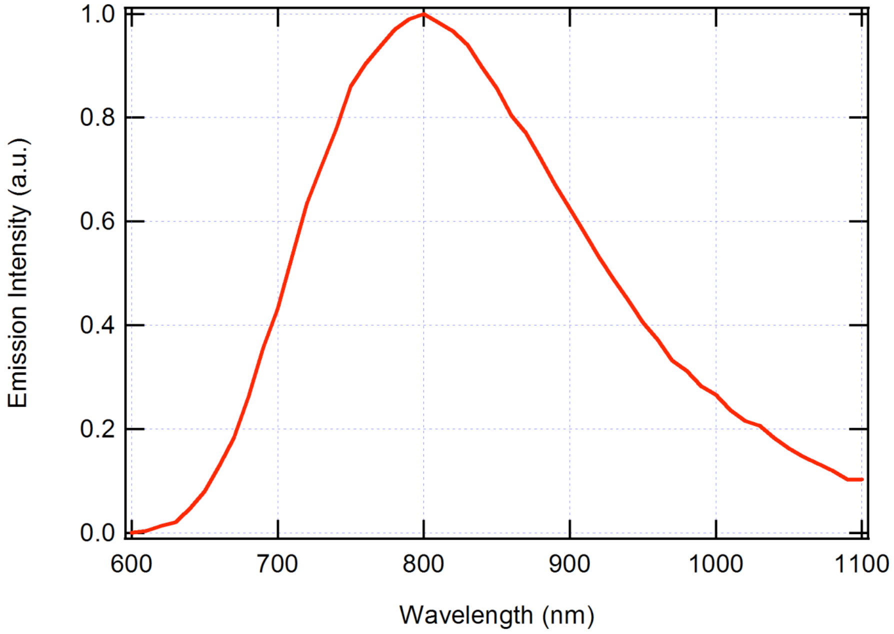

Figure 2.5: Emission spectrum of Ti:sapphire

Ti:sapphire has a relatively high gain cross-section at its peak wavelength ($2.9x10^{18}$ cm^2), however it is difficult to store and extract large amounts of energy due to its limit fluorescence life-time of only 3.2 μs. Because the fluorescence life is so short, flash lamp pumping is very difficult. Therefore it must be pumped by another laser to facilitate large energy storage in a small time window.

Beyond its optical properties, Ti:sapphire has many physical characteristics that also make if favorable. It is chemically inert and mechanically very rigid. Further, since the host medium is sapphire, it has a very high thermal conductivity. Moreover its thermal conductivity dramatically increases when it is cooled to cryogenic temperatures.

Ti:sapphire's most widely used application has been in pulse formation. Since its first demonstration of self mode-locking [12], there has been a significant reduction in achievable pulse durations. Sub-10 fs pulses are now routinely produced from Ti:sapphire oscillators [52, 53], and have even become commercial products. In addition it can also be used as a seed source at a variety of different laser lines. This includes Nd:glass operating beyond 1 μm wavelengths with sufficient bandwidths to produce 100 fs pulse widths. As an amplifier, Ti:sapphire has been used in a wide variety of applications. Due to its good thermal conductivity it has been used to develop kilohertz terawatt laser systems. At lower repetition rates it has been used to amplify a pulse to over 35 J yielding a compressed pulse duration of 33 fs and a focused intensity of 0.85 PW [54].

2.4.2 Nd:glass

Nd:glass was the first medium in which CPA was demonstrated [7]. Laser glass has also been the laser medium of choice for developing high-energy short pulse lasers. Many glasses over the years have been produced, however only two are commercially available to date: phosphate and silicate. Laser glass has many aspects that make it a desired medium for CPA. Foremost laser glasses have emission lines that are inherently broader than many crystals ($\Delta\lambda\sim 28$ nm), because its amorphous structure causes inhomogeneous line broadening. Nd:phosphate and Nd:silicate emit in the 1 μm range (Figure 2.6) and absorb over a large band from the visible to the near IR. Both glasses have a peak absorption line near 800 nm, which make them well suited for diode pumping. However, for high-energy applications they are usually flash lamp pumped to achieve sufficient high irradiance over their fluorescence lifetimes (100-300 μs).

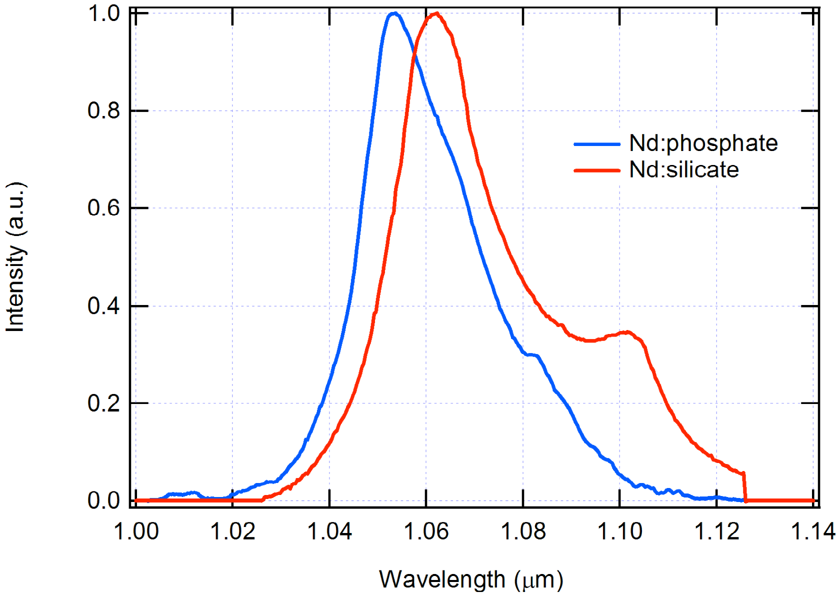

Figure 2.6: Gain cross-section spectra of Nd:phosphate and Nd:silicate laser glass

The most important physical characteristic to laser glass is that it is isotropic in its structure making it very easy to produce in large optical grade quantities in a variety of configurations and sizes. Further it can be doped at very high concentrations with excellent uniformity. However the thermal conductivity of laser glass is considerably lower than most crystals. This causes them to be best suited for low repetition rates and single shot modes depending upon the aperture size of the amplifier. Nd:glasses have relatively large emission cross-sections ranging from $2.9 - 3.5 \times 10^{-20}\,\text{cm}^2$. Laser glasses also have high saturation fluences, which make them suitable for high-energy storage and extraction. They also have small nonlinear indices of refraction ($2.5 - 4.2 \times 10^{-16}\,\text{cm}^2/\text{W}$), which allows for significant energy extraction at high intensities.

Early work in laser glass was done to produce picosecond class pulses at the several Joule level [8, 55, 56]. However hybrid systems including a Ti:sapphire front end were able to produce shorter pulses [20, 57]. Most petawatt laser systems today are being developed with high-energy amplification in laser glass. Several groups have and are combining silicate and phosphate glasses to increase the net spectral amplification bandwidth to produce shorter pulses [22, 23, 27]. Experiments pertaining to this technique will be discussed in detail in chapter 5.

2.4.3 Optical Parametric Chirped-Pulse Amplification

A recent advancement in CPA has been the advent of optical parametric chirped-pulse amplification (OPCPA) [25]. Parametric amplification has demonstrated a unique advancement in many ways. First, parametric amplification provides extremely high gain from a single pass in one crystal ($>10^3$). Second, when properly phase matched it can have nearly uniform gain over an extremely large spectrum (≤ 400 nm). In fact, under strong saturation of the OPA, gain broadening can occur. Phase matching in beta-barium borate (BBO) at 820 nm has demonstrated gain-broadening of a 26 nm FWHM stretched pulse to 49 nm FWHM with a total gain of 10^6 from two single-pass crystals [58].

OPCPA relies on parametric amplification in nonlinear media. The nonlinear media acts as a coupling source which allows for efficient energy transport from one energetic beam (pump) to a lower intensity signal beam [59]. Conservation of energy and momentum also dictates the creation of an idler beam, which is the net difference in the energy and momentum transfer (Figure 2.7). In contrast to conventional energy storage amplifiers, energy transport occurs only when the signal and pump beams are spatially and temporally overlapped in a properly phase matched medium.

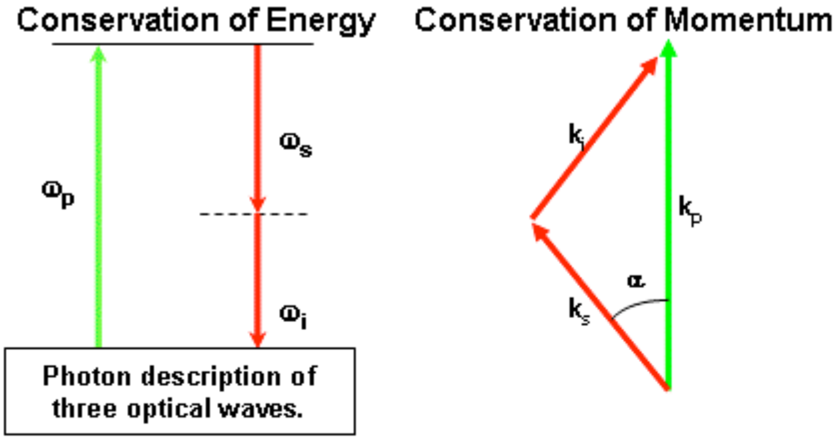

Figure 2.7: Conservation of energy and momentum for optical parametric chirped-pulse amplification (OPCPA)

The difficultly of applying parametric amplification to CPA is two-fold. The first problem stems from temporal overlap of the pump and seed beams. Most pump lasers are Q-switched, frequency doubled Nd:YAG lasers operating at 532 nm with 10 ns scale pulse durations. In contrast stretched pulses are usually on the order of 1 ns. Thus energy transfer occurs on a very short time scale leaving a majority of the pump energy unused. The second difficulty arises from the intensity dependent gain. Energy transfer and gain is directly dependent upon the pump intensity. In Q-switched pulses, the temporal waveform is usually Gaussian and therefore not uniform. In OPCPA the gain is extremely high, and small intensity variations result in significant temporal and therefore spectral modifications to the seed pulse. OPCPA therefore demands a highly formatted pump source with near uniform spatial and temporal profile to present suitable efficient amplification. Pump lasers of this kind are generally very costly requiring single longitudinal mode operation with top-hat spatial profile beams.

With these difficulties in mind, OPCPA poses a great benefit to short pulse laser development. The amount of amplification material is usually very small when compared to energy storage amplification techniques. This results in very low dispersion accumulation on the seed. Second there is little to no heat loading in the crystal producing no thermal aberrations. Also, most nonlinear media have low nonlinear indices of refraction limiting B-integral effects. Nonlinear media are now available in many sizes with apertures up to many tens of centimeters. Many groups are now implementing OPCPA into their short-pulse lasers. If suitable pump lasers become more available, OPCPA could present the path to the first 10 PW laser [25].

2.4.4 Other Solid-State Laser Media

There are many tunable solid-state laser sources available today; however only a few have been aggressively investigated for CPA applications. Chiefly researchers are interested in broad-spectrum tunability coupled to a stable reliable medium. No material has proven better than Ti:sapphire, however many efforts continue to investigate alternative sources. The materials of Cr:LiSrAlf^6 (Cr:LiSAF, or LiSAF), Alexandrite, and Ytterbium-doped phosphate glass (Yb:glass) are each actively researched materials. The attributes and physical characteristics of each will be discussed in this section. Table 2.1 compares the pertinent optical properties of each material.

The biggest interest in Cr:LiSAF from a CPA viewpoint comes from its long fluorescence lifetime when compared to Ti:sapphire. A lifetime of 67 μs allows it to be flash lamp pumped. It also possesses a large tuning range of 180 nm. Although it has a slightly longer peak emission wavelength, it has good spectral overlap with Ti:sapphire making it most suitable for amplification of pulses originating from Ti:sapphire oscillators. It also has a large saturation fluence allowing for ample energy storage in the medium. Flash lamp pumped Cr:LiSAF has been used successfully to amplify broad-band pulses to over 1 Joule [60] and generate TW class pulses [16].

Optical Properties	**Cr:LiSAF**	**Alexandrite**	**Yb:glass**
Peak-Fluorescence Wavelength (nm)	850	750	1032
Line Width (nm) FWHM	180	120	56.5
Peak Stimulated Emission Cross-Section (cm^2)	0.5×10^{-19}	1.0×10^{-20}	1.4×10^{-20}
Saturation Fluence (J/cm^2) at peak emission wavelength	4.7	26.5	13.7
Calculated Radiative Lifetime (μs)	67	260	274
Refractive Index at Peak Spectral Emission	1.41	1.74	1.52
Nonlinear Refractive Index (esu)	0.5×10^{-13}	$\sim 1.0 \times 10^{-13}$	1.22×10^{-13}*

Table 2.1: Comparison of optical properties of alternative tunable solid-state laser media used in chirped-pulse amplification.

There are several key physical characteristics of Cr:LiSAF which have hindered wide spread use of this material; chief of which is the availability of high optical quality crystals. The crystal is relatively soft and mechanically weak, with many physical properties more similar to Nd:glasses than Ti:sapphire. Also its low thermal diffusivity ($\alpha = 0.019$ cm^2/s) permits only modest repetition rates of about 1 Hz. Large aperture rods have been produced as big as 25 mm in diameter, however optical purities are generally poor.

Alexandrite has been another interesting material. It has a long fluorescence lifetime making it also suitable for flash lamp pumping. It is a low gain medium allowing for significant energy storage and large pulse amplification. However its extremely large saturation fluence makes it virtually impossible to saturate using short pulses. Alexandrite absorbs strongly in the visible spectrum with two peaks at 410 and 590 nm. It is a hard crystal that is chemically stable and performs well under high thermal loading. Its peak emission is at 750 nm with a 120 nm tunable spectrum. It does overlap spectrally with Ti:sapphire, but not to the level at which broad spectrum pulse amplification can be done to generate ultrafast pulses. Early CPA work in Alexandrite was done as an amplifier medium for mode-locked dye lasers [61].

Ytterbium doped phosphate glass (Yb:glass) is a unique material that poses an alternative to Neodymium glasses. Both glass have very similar material characteristics, but Yb:glass is optically very different. Foremost is that it has an emission line width of 60 FWHM. This represents a factor two more of bandwidth when compared to Nd:glasses. Next it is strongly peaked at its absorption line of 970 nm. With a lasing peak at 1032 nm, this constitutes a quantum defect of 0.91 producing very low heat loading in the gain media when pumped at this line. Further it has an extremely long upper state lifetime of 2000 μs allowing for tremendous energy storage with a saturation fluence of 13.7 J/cm^2.

The critical downside to this medium is also its chief benefit. The strongly peaked absorption line at 970 nm makes it unsuitable for flash lamp pumping and well suited for diode pumping. However diodes at this wavelength are not readily available. Further the high saturation fluence requires that it be pumped very hard. These two effects make it difficult to generate energetic pulses above 1 Joule. In contrast, current developments on this material are being done to produce the first all diode pumped Petawatt CPA laser with 150 J at 150 fs [62].

2.5 Gain Saturation and Spectral Gain Narrowing

Gain saturation and spectral gain narrowing propose the next major hurdles in CPA. Spectral bandwidth is of critical importance to CPA lasers since because it directly equates to pulse width. Femtosecond pulses generally have bandwidth on the order of a few percent. This comes from the uncertainty principle. Applied to CPA lasers it is called the time-bandwidth product. The time-bandwidth product requires that the product of $\Delta\nu\Delta t$ be greater than approximately 0.5. The actual product value is defined for a given pulse shape with given pulse width (Δt) and bandwidth ($\Delta\nu$). For example for a Gaussian temporal shaped pulse, the intensity is defined by

$$I(t) = I_0 Exp\left[-4\ln 2\left(\frac{t^2}{\tau_{FHWM}^2}\right)\right]. \tag{2.5.1}$$

The pulse is defined in FWHM values for the pulse width (τ_{FWHM}). The time-bandwidth product of this pulse is then

$$\Delta\nu\Delta t = 0.441. \tag{2.5.2}$$

For a hyperbolic secant square pulse (sech^2) the intensity shape is

$$I(t) = I_0 \operatorname{sech}^2\left(\frac{1.76t}{\tau_{FWHM}}\right). \tag{2.5.3}$$

Again the pulse width is defined in terms of the FWHM value. The time-bandwidth product in this case is then

$$\Delta\mathrm{v}\Delta\mathrm{t} = 0.315. \tag{2.5.4}$$

Another way this can be viewed is in terms of the wavelength. For Gaussian pulses, the time-bandwidth product is given by

$$\Delta\mathrm{t}\Delta\lambda = 1.47\lambda_0^2, \tag{2.5.5}$$

The central wavelength λ_0 and bandwidth $\Delta\lambda$ are defined in microns and the pulse width is defined in femtoseconds. For the sech^2 pulse, the product is

$$\Delta\mathrm{t}\Delta\lambda = 1.05\lambda_0^2 \tag{2.5.6}$$

Consider a Gaussian shaped pulse of 50 fs FWHM. The associated bandwidth is then 20 nm. For a 20 fs pulse, the bandwidth is then 50 nm. These bandwidths must be maintained as much as possible throughout the entire laser since narrowing of the spectrum directly corresponds to longer amplified pulses. Some effects that cause spectral narrowing are gain narrowing from frequency dependent gain, frequency dependent reflectivity in dielectric mirrors, and spectral clipping within the stretcher and compressor optics.

Most gain media have frequency dependent gain cross-sections and therefore will spectrally modify the pulse during amplification. Under high gain scenarios where the pulse is amplified many orders in magnitude, the pulse bandwidth can be greatly diminished because the relative frequency amplitude within the pulse is modified. Ti:sapphire has a frequency dependent gain coefficient with its peak centered near 800 nm . Most short-pulse lasers include many tens of nanometers of bandwidth within each pulse. A 20 fs pulse with 50 nm (FWHM) of bandwidth centered at 800 nm will experience a vastly different gain at the various wavelengths. At 800 nm the cross-section is near $3.0\text{x}10^{-18}$ cm^2, where as at 750 and 850 nm the cross-section is reduced to about $2.3\text{x}10^{-18}$ cm^2. In the small signal regime, the gain is exponential. Therefore this constitutes a factor of two difference in the gain between the center frequency and the wings.

A simulation of spectral gain narrowing is relatively straight forward (Figure 2.8). Here a pulse centered at 800 nm with 39 nm FWHM of bandwidth is amplified in Ti:sapphire. Amplification is done in small signal regime avoiding the effects of gain saturation. The pulse is amplified by a factor of 10^6 and is subsequently narrowed to 27.5 nm FWHM. This constitutes a loss of nearly 30% of the original spectrum. If the original spectrum is a Gaussian shaped pulse, the pulse width from the time-bandwidth product is 24 fs. The amplified spectrum results in a 34 fs gain-narrowed pulse.

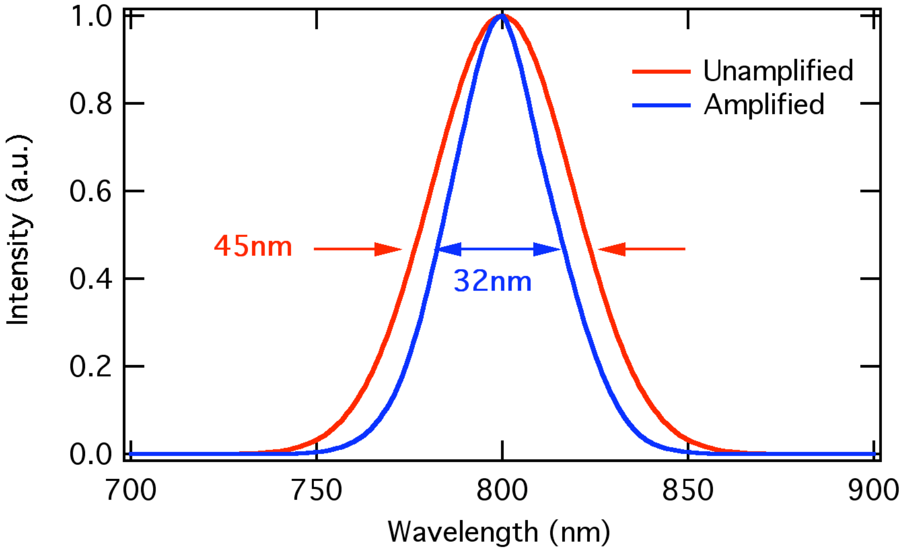

Figure 2.8: Simulated spectral gain-narrowing in Ti:sapphire amplifier. A seed pulse with 45 nm (FWHM) of bandwidth is amplified by 106 in the small signal regime. The amplified spectrum is gain-narrowed to 32 nm (FWHM).

The simulation in Figure 2.8 was amplified in the small signal regime and therefore did not account for gain saturation. Gain saturation occurs when the leading edge of the pulse experiences a higher gain than the trailing edge. This effect comes apparent when the pulse fluence nears that of the saturation fluence. The saturation fluence of a laser material is defined by [63]

$$F_{sat} = \frac{h\upsilon}{\sigma(\omega)}. \tag{2.5.7}$$

Here h is Planck's constant, v is the transition frequency, and $\sigma(\omega)$ is the frequency dependent gain cross-section. The saturation fluence is an important measure of the amount of energy per unit cross-sectional area that can be extracted from a practical laser device. When a pulse nears saturation fluence, the leading edge will experience gains that significantly reduce the total excited atom population of the laser medium. Therefore the trailing edge sees a net lower gain from the amplifier. In CPA systems, the pulse is spectrally stretched in time; therefore different wavelengths will then experience different excited atom populations and gains. If an amplifier is strongly saturated, the spectrum will be significantly shifted toward the red side if the pulse is positively chirped. This steepening of the leading edge will result in the production of wings in the compressed pulse. Ultimately the spectrum after amplification must be smooth and continuous to yield a fast rising, pre-pulse free compressed pulse. This can be better understood by considering a square shaped spectrum. The Fourier transform of this spectrum produces a sinc^2 shaped pulse with significant pre- and post-pulses. The extra pulses are damaging in two ways. First they rob energy from the main pulse effectively lowering it peak intensity. Secondly they can be very intense and therefore detrimental during experiments.

Many groups have sought to compensate for gain narrowing and saturation in various ways. One technique is to spectrally offset the center wavelength away from the peak emission line of the amplifier [64]. Another method is to use spectral filters to modify the spectrum before amplification [14]. Here an optical filter is used to modify the spectrum in the pulse stretcher. Yet another technique is to create spectrally dependent loss directly in the amplifier [65, 66]. In this case an etalon is introduced to the amplifier to induce spectral loss at the peak wavelength of the gain medium. Most importantly the design of an amplifier can directly determine the amount of spectral shift in the laser pulse.

2.6 Amplifier Design

As stated before, the amplification process can significantly shape and shift the spectrum of the pulse. Moreover proper amplifier design can determine the amount of spectral gain-narrowing and spectral shift. There are a variety of options that must be considered that vary with different gain media, final pulse energies and pulse widths. This section will present the basic concepts in the various amplifier designs being used today in CPA laser systems.

2.6.1 Preamplification

Most CPA lasers use a high gain preamplification stage that immediately follows the stretcher. Generally oscillators produce a 1 nJ scale pulse that requires amplification by a factor of at least 10^6. High gain preamplifiers serve to do most of the amplification in any CPA laser producing gains in excess of 10^7 in one laser medium. Routinely sub-10 mJ pulses are produced from this stage. Regardless of wavelength, there are three amplification methods being currently used; regenerative amplifiers, multi-pass amplifiers, and OPAs. All three have distinct benefits and downsides.

A regenerative amplifier (regen) is fundamentally a laser cavity in itself (Figure 2.). In this design a low energy seed pulse is injected into the cavity usually using a fast optical switch like a Pockels cell and polarizer. Once the pulse is trapped in the cavity it will make many roundtrips (>10) through a low gain media. When saturation is achieved, the pulse is ejected from the cavity by again using the optical switch. The benefits of regens are many. Foremost is that the regen is an oscillator which is usually designed to support only the TEM_{00} mode of the cavity. This will then serve to filter spatially the amplified pulse producing a Gaussian-profiled amplified pulse. Additionally the cavity helps to stabilize the laser reducing pointing error, which results from large optical path lengths as in large CPA lasers. Another benefit is that the seed can be well overlapped with the mode of the cavity, which can result in extraction efficiencies that exceed 25%. Regens are usually run in a low gain configuration to avoid amplified spontaneous emission (ASE) buildup in the cavity. If ASE is amplified too much in the cavity, this will serve to be energetic pedestal that the main pulse will travel upon in subsequent amplifiers. It can rob significant amounts of energy from subsequent amplifiers, and most importantly it will not compress. Another negative to regens is that the pulse makes many roundtrips through high index materials like the gain medium and the Pockels cell. This will add significant amount of dispersion to the pulse make compression difficult. Low gain regens also tend to gain-narrow the spectrum more than other amplifier designs [67]. This effect arises when strong saturation is achieved in an amplifier and the spectral wings experience a higher gain than the peak.

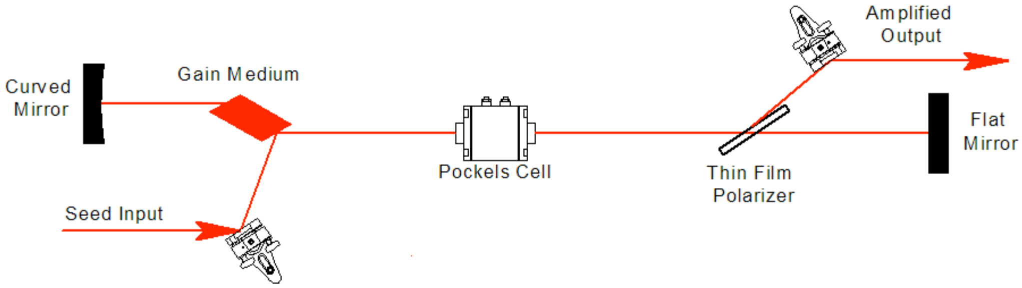

Figure 2.9: Schematic Layout of a regenerative amplifier.

An alternative to regenerative amplification is the high-gain multi-pass amplifier (Figure 2.9). In this design the pulse makes many passes through the gain medium without the use of the optical cavity. A larger area gain volume is used to facilitate larger geometric volume needed for multi-passing the amplifier. Gains tend to be higher than that of a regen and therefore fewer trips through the gain media are needed. Ultrafast lasers with large spectra benefit most from this design. With a smaller optical path length through high index materials, the pulse accumulates less dispersion. Further, saturation is achieved earlier, which provides a broader amplified spectrum. However pulse steepening and spectral shift plays a more dominant role. Additionally, the laser is more subject to pointing error from the unstabilized long optical path length.

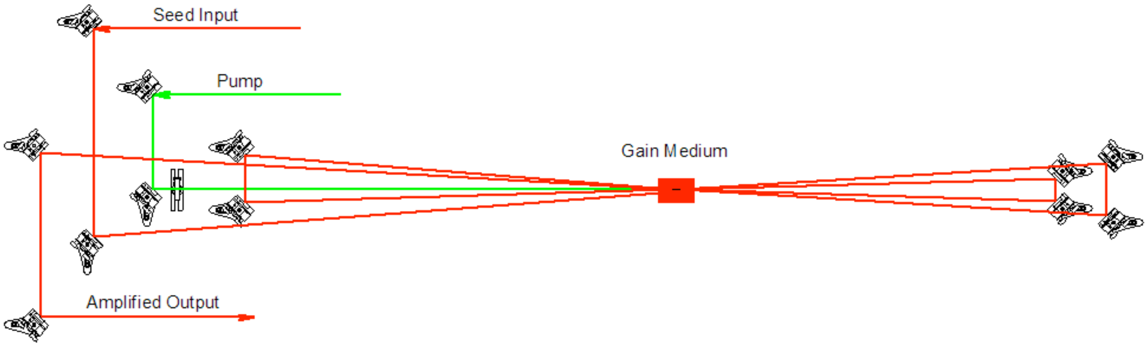

Figure 2.10: Schematic layout of a multi-pass amplifier

A recent option to pulse amplification has been parametric amplification. As discussed in section 2.4.3, OPCPA presents an extremely broad and uniform amplification bandwidth. Single pass gain in one crystal can easily exceed 10^3. Preamplification can be accomplished in just two crystals with the additional benefit of spectral broadening [26]. The optics and setup are also generally simple and few. However OPCPA requires a highly formatted pump laser, which can easily offset its benefits. Moreover if strong saturation is achieved in the OPA, the spectrum will experience significant spectral steepening in the wings and therefore will not be immediately suitable for compression.

2.6.2 High Energy Amplification

In high-energy CPA lasers, the pulse is generally amplified up to and beyond the 1-Joule level. Preamplification generally serves to amplify the pulse to the milijoules regime. This constitutes the bulk of the gain in most lasers; however it becomes increasingly difficult and expensive to progress forward to higher energies. Crystal purity becomes a significant hurdle in large aperture designs. Regardless of the laser medium, contributory amplification is regularly done in either single or multi-pass amplifier designs. Different designs are variations of the common theme; a single medium is multi-passed either spatially or through various optical techniques.

Ti:sapphire is a high gain laser material that is usually not available in long crystal lengths due to crystal impurities. Most crystals are rarely bigger than 2 cm in diameter or length. Therefore many passes must be made through the crystal in order to extract all of the stored energy. These thin disk shapes make it well suited for geometrically multi-pass (bowtie) amplifiers. In this case the pulse travels through the crystal at a small angle away from the normal to crystal axis in an effort to separate spatially the beam pass by pass. This design is extremely simple relying on very few optical components. However, as the diameter of the seed beam increases, the length of the bow-tie arms must increase to spatially separate the larger beam. This therefore requires a larger optical path length. In saturated amplification, the pulse will become super-Gaussian in its spatial profile and therefore will not propagate long distances without significant spatial modulation. In lower gain lasers, this can be difficult requiring relay imaging and spatial filtering. In high gain amplifiers, the gain media itself can serve as an effective spatial filter cleaning the beam at each subsequent pass. Bow-tie amplifiers have been routinely used in Ti:sapphire CPA laser to amplify the pulse well beyond 1 Joule [19, 68, 69].

In other media such as glass and Cr:LiSAF, longer crystal lengths are readily available. High gains are achieved from longer optical path lengths through the crystal. These crystals are not suitable for geometric multi-passing; however sufficient energy can be extracted from a single pass in the longer medium. In large aperture lasers (> 1cm) the pulse is usually one or two passed through a rod or slab geometry amplifier. In many cases two passes are achieved by retro-reflection and rotating the seed polarization 90°. This pulse is then ejected using a thin-film polarizer. In a glass amplifier, a medium that is isotropic, a quarter waveplate can be used in two passes to rotate the polarization. However crystals have preferred optical axes and therefore must use Faraday rotators. This can be difficult at high intensities because Faraday glass and crystals both possess high nonlinear refraction coefficients.

High-energy CPA lasers routinely rely on image relaying from amplifier to amplifier to avoid spatially modulation on the beam, which can easily damage optics even at modest energies. Telescopes and spatial filters are used to relay image planes between each amplifier and finally into the compressor. Strongly saturated super-Gaussian profile beams do not freely propagate long distances without developing spatial modulation; therefore extreme care must be given when injecting the beam onto low damage threshold materials such as the compression gratings.

2.7 Conclusion

This chapter has detailed many of the critical aspects of high-energy CPA laser design. A discussion spectral phase and modulation outlined the important components to describe a chirped pulse and subsequent amplification. Emphasis was placed on stretcher and compressor design for high bandwidth transmission, and several grating technologies were discussed. Further, spectral gain narrowing, its consequences, and avenues for compensation were presented. Fundamentally conservation of the pulse spectrum and its phase are paramount to CPA design.

There are several mature laser media available today for CPA lasers, however the most widely used is Ti:sapphire. No other material has proven to be a better source for generating short pulses. Further it has been the medium of choice for both commercial and laboratory scale CPA lasers. Nd:glass continues to be the best avenue for high-energy CPA lasers, however its limited bandwidth is its Achilles' heal. OPCPA presents a new avenue toward broad-bandwidth pulse amplification. However it has definite disadvantages in the pump laser design that currently hinder it for energetic implementation beyond 1 Joule.

High-intensity short-pulse lasers continue to be rich area of scientific interest. There are many details that must be evaluated in each CPA laser design. Each component must be considered individually and in concert with the integrated laser system in order to produce a well formatted, intense short laser pulse. Developing new technologies will see the implementation of even more intense lasers spawning new scientific discoveries.

3 Design and Performance of the THOR Laser

The medium of Ti:sapphire has been the most versatile host to chirped-pulse amplification in almost every way. It is routinely used for pulse formation and subsequent amplification. Its emission spectrum, which exceeds 400 nm, has allowed for the creation of sub-10 fs pulses [52, 53], and has seen them amplified to over 35 Joules generating 0.85 PW from a single laser medium [54]. In small apertures (< 15 mm), it is a very affordable crystal and is well suited for university-scale research lasers. It has a large gain cross-section and an extremely large tuning bandwidth. Table 3.1 summarizes the pertinent optical properties of this crystal. It has a sufficiently high saturation fluence of 0.9 J/cm^2, which allows for energy extraction on the order of 1 joule from small aperture rods. However it does have a relatively short fluorescence lifetime making it unsuitable for flash lamp pumping. Therefore high-energy pumping must come from another laser source, preferably a Q-switched frequency doubled Nd:YAG laser. Because the host crystal is sapphire (Al_2O_3), it has excellent thermal properties and can diffuse very large thermal loading from high average power pumping.

Several terawatt-class Ti:sapphire lasers have been constructed over the last 15 years, each investigating new ways to achieve shorter pulses, higher energies, and ultimately higher intensities [14, 15, 19, 68-70]. Various techniques of amplifier design, stretcher and compressor design, and pulse management have each been individually investigated thoroughly to determine the most stable terawatt Ti:sapphire laser architecture. It is the motivation of this chapter to present the design and performance of a new 20-TW Ti:sapphire laser system that has been constructed at the University of Texas at Austin.

Optical Properties	Ti:sapphire
Peak-Fluorescence Wavelength (nm)	800
Line Width (nm) FWHM	250
Peak Stimulated Emission Cross-Section (cm^2)	2.8×10^{-19}
Saturation Fluence (J/cm^2) at peak emission wavelength	0.9
Calculated Radiative Lifetime (μs)	3.2
Refractive Index at Peak Spectral Emission	1.76
Nonlinear Refractive Index (esu)	1.3×10^{-13}

Table 3.1: Optical properties of Ti:sapphire

The Texas High-Intensity Optical Research (THOR) Laser is a 700-mJ, 38 fs system that operates at 10 Hz. It was designed as a second generation high-intensity laser that supports various research activities pertaining to high-field sciences. The major design criterion being that it is easy to operate with minimum alignment, and that it is extremely stable for daily operation. Moreover it must be simplistic in its design and robust to serve as an instructional laser for graduate students. This chapter presents a detailed description of the design, modeling, and performance this laser. The laser is discussed at each major component.

The concept of the THOR laser was designed around a master-oscillator power-amplifier (MOPA) configuration (Figure 3.1). The laser is centered at 800 nm with sufficient bandwidth to support 100 nm of spectral content. A commercial Ti:sapphire oscillator is employed producing a sub-30 fs pulse. The stretcher and compressor each

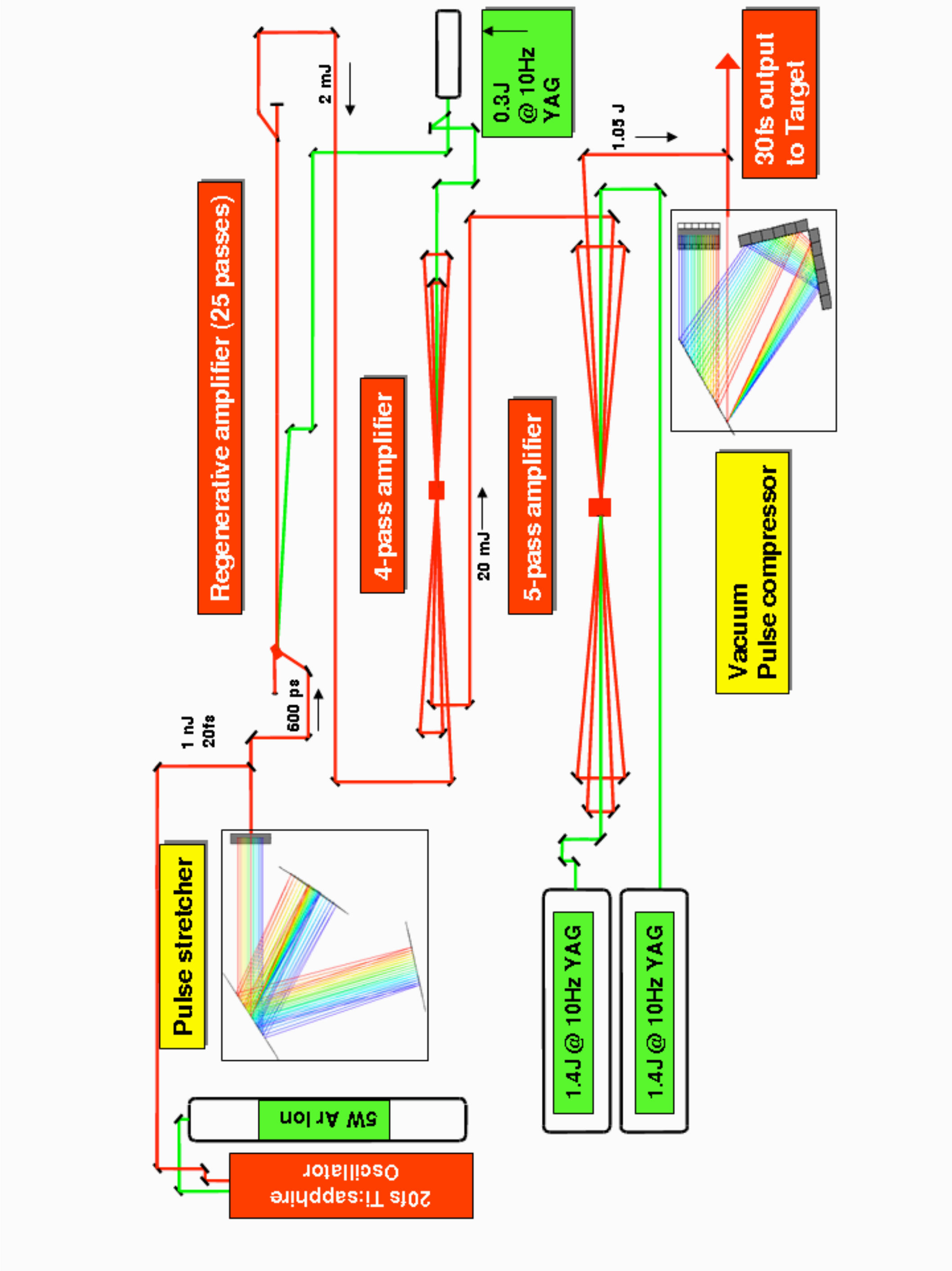

Figure 3.1: Schematic diagram of THOR laser system

consist of a single gold holographic grating with all reflective optics. The laser also has three high-gain amplification stages pumped by commercial Nd:YAG lasers to produce a ≥ 1 J amplified pulse before compression.

In designing this laser system, it was useful to examine three critical elements of the laser before a bulk of the development was performed. First was to estimate a how much spectrum would survive an integrated gain of 10^9, assuming a 1 nJ pulse is amplified to 1 Joule. Second, how much bandwidth could be transmitted in the compressor given a final grating diameter? Third, what is the transform limited compressed pulse width?

To answer the first question of gain narrowing, a simple one dimensional amplification model was developed. Ti:sapphire has a frequency dependent gain cross-section, therefore amplification of many orders of magnitude will dramatically change the final pulse spectrum. The seed pulse was simulated as a 45 nm FWHM Gaussian spectrum centered at 800 nm, which is at the peak of the Ti:sapphire emission curve. The design also mandates the pulse is stretched to 600 ps. Also amplification is simulated entirely in the small signal regime. Gain saturation is a primary concern to CPA design, especially in high gain media such as Ti:sapphire. However, for the purposes of this simulation it is ignored, because we want to understand qualitatively the more dominant effects of the shaped gain spectrum on the seed. A more thorough energetics model, which includes saturation effects, is presented in the following sections. The amplification factor is defined by $G = Exp[\alpha\sigma(\lambda)]$, where $\sigma(\lambda)$ is the wavelength dependent cross-section and α is the amplification factor. The THOR laser is designed to have a net gain of 10^9 so the amplification factor α is scaled accordingly. The results of this simulation, which are presented in Figure 3.2, show the amplified pulse is gain-narrowed to 28 nm FWHM resulting in a 38% loss of the original spectral content. The compressed pulse duration is then estimated from the time-bandwidth product. This dictates that the transform limited pulse width for a 28 nm FWHM Gaussian spectrum will be approximately 34 fs.

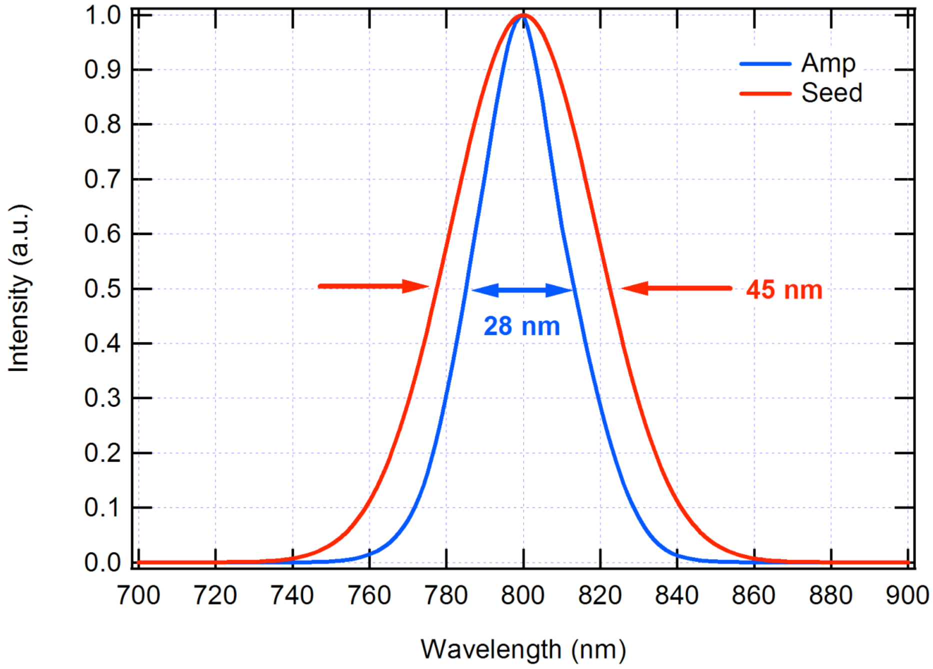

Figure 3.2: Simulated gain narrowing of a laser pulse amplified by 10^9. Seed pulse is a 45 nm (FWHM) Gaussian spectrum. The amplified pulse is gain-narrowed to 28 nm (FWHM).

Figure 3.2 not only predicts the gain-narrowing and pulse width, but it also details how much bandwidth must be passed through the compressor to compress the pulse. To avoid spectral clipping, which can result temporal wings after compression, a bandwidth of at least 80 nm (760-840 nm) must be then passed through the compressor. Further, the amplified pulse energy is designed to be 1 joule. Since the damage threshold for gold gratings is approximately 300 mJ/cm^2, the final beam size entering the compressor is set to be 5 cm. This is oversized to lower the beam fluence. With these details known, a final compressor grating size can be estimated using equation (2.3.1) and equation (2.3.3). These dictate the grating spacing. To compress a 600 ps pulse with 80 nm of bandwidth, the grating spacing is of the order of 1.4 meters. Therefore the diffracted beam size on the second grating of the compressor is about 28 cm in diameter. For a single grating compressor, the grating will have to be wide enough to accommodate both the input and diffracted pulses side by side. The final grating diameter is then estimated to be 40 cm. These simple calculations were used in the preliminary design of the THOR laser and can be transferred to other systems alike.

The subsequent remainder of this chapter will present design and characterization of the laser. Section 3.1 covers the energetics modeling of all amplification systems, and section 3.2 presents the laser design and performance characteristics. Focus is placed on beam quality, spectral management, and phase control.

3.1 Modeling the engergetics of the THOR Laser

To properly understand the pulse energy evolution throughout the amplification process, it is necessary to conduct numerical simulations to study the non-analytical effects of gain saturation. In many cases it is convenient to use a simplified pulse envelope where the transverse component is omitted. However in most systems the gain profile of the medium is not spectrally uniform. Therefore this simplification routinely over estimate the energy buildup, and can miss pertinent gain guiding effects imposed by the gain medium.

This section begins by first deriving gain coefficients in the small signal and saturated regimes. The small signal gain coefficient is derived using the formalism presented by Saleh and Teich [71]. The saturated gain coefficient is derived in the manner of Siegman [72]. Finally a numerical simulation of the THOR energetics investigating gain saturation on the seed pulse is presented. The simulation is performed in 1-dimensional case where the transverse profile of the beam is ignored, and then in the 2-dimensional case where it is included.

3.1.1 Small Signal Gain

To begin, consider a monochromatic plane wave traveling the $\hat{z}$ direction of an optical medium. The medium has a length in the region of $0 \le \mathrm{z} \le \mathrm{L}$. The intensity of the plane wave is proportional to the square of the electric field ($I(z) \propto Abs[E(z)]^2$). For the purpose of this derivation, only 4 level systems are considered, with the approximations that pumping of the upper level and the emptying of the lower level occur infinitely fast. This reduces the system to a simplified two level problem. The numbers of atoms in the lower and upper levels are denoted by N_1 and N_2 respectively. The probability that an atom either absorbs or emits a single photon is given by

$$W_i = \phi(z)\sigma(\nu). \tag{3.1.1}$$

Here $\phi(z)$ is the photon flux density (photons per second per unit area), and $\sigma(\nu)$ is the frequency dependent transition cross-section. This expression is valid for either absorption or stimulated emission.

N_1W_i gives the average density of absorbed photons, and N_2W_i is the average density of emitted photons from stimulated emission. Finally $N = N_2 - N_1$ gives the population difference. If N is greater than zero ($N > 0$), the medium has a population inversion and can amplify the photon density. Conversely if N is less than zero ($N < 0$), the medium is absorbing. Further if N is zero, it is transparent to the optical wave.

To understand how the photon flux density changes, consider an incremental length dz of the optical medium. The change in the photon flux density $d\phi(z)$ over the incremental range is the number of photons gained per unit time and area multiplied by the length,

$$d\phi = NW_i dz\,. \tag{3.1.2}$$

Using equation (3.1.1), this can be rearranged and written in differential form

$$\frac{d\phi(z)}{dz} = N\sigma(\nu)\phi(z)\,. \tag{3.1.3}$$

The equation can be easily integrated to yield an exponentially increasing photon flux density. However the optical intensity is related to the flux density by $I(z) = h\nu\phi(z)$, where h is Plank's constant. Therefore equation (3.1.3) can be integrated to yield the intensity of the pulse as a function of the position within the medium given by

$$I(z) = I(0)e^{N\sigma(\nu)z}\,, \tag{3.1.4}$$

where $I(0)$ is the intensity of the pulse upon entering the medium. The gain is then simply dependent upon the population inversion and the length of the material. The exponential term in equation (3.1.4) is routinely called the small signal gain (G_0). The gain factor is frequency dependent through the transition cross-section. Over large bandwidths, the cross-section can vary significantly which will modulate the amplified spectrum of the seed pulse.

The limit at which small signal gain is valid is when the change in photon flux density is small. In other words, the stored energy (E_{st}) must be much larger than the energy extracted ($G_0 E_{in}$), or $G_0 E_{in} / E_{st} \ll 1$. When this ratio nears unity, the gain is no longer exponential. At this point the pulse begins to significantly extricate the population inversion; therefore the pulse will no longer experience a uniform gain over its duration. The leading edge of the pulse can experience a higher population inversion than the trailing edge. Therefore a more intricate formalism must be given to the amplification process to properly describe the effects of gain saturation.

3.1.2 Saturated Gain

Again consider a monochromatic plane wave traversing a 2 level optical medium of region $0 \le z \le L$. To correct the formalism for saturated gain, we allow for time dependence in both the density of states and photon flux density. In this case $N_1(z,t)$ and $N_2(z,t)$ are the time dependent densities of atoms in the lower and upper states. Further, the net population difference or inversion density $N(z,t)$ and the photon flux density $\phi(t)$ are also time dependent.

To begin, there are several processes occurring within the medium that affect the inversion density: stimulated emission, absorption, and spontaneous decay. The processes all can be expressed in the time rate of change of the inversion density by

$$\frac{\partial N(z,t)}{\partial t} = -2^{*} c\sigma N(z,t)\phi(z,t) - \frac{N(z,t)}{t_f} + W_p \,. \qquad (3.1.5)$$

In this equation $-c\sigma N(z,t)\phi(z,t)$ is the rate of stimulated emission, and $N(z,t)/t_f$ is rate of spontaneous decay, which occurs at a characteristic time scale of t_f. W_p gives the rate of pumping of the excited state. The factor 2^{*} accounts for the bottlenecking that occurs in the lower level of the laser transition. However a 4 level system, where the lower level depopulates infinitely fast, 2^{*} is equal to 1. Several approximations can be immediately made to simplify this equation. First during pulse amplification, the rate of stimulated emission is far greater than the pumping rate. Second is that the pulse amplification occurs on a shorter time scale than the rate of spontaneous emission. Therefore these two terms can be omitted.

Next consider the photon flux density. The total number of photons increases with time and space as the pulse is amplified within the medium. Further, the process is affected by stimulated emission, spontaneous emission, and absorption. The photon transport equation is then

$$\frac{\partial \phi(z,t)}{\partial t} + c\frac{\partial \phi(z,t)}{\partial z} = c\sigma N(z,t)\phi(z,t) + \frac{N(z,t)}{t_s} - \alpha\phi(z,t) \,. \qquad (3.1.6)$$

Again $c\sigma N(z,t)\phi(z,t)$ is the rate of stimulated emission. The rate of spontaneous emission is given by $N(z,t)/t_f$, and $\alpha\phi(z,t)$ is the term describing absorption. Several approximations can also be made here. First stimulated emission is the dominant term over spontaneous emission during pulse amplification. Also, most gain media available today have near optical purity. These equations have been solved with the absorption factor included [73]; however for this derivation it will be omitted. The photon density can also be expressed again in terms of the intensity by $I(z) = h\nu\phi(z)$. Therefore the coupled transport equations are reduced to

$$\frac{\partial N(z,t)}{\partial t} = -\frac{c}{h\nu}\sigma N(z,t)I(z,t)\,, \tag{3.1.7}$$

$$\frac{\partial I(z,t)}{\partial t} + c\frac{\partial I(z,t)}{\partial z} = c\sigma N(z,t)I(z,t)\,. \tag{3.1.8}$$

These equations can be easily integrated after a coordinate transform to a frame that is moving with the laser pulse:

$$\chi = \frac{z}{c}\,, \tag{3.1.9}$$

$$\tau = t - \frac{z}{c}\,. \tag{3.1.10}$$

This coordinate transform reduces the coupled equations to the following:

$$\frac{\partial I(\chi,\tau)}{\partial \chi} = \sigma N(\chi,\tau)I(\chi,\tau)\,, \tag{3.1.11}$$

$$\frac{\partial N(\chi,\tau)}{\partial \tau} = -\frac{\sigma}{h\nu} N(\chi,\tau) I(\chi,\tau) . \tag{3.1.12}$$

Equation (3.1.11) can be rearranged and directly integrated over the length of the amplifier in the form of

$$\int_{I_{out}(\tau)}^{I_{in}(\tau)} \frac{dI}{I} = \sigma \int_{0}^{L} N(\chi,\tau) d\chi . \tag{3.1.13}$$

$I_{in}(\tau)$ and $I_{out}(\tau)$ are the input and output pulse intensities at the entrance and exit planes of the medium respectively. Both are measured in the delayed coordinate frame of τ. Further, the right hand side of the equation can be directly integrated to yield the total number of atoms as a function of time ($N_{tot}(\tau)$), given by

$$N_{tot}(\tau) = \int_{0}^{L} N(\chi,\tau) d\chi . \tag{3.1.14}$$

Now equation (3.1.13) can be solved to produce

$$I_{out}(\tau) = I_{in}(\tau) e^{\sigma N_{tot}(\tau)} , \tag{3.1.15}$$

where $G(\tau) \equiv \exp[\sigma N_{tot}(\tau)]$ is defined to be the time varying partially saturated gain at any instance in the pulse. Equation (3.1.12) can be solved to produce the time response of the total excited atoms. By rearranging and integrating over the length of the amplifier, and also making use of equation (3.1.14) it becomes

$$\frac{\partial N_{tot}}{\partial \tau} = -\frac{\sigma}{h\nu}\int_0^L N(\chi,\tau)I(\chi,\tau)d\chi . \tag{3.1.16}$$

However insertion of equations (3.1.11) and (3.1.15) reduce it to

$$\frac{\partial N_{tot}}{\partial \tau} = -\frac{1}{h\nu}\int_0^L \frac{\partial I}{\partial \chi}\partial\chi = -\frac{1}{h\nu}\left[I_{out}(\tau) - I_{in}(\tau)\right]. \tag{3.1.17}$$

$$\frac{\partial N_{tot}}{\partial \tau} = -\frac{1}{h\nu}\left[e^{\sigma N_{tot}(\tau)} - 1\right]I_{in}(\tau). \tag{3.1.18}$$

Here it is useful to introduce the total initial excited atom population at time t_0 prior to the arrival of the pulse. It is defined by

$$N_0 \equiv \int_0^L N(z,t_0)dz . \tag{3.1.19}$$

This states that the initial single pass gain of the amplifier is then $G_0 = \exp(N_0\sigma)$. Now equation (3.1.18) can be rearranged in to facilitate integration of either side by

$$\int_{N_0}^{N_{tot}(\tau)} \frac{dN_{tot}}{e^{\sigma N_{tot}} - 1} = -\frac{1}{h\nu}\int_{t_0}^{\tau} I_{in}(\tau)d\tau \tag{3.1.20}$$

Another useful parameter is introduced as the input fluence of the laser pulse, i.e. the average energy per unit area defined by

$$F_{in} = \int_{-\infty}^{\tau} I_{in}(\tau)\,d\tau\,. \tag{3.1.21}$$

Now this equation allows equation (3.1.20) to be integrated on both sides and evaluated over the limits. With algebraic manipulation, the time dependence of the total excited atom population can be solved producing

$$e^{\sigma N_{tot}(\tau)} = \frac{1}{1-\left(1-e^{-\sigma N_0}\right)e^{-F/F_{sat}}} \tag{3.1.22}$$

Here the saturation fluence has been defined as $F_{sat} = h\nu/\sigma$. This term can be inserted into equation (3.1.15) to produce a generalized expression for the pulse propagation through the amplifier in measurable laser quantities,

$$I_{out}(t-z/c) = I_{in}(t)\frac{1}{1-\left(1-e^{-\sigma N_0}\right)e^{-F/F_{sat}}}\,. \tag{3.1.23}$$

This expression directly relates the output pulse intensity to the input pulse intensity and the remaining excited atoms N_0. The saturation fluence also serves to regulate the input fluence. When the input fluence nears F_{sat}, the gain experienced by the pulse will no longer be uniform over the pulse duration. This will serve to amplify the leading edge of the pulse more than the trailing edge, and thus changing the spectrum of the chirped pulse (Figure 3.3). This steepening of the leading edge can result in producing wings on the compressed pulse.

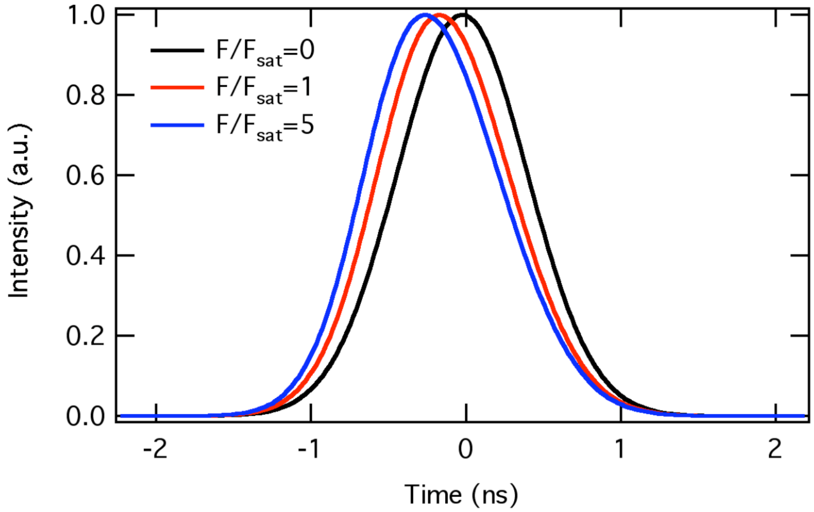

Figure 3.3: Simulated amplified pulse shapes as a function of input pulse fluence. The amplifier is a Ti:sapphire rod with a small signal gain of 5.

3.1.3 Energetics Modeling of the Regenerative Amplifier

This section presents two numerical simulations that model the energetics of the regen designed for the THOR Laser. The regen is designed to amplify the stretched nanojoule pulse from the oscillator by 10^6. The cavity is a linear half-symmetric, confocal resonator consisting of two end mirrors, Pockels cell, polarizer, and a Ti:sapphire crystal. Two energetics models are examined: a one-dimensional case assuming a Gaussian temporal profile with spatial uniformity, and a two-dimensional case with both temporal and radial shape.

In the 1-dimmensional case we assume there is complete spatial uniformity in the seed pulse. It is modeled as a square radial pulse with a Gaussian temporal profile. The seed is a 1 nJ, 600 ps FWHM Gaussian pulse. The gain profile in the amplifier is also modeled to be uniform in the radial dimension. Due to the symmetry of the system, radial calculations are omitted.

The amplification process is enabled by stored energy in the excited atom population contained in the Ti:sapphire crystal before the seed pulse arrives. As in the previous section, several groups have solved the rate equations for population inversions for a variety of input pulse shapes [74-76]. In this model, amplification is done through a process of excited atom accounting [63]. The saturation fluence F_{sat} in a four level system is defined as

$$F_{sat} = \frac{h\nu}{\sigma}, \tag{3.1.24}$$

where $h\nu$ is the photon energy of the seed beam, and σ is the emission cross-section. For Ti:sapphire seeded with a 800 nm source, the saturation fluence is 0.9 J/cm^2. Since Ti:sapphire is usually pumped by another laser source, the pumping fluence is then defined by

$$F_{pump} = \frac{E_{st}}{\pi\omega_0^2}, \tag{3.1.25}$$

where E_{st} is the total stored energy, and ω_0 is the beam radius of the pump beam. The total stored energy is also proportionate to the total number of absorbed pump photons (N) by

$$N = \frac{E_{st}}{h\nu_{pump}}. \tag{3.1.26}$$

In this equation, $h\nu_{pump}$ is the pump laser photon energy. N defines the population inversion of the medium. From this equation, the gain factor G_0 can be approximated to be

$$G_o = \exp\left(N\sigma l\right), \tag{3.1.27}$$

where l is the length of the rod. This is valid in the limit of small signal input where $G_0 E_{in} / E_{st} \ll 1$. This demonstrates that the gain is exponential with the excited atom density.

However this approximation also assumes a square pulse input. Since the pulse in question is Gaussian-shaped in time, a few approximations must be made to make this valid. To account for this effect, the pulse is time sliced to approximate many short duration square pulses. The leading edge of the pulse will undergo amplification and change the excited atom density before the trailing edge of the pulse enters the crystal. Therefore the excited atom density must then be recalculated before the next slice arrives. Effectively each time slice sees small signal gain as it passes through the crystal. In the case of near saturated amplification where $G_0 E_{in} / E_{st}$ nears unity, the leading edge of the pulse will see significantly higher gains than the trailing side. Time slicing will then reveal any gain saturation effects that occurs to the pulse.

After each time slice is amplified, the excited atom density must be recalculated. The new density is directly proportional to the extracted energy by

$$N = N_0 - \frac{E_{out} - E_{in}}{\pi\omega_0^2 l} \frac{1}{h\nu_{800}}, \tag{3.1.28}$$

where $\pi\omega_0^2 l$ is the interaction volume inside the crystal, and N_0 is the initial excited atom density before amplification. This process exactly accounts for the quantum defect by noting that a photon extracted is of energy $h\nu_{800}$, which is different from the absorbed photon energy of $h\nu_{pump}$. An iterative implementation of this process for each time slice demonstrates an accurate model for amplification of the entire pulse. To simulate multiple passes, the model is looped until the pulse has reached saturation and extracted all of the available energy.

Cavity transmission effects are accounted by including a linear attenuation term between each successive complete pass through the amplifier. Another effect that can be included is the exponential fluorescence decay of the excited atoms. Ti:sapphire has relatively short excited lifetime of 3.2 μs compared to other materials. Regen amplifiers require many tens of passes of amplification before the seed pulse reaches saturation. This along with the finite round trip time of the cavity may extend the process to several hundred nanoseconds. Therefore the fluorescence decay becomes appreciable at this time scale. Scaling the density by $\exp(-t/\tau_{sp})$ after each pass through the crystal approximates this effect. Here t is the time between passes, and τ_{sp} is the fluorescence lifetime. Another approximation of the model is that the Ti:sapphire crystal lies far enough away from an end mirror so that there is no pulse overlap within the crystal. In actuality the crystal is placed 10 cm from the curved end mirror, which is just over a 600 ps round trip time. This is where the mode volume of the cavity is largest, allowing crystal to be pumped with the highest possible energy. For modeling simplicity the pulse is assumed to have no temporal overlap between passes in the crystal.

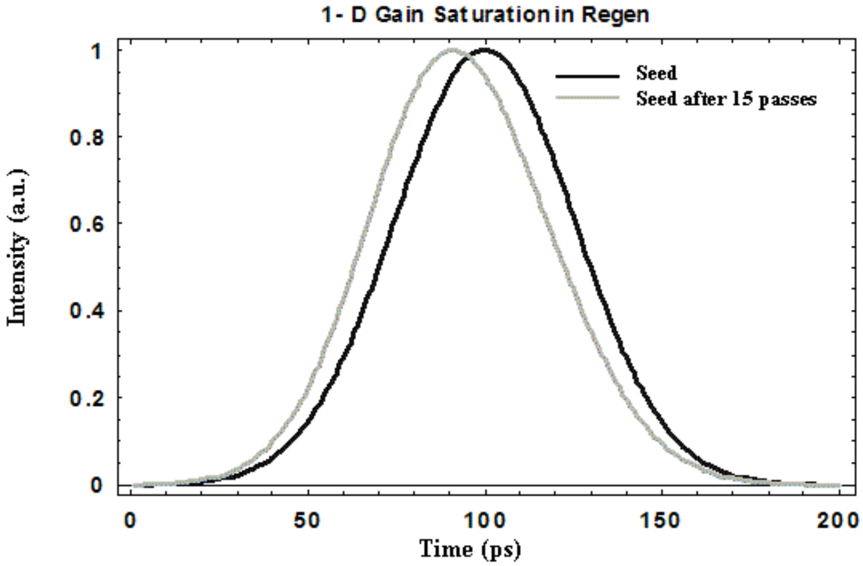

Figure 3.4: Simulated gain saturation from 1 dimensional model of regenerative amplifier. The seed pulse is forward shifted in time by 10 ps after 15 amplification passes through the amplifier.

The results of this model reveal an interesting gain saturation effect. Figure 3.4 contrasts the temporal shape of the seed pulse to the amplified pulse. It shows that the amplified pulse has become shifted forward in time after 15 passes through the amplifier. This is a result of the leading edge of the pulse seeing higher gain than the trailing side.

The 1-dimensional model is sufficient as a first order approximation. However in actuality, the laser pulse does not have a uniform spatial profile. It is both Gaussian in time and space. Additionally since another laser pumps the crystal, the gain of the system has a radial dependence similar to that of the pumping source.

To convert the 1-D model into 2-D, a few simple modifications are made. First, we assume that the laser pulse has angular symmetry eliminating the need for a 3-D analysis. Therefore a Gaussian radial profile is added to each time slice of the seed pulse before amplification. Second, we assume that the pumping laser has radial intensity dependence with angular symmetry. From this approximation any radial shape, such as Gaussian or super-Gaussian can be used to simulate the gain profile. Again we use the same process of excited atom accounting to perform amplification. Only for each time slice, there are individual radial slices that each must be amplified. The gain coefficient of equation (3.1.27) can now vary radially with the intensity profile of the pump laser. A simple modification to the equation yields

$$G_0 = \exp\left[N(r)\sigma l\right]. \tag{3.1.29}$$

Again an iterative process of amplification for each radial slice is done, recalculating the excited atom density for each time slice. Repeating this process to simulate multiple passes will allow the pulse to build and eventually saturate once the excited atom density has been depleted.

A few more aspects must be considered to properly model the system. The regen is an optical cavity designed to support only the TEM_{00} Gaussian spatial mode. However gain saturation will reshape the spatial profile creating higher order modes after each successive pass. Therefore the cavity acts as a loss mechanism that spatially filters out the higher order modes leaving only the TEM_{00} mode to resonate. If cavity effects are not considered, the model becomes inaccurate near saturation. Additionally since both the seed pulse and excited atom density have a Gaussian radial dependence, the center of the beam will build up faster than the wings. If a linear loss term is included in the model, such as transmission, the pulse will become significantly distorted once the excited atom density nears depletion. This effect is illustrated in Figure 3.5.

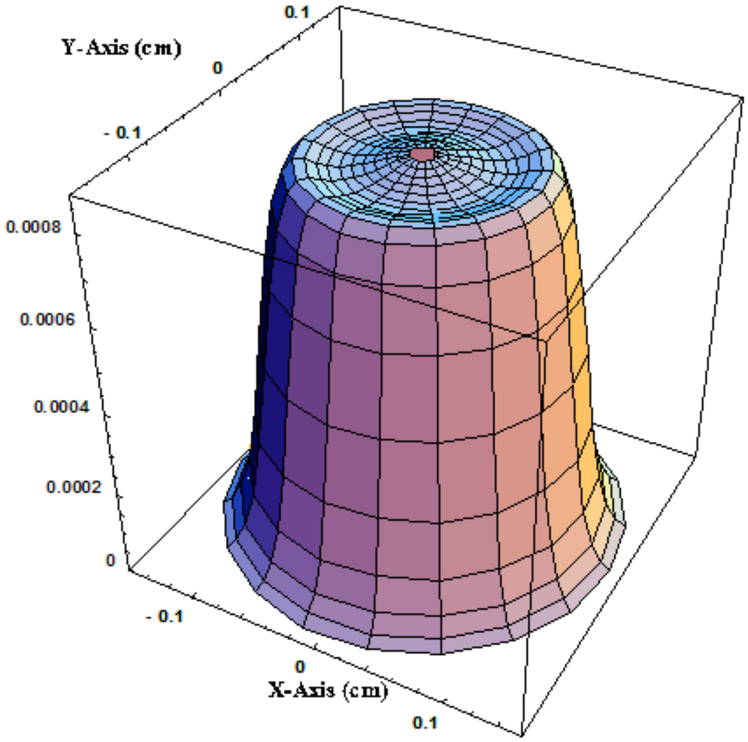

Figure 3.5. 2-D simulation of amplified seed pulse in regenerative amplifier with out cavity normalization effects.

The solution is to series expand the seed pulse into normal modes of the cavity keeping only the lowest order upon each pass through the crystal. Generally the modes are expanded into a Hermitian basis when there is a high degree of angular non-uniformity caused by Brewster faces or wedges within the cavity [77]. In this regen both the Ti:sapphire crystal and the polarizer have Brewster surfaces. However this model is primarily concerned with energetics, therefore angular uniformity is assumed permitting expansion into the simpler Laguerre modes [72]. In the Laguerre expansion, the intensity of each mode is described by

$$I_\rho^l\left(\rho,\theta,\varphi\right) = I_0\left[L_\rho^l\left(\rho\right)\right]^2 Cos^2\left(l\varphi\right)e^{-\rho}, \qquad (3.1.30)$$

where I_0 is the intensity amplitude, and $L_\rho^l\left(\rho\right)$ is the Laguerre function of order l. Since the model is only concerned with the TEM$_{00}$ mode, only the $L_\rho^l\left(\rho\right)$ coefficient needs to be calculated for the expansion. The Laguerre functions are orthonormal obeying

$$\int_{-\infty}^{\infty} L_x^m\left[x\right]L_n^{m*}\left[x\right]dx = \delta_{n,m}. \qquad (3.1.31)$$

From this relation the TEM$_{00}$ coefficient can easily be determined (Figure 3.6).

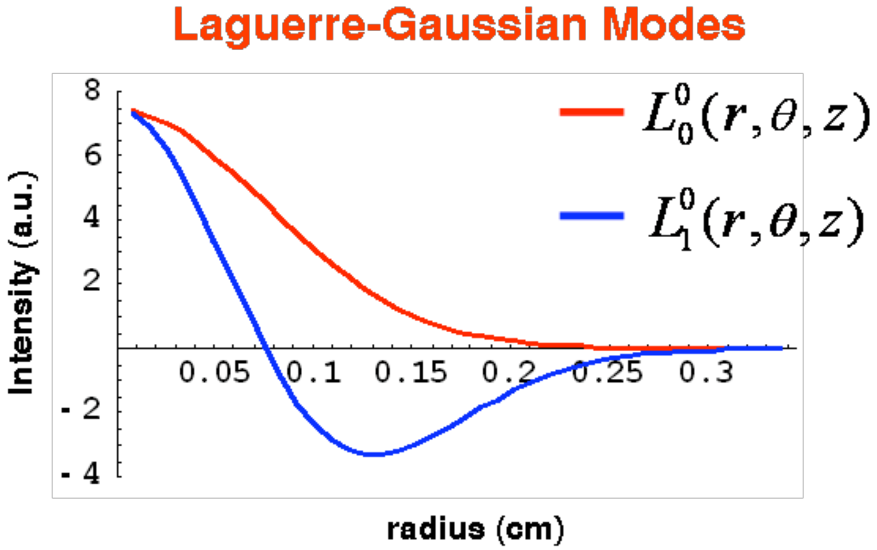

Figure 3.6: Plots of the l=1 and ρ=0 and 1 Laguerre-Gaussian modes.

Further approximations can be made to the model to simplify the calculations. First we assume the incident pulse at the crystal is a plane wave. In actuality the wavefront at the crystal is spherical, but this does not greatly effect the energetics calculations. Also we assume there is complete angular uniformity. These two approximations greatly simplify equation (3.1.30) and allow for a simple calculation of the Laguerre coefficient.

Figure 3.7 shows the peak radial intensity of the amplified pulse from the 2-D model that includes the Laguerre normalization. Contrasted with figure 3.4, it is clear that the amplified pulse is Gaussian, which is expected from a stable TEM_{00} cavity. Another result of the 2-D model is that the build-up time is dramatically longer than the 1-D model (Figure 3.8). This is attributed to the cavity effects on the radial profile of the mode. As gain shaping occurs, energy is put into higher order spatial modes that are not supported by the cavity. These modes are spatially filtered out and present a loss term to model, which extends the build up time.

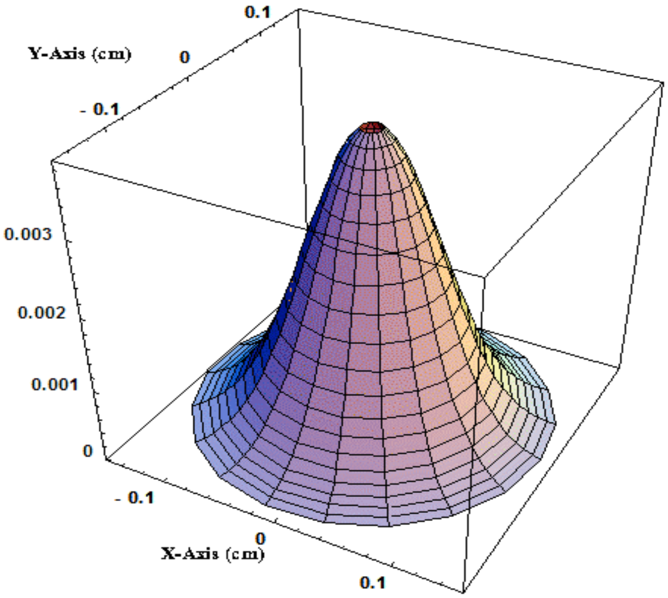

Figure 3.7: 2-D simulation of amplified seed mode in regenerative amplifier with Laguerre cavity mode normalization.

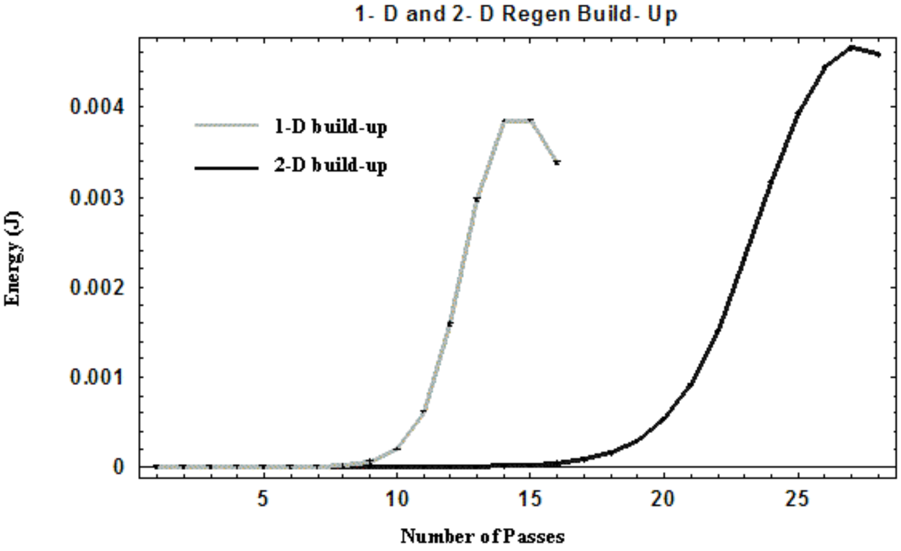

Figure 3.8: Simulation contrasting the buildup of the regen amplifier between the 1D and 2D models. The 1D model predicts saturation after 15 passes. The 2D model predicts saturation after 25 passes with the same pumping conditions.

In summary, the 1-dimensional model of the energetics in the regen proved to be an informative analysis of the amplifier. It reveals basic gain saturation effects and yields a reasonable expectation value to the amplified energy. It is shown in figure 3.7 that both models produce quite similar amplified energies. However the 2-D model is more accurate by accounting for both radial and temporal gain shaping effects. It yields a more accurate build up time and can account for any mode mismatch between the gain profile and the seed. If applied to a non-cavity amplifier, such as a multi-pass bow tie, the 2-D model can account for beam shaping and other effects that would be lost in a 1-D analysis.

3.1.4 Modeling of Multi-Pass Amplifiers

The laser design for THOR includes two additional amplification stages, in which both are multi-pass amplifiers without resonant cavities. The first amplifier is a 4-pass bowtie architecture designed to preamplify the pulse after the regen stage. The final power amplifier is also a bowtie design with the seed making 5 passes through the gain medium. The model used for subsequent amplification is the 2-D code, which accounts for the spatial and temporal shape of the pulse. Again polar angle symmetry is assumed in both cases.

The first bowtie (4-pass) amplifies the seed from the regen by angle multiplexing the beam four times through the gain medium. The seed is enlarged between the regen and 4-pass to accommodate the larger pumping area. Also the seed beam is attenuated by approximately one half by transmission losses from the optics chain between the regen and 4-pass. Therefore the simulated pulse is attenuated by the same amount.

The pump laser used in this amplifier is the same frequency doubled Nd:YAG that is used to pump the regen. It is a stable resonator laser producing a true Gaussian profile beam. There are several loss elements that attenuate the available energy in the 4-pass amplifier. Foremost is that only 90% of the pump light is absorbed by the crystal. Also the same laser pulse pumps both the regen and the 4-pass. Since the pump beam arrives at the 4-pass crystal 350 ns before the seed, there is an appreciable amount of fluorescence decay that occurs before amplification. The excited atom population is then reduced by the scaling factor $\exp(-t/\tau_{sp})$. Here τ_{sp} is the fluorescence lifetime of 3.2 μs, and t is equal to 350 ns. In addition, the time between passes in the bowtie is 7 ns; therefore the excited atom population is further attenuated per pass by a similar factor. The pump beam area is also oversized to accommodate the larger volume needed in the crystal for angle multiplexing.

The model predicts that the laser will be amplified to 27 mJ after 4 passes (Figure 3.9). However saturation is not achieved in the model since the gain per pass does not rollover. It appears to be linear in each pass. This would imply that more gain is available, but more passes are not possible due to the required longer path length for larger angle multiplexing. Further, the pump area would have to be enlarged, directly lowering the single pass gain.

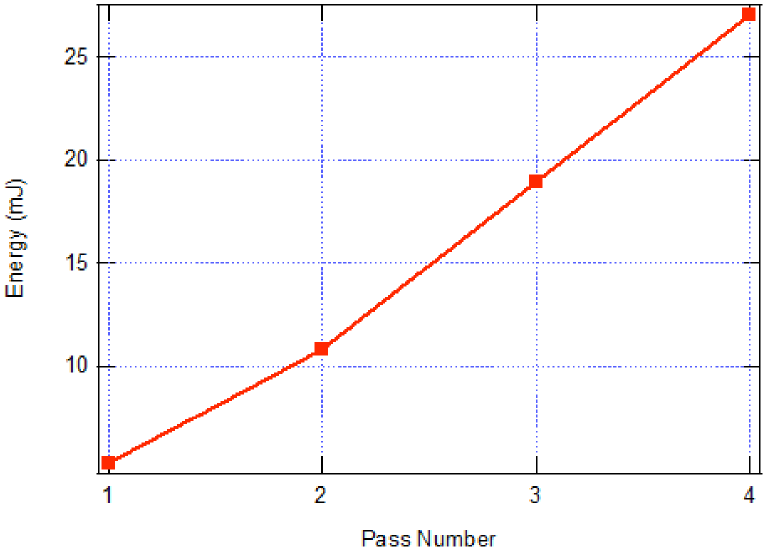

Figure 3.9: Calculated energy after each pass in the 4-pass amplifier.

Gain saturation does not play a major role in this amplifier, because the total integrated gain is about 20. Consequently the pulse is slightly deviated from being a Gaussian mode (Figure 3.10), and the saturation steepens the pulse both temporally and radially (Figure 3.11). The radial axis shows that the total transverse area of the laser is decreased. The simulated intensity is not only increased from the gained energy, but also by the gain shaping of the pulse. In the temporal axis, the pulse is negligibly shifted forward toward the red side of the spectrum.

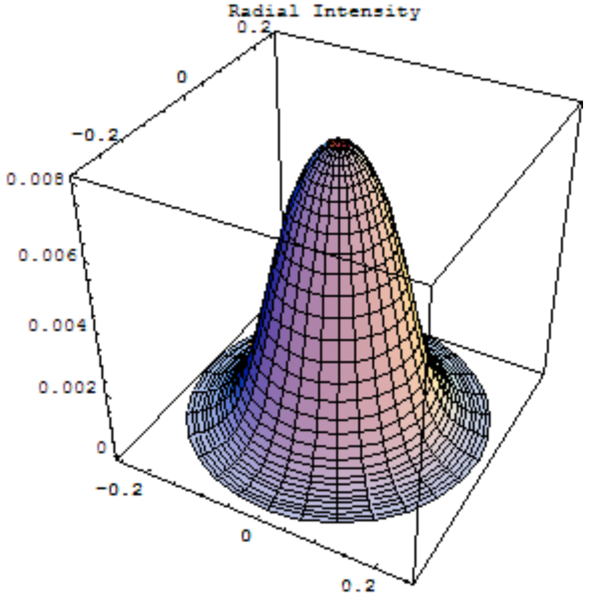

Figure 3.10: Simulation of amplified mode of the laser pulse after 4 passes in the 4-pass amplifier

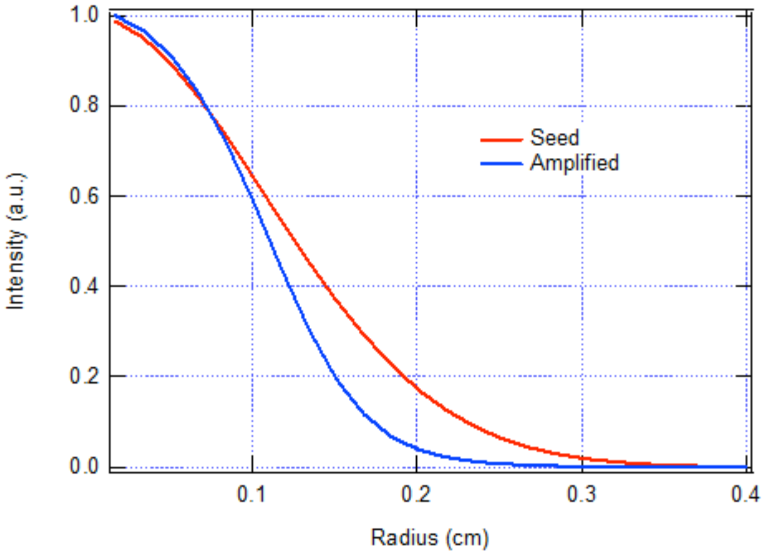

Figure 3.11: Simulated spatial gain saturation arising from 4 pass amplifier

The final power amplifier in the THOR laser is also a multi-pass bowtie (5-pass). It is designed to amplify the pulse to the 1-Joule range by making 5 passes through the amplifier crystal. Before amplification it is resized, spatially filtered, and relay imaged from the prior amplifier to the crystal face on the first pass through the 5-pass. Also a significantly longer beam path is required to spatially separate the larger beam between each pass through the crystal due to the larger pumping volume.

The pump sources for the this amplifier are two frequency doubled Nd:YAG lasers operating at 10 Hz producing a combined 2.4 J. Each beam is relay imaged to the crystal and sized appropriately to give a combined pumping fluence of 1.4 J/cm^2. The spatial profile of each pump beam is a sixth order super-Gaussian, which provide a very uniform pumping volume to amplify the pulse. The entire pump energy is assumed to be absorbed in the crystal since the pump beams are each two passed. Fluorescence decay is negligible in this case since the crystal is pumped nanoseconds before the seed arrives.

In this amplifier the model predicts saturation is achieved in 5 passes (Figure 3.12). The buildup clearly becomes sub-linear after three passes and continues to roll over after each successive pass. Originally the design called for 4 passes in the final amplifier; however the attenuation between bowties required a fifth pass to saturate the crystal. Since strong saturation is achieved, the beam is highly gain shaped after amplification (Figure 3.13). This also is aided by the super-Gaussian profile of the pump beams. The seed pulse was modeled to be 16 mm (1/e^2) in diameter having long spatial wings. The amplifier effectively truncates these wings acting like a gain spatial filter to produce a 15 mm diameter super-Gaussian pulse. The depression at the center of the beam in figure 3.12 arises from transmission losses overcoming the gain. In the center of the beam, the gain is fully depleted after the 5th pass, and therefore the transmission loss carves out the center of the beam.

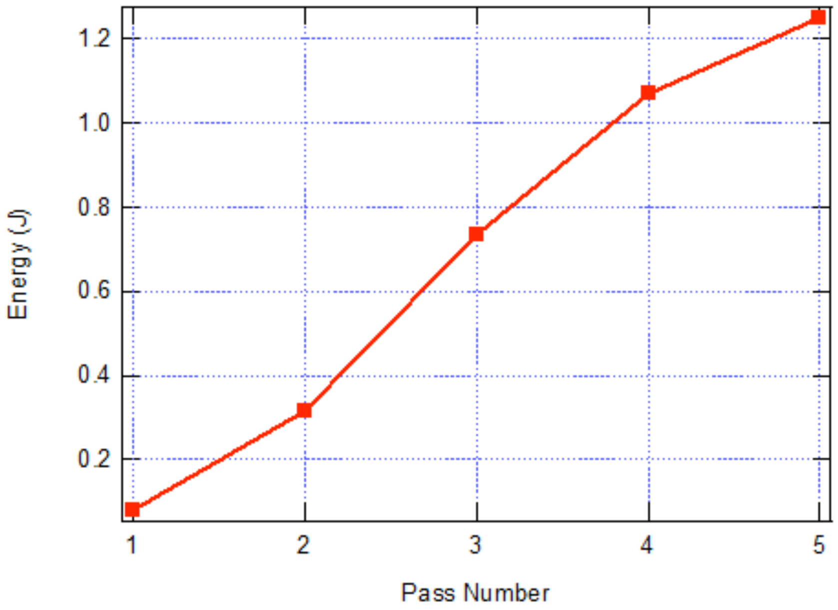

Figure 3.12: Calculated energy after each pass in the 5-pass amplifier

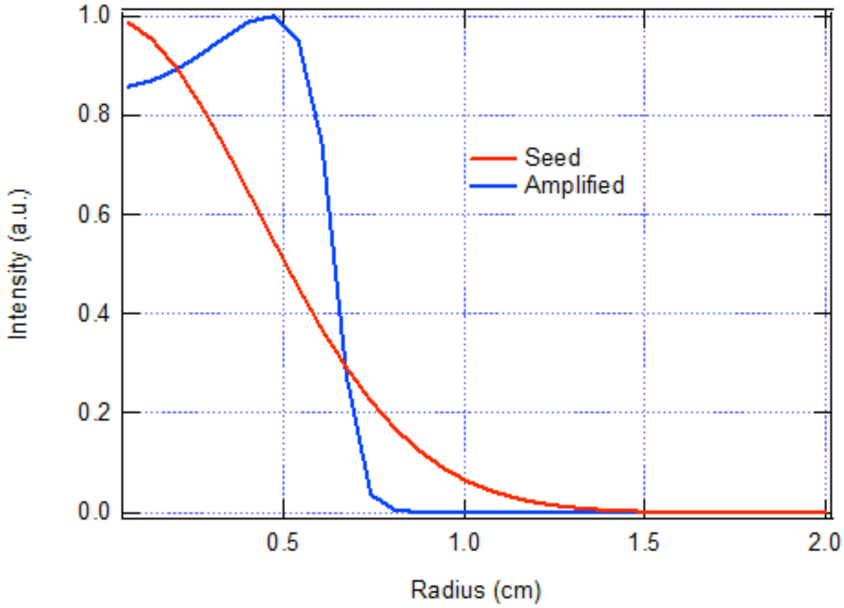

Figure 3.13: Simulation of spatial gain saturation from the 5-pass amplifier

In summary this model predicts the energetic buildup of the seed pulse in each amplifier reasonably well. Gain saturation effects are shown to strongly reshape the beam after final amplification. The multi-dimensional approach yields much more information than the 1-D case. Even though effects of frequency dependent gain are not considered, the model does predict within reasonable error the performance of the real system. A frequency dependent gain model is considered in the next chapter and will be discussed in detail.

3.2 Performance of the THOR laser

This section presents the design and performance characteristics of the THOR laser system. It is a 20 TW Ti:sapphire laser operating at 10 Hz. The laser is centered at 800 nm which is the peak emission wavelength of Ti:sapphire. The laser consists of the following components: oscillator, stretcher, regenerative amplifier, power amplifiers, and a vacuum based pulse compressor. The following subsections discuss each major subsection of the laser with the oscillator and stretcher grouped together to comprise the front end.

3.2.1 Laser Front End

The laser begins with a commercial, self mode-locked Ti:sapphire oscillator (Femto Lasers, model Femtosource Scientific) which produces transform limited pulses with duration of 20 fs (FWHM). The laser mode-locks at a repetition rate of 76 MHz producing 6 nJ of energy per pulse. The oscillator has 45 nm FWHM of spectrum and a total bandwidth exceeding 100 nm. The laser output is collimated with a 2.0 m focal length lens. Pulses are sliced out of the pulse train at 10 Hz using a fast-on/fast-off, half wave Pockels cell and two calcite polarizers. In addition, a Faraday optical isolator is used following the slicer to increase the isolation between the oscillator and the regen. A minimum of 10^6 in isolation is needed to optically isolate the front end from the amplifier chain.

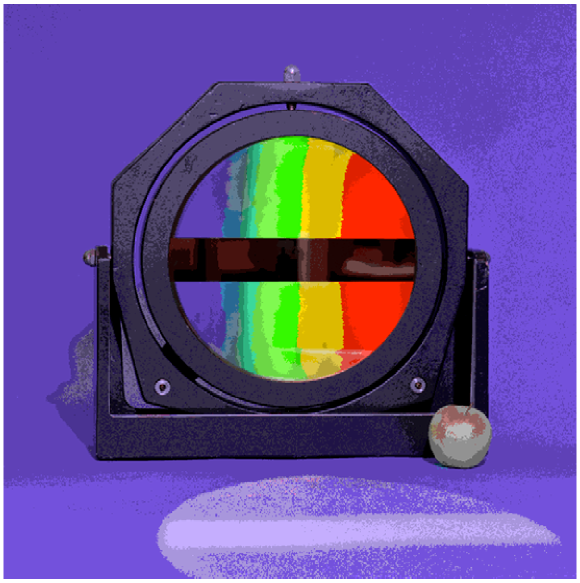

Figure 3.14: Picture of 40 cm diameter gold coated grating used similarly in the THOR laser. The ruling spacing is 1480 lines/mm. A 5 cm tall reflective stripe mirror is placed at the center of the grating. (photo courtesy of LLNL)

The 10 Hz pulse train is then injected to an all-reflective single grating pulse stretcher based upon the design of Banks et al [47]. The stretcher is designed to pass 100 nm of spectrum. The grating is a 35 cm wide gold coated substrate with holographically imposed rulings spaced at 1480 lines/mm (

Figure **3.14**). In addition the grating has a 5 cm tall reflective stripe mirror which traverses across the center of the substrate. This mirror stripe is used to allow on-axis reflection from the curved mirror, thus eliminating spherical aberrations. The gold-coated curved mirror is 30.5 cm in diameter with a 2260 mm radius of curvature. The mirror is placed 45 cm away from the grating to image the diffraction from the m = -1 order. A 30.5 cm diameter gold flat mirror is used to fold the 2 grating stretcher in half, thus eliminating the need for a second grating. The flat mirror retro-reflects the beam back to the second strike on the imaging lens. Finally a gold-coated rooftop mirror is used to return the dispersed pulse back through the system. A full optical ray trace of the stretcher is shown in (Figure 3.15).

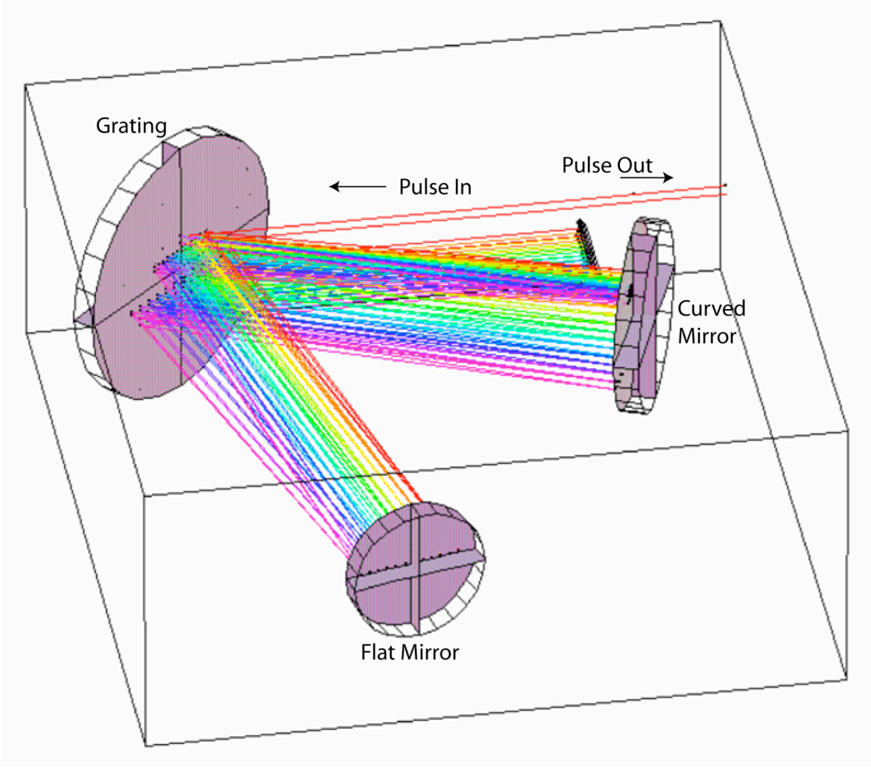

Figure 3.15: Optical ray trace of the THOR stretcher. The stretcher uses all reflective optics and a spherical mirror on-axis to eliminate spherical aberrations.

Following the stretcher, the pulse is injected into an optical fiber. The polarization maintaining fiber is 6 m long, and is used to perform 4th order dispersion compensation for the optical pulse. Initial compression without the fiber yielded a 50 fs pulse width. By including the fiber, the phase of the pulse could be compensated to the 4th order, thus enabling shorter compressed pulses. The pulse is then passed through another Faraday optical isolator to shield the fiber from leakage from the regen. The final spectrum from the laser front end is viewed in Figure 3.16.

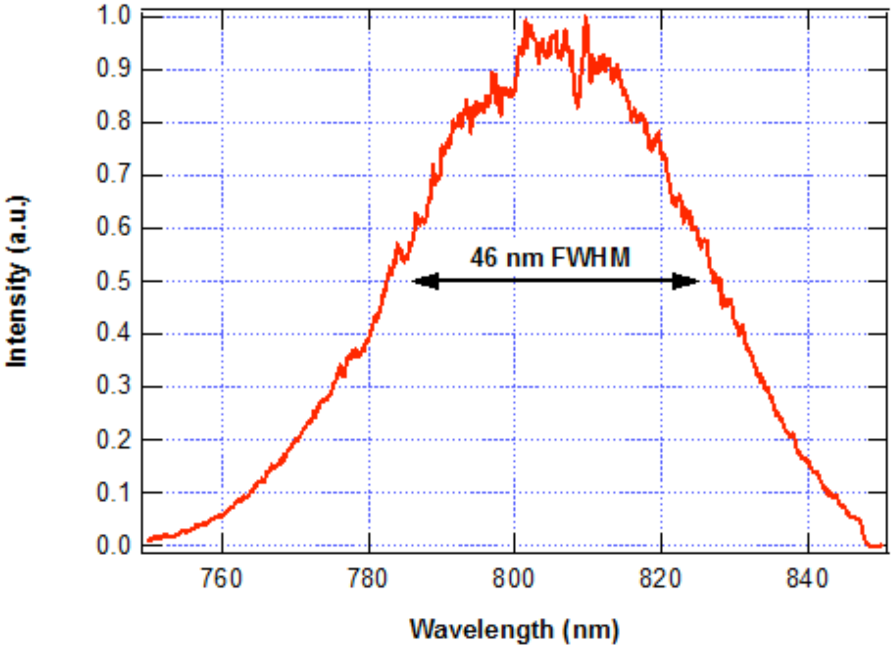

Figure 3.16: Measured spectrum from the output of the fiber following the THOR stretcher.

The entire front end passes almost the entire oscillator bandwidth. Some clipping is visible at 847 nm, but this not sufficient to effect the pulse shape after compression. Gain narrowing in the subsequent amplifiers smoothes out the amplified spectrum.

3.2.2 Regenerative Amplifier

The regenerative amplifier (regen) cavity is a half symmetric confocal linear resonator (Figure 3.17). The cavity employs only two mirrors: a 5-meter radius of curvature dielectric high reflector and a plano-dielectric high reflector. Both mirrors are broadband coated at 800 nm to support a broad amplified spectrum. The mirrors are separated by 225 cm to create a 15 ns roundtrip stable cavity ($g_1 \times g_2 = 0.55$). The mode radii for the resonator are 1.07 mm (1/e^2) at the curved mirror and 0.795 mm at the flat mirror. A 5 mm diameter by 1 cm long Ti:sapphire crystal with Brewster angle wedged faces is used for the gain medium. The crystal is placed 10 cm from curved mirror to allow the largest mode diameter to fill the rod. The mode diameter in the rod is 2.0 mm. The crystal is orientated so only p-polarized light will oscillate in the cavity. TEM$_{00}$ mode operation is maintained by a 2 mm diameter pinhole positioned near the polarizer. A fast-on/fast-off half wave Pockels cell is placed at the midpoint of the cavity for pulse selection. Finally a broadband thin film polarizer is used for pulse ejection after amplification.

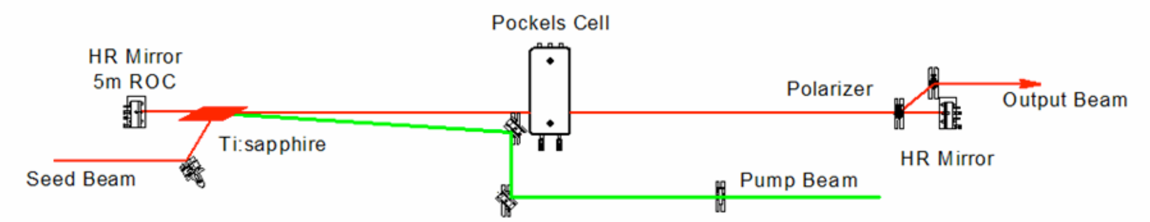

Figure 3.17: Optical schematic of the regenerative amplifier.

The s-polarized seed pulse is injected into the cavity by reflecting off the Brewster face of the Ti:sapphire crystal towards the flat mirror. The seed pulse polarization is then rotated to p-polarization using the Pockels cell; therefore trapping it in the cavity. The cell is placed at the midpoint of the cavity in order to best accommodate the 6 ns switch-off time of the voltage driver. The driver returns to near zero voltage before the pulse returns from the half transit of the cavity. No other polarization rotators are used in this design. This avoids etaloning effects and bandwidth modulation from quartz waveplates. Once the pulse saturates the amplifier, the Pockels cell is fired a second time to rotate the pulse to s-polarization. The polarizer then ejects the pulse.

The regen is pumped by a 10 Hz frequency doubled Nd:YAG laser (Big Sky Laser, model CFR200) producing 200 mJ pulses at 532 nm. The laser uses a stable resonator to produce a low-order Gaussian mode with 12 ns (FWHM) pulse duration. The longer pulse width is desirable because the peak intensity is lower than other similar lasers. The pump beam is beam-split to facilitate pumping both the regen and the 4-pass amplifier. The regen is pumped with 45 mJ, and the beam is focused into the Ti:sapphire crystal 4° off-axis of the regen cavity mode using a 75 cm focal length plano-convex lens. The lens is placed 88 cm from the crystal to allow the pump beam to go through focus before entering. The diameter of the pump is set to 2.0 mm producing a pump fluence of 1.5 J/cm^2.

The regen is timed using a countdown digital clock provided by the Pockels Cell driver. The driver uses a photodiode to monitor the pulse rate frequency of the mode-locked oscillator. The frequency is divided down to 10 Hz to make a master clock for the entire laser. The 10 Hz master clock is also used to trigger a bank of digital delay generators (SRS DG535) which provide slow (ns scale) and fast (>1μs) timing for all laser systems. All timing for the THOR laser is therefore derived from the oscillator eliminating long-term timing drift from thermal fluctuations.

The cavity is seeded by a 1 nJ pulse stretched to 600 ps. The seed is nearly mode-matched to the cavity using a 2.5 m focal length plano-convex lens. The pulse reaches saturation after 22 roundtrips through the cavity (Figure 3.18). It is allowed to make one more roundtrip to ensure consistent saturation to reduce pulse-to-pulse jitter. The total oscillation time is then 350 ns amplifying the pulse to 3.5 mJ. In contrast the modeling in section 3.1.3 predicted saturation after 25 passes under similar pumping conditions. Because the small signal gain per pass is relatively low (G_0=1.90), amplified spontaneous emission (ASE) is minimized. The intra-cavity aperture also further reduces ASE.

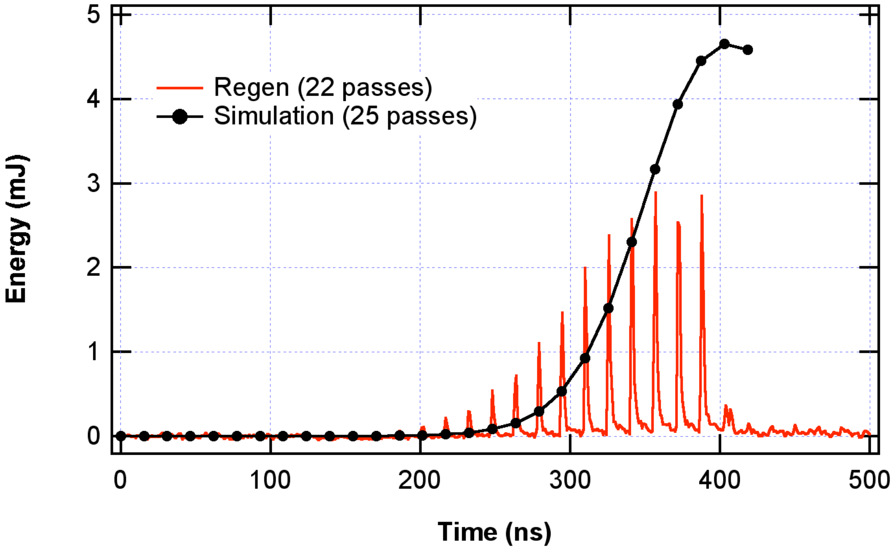

Figure 3.18: Measured buildup of regenerative amplifier and simulated buildup. The pulse reaches saturation in 23 passes (400 ns) at 3 mJ, and the simulation saturates after 26 passes at 4.2 mJ.

The low gain in the regen however does tend to incur stronger gain narrowing than a high gain multi-pass preamplifier [67]. Strong gain narrowing occurs during the unsaturated portion of the amplification process. Since the regen requires many passes to saturate the amplifier and the total gain exceeds 10^6, a majority gain narrowing occurs at this stage. The injected pulse has 46 nm FWHM of bandwidth. The amplified pulse ejected from the cavity is gain-narrowed to 29.9 nm FWHM (Figure 3.19). This is in similar agreement with the model presented in figure 2. The model predicted a 46 nm spectrum would be gain-narrowed to 32 nm after a total small signal gain of $3x10^6$.

The amplified mode shape from the regen is slightly super-Gaussian from gain shaping. The mode diameter is approximately 2.5 mm ($1/e^2$) averaged over both axes (Figure 3.20). Finally the broad-spectrum polarizer ejects the pulse from the cavity. These inherently demonstrate poor polarization contrast in reflection since they are optimized for alignment at 72° normal to the axis of propagation. To increase the contrast, a second reflecting polarizer is employed immediately after the pulse is ejected. The regen output is also further gated by using a Pockels cell pulse picker and high extinction calcite polarizers downstream from the cavity. The pulse picker only allows a 2 ns window to pass to limit ASE leakage from seeding the next amplifier. The pulse is finally collimated using a 2.5 m focal length plano-convex lens. The lens is positioned so that its focus is confocal with the waist of the regen cavity.

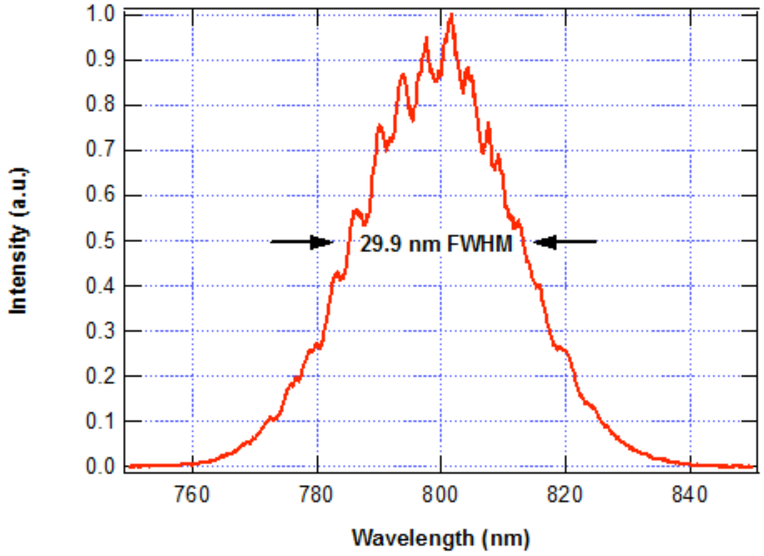

Figure 3.19: Measured spectrum from the pulse after amplification in the regenerative amplifier.

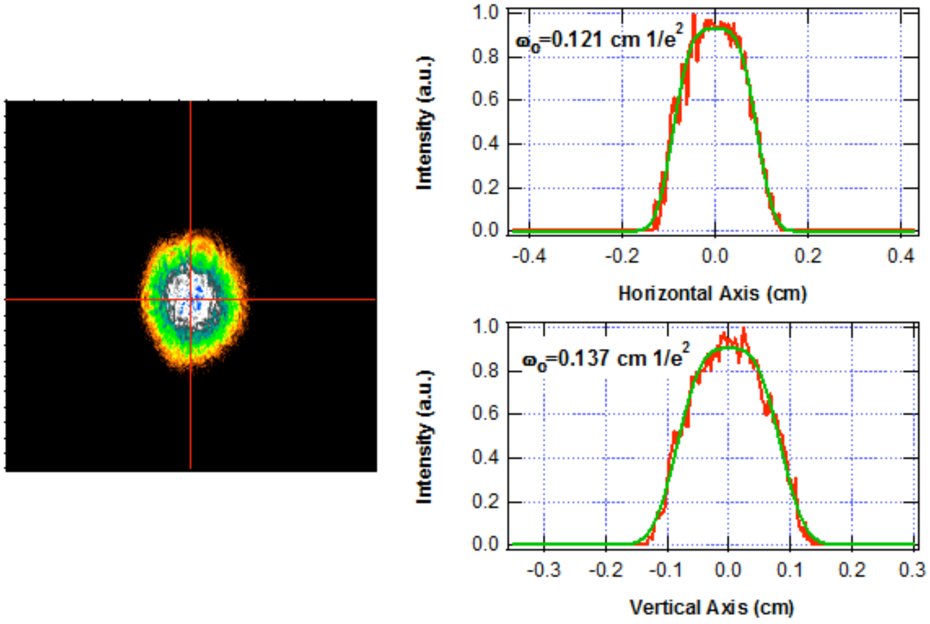

Figure 3.20: TEM_{00} spatial profile of the 3.5 mJ output from the regenerative amplifier.

3.2.3 4-pass Amplifier

The pulse is next injected into the first multi-pass amplifier. The 4-pass is a bowtie design with 6 ns long arms. The Ti:sapphire crystal is 10 mm in diameter and 20 mm long. It has uncoated Brewster angle faces. The absorption constant α of the crystal is measured to be 1.05 cm^{-1}. This yields 90% absorption of the pump beam over the length of the crystal. The crystal is oriented with the Brewster faces pointing upwards so that p-polarized (vertical polarization) light is passed. The pulse makes 4 passes through the crystal with a maximum 4° crossing angle. The amplifier is aligned so the final pass travels nearly down the center of the crystal to ensure the best pump volume overlap.

The amplifier is pumped with 130 mJ, which is the remainder of energy from the frequency doubled Nd:YAG also used to pump the regen. However, 130 mJ is not directly available for amplification, because the same pulse is used to pump both amplifiers. Both amplifier crystals are synchronously pumped, and the regen builds up on the order of 350 ns. Because the fluorescence lifetime of Ti:sapphire is 3.2 μs, approximately 11% of the stored energy in the 4-pass crystal spontaneously decays before the seed pulse arrives. The pump beam is slowly focused into the crystal using a 100 cm focal length plano-convex lens. The lens is positioned so that the pump mode radius is 2.5 mm creating an oversized gain volume to accommodate the cross angle of the seed beam.

The seed pulse energy entering the 4-pass is 1.90 mJ, and the single pass transmission efficiency is 95%. The amplifier initially demonstrates a single pass gain of 2.78 on the first pass (Figure 3.21). After 4 passes, the gain is reduced to 1.38. The seed emerges from the amp with a final energy of 28 mJ. Therefore 30.5% of the available stored energy is extracted when accounting for the quantum defect.

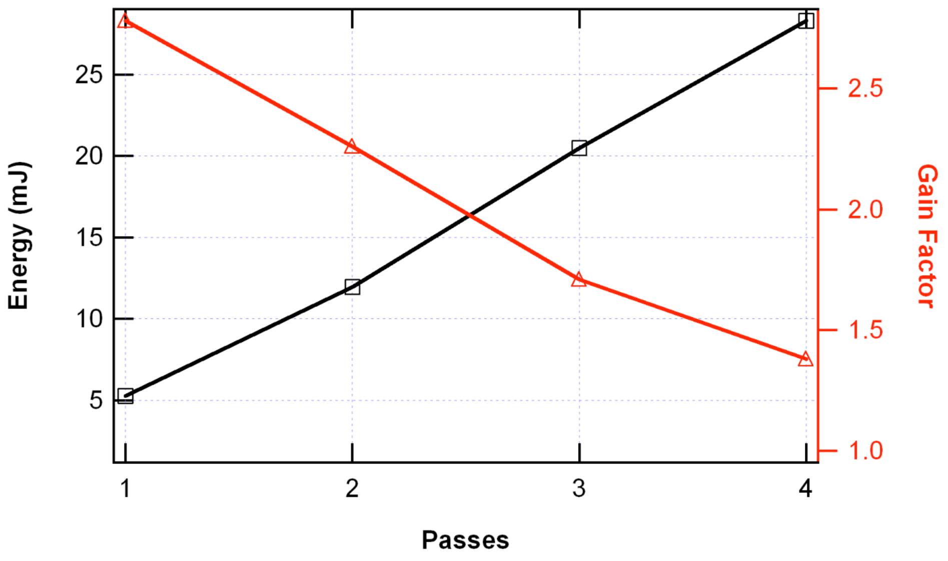

Figure 3.21: Measured gain and amplified energy per pass in the 4-pass amplifier.

Following the 4-pass, the pulse is spatially cleaned using a vacuum spatial filter assembly. The spatial filter removes diffraction generated from multi-passing the 4-pass crystal. The spatial filter is comprised of 1:5 imaging telescope and a 1.0 mm diameter pinhole placed at the focus of the first lens. The seed beam diameter is increased to 9.3 mm after the telescope; however it is not collimated. The telescope was originally designed to relay image the output plane of the 4-pass to the first pass of the crystal in the 5-pass amplifier. Nonetheless the lens spacing of the telescope is set to compensate for the thermally induced lens created in the 5-pass crystal by the pump lasers. This detail is further discussed in the next section.

3.2.4 5-pass Amplifier

Final energy is achieved in a 5-pass bowtie amplifier. The crystal used is a 20 mm diameter by 20 mm long flat faced Ti:sapphire crystal, and is anti-reflection coated for 532 and 800 nm. The absorption coefficient (α) is measured at 2.30 cm^{-1}, with a 90% single pass absorption at 532 nm over the length of the crystal. The crystal axes are orientated for vertical polarization to be passed. The barrel of the crystal is coarse polished and painted black to prevent parasitic oscillations. Finally it is wrapped in 125 μm thick Indium foil and mounted in a water-cooled copper block.

The amplifier is pumped by two frequency doubled Nd:YAG lasers (Spectra-Physics Pro-350) each producing 1.4 J at 532 nm. Each laser has a super-Gaussian spatial profile. The pulses from each laser are mode sized to 16 mm (1/*e*^{2} diameter) and relay imaged to opposite sides of the crystal (Figure 3.22). The combined peak pumping fluence is then 1.4 J/cm^2. Each pump is double passed through the crystal to ensure complete absorption.

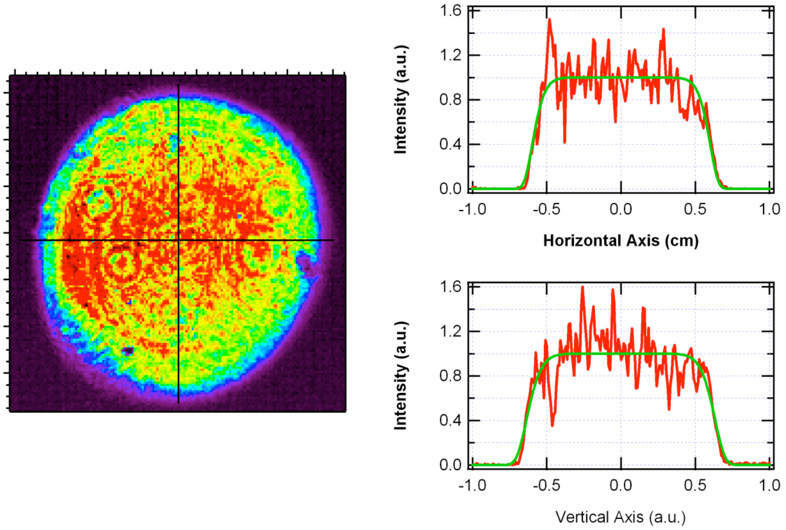

Figure 3.22: Spatial profile of 5-pass amplifier pump beam. The beam is super-Gaussian and sized to 16 mm (1/*e*^{2}).

The pump lasers operate at 10 Hz producing a combined 28 W of average power. If all the available energy is extracted from the crystal, this still leaves over 9 W of heat due to the quantum defect. This subsequent residual heat load produces a thermally induced positive lens in the crystal. This effect arises from the temperature dependent index of refraction. The lens was measured to have a positive focus at 40 meters. After 5 passes, the thermal lens significantly focuses the beam, thus reducing the mode overlap with the pumped volume. To compensate for this effect, the crystal in the amplifier is treated as a series of five thin lenses separated by the spacing of the arms of the amplifier. In the paraxial limit, the lens spacing of the spatial filter before the 5-pass was adjusted to produce a diverging beam. The divergence is then nearly collimated after 5 passes through the crystal, thus maintaining adequate mode overlap in the crystal.

The amplifier is seeded by the spatially filtered output of the 4-pass amplifier. Transmission losses reduce the seed energy into the 5-pass to 20 mJ. The mode is resized to a diameter of 14 mm ($1/e^2$). The seed mode which is nearly Gaussian, is quasi-image relayed to the first pass of the amplifier. Each successive pass propagates freely, subject only to gain guiding by the amplifier medium. The initial single pass gain of the amplifier is measured to be 4.0 (Figure 3.23). The gain is near small signal during the first two passes, whereas the excited atom population clearly begins to be depleted from the third pass on. After 5 passes, the seed is amplified to a final energy of 1.2 J, thus extracting 75% of the available stored energy. Further the gain saturation significantly alters the spatial profile producing a super-Gaussian shaped beam (Figure 3.24). The final beam diameter is measured to be 11.6 mm ($1/e^2$). In order to remove any diffraction from the crystal mount and spatial modulation from free propagation, the pulse is spatially filtered by an imaging telescope and pinhole. However most of the diffraction is eliminated by the gain of the amplifier, since the crystal mount lies several millimeters outside of the gain volume.

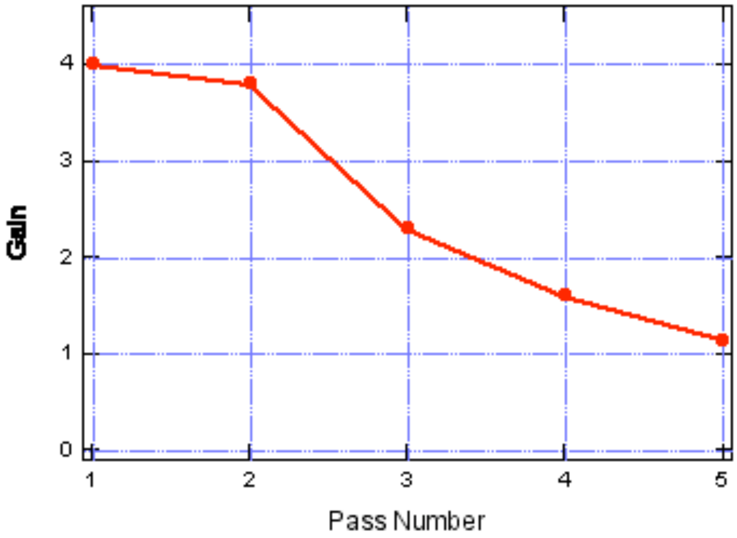

Figure 3.23: Measured gain values per pass for the 5-pass amplifier.

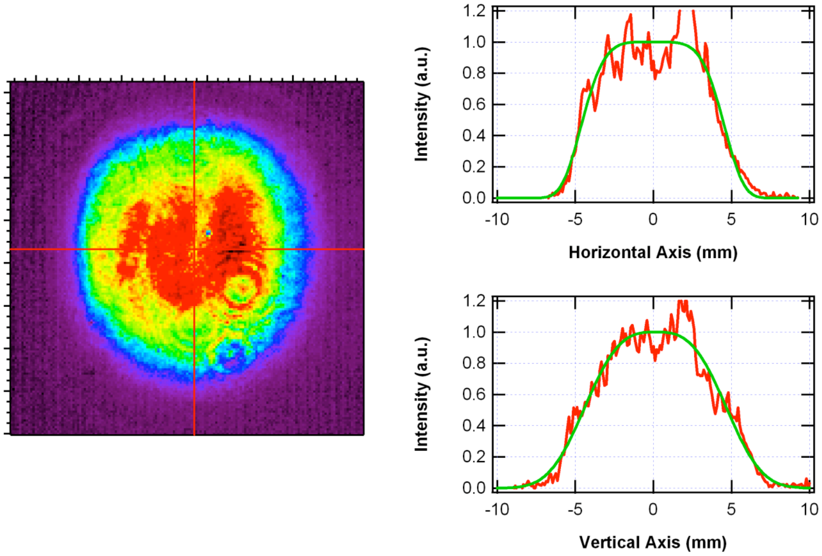

Figure 3.24: Measured beam profile of amplified pulse from the 5-pass amplifier.

3.2.5 Pulse Compressor

After final amplification the pulse is compressed in a vacuum based pulse compressor to avoid B-integral effects from air. The pulse compressor serves as the optical conjugate to the stretcher. It consists of a single 40 cm gold coated grating and two gold-coated rooftop mirror assemblies (Figure 3.25). The grating has a ruling spacing of 1480 lines/mm like the stretcher. The horizontal rooftop is comprised of two 28 by 16 cm rectangular mirrors oriented at 90°. The effective grating spacing, which is determined by the distance of the horizontal rooftop mirrors, is approximately 1.4 meters. The vertical rooftop mirrors are two 17 by 10 cm rectangular mirrors oriented at 90° to give a 7 cm vertical displacement to the pulse for the return pass.

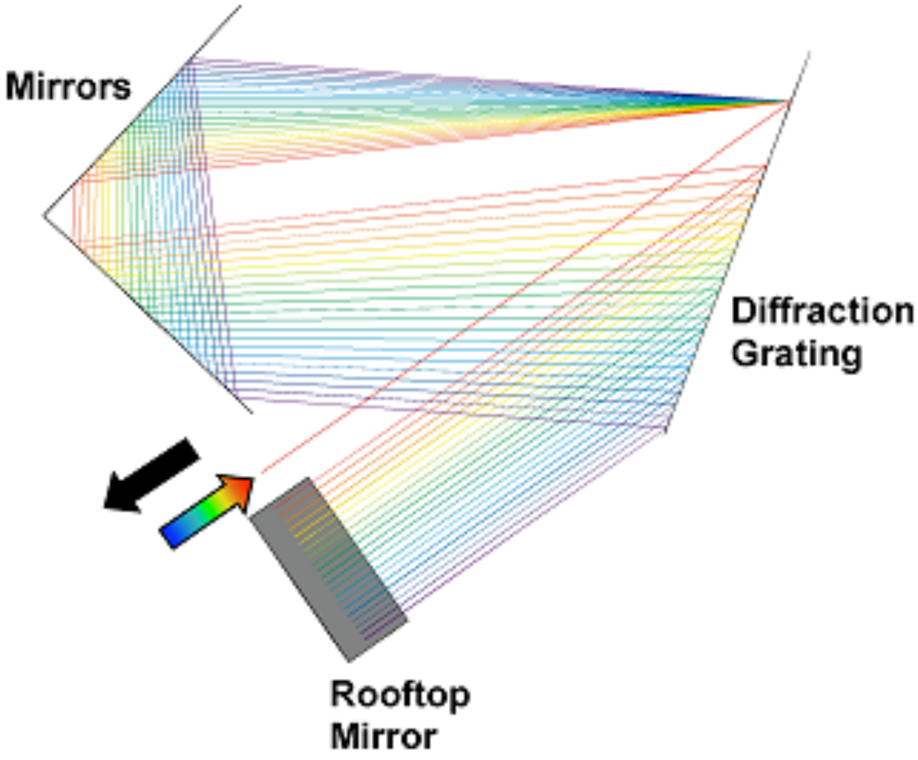

Figure 3.25: Optical ray trace of the THOR compressor.

The compressor is designed to pass a total bandwidth of 90 nm without spectral clipping. The grating also demonstrates an averaged diffraction efficiency of 90% over the entire area at 800 nm. Therefore the transmission efficiency of the entire compressor is measured at 60% for the entire bandwidth of the pulse. Before entering the compressor, the pulse diameter is increased to 5 cm by the vacuum spatial filter. This is to reduce the fluence to below 100 mJ/cm^2. The image plane of the spatial filter is at the first incident surface of the grating. The amplified pulse spectrum is 27.5 nm FWHM. The output spectrum of the compressor shows no indication of spectral clipping in the linear plot, therefore transmitting the entire bandwidth (Figure 3.26). The slight modulation seen in this spectrum is believed to be caused by a post-pulse trailing the main by 550 fs. The post-pulse is created by a small angular misalignment of the 5-pass amplifier crystal.

The final pulse width of the laser is measured using a second order single-shot autocorrelator [78]. The autocorrelation trace has a measured width of 59 fs FWHM. The measured autocorrelation was best traced by a Gaussian fit. Therefore a Gaussian deconvolution suggests the pulse width is then 38 fs FWHM (Figure 3.27). The time-bandwidth product for this pulse is $\Delta\nu\Delta\tau = 0.490$, which is near the transform limit of 0.441. The output energy of the pulse compressor was measured to be 700 mJ. Therefore this constitutes a peak power of 18.4 TW.

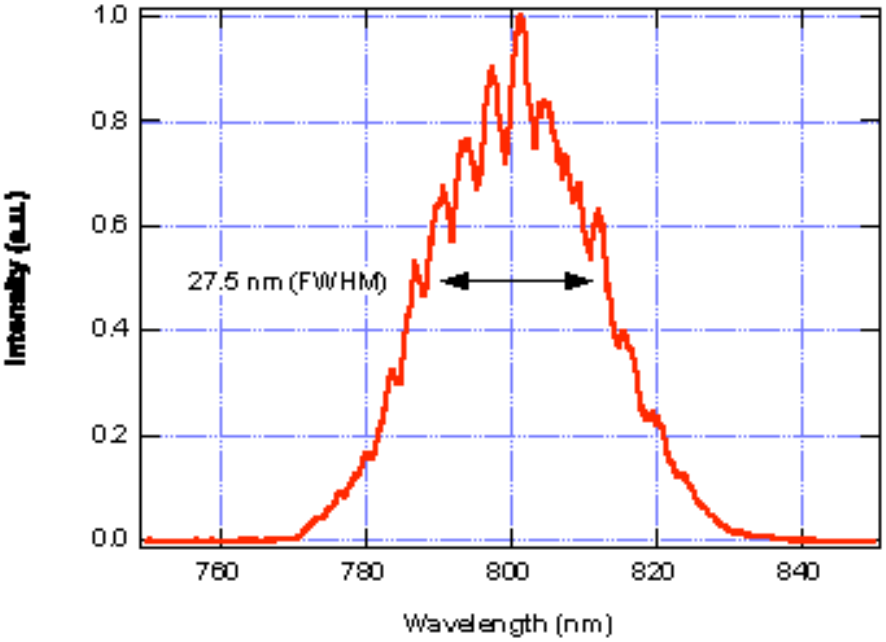

Figure 3.26: Measured spectrum from the output of the THOR compressor. The bandwidth is 27.5 nm (FWHM).

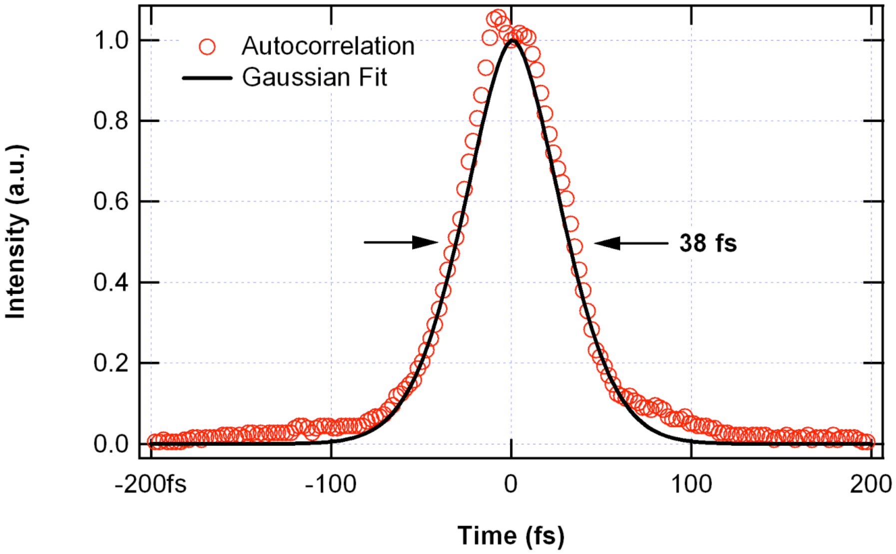

Figure 3.27: Measured 2nd order autocorrelation of the compressed pulse. The compressed pulse energy is 700 mJ with a peak intensity of 18.5 TW.

3.3 Summary

This chapter presented the design and performance of a 10 Hz ultra-fast laser capable of producing femtosecond pulses with a peak intensity of 18.4 TW. The Ti:sapphire based system employs three stages of pulse amplification with a net gain of 10^9. The laser operates at the bandwidth limit of the medium maintaining sufficient spectrum to produce 38 fs pulses. Autocorrelation of the pulse measures the pulse width to be 38 fs, with a near transform limited time-bandwidth product of 0.490. Shorter pulses are possible in similar systems; however this is not without significantly more spectral management. In this design, form and operational reliability are more critical than higher intensity.

Also presented were several energetics-modeling techniques. Models of one and two dimensions were introduced to simulate the pulse evolution and gain saturation. The 1-D model reasonably predicted the output energies of the laser; however the inclusion of the second dimension proved to be more concordant with measured quantities. The regen amplifier in the 1-D case built up and saturated after 14 passes. Whereas the 2-D model, which included cavity mode normalization, accurately predicted the correct number of passes through the gain medium. This is critical in CPA design where the system is a 4th order phase compensated laser.

4 Novel broad spectrum neodymium doped laser glasses for high-energy chirped-pulse amplification

Spectral gain narrowing is one of the primary difficulties in developing sub-100 fs high-energy laser systems with traditional high energy laser amplifiers, such as Nd:glass. The technique of chirped-pulse amplification (CPA) [7] has been applied to various laser host materials in efforts to generate high peak power laser systems. One approach is to use Ti:sapphire as the laser medium to achieve a Joule class laser with extremely short pulses (<20 fs) [79]. However, the short fluorescence lifetime and small aperture size makes realizing higher energies difficult. A recent advancement in CPA design has been the development of optical parametric chirped-pulse amplification (OPCPA) [25, 26]. OPCPA is interesting since the gain is extremely high and uniform over a broad spectrum. Several groups have successfully combined OPCPA front ends with conventional energy storage amplifiers in order to reduce spectral gain narrowing [58, 80]. In these systems, the standard regenerative amplifier is replaced by a broad-spectrum parametric amplifier, which generates a few tens of milli-Joules. Broad spectra can be maintained in this way and some spectral enhancement can be achieved through strong gain saturation. However OPCPA's key constraint is the pump laser. Parametric gain is strongly nonlinear and critically dependent on the pump intensity. Small pump intensity variations will result in drastic temporal and subsequent spectral shaping in the amplified seed pulse. OPCPA pump laser intensities therefore must be well formatted in both temporal and spatial profiles. Since high-energy, high fidelity custom pump lasers are not readily available, OPCPA amplification is generally limited to sub-Joule energies.

In other systems, the availability of large aperture Nd:glass has enabled construction of CPA lasers with energies in excess of 500 Joules and peak powers up to 1 PW [17]; however commonly available phosphate laser glasses are mainly limited by their finite spectral bandwidth (<29 nm FWHM). To circumvent this problem, it is possible to mix various laser glasses with different emission spectra in order to increase the overall gain bandwidth [22-24]. The most straightforward approach is to use Nd:phosphate and Nd:silicate glasses. These two media have peak emission spectra separated by approximately 7 nm, each with >25 nm FWHM of bandwidth. The combination of the two glasses broadens the gain spectrum enabling shorter pulses. However only a handful of these Nd:glasses are commercially available.

During the 1970s Lawrence Livermore National Laboratories conducted an exhaustive evaluation of several hundreds of laser glasses. From these investigations we have identified two broad-spectrum laser glasses that could be used in a mixed-glass architecture to realize gain spectra higher than currently achieved with Nd:phosphate and Nd:silicate combinations. These glasses are designated as K-824 Nd:tantalum/silicate and L-65 Nd:aluminate glass [81]. Neither glass was ever made commercially available; however sufficient spectral and technical data are available to perform a comprehensive evaluation. In this paper we present a study of a mixed glass laser system that combines commercially available Nd:phosphate and each of these new glasses. The goal of this study was to ascertain how broad of an amplified spectrum could be achieved beyond the hundred Joule level. To find the optimum glass we sacrifice the need for high peak gain cross section, and shift the emphasis to finding broader fluorescence spectra with fluorescence peaks further away from the Nd:phosphate peak. We find that with the addition of the new laser glasses in a heterogeneous gain media system, near 100 fs pulses with a gain of 10^4 and 150 fs pulses with a combined gain of 10^8 are achievable.

Energetics and spectral modeling suggest that this novel mixed glass, combined with OPCPA architecture, could be used to achieve in excess of 1 exawatt peak power.

Most neodymium doped laser glasses available today were developed for use in high-energy nanosecond scale laser systems. In these cases the merit function was dominated by peak gain cross-section and low nonlinear coefficient, not total spectral bandwidth. The first glass developed was Nd:silicate. It has a peak spectral emission around 1061 nm and a gain cross-section of approximately 2.4×10^{-20} cm^2. Later phosphate glasses were used with peak emissions at 1054 nm and higher gain cross-sections of $>3 \times 10^{-20}$ cm^2. During the development period of these glasses, many variant mixtures were processed and analyzed in small non-optical quality batches for metrological characteristics. Most of these glasses were cataloged and never further developed. We have isolated two laser glasses that have significantly broader emission spectra than the currently commercially available phosphate and silicate glasses. The two glasses examined are K-824 Nd:tantalum/silicate and L-65 Nd:aluminate. Both were produced by the National Bureau of Standards. Sufficient quantities were produced in order to perform Judd-Ofelt measurements of the spectral intensities [82, 83]. However, no physical or mechanical properties were detailed. Table 4.1 lists both the measured and calculated optical properties pertinent to this investigation.

Unique to the K-824 tantalum/silicate glass is a 30% molar fraction of tantalum oxide (Ta_2O_5). All silicate glasses examined in the catalog that possessed Ta_2O_5 in their chemistry demonstrated significantly broader emission spectra (>30 nm FWHM). The K-824 glass contained the highest molar fraction of them all, and had the broadest emission line width. In contrast, the aluminate glass is dominated by aluminum oxide (Al_2O_3) in its chemistry (50% molar fraction).

Table 4.1: Optical properties of Neodymium doped laser glasses.

Optical Properties	APG-1 Phosphate	Q-246 Silicate	K-824 Silicate	L-65 Aluminate
Peak-Fluorescence Wavelength (nm)	1053.9	1061	1064.5	1067
Line Width (nm) FWHM	27.8	28.5	38.2	41.23
Peak Stimulated Emission Cross-Section (cm^2)	3.4×10^{-20}	2.4×10^{-20}	2.4×10^{-20}	1.8×10^{-20}
Saturation Fluence (J/cm^2) at peak emission wavelength	5.5	7.0	7.0	10.0
Calculated Radiative Lifetime (μs)	370	406	274	349
Refractive Index at Peak Spectral Emission	1.537	1.558	1.70327	1.6637
Nonlinear Refractive Index (esu)	1.13×10^{-13}	1.49×10^{-13}*	3.44×10^{-13}*	2.92×10^{-13}*

*Measured and calculated values listed from data sheets provided by Lawrence Livermore National Laboratories.

APG-1 is a common phosphate glass available from Schott Glass Technologies that exhibits a 27.8 nm bandwidth centered at 1053.9 nm. It was developed for high-average power applications and is used in our calculations. We also considered Q-246 silicate glass from Kigre, Incorporated. This commercially available glass emits at 1061 nm with a 28.5 nm FWHM bandwidth. Typical of silicate glasses, Q-246 has an extended red spectral foot that is broader in total bandwidth than phosphate glass. This is shown more clearly in Figure 4.1. In contrast to Q-246, both the tantalum/silicate and aluminate glasses exhibit much broader emission spectra, 38.5 nm and 41.2 nm respectively. Furthermore, both glass spectra are centered further to the red side of the spectrum. This is more appealing because, when combined in a heterogeneous amplifier, the net available gain bandwidth is broader. Another key point of interest in high-gain scenarios is the relative shape of the spectra. At 80% of the peak emission cross-section spectrum, Q-246 is approximately 14 nm wide. However, the tantalum/silicate and aluminate glasses are both 19 nm wide. This is the spectral region where most of the bandwidth will survive after high amplification (>10^4).

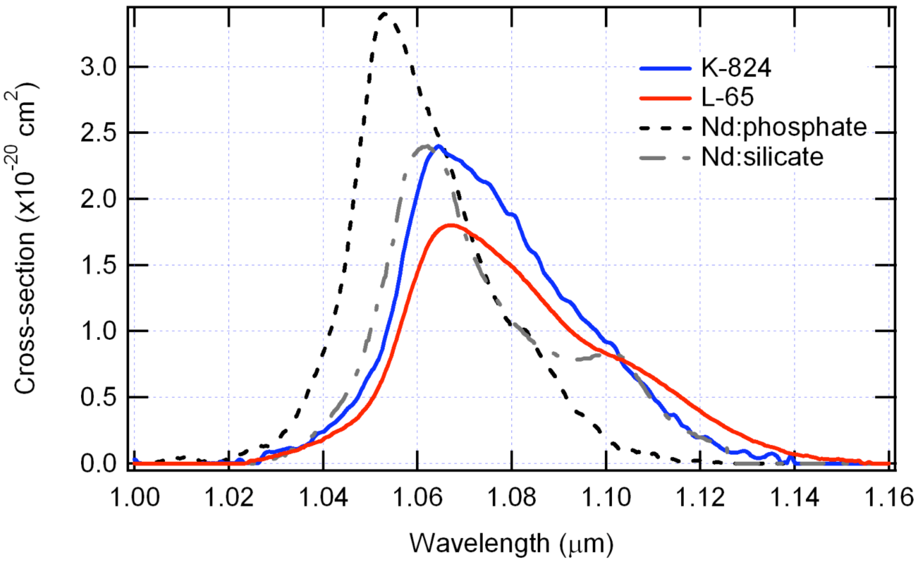

Figure 4.1: Stimulated emission cross-sections of Neodymium doped laser glasses.

There are a few important optical limitations of the new glasses. First, the gain cross-section in aluminate is significantly smaller at 1.8×10^{-20} cm^2 than other silicate glasses. This then requires more passes through the gain medium to accumulate the necessary gain. In addition, the estimated nonlinear coefficients in both the tantalum/silicate and aluminate glasses (3.44×10^{-13} and 2.92×10^{-13} esu, respectively) are greater than, by a factor of two, Q-246 and are a factor of three larger than APG-1. This will inherently affect the nonlinear phase accumulated in each amplifier (B-integral). High-fluence saturation of an aluminate or tantalum/silicate amplifier will have to be carefully considered.

The goal of this investigation was to examine the energetics versus gain narrowing effects in a mixed glass heterogeneous amplifier chain. We considered the mixing of APG-1 phosphate glass with either Nd:tantalum/silicate or the Nd:aluminate. The primary focus was to ascertain the total gain and the best gain ratio between the mixed glass amplifiers in order to maintain sufficient bandwidth for 100 fs pulses.

We employed a one-dimensional small signal gain amplification code in order to simplify the model. It is difficult to achieve saturation in glass amplifiers since the saturation fluence is generally large (Table 4-1). This fact, coupled to high nonlinear coefficients and impurity inclusions in the material, makes the effects of gain saturation small in comparison with spectral shaping from gain spectra. Pulses must exceed 5 J/cm^2 in these materials before saturation effects become prevalent. Further, for chirp factors ≤100 ps/nm, nonlinear phase accumulation becomes significant at fluences above 2 J/cm^2 for the bandwidths considered here. Therefore gain saturation was not considered in these simulations. Using the measured and published spectral gain curves for APG-1 and the other glasses, a wavelength dependent gain spectrum for the mixed media was generated. To vary the balance in gain between the two glasses, the method used by Ross *et al.* [24] was utilized. The output spectrum from the mixed glass amplifier depends only on the ratio from the exponents in gain factor shown in equation (4.0.1)

$$\frac{1-\kappa}{\kappa} = \frac{\sigma_{phos}}{\sigma_{\beta}} \frac{\ln G_{\beta}}{\ln G_{phos}} \tag{4.0.1}$$

Here σ_{phos} and σ_{β} are the gain cross-sections, and G_{phos} and G_{β} are the gain factors of Nd:phosphate and the alternate glasses respectively. The subscript β is used to identify either tantalum/silicate or aluminate glass. The parameter κ, which ranges from 0 to 1, varies the net gain between the two media. When κ is 1, the gain is entirely in the phosphate amplifier. Oppositely when it is 0, the gain is entirely done by the alternate glass. Amplified spectra were evaluated at each gain order of magnitude. The net gain between the two glasses was kept constant while κ is varied from 0 to 1. The gain factor α represented by

$$\begin{aligned} Gain &= Exp[\alpha(\sigma_{phos}\kappa + \sigma_{\beta}(1-\kappa))], \\ \alpha &= \frac{n \ln 10}{\sigma_{phos}\kappa + \sigma_{\beta}(1-\kappa)}, \end{aligned} \tag{4.0.2}$$

is the product of the excited atom population and total length of amplifier material. It indicates how hard each glass should be pumped for a given gain length. Here n, which was varied from 0 to 8, represents the exponential peak gain order of magnitude.

The amount of bandwidth required for mixed glass amplification is determined by the relative separation of the peak emissions of the two glasses. Most of the spectral amplification by each glass is accomplished in a region that lies within 20% of its peak gain cross-section. In the mixed glass system, the blue side of phosphate and the red side of the silicate glass defines this space. For the two novel glasses, this region is approximately 30 nm. Therefore, seeding with a spectrum that is broader than 30 nm is required.

Initially a variety of seed beams and spectra from various front-end amplification systems were considered. Ultimately a Ti:sapphire oscillator followed by an OPCPA pre-amplifier chain was determined most suitable. Commercially available Ti:sapphire oscillators operating beyond 1 micron can have sufficient bandwidth to generate 100 fs pulses. Parametric amplification is then effective because of the high gain that can be achieved with relatively small material path length. Most importantly a strongly saturated parametric amplifier will spectrally broaden the seed pulse. Several groups have recently demonstrated broad bandwidth pulse compression of a spectrally broadened OPCPA pulse [84, 85]. Furthermore, pre-pulse contrast $>10^7$ has been achieved by appropriately tailoring the geometric and temporal windows of the pump [86, 87].

The pulse used in this simulation to seed the mixed glass amplifiers was modeled as a 16 nm FWHM Gaussian spectrum. The pulse width from the Fourier transform limit is 100 fs. The pulse was first preamplified using a 1-D parametric amplification code [88] to simulate a spectrally saturated broadened pulse with 42 nm FWHM of bandwidth. Once the preamplified spectral profile was generated, it could be shifted in wavelength to facilitate seeding various wavelength centers in an effort to broaden the amplified output spectrum. The 42 nm seed spectrum represents amplification of the entire 16 nm FWHM Gaussian pulse. No spectral clipping is assumed from the stretcher. We performed simulations with narrower bandwidth seed pulses, and determined this was the optimum bandwidth.

A variety of wavelength centers were used for the OPCPA spectrally broadened pulse. APG-1 has a peak gain centered at 1053.9 nm, tantalum/silicate at 1064.5 nm, and aluminate at 1067 nm. Also, the band pass limit of the pulse stretcher further establishes the finite bandwidth of the seed. Therefore seed spectra with centers ranging from 1053 nm to 1080 nm were examined during this simulation. APG-1 has the largest gain cross-section, so it will contribute most to the spectral shaping in the amplifier chain. As a result it was found that the most effective wavelength at which to seed was 1070 nm. Here the strong gain pulling from the APG-1 could be best utilized while still accessing the lower gain available on the red side of the spectrum from either the tantalum/silicate or aluminate. Figure 4.2 illustrates the seed centered at 1070 nm being amplified by a

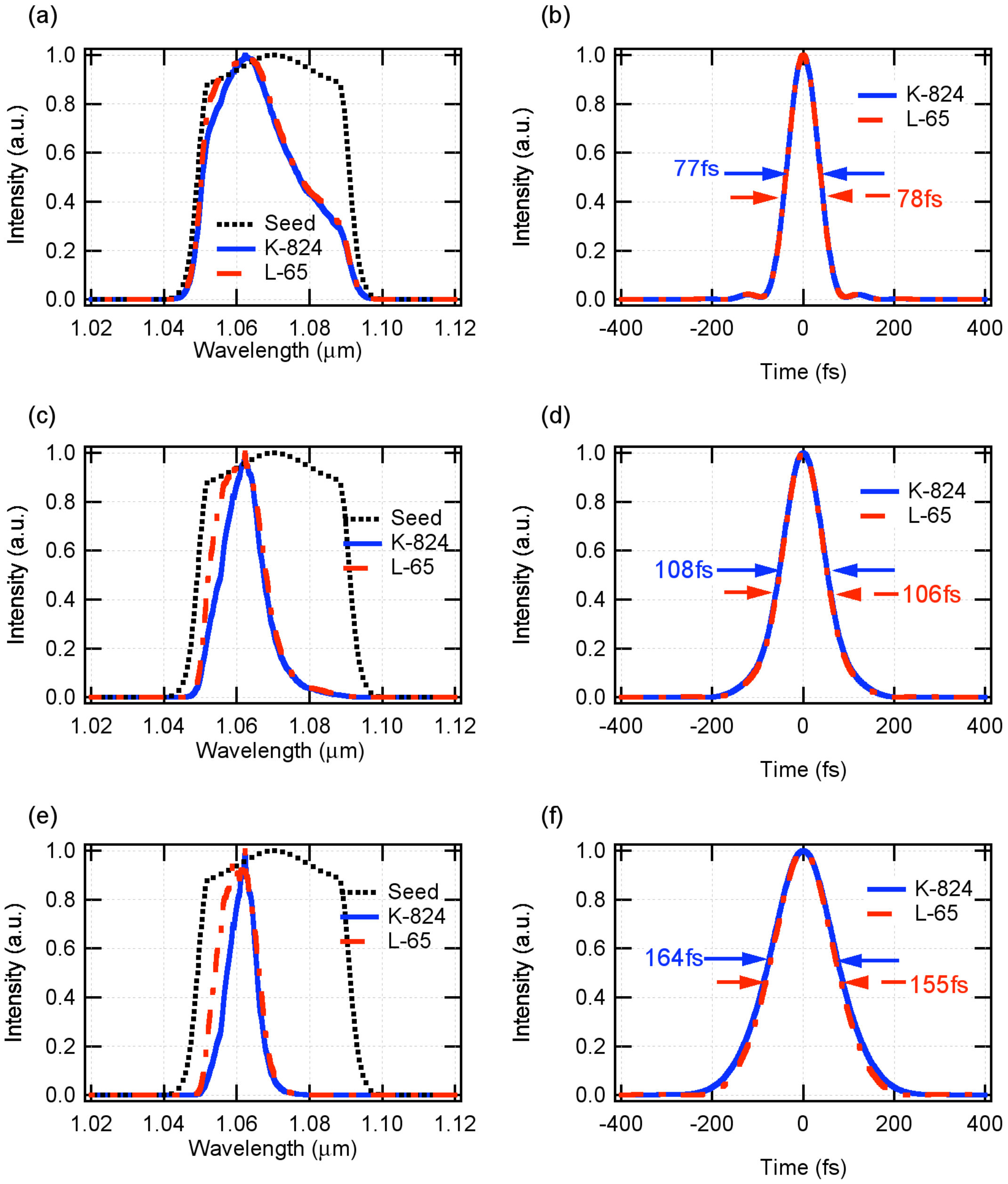

Figure 4.2: Simulated spectral gain narrowing and the conjugate Fourier transform pulse widths from mixing APG-1 Nd:phosphate glass with either K-824 Nd:silicate or L-65 Nd:aluminate glass. Gain balance factor ($\varkappa$) is set to 0.5 in all graphs: (a) amplified pulse spectra with total gain of 10^1, (b) Fourier transform pulse widths for 10^1, (c) amplified pulse spectra with total gain of 10^4, (d) Fourier transform pulse widths for 10^4, (e) amplified pulse spectra with total gain of 10^8, (f) Fourier transform pulse widths for 10^8.

attributed to gain pulling of the spectra from the longer to shorter wavelengths. Hence the same net amplified bandwidth survived at different wavelength centers with different values of κ.

The point at which the new glasses become most attractive is when the combined glass gain exceeds 10^3. Figure 4.3 illustrates that the broader spectra glasses mixed with a phosphate amplifier show a marked improvement in amplified bandwidth over the standard silicate glass. When seeding the mixed-glass amplifier containing tantalum/silicate with a spectrum centered at <1065 nm, the optimum values of κ ranged from 0.25 to 0.5. Here amplified bandwidths were sufficient to generate 100 fs pulses. In this case more gain is needed from the tantalum/silicate to maintain the longer wavelengths. However by shifting the seed spectrum to >1065 nm, 100 fs pulses could still be achieved with an increased gain of 10^4. Further κ shifted to an optimum value range of 0.5 to 0.625 relying on more gain from phosphate. With the higher nonlinear coefficient coupled with the ample supply of phosphate glass, this is a clear systematic improvement. At this gain level the aluminate glass performed very similar to tantalum/silicate with minutely more amplified bandwidth. This occurred primarily from its broader gain spectrum.

When the gain in the heterogeneous amplifiers was increased to 10^8, both glasses were able to support sufficient bandwidth to produce 150 fs pulses. Conversely a mixture with a standard silicate glass narrowed the spectrum dramatically more. At this level of amplification, gain narrowing is the dominant effect regardless of seed wavelength. With tantalum/silicate, amplified pulses were generally >150 fs and κ was optimum at ~0.5.

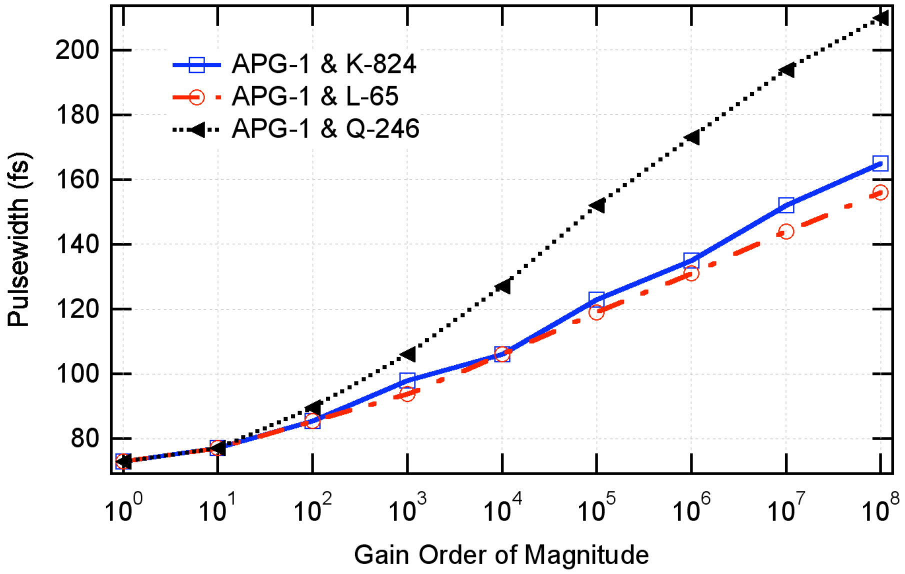

Figure 4.3: Fourier transform limit pulse widths as a function of peak spectral gain order of magnitudes (n from Eq. 4.0.2).

Shifting the seed wavelength led to only small improvement. When seeding at 1057 nm, the Fourier transform of the amplified bandwidth yielded 172 fs. Seeding at 1070 nm the transform produced a 165 fs pulse. The benefits of the broader spectrum aluminate glass also become more obvious at this level of amplification. Aluminate amplified bandwidths were generally about 10% broader, producing a best pulse width of 152 fs pulse when seeded at 1070 nm. Seeding at 1057 nm produced a 161 fs pulse. However the optimum κ value was shifted to 0.375, thus requiring more gain from aluminate glass than the phosphate.

Although both glasses performed similarly in their amplified spectral content, overall, tantalum/silicate showed higher merits. Even though it does not exactly match the spectral content of the aluminate, it has an equivalent gain cross-section to standard silicate glasses. This dramatically reduces the pumping level and/or the total amount of material that needs to be passed to extract the same energy. Tantalum/silicate equaled aluminate with nearly the same amount of amplified bandwidth maintained throughout all gain levels. Conversely tantalum/silicate does possess a larger nonlinear coefficient that will contribute to larger B-integral accumulation.

Acquisition of these new glasses poses the most difficult challenge. Currently it would be difficult to procure these new glasses in any form other than a large aperture rod (>5 cm). With that caveat aside, implementation of these glasses into present day high-energy CPA glass lasers could be relatively simple. An OPCPA front-end can easily generate >50 mJ with a significantly gain broadened spectrum. Next a <5 cm aperture tantalum/silicate rod could be multi-passed to extract a gain $>10^2$. The final energy would then be extracted and gain-balanced from more affordable large aperture Nd:phosphate slab amplifiers. Energies could easily exceed several hundreds of Joules with sufficient bandwidth to generate 100 fs pulses. With current technologies this could be a straight forward path to multi-petawatt lasers.

If large aperture slabs (>10 cm) of these glasses could be attained, the design of a mixed-glass exawatt laser system is possible. This laser could be constructed with further development of current technologies, incorporating OPCPA, mixed-glass amplification, and tiled gratings in the pulse compressor [89]. We offer here the conceptual design of a Nd:glass laser system with an integrated peak power of one exawatt from eight beam-lines comprised of one national ignition facility (NIF) amplifier bundle (Figure 4.4).

Pulse generation would come from a 100 fs, mode-locked oscillator producing 16 nm FWHM Gaussian spectrum at 1.065 μm. In order to avoid significant nonlinear phase accumulation in the final amplifier, this pulse is stretched to 8 ns using 1740 lines/mm diffraction gratings with a band-pass of >40nm. Preamplification to 1 Joule would be accomplished in a multi-stage broad-band OPCPA to produce a super- saturated

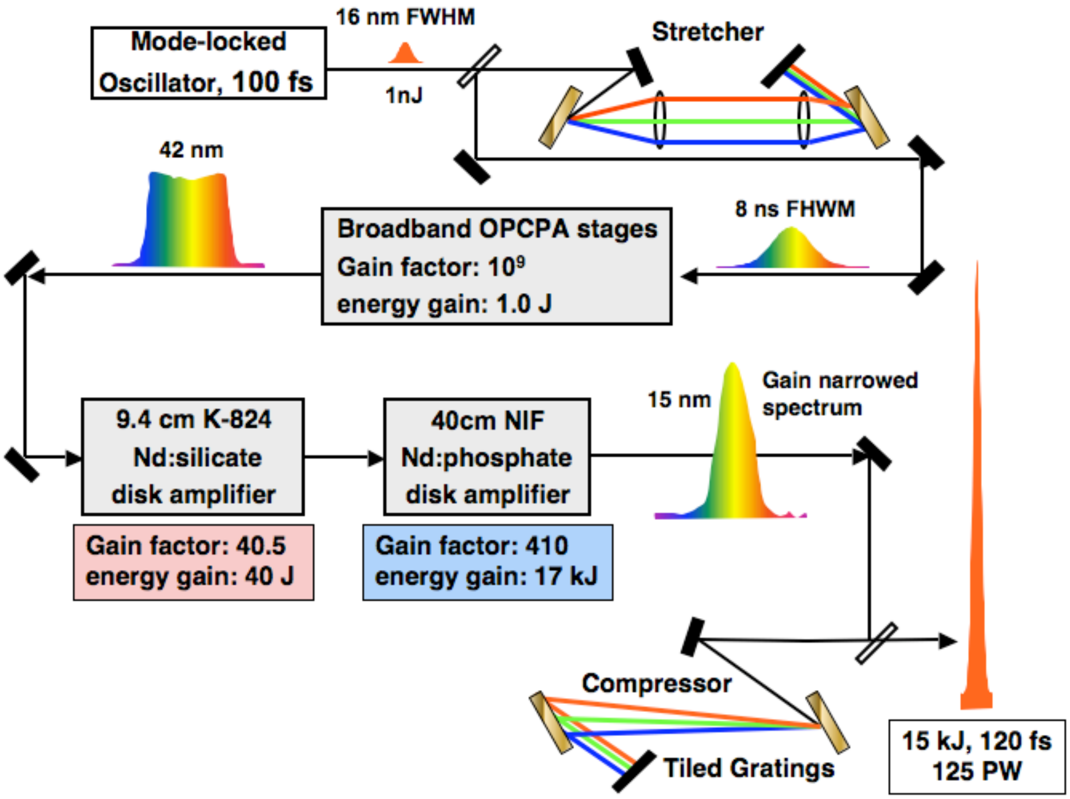

Figure 4.4: Conceptual schematic of one of eight beam-lines comprising an exawatt laser system.

40 nm FWHM spectrum [90]. Mixed glasses would be used for the final amplification with a κ-value of 0.5 and a combined gain of 1.7×10^4. Using multi-passed 9.4 cm diameter slab amplifiers with Nd:tantalum/silicate glass, the pulse would be amplified to ~50 Joules. Finally the pulse is injected into a NIF-style, 40 cm Nd:phosphate glass amplifier to increase the energy to ~17 kJ [91].

We performed a numerical simulation of this system, which included gain saturation and nonlinear phase accumulation. Saturation effects were included here since the final amplifiers achieve an output fluence of >10 J/cm^2. The small signal gain model predicted a transform limited pulse width of 115 fs. In contrast, inclusion of gain saturation reduced the simulated bandwidth and produced a transform limited pulse width of 135 fs. This is primarily attributed to square pulse distortion, and could be pre-compensated before glass amplification. The model also predicts an accumulated *B*-integral of 0.9 from the glass amplification. The majority of the nonlinear phase arises from the phosphate amplifier ($B = 0.85$), which experiences the highest fluence and longest optical path length.

Ultimately the final technological barrier would be compression grating diameter. At high energy the damage threshold will dominate grating size over diffractive dispersion from the increased bandwidth. However using tiled multi-layer dielectric grating technology a two grating single-pass compressor could be constructed [89]. Allowing for a 1 J/cm^2 beam fluence exiting the compressor, a pair of tiled gratings with 7.5 and 10.5 m^2 of area respectively with about 80% fill factor will be required to compress the pulse. The first grating would be comprised of a 3x5 tiled array of 0.5 m x 1m gratings. The second grating horizontal diameter would increase to a 3x7 tiled array. To compress the pulse with a 500 ps/nm chirp in single pass, the nominal grating separation would be 13.4 meters. The exiting beam diameter would be 130x170 cm with an approximate lateral chirp of 10mm/nm. The lateral chirp will cause the pulse front to tilt in the far field; however it is small in comparison to the overall size of the beam. With >90% transmission from the compressor, each beam-line should compress 15 kJ to 120 fs producing a 125 PW peak power. The eight 125 PW beam lines could combine to deliver 1 exawatt in peak power.

In conclusion we have shown that ultrafast high-energy pulses can be achieved with a high gain in glass. Implementation of novel broad-spectrum glass in a mixed-glass architecture can decrease amplified pulse widths to the 150 fs regime with up to 8 orders of magnitude in amplification. This could clearly pave the way for the next generation multi-petawatt and even exawatt laser.

5 Design and Performance of the GHOST Laser

In the realm of high energy, short pulse lasers, neodymium doped laser glasses have been the principle gain medium of choice. The availability of large aperture Nd:glass has enabled many systems to achieve peak intensities exceeding many tens of terawatts [20-22]. The first Petawatt laser was successfully deployed at Lawrence Livermore National Laboratory in 1996 [92]. Here petawatt intensity was achieved by pulse amplification to the near kilo-Joule level in large aperture Nd:glass amplifiers. However the primary limitation of Nd:glass is its finite spectral bandwidth. With an emission spectrum of 27 nm (FWHM), achieving compressed pulsewidths less than 300 fs becomes exceedingly difficult with gains in excess of 10^3. Therefore these systems have relied upon other gain mediums in combination with laser glass to produce short duration, high-energy pulses. Most lasers preamplify in Ti:sapphire to tens of milijoules to reduce the needed gain in glass. However at 1 μm wavelengths, the gain in Ti:sapphire is very low and requires many passes through the gain material. This generally results in large ASE accumulation, which degrades the pulse contrast.

The recent technique of optical parametric chirped pulse amplification (OPCPA) [25] has strongly reduced the bandwidth limiting effects in high-energy laser glass systems [26, 80, 93]. OPCPA is a nonlinear process based upon difference frequency generation (DFG). It demonstrates extremely high single pass gain ($>10^3$) with a large and uniform amplification bandwidth (>100 nm). In addition, since OPCPA is generally achieved in single pass amplification, pre-pulse and ASE are usually eliminated; therefore producing a high-contrast ($>10^8$) laser pulse [94]. The largest obstacle in extending OPCPA to high energies (>100 mJ) is the pump laser. Parametric amplification with high conversion efficiency is accomplished by spatially and temporally aligning the seed and pump pulses. Commercially available Q-switched pump lasers are generally >10 ns in pulsewidth, and most stretched seed pulse durations in CPA are limited to a few nanoseconds (<4 ns). Further OPCPA requires near uniform intensity from the pump pulse in order to avoid strong spectral modulation. Therefore, high fidelity well formatted pump lasers are costly and not readily available. Although some groups have demonstrated high energy amplification from OPCPA [84], this technology is not easily applied to common table-top systems today.

Recently several groups around the world have started developing the next generation Petawatt lasers using many of the aforementioned techniques to increase the amplified spectral content, therefore reducing the need for kilo-Joule energies. One approach is to utilize the shifted spectral lines of Nd:phosphate and Nd:silicate glass [24]. The peak emission lines of phosphate and silicate glasses are separated by 8 nm and overlap very well. By using a mixed glass amplifier chain, a larger gain spectrum is available permitting broader spectrum amplified pulses (Figure 5.1). A few groups have demonstrated preliminary spectral broadening results from mixed glass architectures [22, 23]. However only a minimal spectral enhancement has been demonstrated in either case because high gain factors are required.

Our efforts have been to develop a hybrid short-pulse, 150-Joule Petawatt laser system utilizing all three of the previously mentioned techniques. We are developing a unique CPA laser that will combine the laser mediums of Ti:sapphire, optical parametric chirped-pulse amplification (OPCPA), and mixed laser glasses in an effort to maintain an amplified spectrum of up to 16nm FWHM. By using an OPCPA front-end to pre-amplify the broad-spectrum pulse to the 1-Joule level, we can reduce the necessary gain from Nd:glass to 2 orders of magnitude. This will keep the spectral gain narrowing to a minimum. However, to date a thorough experimental investigation of the precise gain ratio for broad-spectrum amplification between the two laser glasses has not been accomplished.

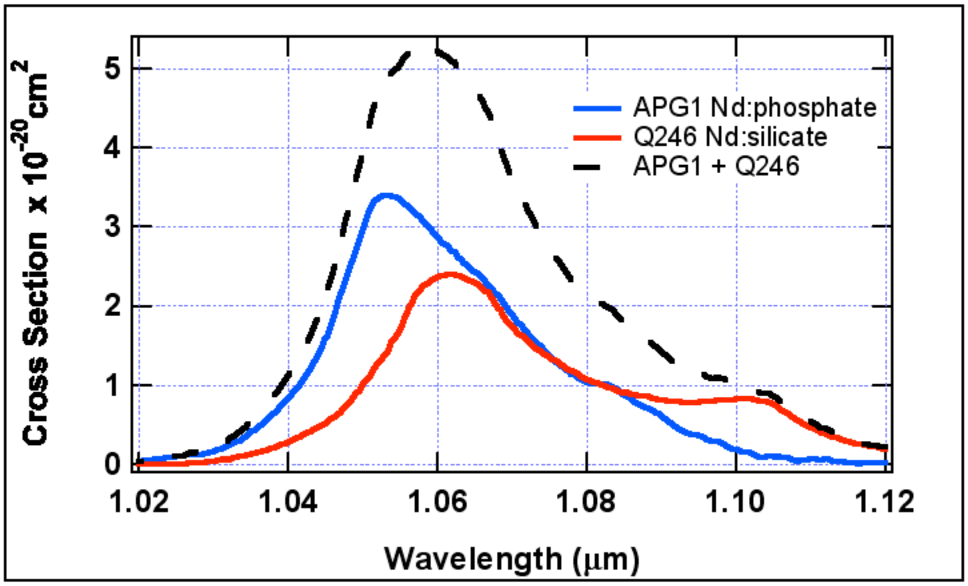

Figure 5.1: Plots of gain cross-section spectrum for Nd:phosphate and Nd:silicate laser glasses. The dotted line shows the sum of the two cross-sections.

This chapter presents a detailed analysis and results of broad-spectrum short pulse amplification in mixed-glass amplifiers. The experiment was performed on a scale model of the Texas Petawatt Laser. The Glass Hybrid OPCPA Scaled Test-bed (GHOST) is a 20 TW tabletop laser designed to investigate the critical elements of the Petawatt, and be a proof of principle model (Figure 5.2). The GHOST laser was constructed to address three critical design elements for the Petawatt: 1) Can a super-saturated, broad-spectrum (>30 nm FWHM) preamplified seed be produced from an OPCPA front-end? 2) What is the optimum gain ratio between the mixed-glass to produce the broadest amplified spectra? 3) What is the optimum wavelength to seed the mixed-glass amplifiers? We

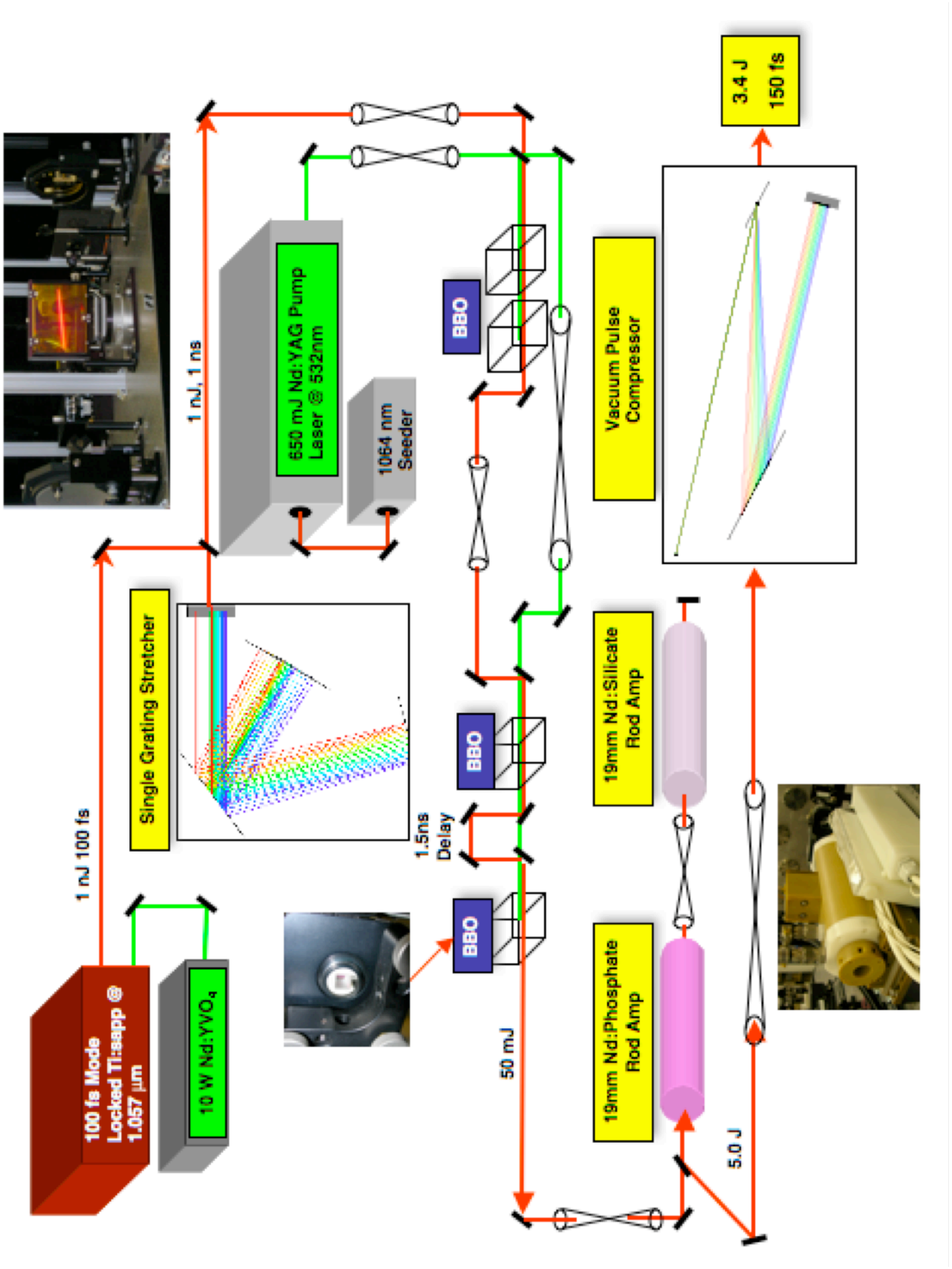

Figure 5.2: Optical schematic of the GHOST laser.

report here experimental results and numerical simulations of spectral gain narrowing from a mixed glass amplifier chain. An optimized gain balance between the two media is examined in an effort to maintain sufficient bandwidth to achieve near 100 fs pulses from the final amplifiers.

The first section of this chapter addresses parametric amplification. A complete derivation of the coupled wave equations for DFG is presented. Section 5.2 discusses the energetics modeling for the GHOST laser. A one-dimensional energetics and phase code was developed to examine broad-spectrum parametric amplification. A separate energetics code was also developed to analyze the gain ratio in a mixed glass laser. Section 5.3 examines stretcher and compressor designs, and both linear and nonlinear phase accumulation in the entire laser system. Section 5.4 details the laser design and its characterization, and section 5.5 discusses the results of the mixed glass amplification measurements. Finally section 5.6 summarizes the results of the GHOST laser.

5.1 Differ Frequency Generation for Optical Parametric Chirped Pulse Amplification

This section presents the derivation of difference frequency generation (DFG) for the purpose of OPCPA. The first section will begin by deriving the classical interpretation of nonlinear wave equation for nanosecond laser pulses in a nonlinear material beginning with Maxwell's equations. Next the equation is solved to for the case of difference frequency generation to produce the coupled wave equations. Section 5.1.3 shows analytic solutions for electric field amplitude and their qualitative behavior are discussed. Also presented are the analytic solutions for gain in the small signal regime.

Finally section 5.1.4 discusses considerations for angular phase matching in type I negative uniaxial crystals.

5.1.1 The Nonlinear Wave Equation

We begin with a classical approach to three-wave optical parametric interactions. Although quantum mechanics is needed to describe fully these phenomena, a classical or semi-classical interpretation is adequate and quite illustrative for this work. For this work I will follow the method taken by that of Boyd [95], Yariv [96], and Shen [97]. The derivation is performed in SI units, since they are the units easily measured in the laboratory.

To derive the wave equation for the propagation of light through a nonlinear medium, we begin with Maxwell's equations stated in SI units

$$\nabla \cdot \mathbf{D}(\mathbf{r},t) = \rho(\mathbf{r},t)\,, \tag{5.1.1}$$

$$\nabla \cdot \mathbf{B}(\mathbf{r},t) = 0\,, \tag{5.1.2}$$

$$\nabla \times \mathbf{E}(\mathbf{r},t) = -\frac{\delta \mathbf{B}(\mathbf{r},t)}{\delta t}\,, \tag{5.1.3}$$

$$\nabla \times \mathbf{H} = \mathbf{J}(r,t) + \frac{\delta \mathbf{B}(\mathbf{r},t)}{\delta t}\,, \tag{5.1.4}$$

where **D** is the electric displacement, **E** is the electric field, **B** is the magnetic induction, **H** is the magnetic field, ρ is the charge density, and **J** is the current density. These equations can be immediately simplified by applying the appropriate conditions of a uniform, lossless, non-magnetic, nonlinear media. First, there are no free charges or currents so that

$$\rho(\mathbf{r},t) = 0\,, \tag{5.1.5}$$

and

$$\mathbf{J}(r,t) = 0\,. \tag{5.1.6}$$

Further, since the medium is non-magnetic, the magnetic field and induction are related by

$$\mathbf{B}(\mathbf{r},t) = \mu_0 \mathbf{H}(\mathbf{r},t)\,, \tag{5.1.7}$$

where μ_0 is the magnetic permeability. However since the medium is nonlinear, the polarization vector **P** links the electric displacement and electric field through

$$\mathbf{D}(\mathbf{r},t) = \varepsilon_0 \mathbf{E}(\mathbf{r},t) + \mathbf{P}(\mathbf{r},t)\,, \tag{5.1.8}$$

where ε_0 is the dielectric constant of vacuum.

The wave equation is derived in the usual fashion by taking the curl of equation 5.1.3. It is assumed to be separable in space and time, so that the time derivative on the right hand side can be interchanged with the spatial derivative to yield

$$\nabla \times \nabla \times \mathbf{E}(\mathbf{r},t) = -\mu_0 \frac{\partial^2 \mathbf{D}(\mathbf{r},t)}{\partial t^2}\,. \tag{5.1.9}$$

In order to introduce the nonlinearity to equation 5.1.9, the nonlinear polarization is usually expressed as a power series in field strength of **E**, so that

$$\mathbf{P}(\mathbf{r},t)=\sum_{i}^{\infty}\mathbf{P}^{(i)}(r,t)=\mathbf{P}^{(1)}(r,t)+\mathbf{P}^{(NL)}(r,t), \tag{5.1.10}$$

where the $\mathbf{P}^{(1)}$ and $\mathbf{P}^{(\mathrm{NL})}$ are the linear and nonlinear polarizations respectively. The linear polarization is defined by

$$\mathbf{P}^{(1)}(\mathbf{r},t)=\varepsilon_0\chi^{(1)}\mathbf{E}(\mathbf{r},t), \tag{5.1.11}$$

where $\chi^{(1)}$ is the linear susceptibility tensor. DFG is a 2nd order nonlinearity, independent of higher order terms; therefore the nonlinear polarization in this case is

$$\mathbf{P}^{(2)}(\mathbf{r},t)=\chi^{(2)}\mathbf{E}(\mathbf{r},t)\cdot\mathbf{E}(\mathbf{r},t). \tag{5.1.12}$$

Again $\chi^{(2)}$ is the 2nd order nonlinear susceptibility tensor. Likewise we can also express the displacement vector in terms of the polarization series by

$$\mathbf{D}(\mathbf{r},t)=\varepsilon_0\left(1+\chi^{(1)}\right)\mathbf{E}(\mathbf{r},t)+\mathbf{P}^{(NL)}=\mathbf{D}^{(1)}(\mathbf{r},t)+\mathbf{P}^{(NL)}(\mathbf{r},t). \tag{5.1.13}$$

By substituting in equation 5.1.13, equation 5.1.9 now becomes

$$\nabla\times\nabla\times\mathbf{E}(\mathbf{r},t)+\mu_0\varepsilon\frac{\partial^2\mathbf{D}^{(1)}(\mathbf{r},t)}{\partial t^2}=-\mu_0\frac{\partial^2\mathbf{P}^{(2)}(\mathbf{r},t)}{\partial t^2} \tag{5.1.14}$$

Here $\varepsilon=\varepsilon_0\varepsilon_r=\varepsilon_0\left(1+\chi^{(1)}\right)$ is defined as the total permeability of a dielectric material. Equation (5.1.14) describes the motion of an inhomogeneously driven wave, where $\mathbf{P}^{(2)}$ acts as the source/driving term. For the homogenous case ($\mathbf{P}^{(2)}=0$), the solution is the usual electro-magnetic wave propagating through a dielectric material with phase velocity $1/\sqrt{\mu_0\varepsilon} = c/\sqrt{\varepsilon_r}$.

In the case of OPCPA, we are dealing with broadband pulses in a dispersive material. Therefore we must express wave equation in terms of the frequency-dependent components. We can decompose **E**(**r**,t), **D**(**r**,t), and **P**(**r**,t) into their Fourier components of positive frequencies and complex amplitudes as:

$$\mathbf{E}(\mathbf{r},t) = \sum_n \mathbf{E}_n(\mathbf{r},t) = \sum_n \left(\mathbf{E}_n(\mathbf{r})e^{-i\omega_n t} + \mathbf{E}_n^*(\mathbf{r})e^{i\omega_n t}\right), \tag{5.1.15}$$

$$\mathbf{D}^{(1)}(\mathbf{r},t) = \sum_n \mathbf{D}_n^{(1)}(\mathbf{r},t) = \sum_n \left(\mathbf{D}_n^{(1)}(\mathbf{r})e^{-i\omega_n t} + \mathbf{D}_n^{*(1)}(\mathbf{r})e^{i\omega_n t}\right), \tag{5.1.16}$$

and

$$\mathbf{P}^{(2)}(\mathbf{r},t) = \sum_n \mathbf{P}_n^{(1)}(\mathbf{r},t) = \sum_n \left(\mathbf{P}_n^{(1)}(\mathbf{r})e^{-i\omega_n t} + \mathbf{P}_n^{*(1)}(\mathbf{r})e^{i\omega_n t}\right). \tag{5.1.17}$$

The linear displacement is described in terms of a real, frequency-dependent dielectric tensor by

$$D_n^1(\mathbf{r}) = \varepsilon^{(1)}(\omega)\cdot\mathbf{E}_n(\mathbf{r}) = \varepsilon_0\left(1+\chi^{(1)}(\omega)\right)\cdot\mathbf{E}_n(\mathbf{r}), \tag{5.1.18}$$

where the frequency dependence is arrived at by the Fourier transform of the time-dependent susceptibility by

$$\chi^{(1)}(\omega) = \int_{-\infty}^{\infty} \chi^{(1)}(t)e^{-i\omega t}dt\ . \tag{5.1.19}$$

When equations (5.1.15) through (5.1.17) are introduced into equation (5.1.14), we obtain a wave equation valid for each frequency component for the electric field:

$$\nabla\times\nabla\times\mathbf{E}_n(\mathbf{r},t)+\mu_0\varepsilon^{(1)}(\omega_n)\frac{\partial^2\mathbf{E}_n(\mathbf{r},t)}{\partial u^2}=-\mu_0\frac{\partial^2\mathbf{P}_n^{(2)}(\mathbf{r},t)}{\partial u^2}. \tag{5.1.20}$$

Moreover, the parting of the fields into the Fourier components permits direct evaluation of the time derivatives in equation (5.1.20) which reduce to

$$\nabla\times\nabla\times\mathbf{E}_n(\mathbf{r},t)-\omega_n^2\mu_0\varepsilon^{(1)}(\omega_n)\mathbf{E}_n(\mathbf{r})=\omega_n^2\mu_0\mathbf{P}_n^{(2)}(\mathbf{r}). \tag{5.1.21}$$

The wave equation can be finally simplified by the use of the vector identity $\nabla\times\nabla\times\mathbf{E}=\nabla(\nabla\cdot\mathbf{E})-\nabla^2\mathbf{E}$. In the case of plane waves, the first term on the right hand side of this identity vanishes. This leaves the wave equation in the form of an inhomogeneous Helmholtz equation:

$$\nabla^2\mathbf{E}_n(\mathbf{r},t)+\omega_n^2\mu_0\varepsilon^{(1)}(\omega_n)\mathbf{E}_n(\mathbf{r})=-\omega_n^2\mu_0\mathbf{P}_n^{(2)}(\mathbf{r}). \tag{5.1.22}$$

This set of inhomogeneous Helmholtz equations formulates a sufficient description for the nonlinear processes of nanosecond-scale pulses, especially since each can be described by a superposition of infinite plane waves.

5.1.2 The Coupled Wave Equations for Difference Frequency Generation

The nonlinear wave equation (5.1.22) is generally used to describe the interaction of simple plane waves in a nonlinear medium. In this case, DFG is a second-order nonlinear process similar to sum-frequency generation (SFG) and second-harmonic generation (SHG). Therefore we are only interested in the component of $\mathbf{P}^{(NL)}=\mathbf{P}^{(2)}$. In the conditions of DFG, three waves propagate through the medium and couple via the nonlinear polarization. Through this coupling energy is transferred back and forth between the three waves. As $\mathbf{P}^{(NL)}$ increases, the more pronounced the effect should be.

The wave equation must hold for each frequency component of the field. In this case, two waves of frequency ω_3 and ω_1 interact in a lossless optical medium to produce an output wave at the difference frequency of $\omega_2 = \omega_3 - \omega_1$ (Figure 5.3). More specific to parametric amplification, a strong pump pulse ($\omega_p = \omega_3$) transfers energy to the lower energy signal ($\omega_s = \omega_1$). In turn the idler wave ($\omega_i = \omega_2$) is created to satisfy the conservation of energy and momentum. If $\mathbf{P}^{(NL)} = 0$, each wave is free to propagate through the medium with constant amplitude and the third wave is not generated.

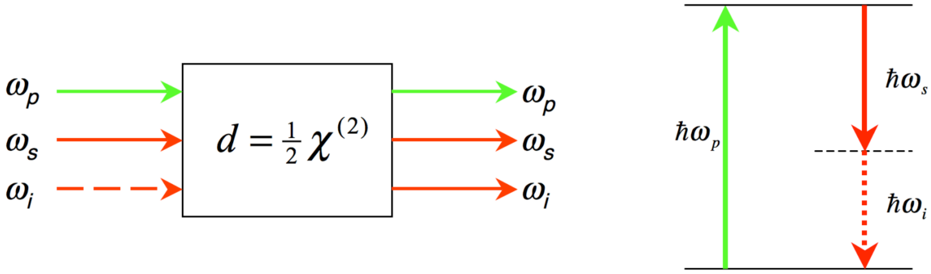

Figure 5.3: Optical description of DFG. Generally no input field at ω_i is applied at the entrance of the medium.

In order to solve the nonlinear wave equation, we must first isolate the component of $\mathbf{P}^{(2)}$ that governs DFG. In the general case of two waves interacting with fields E_j and E_k and with frequencies ω_j and ω_k respectively, the second order nonlinear polarization takes the form of

$$\begin{aligned}P^{(2)}(\mathbf{r},t) = \varepsilon_0\chi^{(2)}[&E_j^2(\mathbf{r},t)e^{-2i\omega_j t} + E_k^2(\mathbf{r},t)e^{-2i\omega_k t} \\ &+2E_j(\mathbf{r},t)E_k(\mathbf{r},t)e^{-i(\omega_j+\omega_k)t} + 2E_k^*(\mathbf{r},t)E_j(\mathbf{r},t)e^{-i(\omega_k-\omega_j)t} + c.c]. \\ &+2\varepsilon_0\chi^{(2)}\left(\left|E_j\right|^2 + \left|E_k\right|^2\right)\end{aligned} \quad (5.1.23)$$

We can now isolate the component of equation (5.1.23) governing DFG ($\omega_i = \omega_k - \omega_j$) to yield

$$P^{(2)}(\mathbf{r},t) = 2\varepsilon_0\chi^{(2)}\left[E_k^*(\mathbf{r},t)E_j(\mathbf{r},t)e^{-i(\omega_k-\omega_j)t} + c.c\right]. \quad (5.1.24)$$

The above equation is valid for any one of the three waves considered in DFG.

In the case of the homogeneous solution to the nonlinear equation where the nonlinear term is zero, we expect the solution to be in the form of infinite plane wave with constant amplitude traveling in the $\hat{z}$-direction. Further, all three waves are assumed to be collinear. Each wave will have a general solution in the form of

$$\mathbf{E}_n(z,t) = A_n e^{i(k_n z - \omega_n t)} + c.c., \quad (5.1.25)$$

where A_i is the constant field amplitude. The wave vector and phase velocity are respectively

$$k_n = \frac{n_n\omega_n}{c} \quad (5.1.26)$$

and

$$n_n = \left[\varepsilon^{(1)}(\omega_n)\right]^{1/2}. \quad (5.1.27)$$

However when the nonlinear polarization term is non-zero, we must modify the inhomogeneous solution. If the nonlinearity is not too large, the inhomogeneous solution will behave similarly to equation (5.1.25), but the amplitude will become a slowly varying function of z. For the signal wave, the trial solution becomes

$$E_1(z,t) = A_1(z)e^{i(k_1 z-\omega_1 t)} + c.c.. \tag{5.1.28}$$

The nonlinear coupling term for the signal wave in DFG is described by

$$P_1(z,t) = P_1(z)e^{-i\omega_1 t} = 4\varepsilon_0 d_{eff} A_2^*(z)A_3(z)e^{-i[(k_3-k_2)z-\omega_1 t]} + c.c\,. \tag{5.1.29}$$

We have made the substitution of $d_{eff} = \chi^{(2)}/2$, which is called the effective nonlinearity. We can now substitute equation (5.1.29) into equation (5.1.22) to produce the nonlinear wave equation describing the signal wave. Also since the plane waves are traveling only in the $\hat{z}$-direction, we can drop the transverse components of the wave equation to yield

$$\begin{aligned} &\left(\frac{d^2A_1(z)}{dz^2} + 2ik_1\frac{dA_1(z)}{dz} - k_1^2A_1(z) + \omega_1^2\mu_0\varepsilon^{(1)}(\omega_1)A_1(z)\right)e^{i(k_1 z-\omega_1 t)} + c.c. \\ &\qquad = -4d_{eff}\frac{\omega_1^2}{c^2}A_2^*(z)A_3(z)e^{-i[(k_3-k_2)z-\omega_1 t]} + c.c. \end{aligned} \quad . \tag{5.1.30}$$

It should be pointed out that the partial derivatives have been replaced with total derivatives because the amplitudes are only a function of z. Also from equations (5.1.26) and (5.1.27), the third and fourth terms on the left-hand side of equation (5.1.30) cancel.

To further simplify this equation, we can collect the exponential terms on one side, and ignore the complex conjugate terms to produce

$$\frac{d^2A_1(z)}{dz^2}+2ik_1\frac{dA_1(z)}{dz}=-4d_{eff}\frac{\omega_1^2}{c^2}A_2^*(z)A_3(z)e^{i[(k_3-k_2-k_1)z-\omega_1 t]}. \qquad (5.1.31)$$

One final simplification can be made which makes it permissible to ignore the second-order spatial derivative. This is called the slowly varying amplitude approximation, i.e.,

$$\left|\frac{d^2A_1(z)}{dz^2}\right|\ll\left|k_1\frac{dA_1(z)}{dz}\right|. \qquad (5.1.32)$$

This stipulation is valid if the relative change in the field amplitude is small within the distance of one wavelength. If so, the second-order derivative is much smaller than the first-order, and therefore it can be ignored. With this approximation, equation (5.1.31) finally simplifies to

$$\frac{dA_1(z)}{dz}=i\frac{2d_{eff}\omega_1^2}{k_1c^2}A_2^*(z)A_3(z)e^{i\Delta kz}, \qquad (5.1.33)$$

where $\Delta k=k_3-k_1-k_2$ is called the wave vector mismatch. Also note that the time component has be eliminated. Using the same derivation as above, we can find two additional wave equations for the idler (ω_2) and pump waves (ω_3). These two equations are

$$\frac{dA_2(z)}{dz} = i\frac{2d_{eff}\omega_2^2}{k_2c^2}A_1^*(z)A_3(z)e^{i\Delta kz} \tag{5.1.34}$$

and

$$\frac{dA_3(z)}{dz} = i\frac{2d_{eff}\omega_1^2}{k_3c^2}A_1(z)A_2(z)e^{-i\Delta kz}\,. \tag{5.1.35}$$

These equations are known as the coupled-amplitude equations for difference frequency generations, because the amplitude of each wave is coupled to each of the others through the nonlinear polarization. It should be restated that several simplifying approximations have been made. Among them are the slowly varying amplitude approximation, the infinite plane wave approximation, and the constant pump intensity approximation. Additionally the medium is lossless so that no linear loss terms appear in these equations.

5.1.3 Solutions to the Coupled Wave Equations for Parametric Amplification

This section presents the solutions for the coupled wave equations describing the field amplitudes of infinite plane waves as a function of position within the nonlinear medium. These solutions require that the nonlinear medium be lossless, the wave is propagating the $\hat{z}$-direction, and that the pump wave (ω_3) is much stronger than the other two waves. This approximation stipulates that the amount of energy transferred to the signal and idler fields from the pump is negligible in comparison to the total field energy of the pump itself. This allow us to treat the amplitude of the pump as a constant throughout the nonlinear medium ($A_3(z) = constant$). Even though true laboratory scale waves are not infinite plane waves, this approximation is valid if spatial diameter of the output wave is much larger than it's wavelength.

We will begin solving the coupled wave equation for the case of zero-dephasing or perfect phase matching ($\Delta k = 0$). First differentiate equation (5.1.33) with respect to z and yield

$$\frac{d^2 A_1(z)}{dz^2} = -\Delta k \frac{2d_{eff}\omega_1}{n_1 c} \frac{dA_2^*(z)}{dx} A_3 e^{i\Delta kz} . \tag{5.1.36}$$

Here the spatial dependence of A_3 has been dropped since we are in the undepleted pump regime. We can eliminate the first order derivative by substituting in the complex conjugate of equation (5.1.34) by

$$\frac{d^2 A_1(z)}{dz^2} = i\Delta k \frac{4d_{eff}\omega_1\omega_1}{n_1 n_2 c^2} |A_3|^2 A_1(z) . \tag{5.1.37}$$

We can further simplify this equation by introducing the coupling constant

$$\kappa_{1.2} = i\frac{2d_{eff}\omega_{1,2}}{n_{1,2}c} A_3 . \tag{5.1.38}$$

The differential equation for A_1 takes the final form of

$$\frac{d^2 A_1(z)}{dz^2} + i\Delta k\kappa_1\kappa_2 A_1(z) = 0 . \tag{5.1.39}$$

The general solution of this equation is given by

$$A_1(z) = C\sinh(gz) + D\cosh(gz) , \tag{5.1.40}$$

where the amplitudes C and D plus the spatial variation phase term g must be solved by the application of the appropriate boundary conditions. The complete solutions for the coupled wave equations for DFG with arbitrary phase and boundary conditions are given by [96]

$$A_1(z) = \left[A_1(0)\left(\cosh(gz) - \frac{i\Delta k}{2g}\sinh(gz) \right) + \frac{\kappa_1}{g} A_2^*(0)\sinh(gz) \right] e^{i\Delta kz}, \quad (5.1.41)$$

and

$$A_2(z) = \left[A_2(0)\left(\cosh(gz) - \frac{i\Delta k}{2g}\sinh(gz) \right) + \frac{\kappa_2}{g} A_1^*(0)\sinh(gz) \right] e^{i\Delta kz}. \quad (5.1.42)$$

The spatial variation phase component is defined by the identity

$$g = \sqrt{\kappa_1\kappa_2 - \frac{\Delta k^2}{4}}. \quad (5.1.43)$$

The general solution is valid for the undepleted pump pulse. If the seed and idler waves become large and begin to extract significant energy from the pump, this solution is no longer valid [4].

In the case of parametric amplification, usually only the seed and pump waves are present at the input; therefore $A_1(0) = 0$ and $A_2(0)$ is arbitrary. These are the conditions for small signal parametric amplification. The field amplitudes for these boundary conditions are

$$A_1(z) = A_1(0)\left(\cosh(gz) - \frac{i\Delta k}{2g}\sinh(gz)\right)e^{i\Delta kz}, \tag{5.1.44}$$

and

$$A_2(z) = A_1^*(0)\frac{\kappa_2}{g}\sinh(gz)e^{i\Delta kz}. \tag{5.1.45}$$

When there is no phase mismatch between the fields, the seed and idler waves grow exponentially like e^{gz}. However when dephasing occurs, this can suppress the gain very effectively. Figure 5.4 plots the intensity ($|A_n(z)|^2$) behavior of equations (5.1.44) and (5.1.45). As the phase mismatch increases, energy is transferred back and forth between the seed and idler waves. As Yariv has pointed out [96], parametric amplification is a phase sensitive amplifier providing gain to sympathetic signals at $\phi = 0, \pi$ and de-amplifying signals with $\phi = \pi/2, 3\pi/2$.

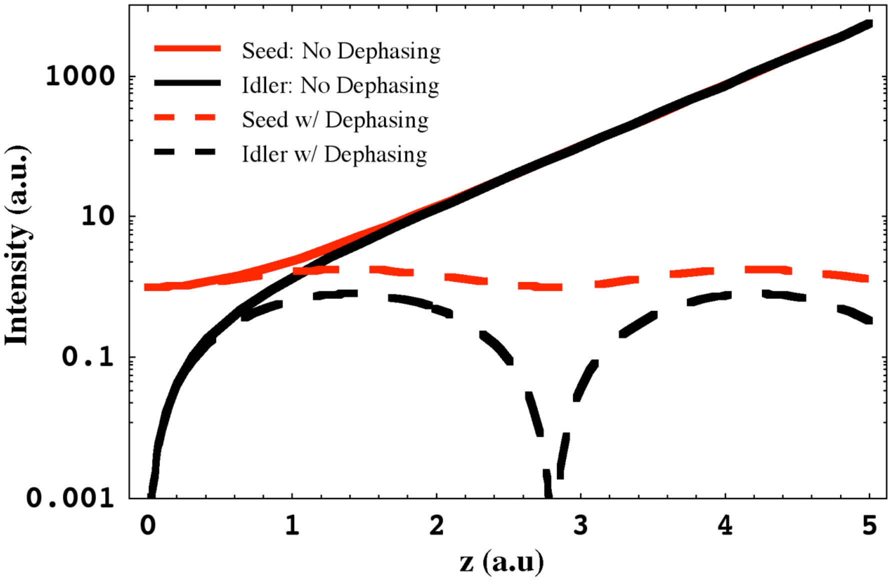

Figure 5.4: Electric field intensity plots for the seed and idler beams as function of crystal length in the case of an undepleted pump pulse. Dephasing solutions are plotted with $\Delta k = 3\kappa_1\kappa_2^*$.

5.1.4 Angular Phase Matching in Type I Negative Uniaxial Crystals

As shown in Figure 5.3 parametric amplification is strongly coupled to the phase matching condition. Conversion is maximized when $\Delta k = k_3 - k_1 - k_2 = 0$. A change in the phase relationship or when Δk becomes non-zero, will cause back conversion where energy flows back from the seed and idler to the pump. Therefore the phase mismatch defines a coherence length, $L_c = 1/\Delta k$. For the case of small signal gain in parametric amplification, the gain equation [88] can be simplified to

$$G \simeq (gL)^2 \operatorname{sinc}^2\left(\frac{\Delta kL}{2}\right), \tag{5.1.46}$$

where L is the length of the nonlinear medium and g is the gain coefficient. For the sinc^2 dependence, the coherence length is defined as

$$L_c = \frac{\pi}{|\Delta k|}. \tag{5.1.47}$$

This is the scale length over which this function goes to zero. Moreover the points where the function is reduced to ½ defines the phase matching bandwidth, and is shown by

$$\Delta k_{BW} = \frac{2.784}{L}. \tag{5.1.48}$$

This function is plotted in (Figure 5.5).

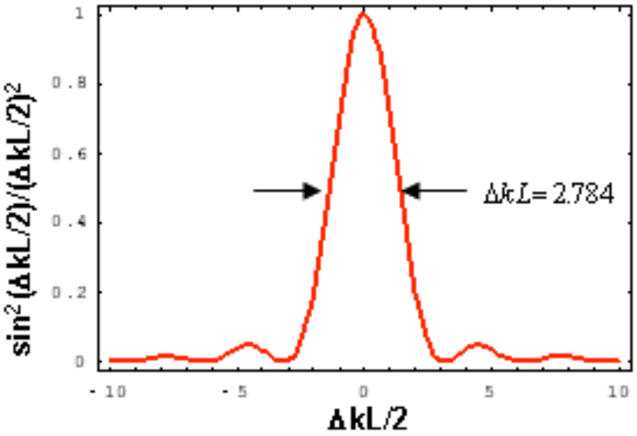

Figure 5.5: Plot of phase matching component from the small signal DFG gain equation. Gain is dependent upon the phase mismatch between the three optical waves.

The phase matching condition can be expressed in terms of the three interacting wave vectors by

$$\mathbf{k}_1 + \mathbf{k}_2 = \mathbf{k}_3 \tag{5.1.49}$$

However if all three waves are collinear, the vectors can be reduced to their scalar form $k_1 + k_2 = k_3$. For collinear beams the phase matching condition is

$$n_1\omega_1 + n_2\omega_2 = n_3\omega_3 , \tag{5.1.50}$$

where n is the linear index of refraction. The condition is very difficult to achieve because the index of refraction in lossless materials often displays normal dispersion. This is where the index of refraction is an increasing function with frequency. In fact phase matching can never be achieved in a normally dispersive medium if $\omega_3 > \omega_2 > \omega_1$, because the increasing index violates the conservation of energy. In turn phase matching can be achieved via anomalous-dispersion, i.e. n decreases with frequency.

Various phase matching mechanisms have been developed in order to increase coherence length of the interaction [88]. The most common technique is to use a birefringent crystal. Birefringence is the dependence of the index of refraction on the direction of the polarization of the optical radiation. Here phase matching is achieved by polarizing the ω_3 wave in the direction of the smallest possible n. Birefringence can generally be observed in non-isotropic crystals.

Uniaxial crystals are commonly used for phase matching in various nonlinear processes. They are crystals that are characterized by a single optical axis called the *c*-axis. The birefringence of the crystals varies by the orientation of the polarization with respect to the *c*-axis. In this case, the pump wave is polarized along the extraordinary axis. This is a plane that is parallel to both the axis of propagation and the *c*-axis. Orientation of the polarizations for the other two waves depends on the type and kind of phase matching.

There are three general methods of phase matching for uniaxial, birefringent crystals: angular phase matching, temperature phase matching, and quasi-phase matching. Angular phase matching was the first experimentally demonstrated technique [98, 99], and will be the technique on which we focus. Temperature phase matching is a process by which the index of refraction along the principle axis can be adjusted with temperature. When beams propagate along the principle axis of the crystal, this is called non-critical phase matching. It has the benefit of no transverse walk-off of the electric fields. This increases conversion efficiency and improves spatial overlap. Quasi-phase matching is where the sign of the nonlinearity varies along the axis of propagation. The period of the variation is usually a single coherence length. The benefit being that a very long interaction length can be achieved without walk-off, and wavelength tuning is produced directly by tuning the period length.

For the case of angle tuning the phase matching condition, there are two types of processes for DFG in a negative uniaxial crystal: type-I is where the signal and idler waves are polarized upon the ordinary axis, and type-II where the lowest frequency wave is polarized along the ordinary axis and the middle frequency (ω_2) is along the extraordinary axis. The plane that is perpendicular to both the axis of propagation and the *c*-axis defines the ordinary axis. Here the extraordinary index of refraction varies with the angle between the axis of propagation and the *c*-axis. Therefore phase matching is achieved by tuning this angle. The indices of refraction for the crystal obey the relation

$$\frac{1}{n_e^2(\theta)} = \frac{\cos^2\theta}{n_o^2} + \frac{\sin^2\theta}{\overline{n}_e^2}. \tag{5.1.51}$$

Here $\overline{n}_e$ is the principle value of the extraordinary index, $n_e(\theta)$ is the angular dependent value, and n_o is the ordinary index. Figure 5.6 is a diagram showing geometry for type I phase matching in a negative uniaxial crystal. The ordinary axis extends out of the plane of the page, where the extraordinary and the *c*-axis lie within the plane of the page. The angle θ spans between the c-axis and the direction of propagation (**k**).

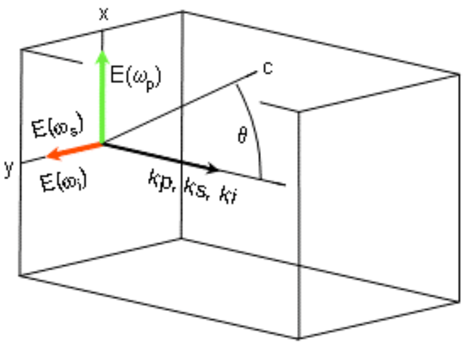

Figure 5.6: Type I phase matching in a birefringent uniaxial crystal. Phase matching is achieved by angle tuning the extraordinary (x-axis) crystal axis. The pump beam is polarized along the extraordinary axis, and the seed and idler beams are polarized along the ordinary axis (y-axis).

For the case of OPCPA we are interested in uniform, broad bandwidth signal gain. There are two types of processes that are relevant for type I phase matching for OPCPA. The first case is when the OPA is operated close to degeneracy $\omega_i \approx \omega_s$ with near collinear geometry, and the second is when the OPA is operated away from degeneracy $\omega_i < \omega_s$ with non-collinear geometry [25]. The first process is valid for all crystals and pump wavelengths; however the signal gain bandwidth demonstrates large variations at different wavelengths and crystals. Therefore second process is most commonly chosen. In this process, broad bandwidth phase matching is achieved by continuously varying the direction of the idler beam. This causes the idler to be strongly dispersed.

For non-collinear geometry the phase matching needs to satisfy the vector form of equation (5.1.49). Figure 5.7 illustrates that both conservation of energy and momentum must be satisfied for perfect phase matching and efficient energy conversion. The signal and pump beams propagate through the crystal at the small input small angle α. The generated idler beam is the frequency difference between the pump and signal to satisfy the conservation of energy

$$E_3 = E_1 + E_2\,, \tag{5.1.52}$$

where E_1, E_2, and E_3 are the photon energies of the three interacting waves. The idler also propagates oppositely of the signal to satisfy the conservation of momentum.

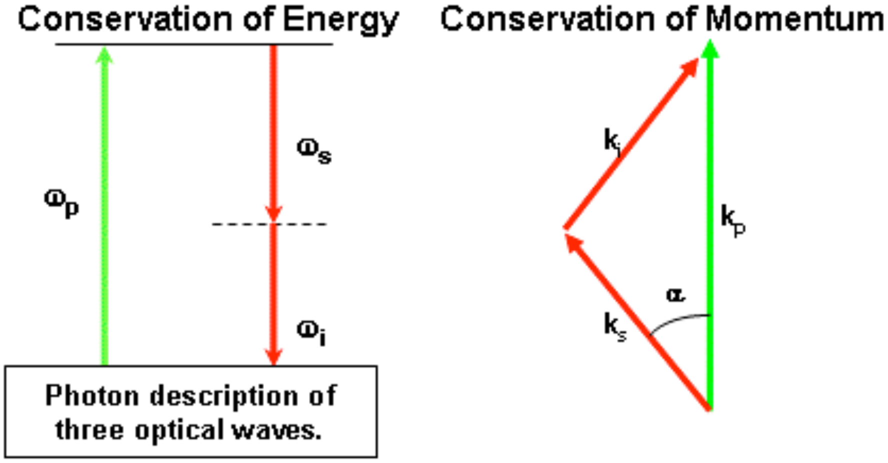

Figure 5.7: Photon and wave vector description of conservation of energy and momentum for type I phase matching in Difference Frequency Generation.

Armed with these conditions, we can now solve equations (5.1.49), (5.1.51), and (5.1.52) for the type I phase matching angle θ in a negative uniaxial crystal

$$\sin^2\theta = \left(\frac{n_o^2 n_e^2}{n_o^2 - n_e^2}\right)\left[\frac{1}{\lambda_3^2\left(k_2\cos\alpha + \sqrt{k_1^2 - k_2^2\sin^2\alpha}\right)} - \frac{1}{n_o^2}\right]. \tag{5.1.53}$$

Here λ_3 is the wavelength of the pump. Again the signal and idler waves are polarized along the ordinary axis, and the pump is polarized along the extraordinary axis. The pump propagates through the crystal along $\mathbf{k}_3$, which is at an angle θ to the *c*-axis. Figure 5.8 plots the phase matching condition for equation (5.1.53) for DFG using a pump wavelength of 532 nm.

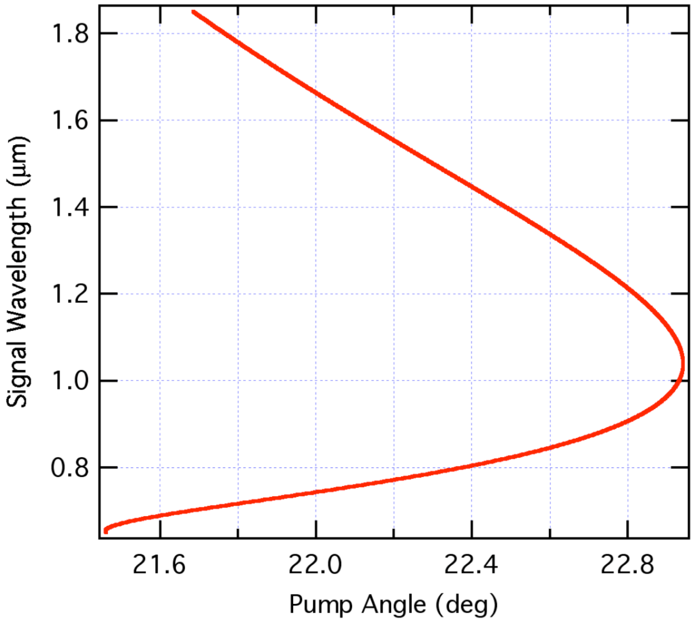

Figure 5.8: Phase matching angle for BBO. Adjusting the crystal angle tunes the phase matching of the pump beam at 532 nm to the seed and idler beams.

5.2 Energetics Modeling

Two different energetics models are presented here that examine the parametric amplification and the mixed glass amplifiers of the GHOST laser. Both models each address several issues pertinent to the laser design. The primary motivation is to simulate energetic (> 1 J) 100 fs pulse amplification in mixed glasses; however, there are several critical details of each amplifier that must be investigated separately. The first model was designed to examine the parametric amplification stage in order to predict the level of spectral saturation that occurs in the seed pulse spectrum. Also, reasonable expectation values of the seed pulse energy from the OPCPA preamplifier needed to be established. The second model was developed to assess spectral gain narrowing in the mixed glass amplifiers. More specifically, amplified spectral bandwidth as a function of gain ratio between the two laser glasses was simulated. Section 5.2.1 details the parametric amplification model and its results, and section 5.2.2 discusses the simulations on the mixed glass amplifiers.

5.2.1 OPCPA Simulations

The parametric amplifiers were modeled to estimate the effects of spectral saturation on the seed pulse. In order to minimize the spectral gain narrowing from the glass amplifiers, the seed pulse spectrum must have sufficient bandwidth that exceeds the spectrum defined by the two glass peak emission wavelengths. Ideally we would like to seed the glass amplifiers with a white light spectrum. Therefore the GHOST laser design requires the oscillator to produce 100 fs pulses with >16nm (FWHM) Gaussian spectra. Further, the spectra should be centered at 1057 nm, which is the midpoint between the peak emission lines of Nd:phosphate and Nd:silicate laser glasses. If the full bandwidth of the spectrum is available for amplification, the OPA must be able to amplify over 40 nm of light.

In the domain of the undepleted, uniform spatial and temporal profile pump pulse, the signal intensity gain for pulsed parametric amplification can be solved through the analytic solutions of the coupled wave equations given in equations (5.1.41) and (5.1.42). The signal intensity, which is proportional to the square of its field amplitude, is given by

$$I_s(z) = 2\pi\varepsilon_o nc\left|A_s(z)\right|^2 . \tag{5.2.1}$$

The intensity gain in the parametric amplifier is then defined through

$$\frac{I_s(L)}{I_s(0)} = 1 + G , \tag{5.2.2}$$

where L is the length of the nonlinear medium and G is the gain factor. It is given by

$$G = (\gamma L)^2 \frac{\sinh^2\left(\sqrt{(\gamma L)^2 - (\Delta kL/2)^2}\right)}{(\gamma L)^2 - (\Delta kL/2)^2} , \tag{5.2.3}$$

where the gain coefficient γ is

$$\gamma = 4\pi d_{eff}\sqrt{\frac{I_p(0)}{2\varepsilon_0 n_p n_s n_i c\lambda_s\lambda_i}} . \tag{5.2.4}$$

Here $I_p(0)$ is the initial intensity of the pump pulse. The indices of refraction of the three fields are derived from the dispersion curves of the nonlinear medium.

The bandwidth of the gain function can be extremely large. Shown here in Figure 5.9 is the gain function plotted for parametric amplification in a 15 mm long BBO crystal with a 350 MW/cm^2 pump pulse. The gain is nearly uniform for the 40 nm region centered at 1057 nm.

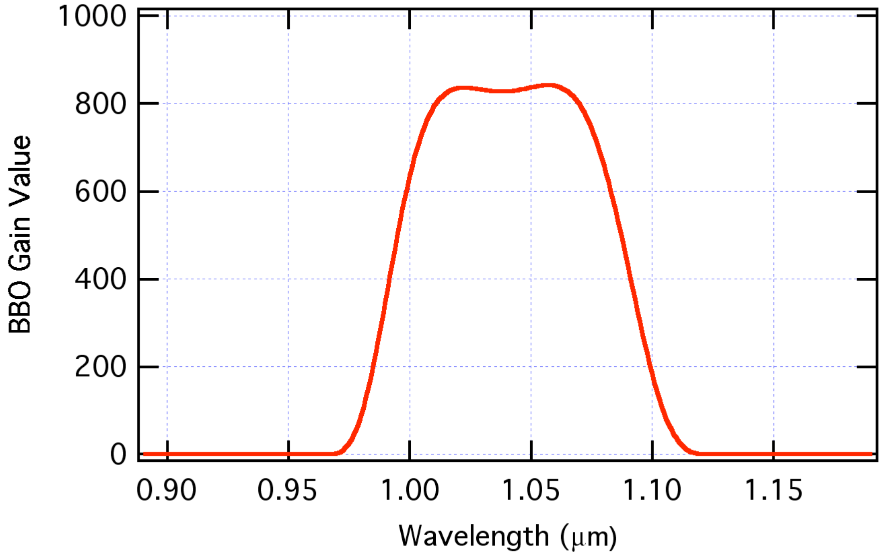

Figure 5.9: BBO gain spectrum as a function of wavelength. The plot is for non-collinear parametric amplification with a 1° cross angle between the signal and pump pulses. The pump intensity is 350 MW/cm^2, and the crystal length is 15 mm.

The modeling shown here was performed to analyze the spectral gain saturation in the multi-crystal OPA for the GHOST laser. GHOST uses a frequency doubled, Q-switched Nd:YAG laser to pump the OPA crystals. The pump pulse duration is 12 ns FWHM with a total of 650 mJ in energy. The pulse is split into two beams in order to pump multiple crystals with different beam diameters, but with similar intensities. The modeling incorporates the Gaussian temporal profile of the pump pulse, but assumes that the beam is spatially uniform. This allows for a one-dimensional code to simulate the interaction in time. However Poynting vector walk-off and transverse spatial walk-off of the beams crossing at a 1° angle and are not included because of the dimensional simplification. Nevertheless energy depletion of the pump pulse can be considered by time slicing the pulse and the crystal. By treating the crystal as a series of thin parametric amplifiers, energy can be transferred to the signal beam and removed from the pump at each slice. Further each temporal slice of the signal beam is then mixed with its corresponding pump slice within the crystal slice. This allows for a temporally non-uniform pump pulse to be considered.

Preliminary modeling simulated a 1 nJ seed pulse being amplified in three OPA crystals. The seed is a 16 nm FWHM Gaussian spectrum centered at 1057 nm. The transform limit of this spectrum equates to 102 fs FHWM. For amplification, it is spectrally chirped to a 1 ns pulsewidth. The simulated pump pulse is Gaussian in time with 12 ns FHWM duration. The pulse is split into two beams: one with 120 mJ to pump the first two OPAs, and the other with 450 mJ to pump the third OPA. The net energy here is less than the laser output to simulate energy loss by the transport optics. The peak pump intensity in each crystal is set to 350 MW/cm^2. Also in all cases the peak intensities of the seed and pump pulses are temporally aligned.

The results from this simulation indicate that the seed is amplified to 835 nJ in the first crystal with an integrated gain of 835. In the second crystal the pulse is amplified to 675 μJ with an integrated gain of 808. The slightly lower gain in the second OPA is attributed to the lowered peak intensity of the pump pulse from amplification in the first crystal. Almost no change can be seen in the signal spectrum in either of the first two OPAs (Figure 5.10). No spectral loss or saturation is achieved since the gain spectrum is near uniform over this bandwidth and neither OPA is saturated.

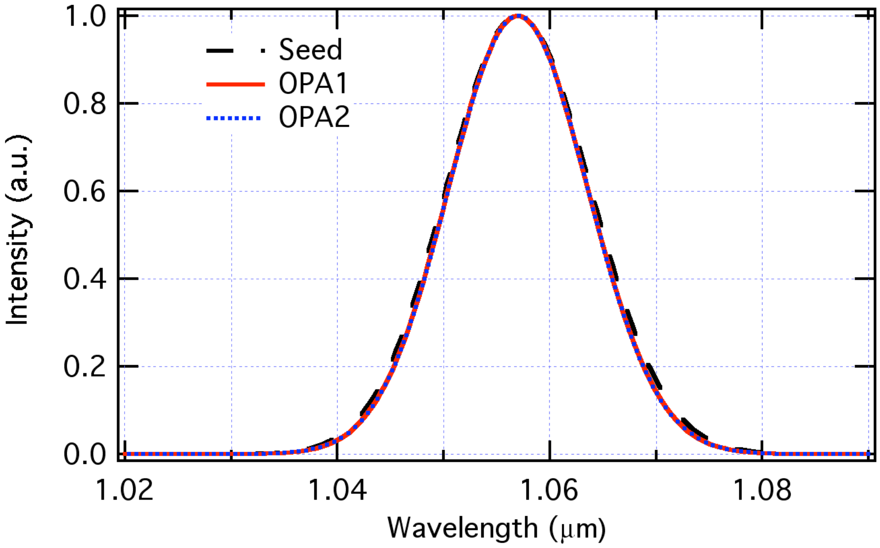

Figure 5.10: Simulated spectral amplification of the signal beam in the first two parametric amplifiers.

In the third crystal the simulation shows the signal amplified to 43 mJ with an integrated gain of 64. The gain is dramatically reduced since the signal strongly saturates the OPA. Also, as it is shown latter in the experimental results section, the model significantly overestimates the amplified energy from the third OPA. This is primarily attributed to the simplifications of the one-dimensional model. As stated before, the model does not account for spatial or Poynting vector walk-off. Further the model does not allow for reverse energy transfer. As the signal intensity becomes comparable to that of the pump, energy transfer can reverse direction. In this case the signal can return energy back to the pump pulse. However the simulation does shows a strongly saturated super-Gaussian spectral profile for the signal pulse (Figure 5.11). Effectively the entire bandwidth of the seed achieves saturation in this stage.

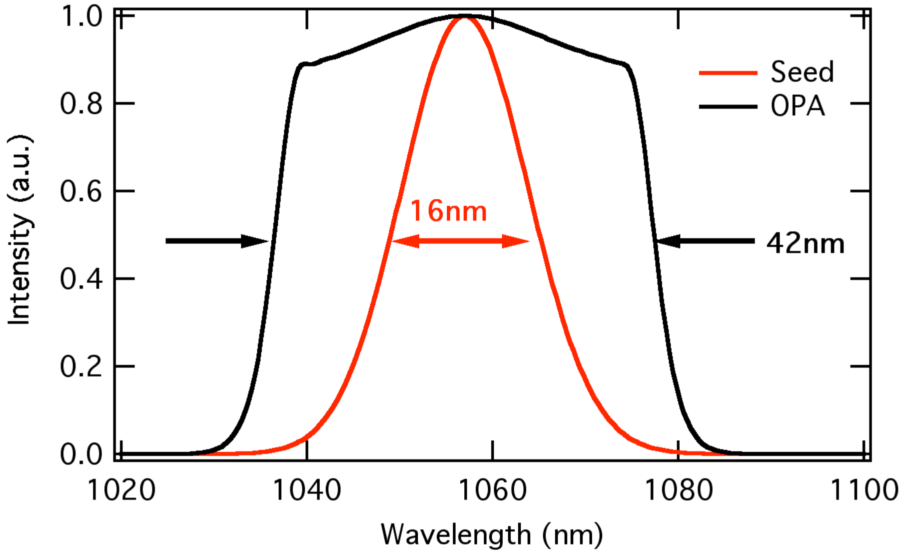

Figure 5.11: Plot of simulation depicting spectral saturation from amplification in the third OPA

Another factor analyzed in the simulations is the temporal mismatch between the signal and the pump pulses. The chirped seed is stretched to 1 ns FWHM, and the pump pulsewidth is 12 ns FWHM. Since parametric amplification only occurs while the pulses are temporally aligned, most of the pump energy is lost. A novel approach taken on the GHOST laser has been to examine multiple temporal alignments (i.e., temporal multiplexing) of the signal to the same pump pulse in sequential amplifiers. The motivation is to extract more energy from the pump without drastically altering the spectrum of the signal. Ideally the pump pulse would be a flattop temporal profile beam; however the pump laser used on GHOST is Gaussian in time. Since small variations in the pump intensity can drastically alter the temporal and subsequent spectral profile of the seed, the most suitable region for amplification in this case is at the peak temporal intensity. This is where the pump beam is most temporally uniform.

This simulation examines temporal multiplexing in both saturated and unsaturated amplifiers. In the first case, the seed is amplified in two OPA crystals, experiencing small signal gain (~10^3) in both amplifiers. The seed is temporally placed 0.75 ns in front of the peak of the pump pulse in the first OPA and 0.75 ns behind the peak of the pump in the second OPA (Figure 5.12). Over this interval the peak intensity of the pump varies less than 3%. Since the pump intensity is increasing in time in the first OPA, the gain will be higher on the red side of the spectrum. Oppositely in the second amplifier, the intensity is decreasing in time; therefore the gain will be higher for the blue side. In the case of small signal amplification where saturation is not achieved, the varying pump intensity is symmetric in the combined amplifiers and should cancel any spectral modulation.

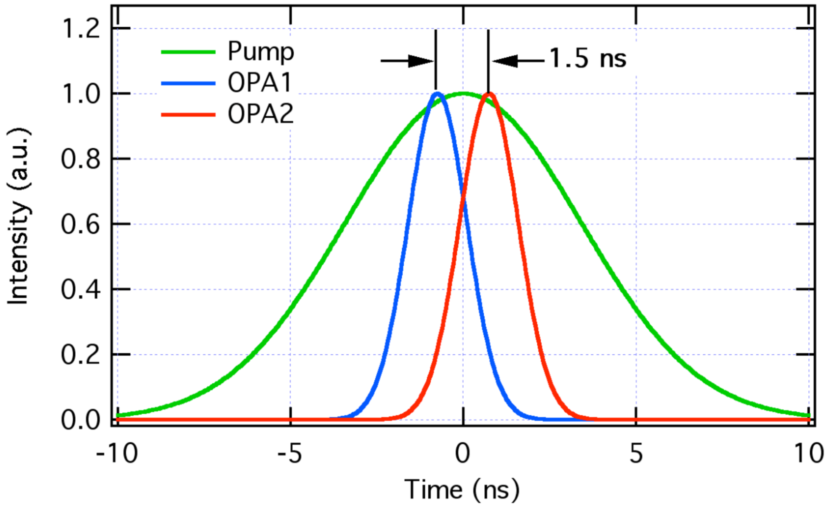

Figure 5.12: Plot of the simulated temporal overlap of the seed and pump beams in the 1st and 2nd OPA crystals. The seed beam in the 1st crystal is aligned 0.75 ns ahead of the peak intensity of the pump beam. The seed beam in the 2nd crystal is temporally aligned 0.75 ns after the peak intensity of the pump beam.

The result of this simulation is that the frequency center is gain pulled in each amplifier (Figure 5.13). In the first OPA the peak of the seed is gain pulled to 1.054 μm, and then is pulled back to the red in the second crystal. Since neither amplifier is saturated, the bandwidth of the seed is subsequently gain narrowed with no significant change in the shape of the spectrum. The simulated pump intensity in both OPAs is 300 MW/cm^2, producing a calculated gain in each crystal of 10^3.

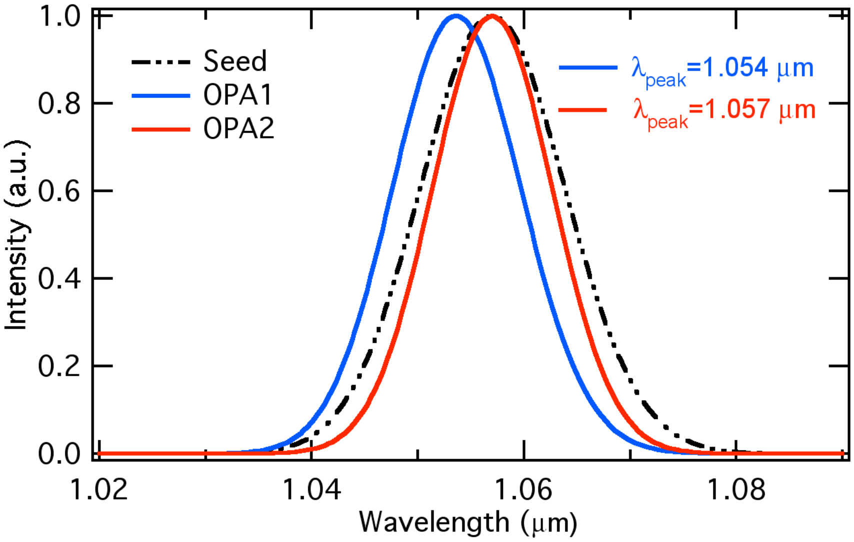

Figure 5.13: Simulated spectral gain pulling in OPAs. The wavelength center is pulled by temporally offsetting the peak of the seed pulse. The peak of the seed is placed 0.75 ns before the pump pulse in the first OPA and 0.75 ns after the pump in the second OPA. Gain narrowing in the 2nd crystal occurs because neither amplifier is saturated.

The next simulation examines temporal multiplexing in a pair of saturated OPAs. Again a 12 ns pump pulse is used with peak intensity of 300 MW/cm^2. Both OPAs are modeled to yield a small gain of 10^3. In this case the seed is preamplified to approximately 1 mJ in two prior OPAs shown in Figure 5.12. For saturation to be achieved, the integrated seed energy before amplification must be within a factor of 10^3 of the integrated pump energy contained within the temporal window of the seed. Therefore the pump is normalized to a total of 500 mJ. Also the same temporal offset of 1.5 ns as described in Figure 5.12 is used.

Strong saturation is achieved in the third OPA producing a symmetric gain broadened spectrum with a bandwidth of 20 nm FWHM (Figure 5.14). The Fourier transform of this spectrum is 114 fs, where the Fourier transform of the original seed is 112 fs. Effectively the gain broadening overcomes the gain narrowing produced in the first OPA preamplifiers. Additionally the pulsewidth of the seed is also increased due to the gain broadening. Since the pulse is chirped, spectrum is also equated with time.

In the fourth OPA the seed is temporally pushed back 1.5 ns. However it does overlap a gain-depleted portion of the pump pulse from the prior amplifier caused by the temporal broadening. This intensity depression on the pump gain shapes the seed in the fourth OPA and reduces the spectral saturation on the blue side of the spectrum. In turn, the red side of the seed spectrum experiences undepleted intensity in the pump and is significantly gain broadened. Uniform spectral saturation is not achieved here, which is attributed to the falling edge of the pump pulse. As stated before, the code overestimates the amplified energy (80 mJ) by not accounting for back conversion and the omission of the spatial dimension. However the pulse is increased by a factor of 2 in the fourth OPA by moving to a new temporal position. Further the Fourier transform of the final spectrum is 102 fs, indicating temporal multiplexing the seed on the pump produces no detrimental spectral modifications.

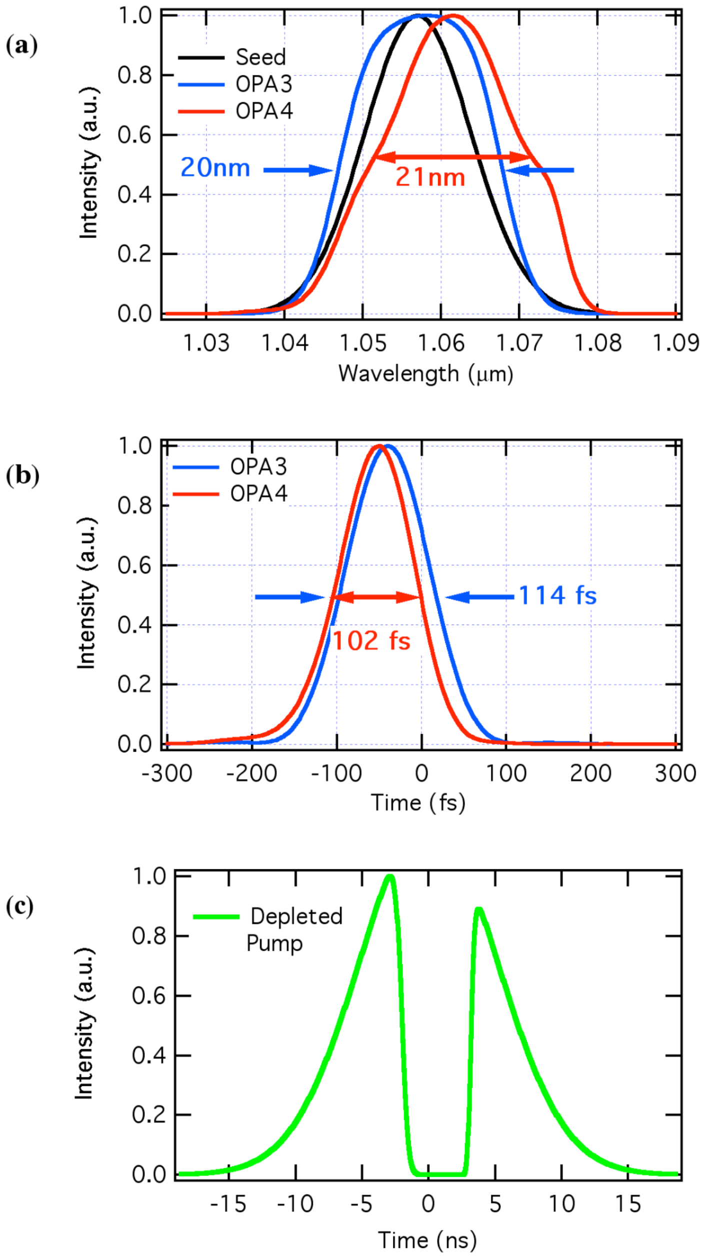

Figure 5.14: Simulation of the seed pulse amplified in two temporally multiplexed OPAs. The seed pulse is temporally aligned 0.75 ns ahead of the pump in the 1st OPA, and is 0.75 ns behind the pump in the 2nd OPA. Saturation is achieved in both amplifiers. a) Simulated amplified spectra of the seed pulse from both OPAs. b). Conjugate simulated Fourier transform pulsewidths from the OPAs. c) Depleted pump temporal profile after amplification.

5.2.2 Mixed Glass Simulations

The mixed-glass modeling was performed to ascertain the best gain ratio between the Nd:phosphate and Nd:silicate laser glasses. Further we needed to establish the amount of bandwidth that will survive the gain in the final amplifier stages of the GHOST laser. From these simulations, the final compressed pulsewidth can then be estimated by the Fourier transform of the amplified seed spectrum. The amplification criteria for the GHOST laser is to achieve gains ranging from 100 to 300 in mixed-glasses using two 19 mm glass rod amplifiers. Hence the model used here is similar to the one introduced in chapter 4, by which a spectrally broadened seed is amplified in a heterogeneous amplifier containing mixed glasses. The gain ratio is varied between the two glasses while maintaining a constant total gain value. The gain ratio is varied through the parameter κ by

$$\frac{1-\kappa}{\kappa} = \frac{\sigma_{phos}}{\sigma_{sil}} \frac{\ln G_{sil}}{\ln G_{phos}}, \tag{5.2.5}$$

where σ_{phos} and σ_{sil} are the wavelength dependent gain cross-sections, and G_{phos} and G_{sil} are the gain factors of Nd:phosphate and Nd:silicate respectively [24]. The model is simplified to one dimension by assuming the pulse has a flattop spatial profile. Further, only small signal gain is considered, since the saturation fluences of these glasses are well in excess of the limit at where nonlinear phase accumulation becomes significant for these pulse durations.

The saturated seed spectrum used in this simulation is shown in Figure 5.11. It is centered at 1057 nm with 42 nm FWHM of bandwidth. The model simulates amplification at total gain values of 100, 150, 200, 250, 260, and 300. At each gain value, κ is varied between 0 and 1. When κ is equal to 0, the gain is entirely in the silicate amplifier. Oppositely when it is equal to 1, the gain in entirely in the phosphate amplifier. Figure 5.15 summarizes the results of this simulation. At all levels when the pulse is amplified entirely in silicate, the survived bandwidth is approximately 10 nm (Figure 5.15a). Oppositely when the gain is done in the narrower spectrum phosphate glass, the survived bandwidth is approximately 10% lower. Shown most importantly is a peak in the amplified bandwidth when the gain ratio (G_{phos}/G_{sil}) ranges between 0.65 and 2.7 ($0.375 \leq \kappa \leq 0.50$). For gains ≤ 200 in this range, the amplified bandwidth exceeds 14 nm. When the gain is increased, the survived bandwidth reduces to 13 nm. The relatively large range is attributed to gain pulling by each amplifier. Different gain ratios yield similar net bandwidths with the peak located at different wavelengths.

The Fourier transformed pulsewidths versus the gain ratio for the amplified spectra are shown in Figure 5.15b. Shown here is a minimum for the pulsewidths that occurs over a much broader range of the gain ratio. For a gain of 100, sub-100 fs pulses are produced from the gain ratio ranging from 0.7 to 11. For the gain of 200, the gain ratio varies more than three orders of magnitude and still yields the same pulsewidth of 106 fs. Again this is attributed to the gain pulling of each glass. Even though the amplified FWHM bandwidth varies as much as three nanometers, sufficient spectrum survives in the wings to compress to 106 fs in each case. With higher gains (>200), the amplified bandwidth FWHM maximum begins to flatten, but the pulsewidth minimum narrows. At a gain of 300, the ratio lies between 1.5 and 11.5. Most importantly the best gain ratio is greater than 1. This relies on more gain from the phosphate glass than the silicate, which is desirable since phosphate has a larger gain cross-section and lower

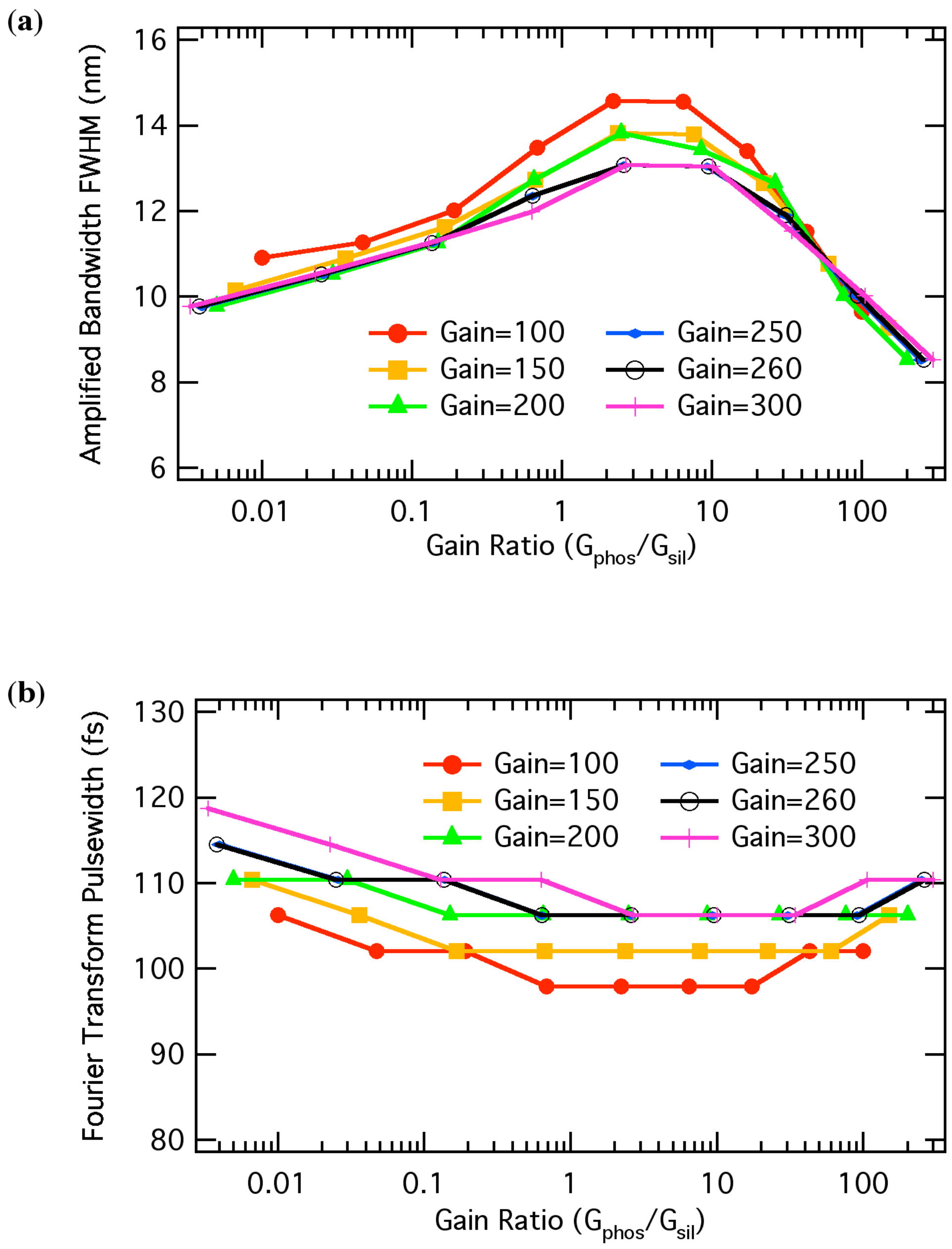

Figure 5.15: Simulation depicting an OPA gain-broadened seed being amplified in mixed-glass amplifiers. Nd:phosphate and Nd:silicate glasses are used. Each colored line represents amplification at a constant gain value with a varying gain ratio ($G_{\mathrm{phos}}/G_{\mathrm{sil}}$). a). FWHM Bandwidth of 1057nm seed after mixed-glass amplification. b). Fourier transformed pulsewidth of seed after mixed-glass amplification.

nonlinear index of refraction. It should be noted that the Fourier-transformed pulsewidths are calculated at the resolution limit of the numerical simulation.

5.3 Phase Simulations

Chirped pulse amplification requires precise management of the spectral phase accumulated by the laser pulse before, during, and after amplification. In order to produce a transform limited compressed pulse, the compressor must be able to compensate for the dispersion effects of the stretcher and all the optical materials in the laser path ($\phi_c(\omega) = \phi_s(\omega) + \phi_m(\omega)$). The GHOST laser operates with a relatively large bandwidth (>30nm). A majority of the optical phase arises from the initial linear chirp from the stretcher; however the frequency dependent index of refraction adds additional dispersion from the various materials. This effect can be very pronounced in high index material such as Faraday rotator crystals and Pockels cells. For pulsewidths ≥100 fs, higher order dispersion can be ignored because the grating spacing in the compressor easily compensates the majority of the dispersion. However, grating spacing cannot compensate nonlinear effects. In fact they must be carefully managed and minimized. The general "rule of thumb" is that the combined B-integral be kept ≤1.

Two numerical calculations are presented here that simulate the phase of the GHOST laser. The first is an optical ray trace of the stretcher and compressor. Shown are the design of both optical assemblies and the group delay from each unit. Next is the calculation of the nonlinear phase accumulation from the entire amplifier chain. A discussion is on nonlinear phase on pulse compression is also presented.

5.3.1 Stretcher and Compressor Design

As with any CPA laser, the compressor drove much of the design of the GHOST laser. The limited availability of large aperture dielectric diffraction gratings demanded that gratings with 1740 lines/mm ruling spacing be used. These gratings demonstrate very high diffraction efficiency into the -1 order (>95%) at 1 μm wavelengths. However they do pose some difficulties in the optical design, most of which comes from the input angle of incidence and the angular separation between it and the first order diffracted beam. Figure 5.16 plots both of these as a function of the input angle. For 1057 nm, the littrow angle is already very steep at 66.8°. In order to spatially separate the input and diffracted beams, the angular separation must be 10° at minimum. Moreover, the lateral beam size on the grating goes as $1/\cos\theta_{in}$. Therefore large aperture gratings must be used for modest band-pass transmission (~30 nm). In turn the high angle of incidence provides very high chirp factors. The grating angle for the GHOST laser is set to 74.7°, with the diffracted beam exiting at 61°. This creates an angular separation of 13.7°. The benchmark for the stretched pulsewidth on GHOST is 1 ns FWHM for a 16 nm Gaussian spectrum. This constitutes a 62.5 ps/nm chirp factor, requiring a compressor grating spacing of ~80 cm.

The pulse stretcher used on GHOST is of the Martinez design [13], which incorporates an optical imaging telescope to create a positive frequency chirp on the pulse. The presence of telescopic optics in the stretcher does not allow for an analytical solution for the path length difference in the stretcher; therefore a numerical calculation must be done for a range of frequencies spanning the pulse bandwidth. We have employed the *Mathematica* package of *Optica* to ray-trace both the stretcher and compressor designs. This ray trace gives a set of frequency dependent path lengths, which are then fit to an 8th-order polynomial. The frequency resolution of this trace is 2

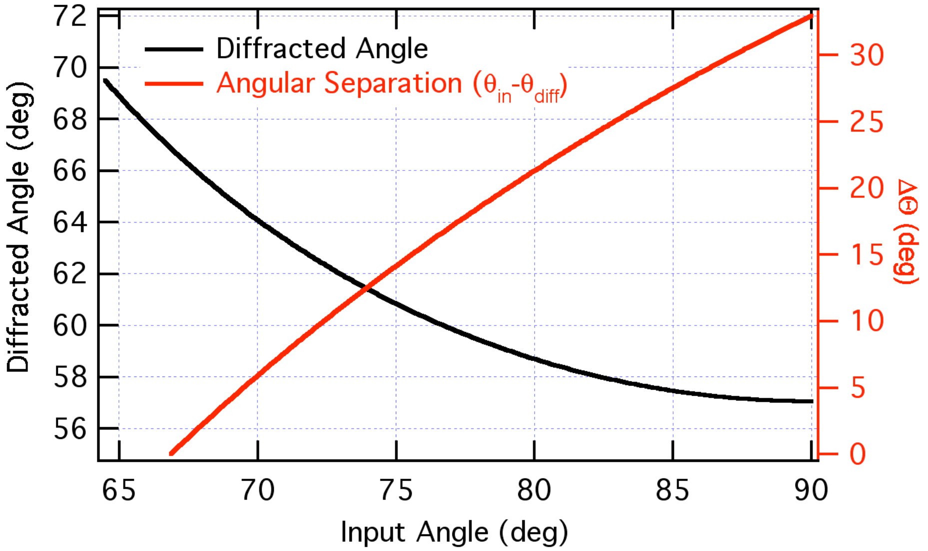

Figure 5.16: Plot of the -1 order diffraction angle (left axis) and the angular separation between the input and diffracted order (right axis) for 1057 nm as a function of input angle from a 1740 lines/mm grating.

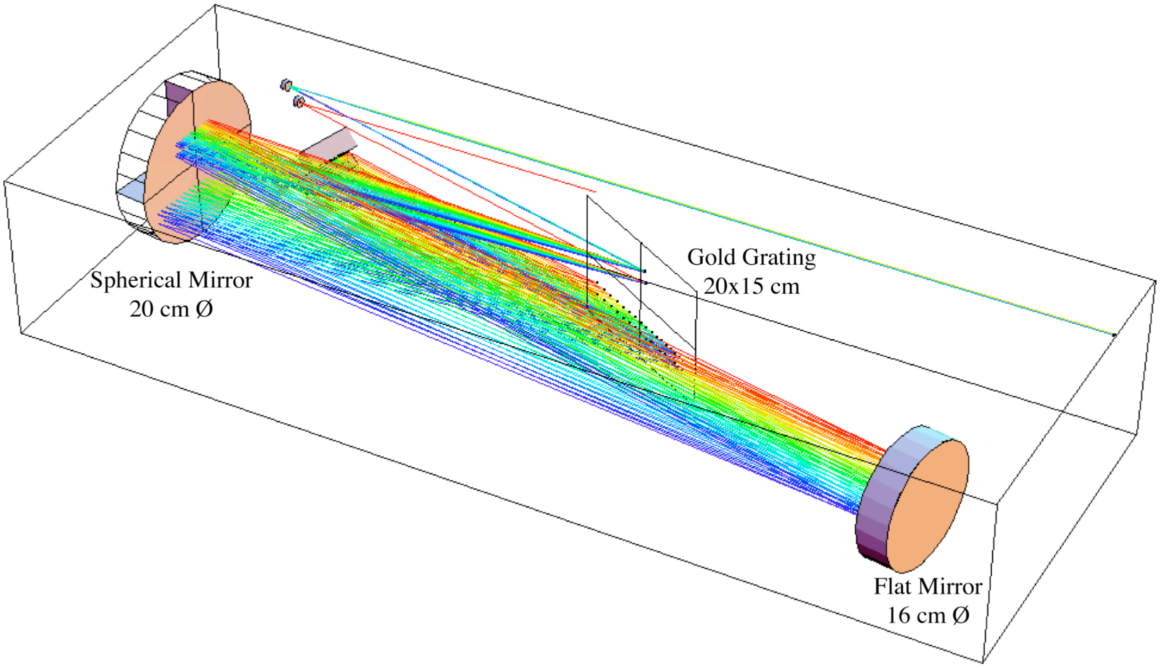

Figure 5.17: Optical ray trace of GHOST stretcher.

nm per ray over a 30 nm bandwidth centered at 1057 nm. The full ray-trace of the GHOST stretcher is shown in Figure 5.17.

The 1740 line/mm gold coated grating has a clear aperture of 20 x 15 cm. The input laser pulse strikes the grating 30 mm above the centerline at 74.7°. The diffracted beam is then imaged to the second grating strike using a 20 cm diameter dielectric mirror with 2.0 meter radius of curvature. The mirror is placed 60 cm from the grating surface, with the object plane 40 cm behind the substrate. Because of the steep angle of incidence on the grating, the mirror can reflect slightly off-axis by 3° and miss the grating. Although the Banks stretcher design [47] would be more desirable, the steep angle of incidence on the grating would require that the mirror stripe be significantly wider than the grating substrate. This obviously becomes cost prohibitive. Also the modest bandwidth (16 nm FWHM) causes little to no spherical phase aberrations from off-axis reflection by the spherical mirror. Next a 16 cm diameter plano-mirror is placed at the Fourier plane of the imaging telescope at normal incidence to retro-reflect the beam back for the second grating strike. A pair of rooftop mirrors is used to step the beam down 25 mm and return the beam back through the second pass. The beam finally exits the optical assembly 25 mm above the input beam line.

The GHOST compressor is a classic 2-pass parallel grating design (Figure 5.18). The dielectric gratings have a 35 x 15 cm clear aperture, and are placed 80 cm apart. The chirped beam enters 4.5 cm above centerline and strikes the grating at 74.7° from normal. Two rectangular dielectric mirrors (10 x 12 cm) displace vertically the beam down and return it for the second pass. Even thought the compressor design calls for a 5 cm beam diameter with a band pass of >30 nm, it can actually pass >40 nm of bandwidth at the same aperture because of the large grating diameter. Inversely it can transmit an 7.5 cm beam with 9 nm of bandwidth. The calculated group delay of both the stretcher and compressor are shown in Figure 5.19. The ray-trace indicates that the compressor with matched grating angles directly compensates the phase chirp of the stretcher.

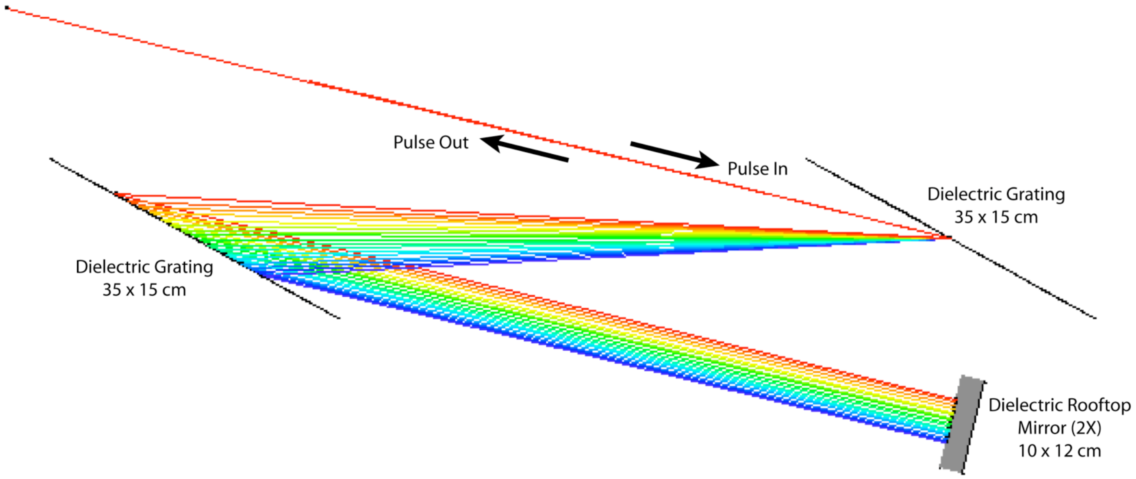

Figure 5.18: Optical ray trace of GHOST compressor.

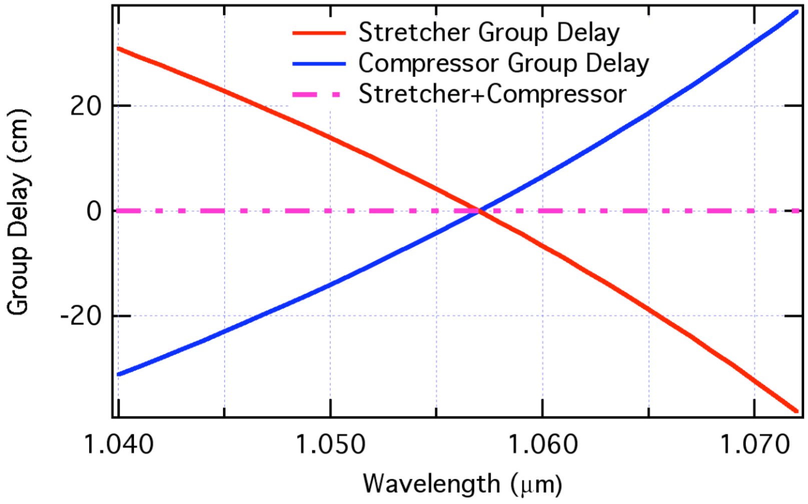

Figure 5.19: Calculated Group Delay from the Stretcher and Compressor in the GHOST laser. The dashed line represents the sum of the two group delays.

The *Dispersomatic* code from Craig Siders was employed to model the higher order material dispersion in the laser (Table 5.1). The input wavelength was set to 1057 nm with 16 nm FWHM of bandwidth. The software does not accommodate for the GHOST stretcher design; therefore an ideal stretcher simulation was substituted. The primary source of material optical path length in the laser is from the laser glasses. Additionally there are several nonlinear crystals and a Faraday rotator in the laser design. All of these elements were included in this simulation. The one meter of Nd:phosphate and Nd:silicate glass was approximated as BK7 quartz glass. The results from the simulation indicated increasing the compressor-grating angle to 74.71° ($\Delta\theta = 0.01°$) and the increasing the compressor grating spacing by 64 μm would compensate the total material dispersion.

Bandwidth and Phase Orders	Simulation Value
Central Wavelength (nm)	1057
Stretcher Transmission Bandwidth (nm)	1038 - 1072
Paraxial Pulse Width (fs)	100.02
Group Delay (fs)	6.3081714×10^6
Group Delay Dispersion – GDD (fs^2)	-219.440586
Group Delay Dispersion Fit – GDD (fs^2)	-2.194406×10^2
3rd Order Dispersion – TOD (fs^3)	4.544548×10^4
4th Order Dispersion – FOD (fs^4)	9.043824×10^6
5th Order Dispersion – 5OD (fs^5)	-5.529483×10^8

Table 5.1: Calculated spectral phase after compression of the GHOST pulse.

5.3.2 Nonlinear Phase Calculations

As stated before, the nonlinear phase and B-integral accumulation can be very detrimental to the fidelity of the laser pulse. The accumulation of spectral phase must be carefully regulated and minimized at all points throughout the laser systems. In most gain media, the accumulation of spectral phase is associated with the nonlinear index of refraction where an intense pulse propagates through a long gain material. However in the case of OPCPA, spectral phase develops as the result of the wave vector mismatch among different spectral components between the three interacting waves. In many cases, grating spacing cannot compensate these effects. Further, spectral phase must be simulated numerically since analytical solutions are usually not solvable. This section details the numerical simulations of the spectral phase accumulation from the parametric and glass amplifiers.

Figure 5.20 plots the calculated spectral phase imparted from one BBO parametric amplifier crystal in the undepleted pump regime. The crystal length is 15 mm with a pump intensity of 500 MW/cm^2. The spectral phase function is very complex over the larger bandwidth (fig. 5.20a). However if we zoom into the region of the GHOST seed bandwidth centered at 1057 nm (fig. 5.20b), the function is much better behaved. The nonlinearity in this area is quite small. The spectral phase can be easily compensated by a variety of mechanisms: compressor grating spacing, compressor grating angle, and even an acousto-optical phase modulator. These effects are sufficiently small and suitable for femtosecond pulse amplification. Table 5.2 summarizes the phase orders of the curve fit to the nonlinear phase shown in Fig. 5.20b. More over the spectral phase accumulation from the nonlinear index in the OPA is also quite small, because of the short optical path length through the gain medium.

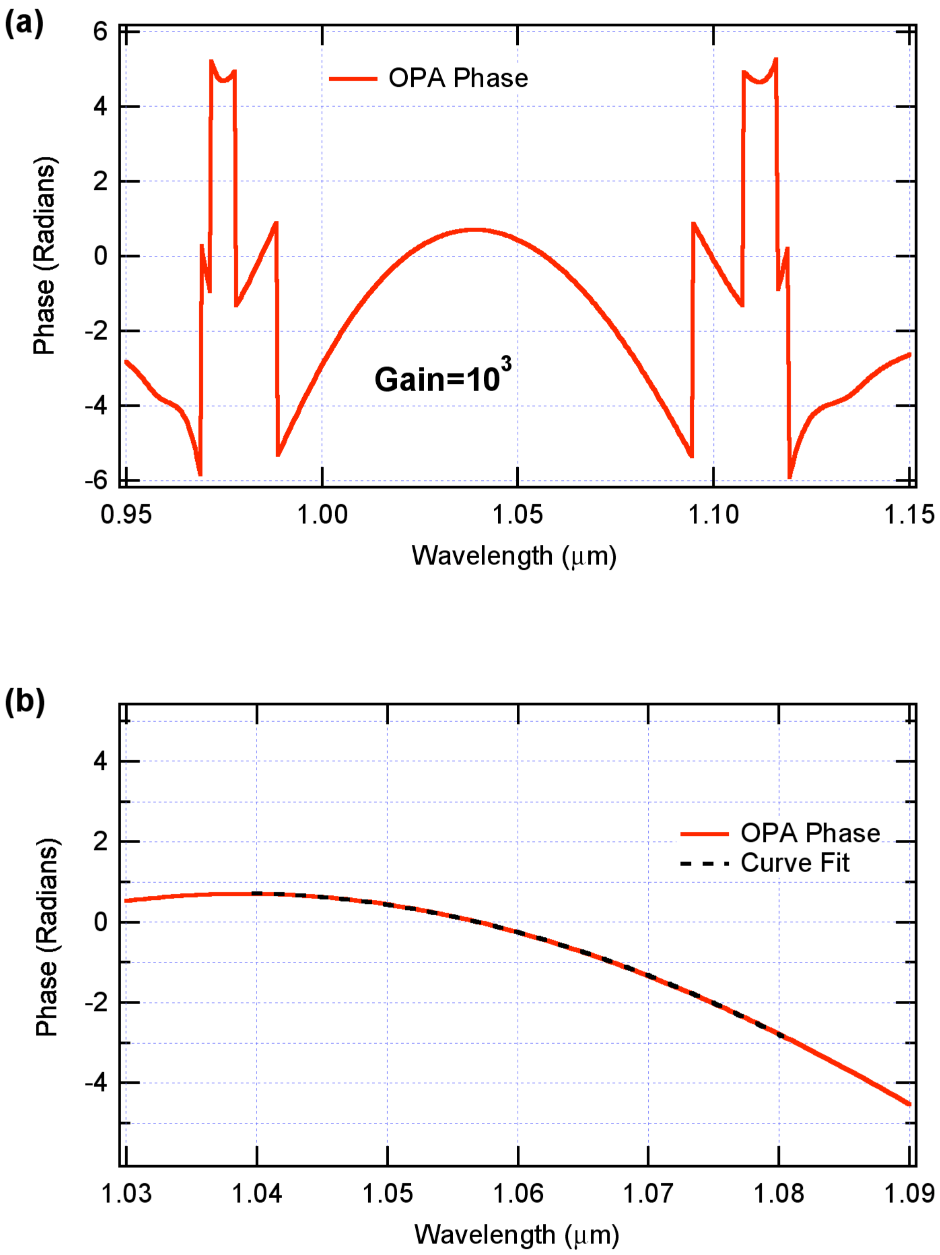

Figure 5.20: a). Calculated spectral phase from parametric amplification in a single BBO crystal. The crystal length is 15 mm and the gain is 10^3. b). Zoom plot of the spectral phase over the bandwidth for the GHOST laser pulse. The spectral phase is small over this region and is near linear. The black line is a polynomial fit from 1040 to 1080 nm.

Bandwidth and Phase Orders	Calculated Value
Central Wavelength (nm)	1057
Curve Fit Bandwidth (nm)	1038 - 1072
Group Delay (fs)	-3.1304×10^4
Group Delay Dispersion – GDD (fs^2)	2.4368×10^4
3rd Order Dispersion – TOD (fs^3)	1.1805×10^4
4th Order Dispersion – FOD (fs^4)	-3.1057×10^4
5th Order Dispersion – 5OD (fs^5)	1.0532×10^4

Table 5.2: Calculated spectral phase orders imparted to the seed from one BBO crystal pumped at 500 MW/cm^2.

The vast majority of nonlinear phase accumulation in the GHOST laser is in the glass amplifier rods. Each rod is 19 mm in diameter and 250 mm long. The amplifier geometry, shown in Figure 5.2, double-passes both rods. First the pulse makes one pass through the phosphate rod. Then it makes two passes through the silicate before making the final pass through the phosphate again. Nd:silicate has the higher nonlinear coefficient, so it is oriented where it can experience the least intense portion of the pulse during amplification. Also the 0° mirror is placed sufficiently far away to prevent any pulse overlap in the silicate rod.

For this simulation the amplifiers are seeded with the fully saturated, 20 mJ spectrum shown in Figure 5.11. The amplifiers are normalized to produce an average (not peak) single-pass gain of 5.1 and 2.85 in the phosphate and silicate rods respectively. In double pass, the total integrated gain is 200. This constitutes a gain ratio of 3.1 (G_{phos}/G_{sil}). Even though gain saturation is included here, its effect is negligible because of the high saturation fluences of both materials. The amplified energy spectrum and accumulated nonlinear spectral phase are plotted in Figure 5.21. The general mandate is that the B-integral be kept less than 1. At this level of amplification, the peak spectral phase is 0.8 radians. Even though the stored energy of these amplifiers significantly exceeds the extracted energy, the amplifiers are clearly B-integral limited because of the short pulse duration. Moreover, this simplified code assumes a flattop spatial profile. Any small aberrations in the real beam could produce a localized intensity spike and cause self-focusing. Therefore, for experimental purposes, the total extracted energy from the actual amplifiers will be limited to 4.0 Joules.

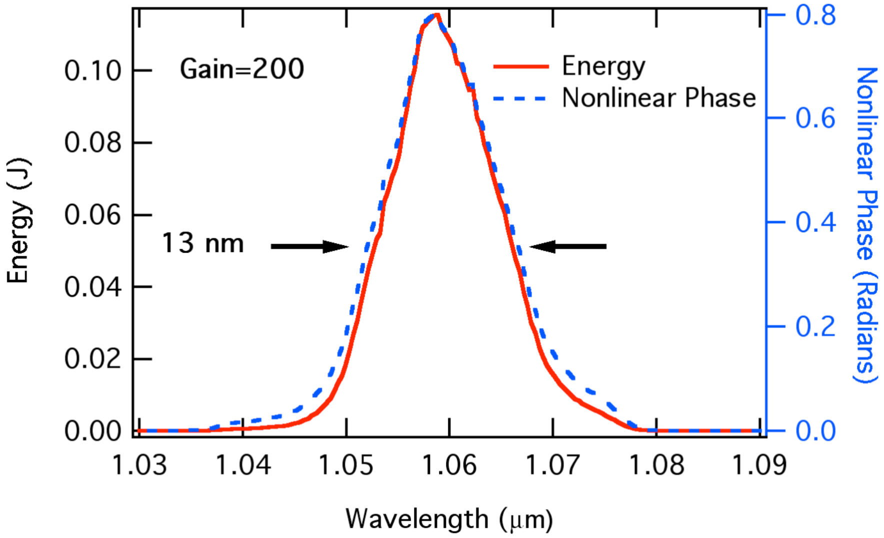

Figure 5.21: Calculated amplified energy spectrum (red line) plus nonlinear phase accumulation (blue line). The pulse is amplified to 4.0 Joules by double-passing a Nd:phosphate and a Nd:silicate rod.

Taking the Fourier transform of the amplified spectrum and including the spectral phase components can readily demonstrate the effects of the spectral phase accumulation on the compressed pulse (Figure 5.22). Shown here are the transforms with and without the accumulated nonlinear phase of the amplified pulse spectrum. The addition of the nonlinear phase increased the transform limited pulsewidth from 123 to 129 fs. This directly reduces the peak intensity of the laser pulse. Additionally a transform is shown with the nonlinear phase from the glass and from the parametric amplifiers. As stated before, this effect is small over this spectral region and is correctable with the compressor; however it is informative to view the uncompensated effect of the 20 fs pulsewidth increase.

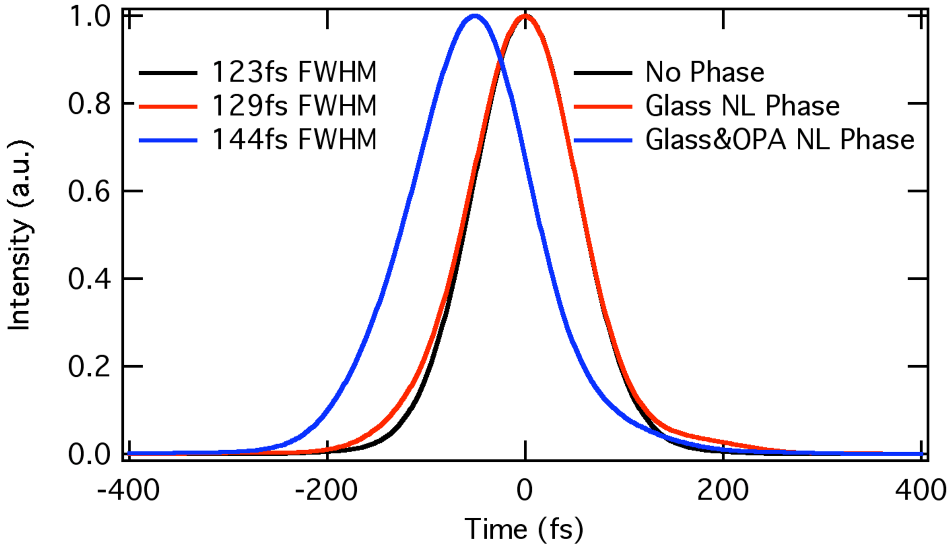

Figure 5.22: Fourier transforms of the amplified pulse with and without the nonlinear phase from amplification.

5.4 Laser Architecture and Characterization

This section details the GHOST laser architecture and its performance (Figure 5.2). GHOST operates in single shot mode with a peak intensity that could eventually exceed 30 TW. The laser incorporates a hybrid amplifier design, which uses both parametric preamplifiers and Nd:glass rods for final pulse amplification. OPCPA is used to generate a spectrally saturated seed with sufficient bandwidth that can defeat the strong gain narrowing of the glass amplifiers. Additionally mixed-glasses are employed to increase the amplification bandwidth. The pulse spectrum is centered at 1057 nm, which is the midpoint between the peak emission lines of Nd:phosphate and Nd:silicate laser glasses. The following subsections detail each major component of the laser, with the oscillator and stretcher grouped together to comprise the front end.

5.4.1 Laser Front End and Timing

A *Coherent Mira* 900-F Ti:sapphire oscillator operating at 1057 nm provides pulse formation for the GHOST laser. The Kerr-lens modelocked oscillator produces 94 fs pulses (Figure 5.23) with a 16 nm FWHM Gaussian-profile spectrum. The *Mira* is pumped by a 10 Watt, frequency doubled Nd:YVO_4 laser (*Coherent Verdi* V10). The oscillator generates 200 mW of average power at 75 MHz with 2.7 nJ of energy per pulse.

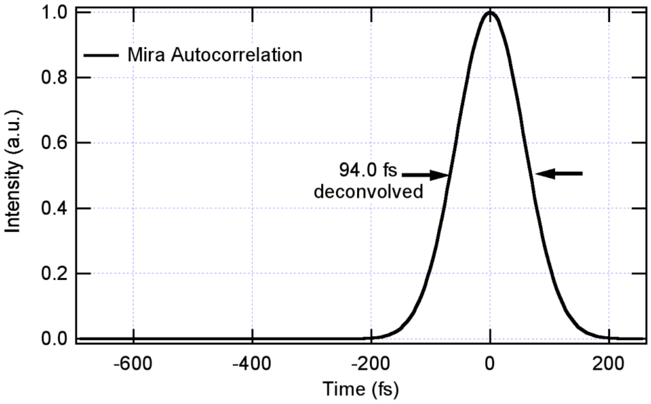

Figure 5.23: Scanning autocorrelation of the Mira oscillator. The measured pulsewidth is 94 fs when deconvolved as a Gaussian spectrum.

The output beam of the oscillator is collimated and sized to a 3 mm diameter using a Galilean telescopic lens pair. Next a Faraday rotator with two crossed calcite polarizers are used to optically isolate the oscillator from the amplification stages. Finally the 10 Hz seed pulse train is sliced out of the 75 MHZ using a fast-on/fast-off Pockels cell with an additional calcite polarizer.

The pulse is chirped to 1 ns FWHM using the all-reflective, single grating pulse stretcher described in section 5.3.1. The stretcher consists of four optical elements; a rectangular grating, a 20 cm diameter curved mirror, a 16 cm diameter flat mirror, and a rooftop mirror. The gold-coated diffraction grating has a 20x15 cm clear aperture, and is ruled to 1740 lines/mm (Figure 5.24). The grating exhibits >90% diffraction efficiency across its full aperture.

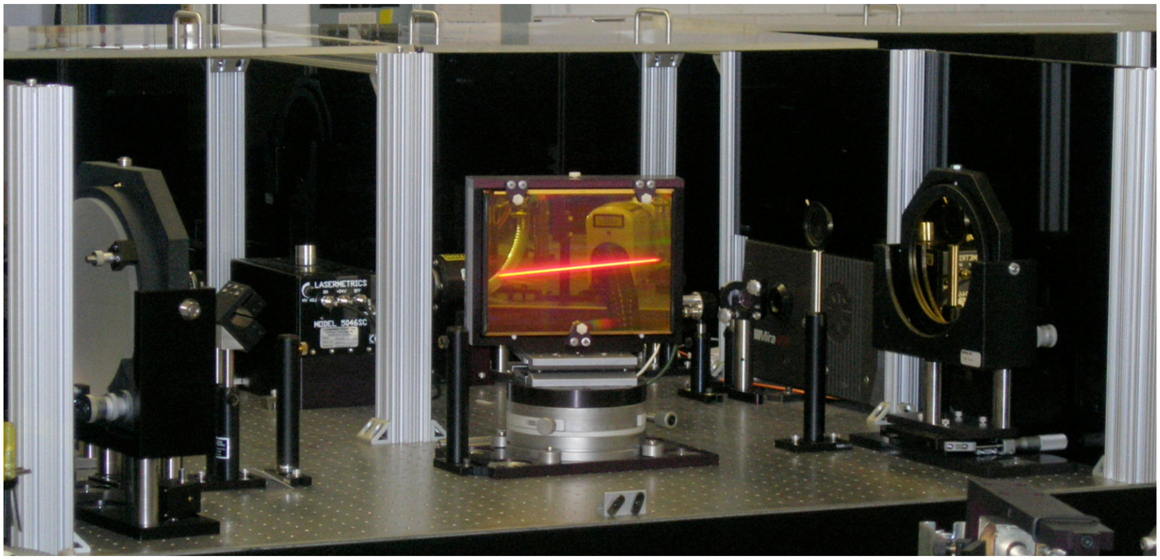

Figure 5.24: Picture of GHOST gold stretcher grating. The clear aperture is 20 cm wide by 15 cm tall. The ruling period is 1740 lines/mm.

The seed pulse strikes the grating at angle of 74.7°, 30 mm above the centerline. It is diffracted to a 2-meter radius of curvature dielectric mirror that is used to image the beam to the second grating. The curved optic is placed 60 cm from the grating, which is 40 cm in front of the focal plane of the mirror. A 16 cm diameter flat mirror is positioned at the opposite focal plane of the curved mirror, thereby forming the mirror image. This allows the use of a single grating and single curved optic. The curved mirror is able to reflect the diffracted beam 3 degrees off-axis to the flat mirror in order to miss the grating. The relatively small angle of off-axis reflection produces minimal spherical aberration, and as it will be shown does not affect pulse compression. This is made possible by the steep angle of incidence of the seed on the grating. The flat mirror retro-reflects the beam back to virtual second grating. The rooftop mirror steps the beam down 25 mm and returns the seed back through the stretcher for the second pass. The pulse exits the stretcher 25 mm above the input beam line with a chirp factor 62.5 ps/nm. The total band pass is 33 nm, clipping the spectrum at 1039 nm and 1072 nm (Figure 5.25).

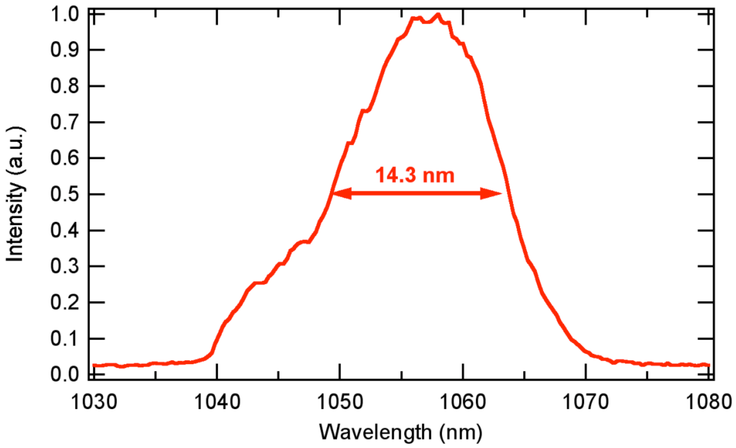

Figure 5.25: Plot of the stretched oscillator spectrum. The pulse is chirped to 1 ns FHWM. The stretcher hard clips the spectrum at 1039 and 1072 nm. The total band pass is 32 nm.

The electronic timing for the laser is derived from a 10 Hz master clock and the oscillator pulse frequency. The RF pulse train from the oscillator is sampled using a photodiode. Next the signal is preamplified using a 1 GHz bandwidth RF amplifier to increase the signal strength. A Stanford Research Systems DG-535 digital delay generator provides the 10 Hz "slow-timing" master clock. The "slow-timing" provides course triggering for all devices that do not need to be precisely synchronized to the pulse, such as the flash lamps. Finally a 10 Hz "fast-timing" trigger is produced by a digital AND-gate, which synchronizes the oscillator RF and the 10 Hz master clock. An additional digital delay generator, triggered by the synchronized "fast-timing" pulse, is used to trigger all devices that require nanosecond accuracy. These items include the pulse slicer and the pump laser Q-switch.

5.4.2 OPAs

Preamplification on the GHOST laser is accomplished through optical parametric chirped-pulse amplification. The design criteria for the OPA stage are to preamplify the seed pulse to a few tens of milijoules, and to create a spectrally saturated seed spectrum that extends beyond the peak gain regions of the mixed-glasses used in the final amplifiers. The system is a two-stage amplifier consisting of two pairs of sequentially pumped BBO crystals. A frequency doubled Nd:YAG laser is beam-split into two beams that each pump the separate stages of the OPA. The following discussion details the design and performance of the parametric preamplifiers.

The pump laser is a *Spectra-Physic*s GCR-270-10 frequency doubled Nd:YAG laser operating at 10 Hz. It produces 680 mJ per pulse at 532 nm with a super-Gaussian spatial mode (Figure 5.26). The temporal profile of the pump is Gaussian with 12 ns (FWHM) duration. The GCR incorporates an unstable resonator, which produces a radially varying spatiotemporal evolution [100]. Therefore the buildup time for the pulse varies with radial position of the pulse. Figure 5.27 shows the measured temporal evolution of the pump pulse. This was measured by scanning a 750 μm pinhole across the pump laser mode. A fast photodiode and oscilloscope was used to collect a 100 pulse average of the temporal profile slice. Even though the radial wings of the pulse suffer a significant delay with respect to the center, the central mass is relatively uniform over a 2 ns duration to accommodate seed amplification.

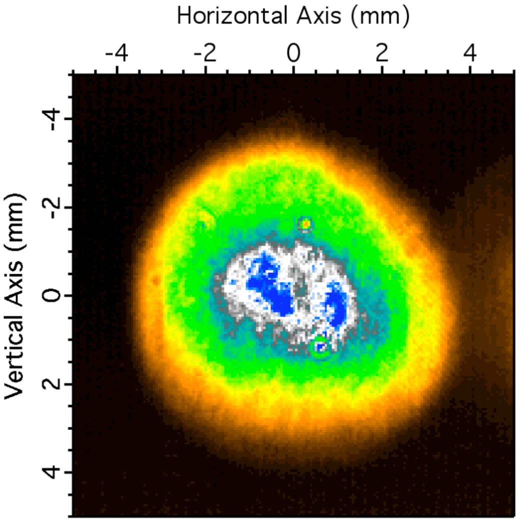

Figure 5.26: Spatial mode at the output of the pump laser. The energy is 680 mJ with 12 ns (FWHM) pulsewidth.

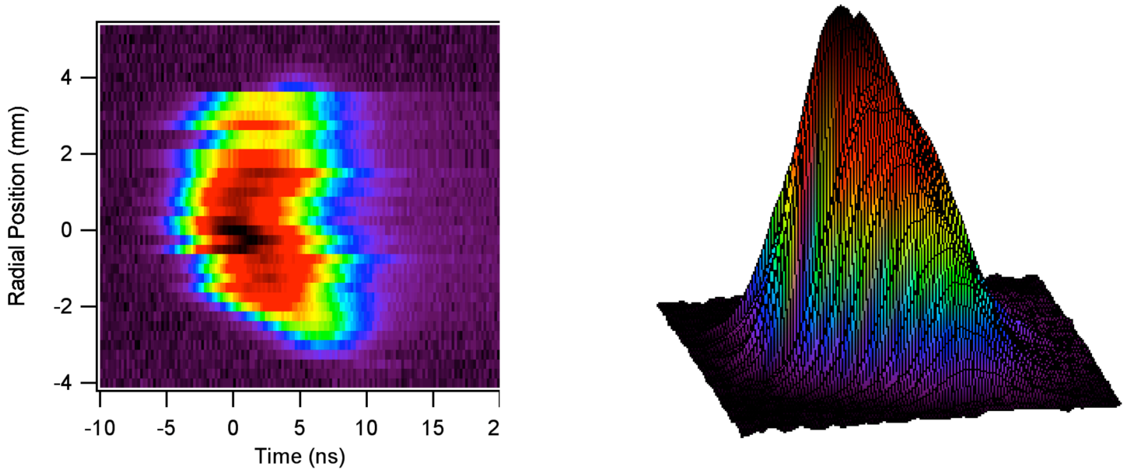

Figure 5.27: Spatiotemporal evolution of GCR-270 pump beam. Although the wings demonstrate a significant delay, the center mass of the pump buildup is near uniform over a 2 ns duration for the seed.

The pump laser is injection-seeded by a *Lightwave Electronics* model 101 seed laser to produce a single longitudinal mode (SLM) pulse. An SLM pulse is required for OPCPA to smooth the temporal profile of the pump. Without the injection seeder, the pulse suffers temporal mode beating which can dramatically alter the seed during amplification. Injection seeding forces the pump pulse to buildup faster than the unseeded Q-switched laser (Figure 5.28), because the seed light is many orders of magnitude more intense than the spontaneous emission trapped in the resonator. Generally the buildup time reduction is about the duration of a single pulse length. Further, the cavity length is actively tuned to frequency lock the resonator to the seed laser. The accuracy of the frequency lock can also introduce temporal jitter in the pulse timing. If the cavity frequency does not exactly match the seed laser or deviates slightly from the active tuning, the buildup time will vary several nanoseconds. This is the primary source of temporal instability of the laser. Even though the energy output of the

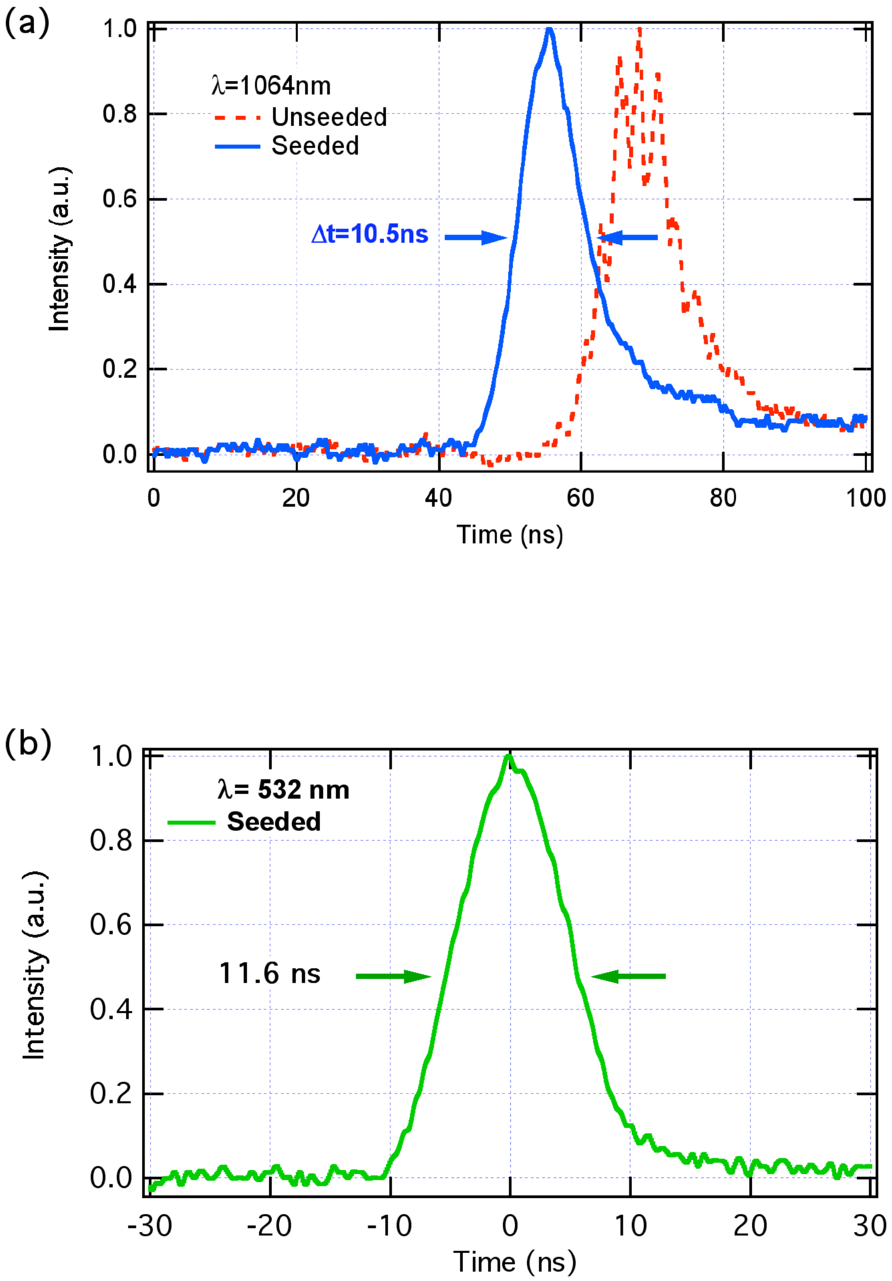

Figure 5.28: Temporal profile of GCR-270 laser pulse: a). The plot shows both the seeded and unseeded temporal shapes, and the buildup time difference of the Q-switched 1 µm laser pulse. b). The temporal profile of the second-harmonic from the GCR pump laser. Saturation of the doubling crystal increases the pulsewidth of the second harmonic to 11.6 ns.

GCR is very stable (Figure 5.29), the temporal instability is the primary source of pulse-to-pulse jitter in the OPAs. Small variations in the pump intensity from temporal jitter will cause dramatic gain variations in the OPAs since the gain is so high.

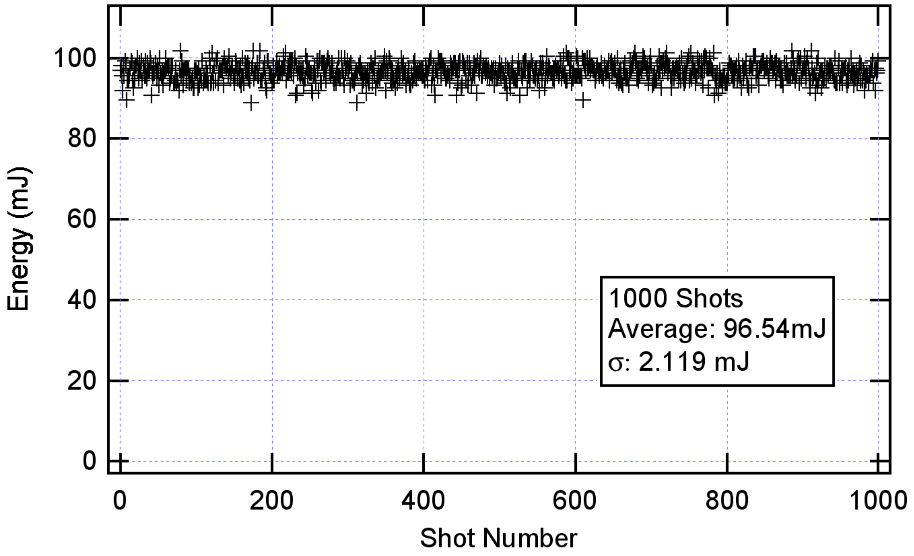

Figure 5.29: Energy stability of GCR-270 over 1000 pulses.

The output of the pump laser is split into two beams using a half-wave plate and polarizer. The low energy beam containing 110 mJ pumps the first stage OPA. The pulse is de-magnified 3.6 times and relay imaged from a plane near the doubling crystal in the pump laser to the first BBO crystal in the OPA (Figure 5.30). Transmission losses and a 2.0 mm beam diameter produce a pump intensity of 263 MW/cm^2. The first stage OPA consists of two sequentially pumped BBO crystals separated by 2 mm. Each have a 7 mm square aperture and are 15 mm long. The coherence length of the FWHM points of the seed spectrum (1049 and 1067 nm) defines the 15 mm crystal length. The interaction has infinitely long phase matching for 1057 nm; however the coherence length diminishes increasingly as the seed wavelength deviates from the central frequency. The back surface of the crystals are wedged 3° to reduce parasitic amplification within the crystal. The wedge is oriented on the ordinary axis to prevent significant beam steering when phase matching the extraordinary axis. In addition the crystals are oriented for Poynting vector walk-off compensation [101]. The sign of d_{eff} is inverted by rotating the second crystal 180° about the axis of propagation.

In birefringent media, the direction of wave propagation ($\vec{k}$) for an extraordinary wave is not generally the same direction of the energy propagation (Poynting vector). This is caused by the induced polarization of the pump wave, which is along the crystal axis, not the axis of propagation. BBO is a negative uniaxial crystal; therefore the extraordinary polarized pulse ($\vec{E}_{pump}$) walks off away from the crystal principal axis. Rotating the crystal about the propagation direction is equivalent to reversing driving fields ($\vec{E}_{pump}, \vec{E}_{signal}$) and the induced polarization, so the sign of d_{eff} is reversed.

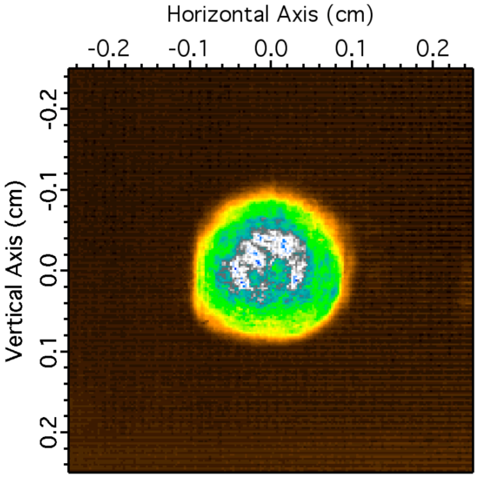

Figure 5.30: Pump mode at first OPA BBO crystal. The beam is 2.0 mm ($1/e^2$) in diameter with 99 mJ of energy. The peak intensity is 263 MW/cm2.

The horizontally polarized pump pulse enters both crystals at normal incidence after passing through a 45° dichroic mirror to combine it with the seed (Figure 5.31). After the BBO crystals it passes though another 45° dichroic and is dumped. Before amplification the seed/signal pulse is de-magnified to a mode diameter of 0.88 mm ($1/e^2$). Transmission losses of the laser front end reduce the seed energy to 500 pJ at the first OPA. It is aligned at a 1° crossing angle to the pump in the horizontal plane (extraordinary axis) after reflecting off the 45 dichroic. After two crystals the seed is amplified to 1.6 mJ with a combined gain of $3.2\text{x}10^6$. This is almost 5 times larger than the simulated gain shown in Figure (5.10) with a pump intensity of 350 MW/cm^2. The amplified seed spectrum from the first two crystals is slightly gain narrowed since the amplifiers are not saturated (Figure 5.32). The idler pulse is generated at a 1° angle opposite to the signal pulse, and is observed to be in the same plane. It is allowed to propagate freely to facilitate spatial separation from the seed pulse, and then is dumped. The seed is finally separated from the pump by reflection from the second dichroic mirror.

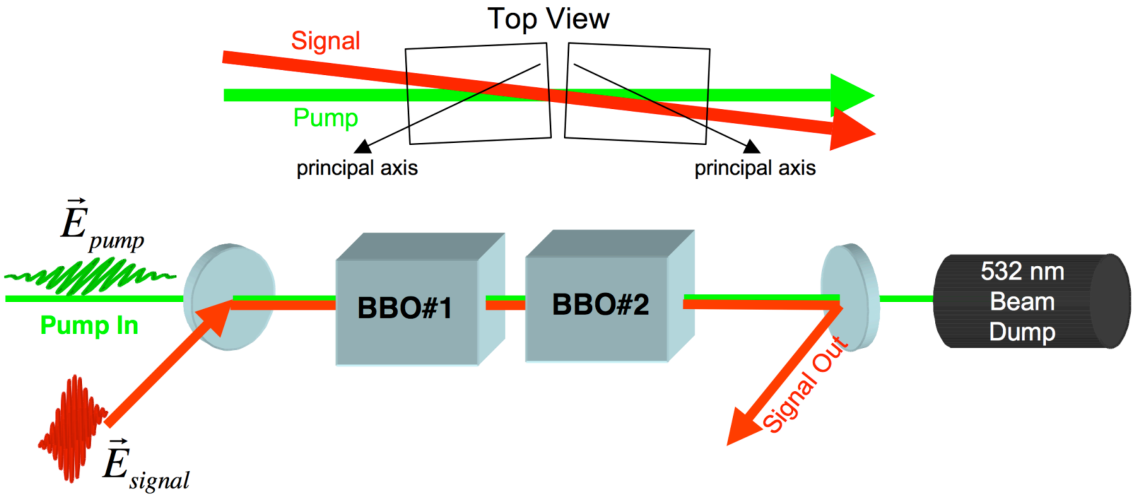

Figure 5.31: Optical schematic of the pump and seed pulses in the first OPA pair. The pump and seed are crossed at 1° inside the BBO crystals.

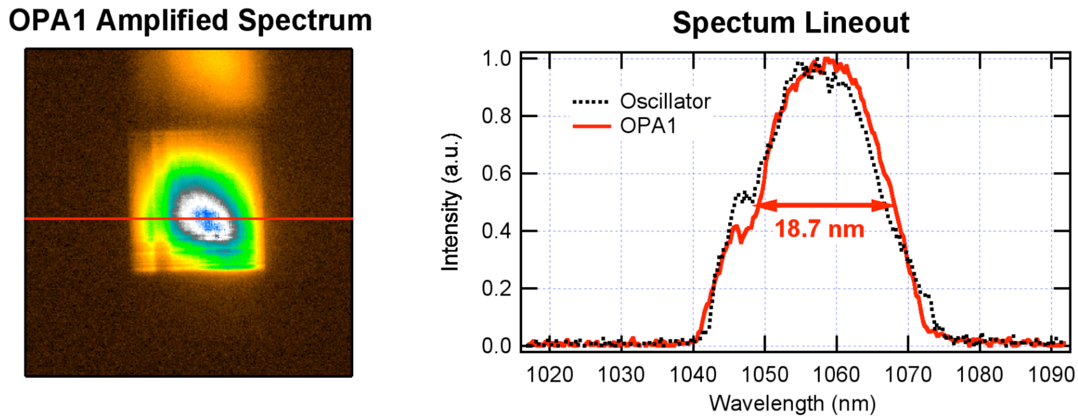

Figure 5.32: Amplified seed spectrum after the first OPA pair. The oscillator spectrum is 20.3 nm FWHM, and the amplified spectrum is slightly gain narrowed to 18.7 nm FWHM.

After the first stage OPA, the seed is resized and spatially filtered for the second stage amplification. The pulse diameter is increased to 4.5 mm ($1/e^2$) and spatially filtered with a 2.3 times diffraction limited, 150 µm pinhole (Figure 5.33). Strong spatial filtering is used to increase the optical isolation and reduce cross talk between the first and second OPA stages. The mode is slightly elliptical due to the astigmatism produced by the oscillator, but the strong spatial filtering between the OPA stages reduces this. In turn, approximately 300 µJ of energy is clipped by the pinhole.

The beam is slightly oversized with respect to the pump mode for the second OPA. This is done to overfill the gain volume and produce a super-Gaussian mode in the second stage. The pump beam for the second stage is also relay-imaged from a plane near the doubling crystal of the pump laser to the first crystal in the second OPA stage (Figure 5.34). It is de-magnified 1.66 times to a mode diameter of 4.0 mm ($1/e^2$) with 500 mJ of energy. This produces a pump intensity of 330 MW/cm^2 at the third crystal. Also the same 7 mm aperture, 15 mm long BBO crystals are used in the second stage.

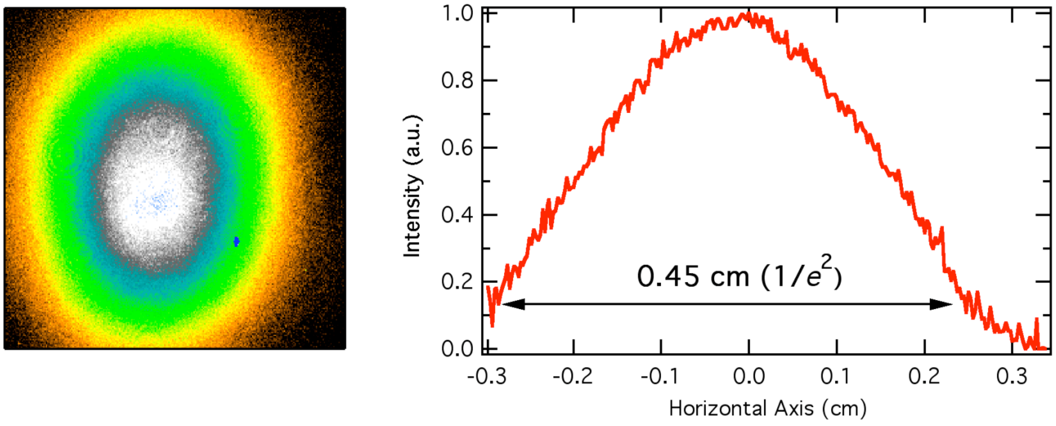

Figure 5.33: Amplified seed mode from first two OPA crystals. The beam is 500 μJ and enlarged to a 0.45 cm 1/e^2 diameter.

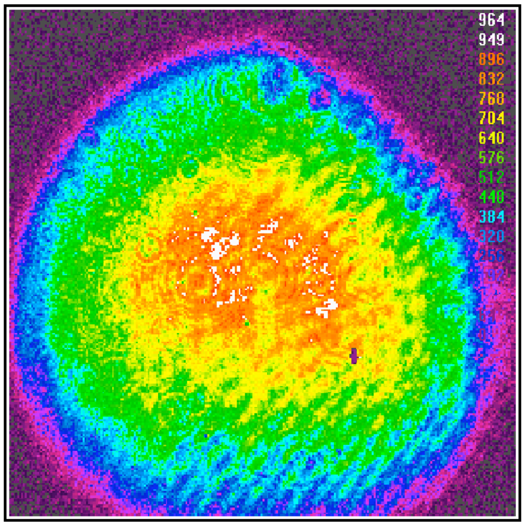

Figure 5.34: Image of GCR-270 pump beam mode at plane of third BBO crystal. The energy is 500 mJ with a 4 mm (1/e^2) beam diameter.

Two amplifier geometries were evaluated for the 2nd stage OPA. Since the first stage produces >1 mJ of amplified energy, saturation is easily achieved in the third crystal. Therefore only a nominal energy exchange will occur in a 4th crystal that is placed immediately following the third. Additionally because of the large temporal mismatch between the pump and seed, a majority of the pump light is wasted. In the first amplifier geometry for the 2nd stage, the two crystals were placed in sequential order and spaced by 2 mm. This orientation maintains the same temporal alignment of the pump and seed in both crystals (Figure 5.35). Here the pump passes through the combining dichroic and sequentially pumps both crystals. Then it passes through the separation dichroic and is dumped. Again the vertically polarized seed is aligned at the 1° cross-angle in the horizontal plane and mixes with the horizontally polarized pump. The crystals are also orientated for walk-off compensation.

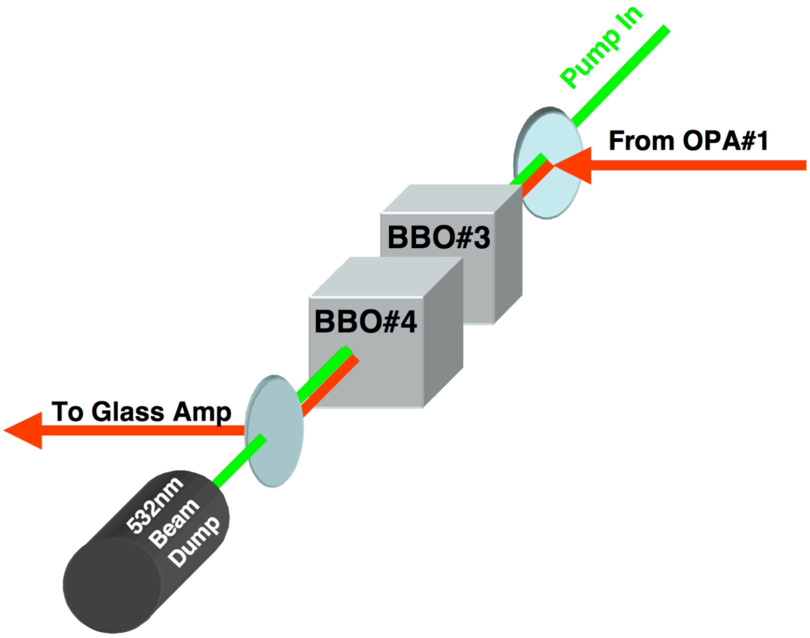

Figure 5.35: Optical schematic showing temporally aligned OPA crystals. The seed and pump pulses are temporally aligned in both crystals.

Figure 5.36 shows the amplified spectra and energy from this configuration. In the 3rd crystal, the seed is amplified to 10 and then 20 mJ with a maximum gain of 20. Adjusting the phase matching angle of the BBO crystal varies the energy. Here strong gain saturation is seen because the spectral wings of the seed have significantly amplified to form a top-hat spectrum. The blue line shows the amplified spectrum after phase matching the fourth crystal. The seed extracts an additional 5 mJ from the pump; however the spectrum becomes highly modulated. Here back conversion at the center of the spectrum has transferred energy from the seed back to the pump. Moreover parasitic fluorescence becomes increasingly prevalent since the two crystals are in such close proximity. This can be seen on the blue side of the blue line spectrum. Since the band pass of the stretcher is from 1039 to 1072 nm, any light generated beyond this region is attributed to parametric fluorescence.

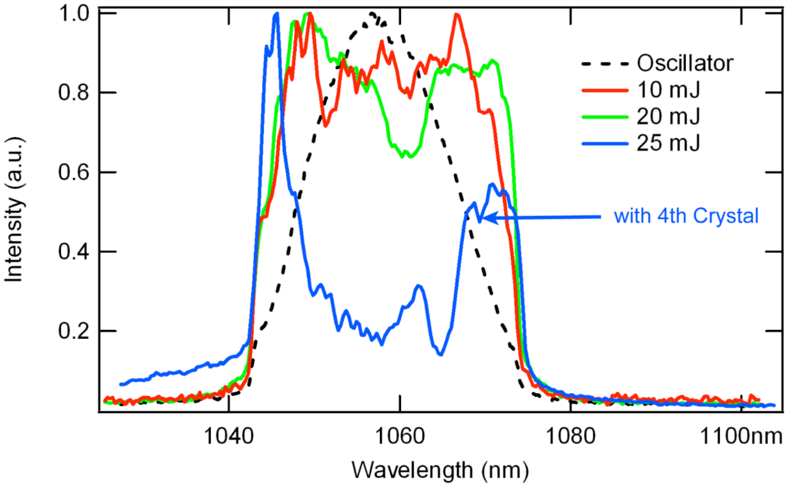

Figure 5.36: Amplified spectra from third and fourth OPA cyrstals that are temporally aligned. The red and green lines show the amplified spectra from the 3rd OPA crystal. The energy is varied by adjusting the phase matching angle. The blue line shows the amplified spectra from the 4th OPA crystal. An additional 5 mJ is extracted from the pump beam and strong spectral saturation is achieved. The center depression on the blue spectrum is attributed back conversion from the signal to the pump beam.

A second optical layout was evaluated in order to increase the amplified energy of the seed and to extract more energy from the pump beam. In this design, a variable delay leg was introduced to the seed beam between the third and fourth crystals (Figure 5.37). Here the seed beam is separated from the pump beam after the third crystal using a dichroic mirror. Next it is passed through a delay leg, which can vary from 1 to 4 ns. It is recombined with the pump via another dichroic mirror. The use of the delay leg allows the seed to shift to a new temporal position and mix with an undepleted section of the pump pulse.

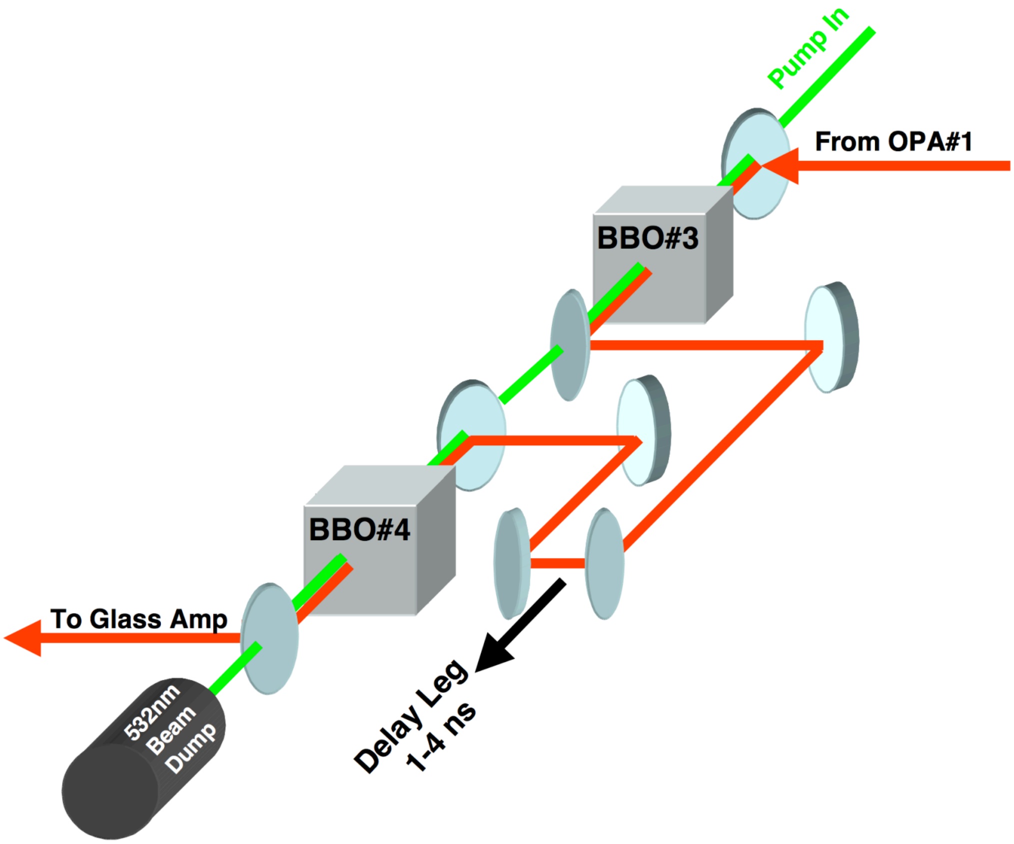

Figure 5.37: Optical schematic of the delay leg used to temporally shift the seed pulse to a different temporal alignment on the pump pulse. The delay leg is variable from 1 to 4 ns.

In this setup, the delay leg was varied in 0.25 ns intervals. Figure 5.38 plots the amplified spectrum at each temporal delay. At each position the pump pulse timing was optimized to give the best amplified spectrum. At the 1.0 ns delay (red line), the amplified energy was increased to 33 mJ in the fourth crystal; however the spectrum becomes highly modulated. When the seed spectrum saturates in the 3rd crystal, its FWHM duration is increased to 2 nanoseconds. Spectral chirp causes this, because wavelength is time in CPA. At this delay, the seed is temporally overlapped with a depleted portion of the pump from the 3rd crystal, and therefore sees a lower gain on the blue side of the spectrum. Also, strong back conversion is seen at the 1064 nm line of the seed, and parametric fluorescence occurs beyond 1080 nm. When the delay is increased to 2.0 ns the amplified energy increases to 44 mJ and is also highly modulated. Also a large amount of parametric fluorescence was measured. At this delay, the seed overlaps the pump a combined 4 ns window in the 3rd and 4th crystals. Here the intensity variation from the rising and falling edge of the pump pulse becomes increasingly pronounced. Also if the seed does not reach full saturation in the third crystal, this delay can cause the seed to miss the peak intensity of the pump in both crystals. The optimum delay was found to be at 1.5 ns. Here the pulse was amplified to 40 mJ with a uniformly saturated spectrum with minimal parametric fluorescence. The spike seen at 1064 nm on the spectrum (black line) is attributed to the second order diffracted line from stray pump light at the spectrometer.

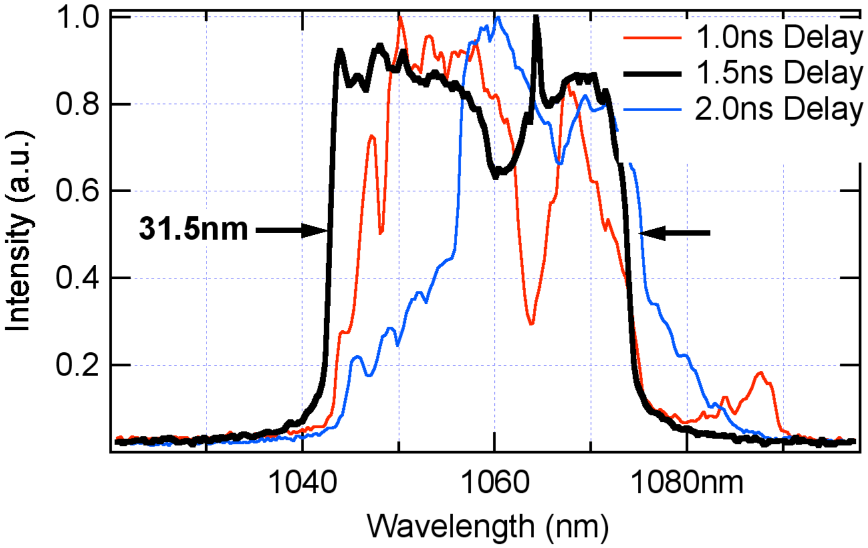

Figure 5.38: Amplified spectra from OPA crystals 3 and 4 as function of temporal delay.

The delay leg in the second stage OPA was ultimately adopted for the final laser design, because of the increased energy. In contrast, the amplified beam quality from the final crystal is significantly reduced compared to the third crystal (Figure 5.39). The ring structure seen in the amplified mode from the 3rd crystal arises from the pump beam. The GCR-270 incorporates and unstable resonator with a Gaussian reflectivity profile output coupler. The pump therefore has a slight diffraction ring on the spatial mode that can be seen in Figures 5.30 and 5.34. This structure is then transferred to the seed when saturation is achieved, and therefore not seen in the first stage. In the third crystal the beam strongly saturates the pump and becomes super-Gaussian. The beam quickly experience spatial modulation as the pulse travels to the fourth crystal. Additionally the higher order spatial frequencies of the pump modulate very quickly to deteriorate the pump quality. These two effects combine to produce the hot spot from the 4th crystal mode. Ideally the seed would be image relayed from crystal to crystal, but the complex optical path of the delay leg prevents this. To correct this modulation, the pulse is highly spatial filtered before the next amplification stage. Subsequently the aperture clips off a large portion of the increased amplified energy.

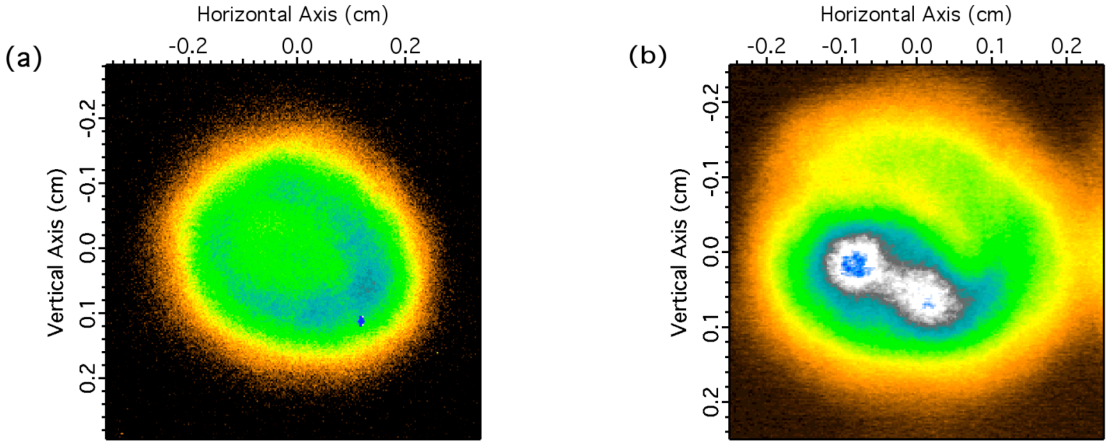

Figure 5.39: Amplified spatial modes from the second stage OPA. a) 3rd OPA amplified mode. The energy is 25 mJ with a 3.5 mm ($1/e^2$) beam diameter. b) amplified seed mode from 4th OPA crystal. The energy is 42 mJ with a 4 mm ($1/e^2$) beam diameter.

As it has been shown, parametric fluorescence is of significant concern. The combined small signal gain of the four BBO crystals is over 10^{12}. If the 150 μm pinhole is removed from the telescope between the two stages and the seed is blocked, over 20 mJ of amplified parametric fluorescence is observed after the 4^{th} crystal with a white light spectrum. With the pinhole in place, this is reduced to less than 3 mJ. In this case, the gain is undepleted and fluorescence is free to be generated. But when the seed is amplified, most of the peak intensity gain is extracted thus eliminating the fluorescence.

No fluorescence is measured when the seed is blocked and the optical path between the two OPA stages is blocked. This suggests the first two crystals are seeding the second two. Moreover, when the crystals in the second stage are in the temporally aligned configuration, over 15 mJ of amplified parametric fluorescence is measured with the 150 μm pinhole in the spatial filter. Therefore the combination of the delay leg and the spatial filter pinhole help to minimize this effect.

Figure 5.40 plots the energy stability of the second stage OPA over 1000 shots. In both cases, the standard of deviation is 10%. As shown in Figure 5.29, the energy stability of the pump laser is ±3%, but this contributes to only a small portion of the instability. Most of the energy variation arises from the seeding instability of the GCR.

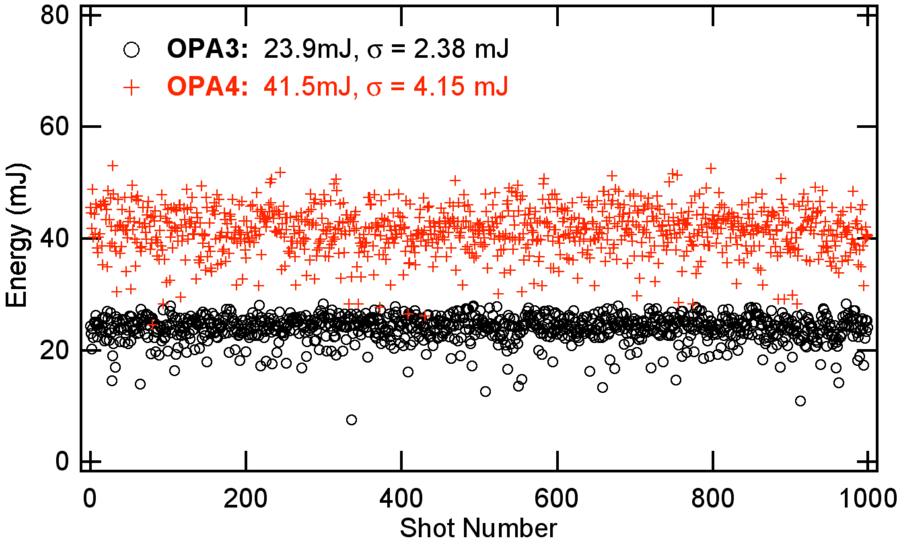

Figure 5.40: Energy stability from the second stage OPA over 1000 shots. The third crystal is plotted in red crosses, and the fourth crystal is plotted in black circles.

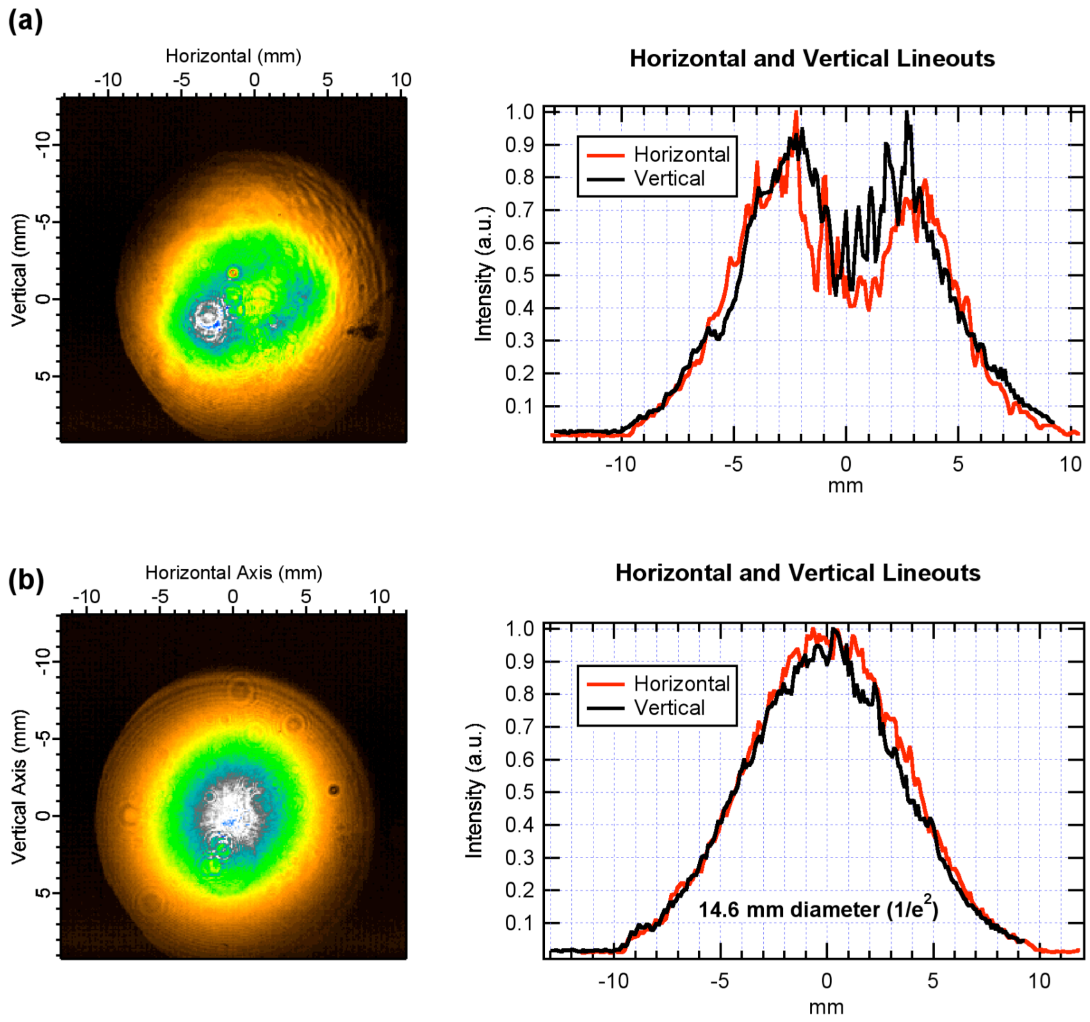

Figure 5.41: Glass amplifier seed mode after the first vacuum spatial filter. a) Spatial mode after the telescope without the pinhole. The energy is 27 mJ with a 15.4 mm (1/e^2) diameter. b) Spatial mode after the telescope with a 200 μm diameter pinhole. The energy is reduced to 20 mJ with a 14.6 mm (1/e^2) diameter.

After the second stage OPA, the seed is resized and image relayed to the glass amplifiers. A vacuum telescope is used to magnify the seed diameter by four times. Additionally a spatial filter is included to improve the mode quality for the final amplification. The primary lens in the telescope has a focal length of 25 cm (f/#=10). This produces a 160 μm diffraction limited spot size at the focus. A 200 μm pinhole is used in order to clip off the higher order spatial frequencies produced in the second stage OPAs. As a result a significant portion of the amplified energy is deposited on the pinhole. Figure 5.41 shows the amplified mode transmitted through the vacuum spatial filter with and without the pinhole. Approximately 26% of the beam energy is clipped off. Moreover, to improve the mode quality, the mode is changed from a top-hat spatial profile to a Gaussian mode. Even though the mode quality is improved, a top-hat mode is more desirable for seeding the glass amplifiers.

5.4.3 Glass Amplifiers

Final amplification is achieved in two 19 mm diameter by 250 mm long Nd:glass rods, one containing Nd:phosphate glass and the other Nd:silicate. The goal of the amplifiers is to achieve as much energy possible while managing the nonlinear effects. The saturation fluences of both glasses are ≥5 J/cm^2; however the B-integral threshold has been established at 1.5 GW/cm^2. This equates to a fluence of 1.5 J/cm^2 for a 1 ns pulsewidth. Even though the seed pulse for the rods has been gain broadened by the OPAs to 2 ns (FWHM), the pulsewidth will be immediately truncated by gain narrowing in the first rod amplifier. Further, because of the relatively small gain coefficient of Nd:glasses, both materials require a long optical path length to integrate high gain factors. This exacerbates the B-integral accumulation. These effects combine to establish immediately that the rods cannot be saturated, and the gain will be entirely in the small signal regime.

The rods are configured in sequential order with a relay-imaging telescope in

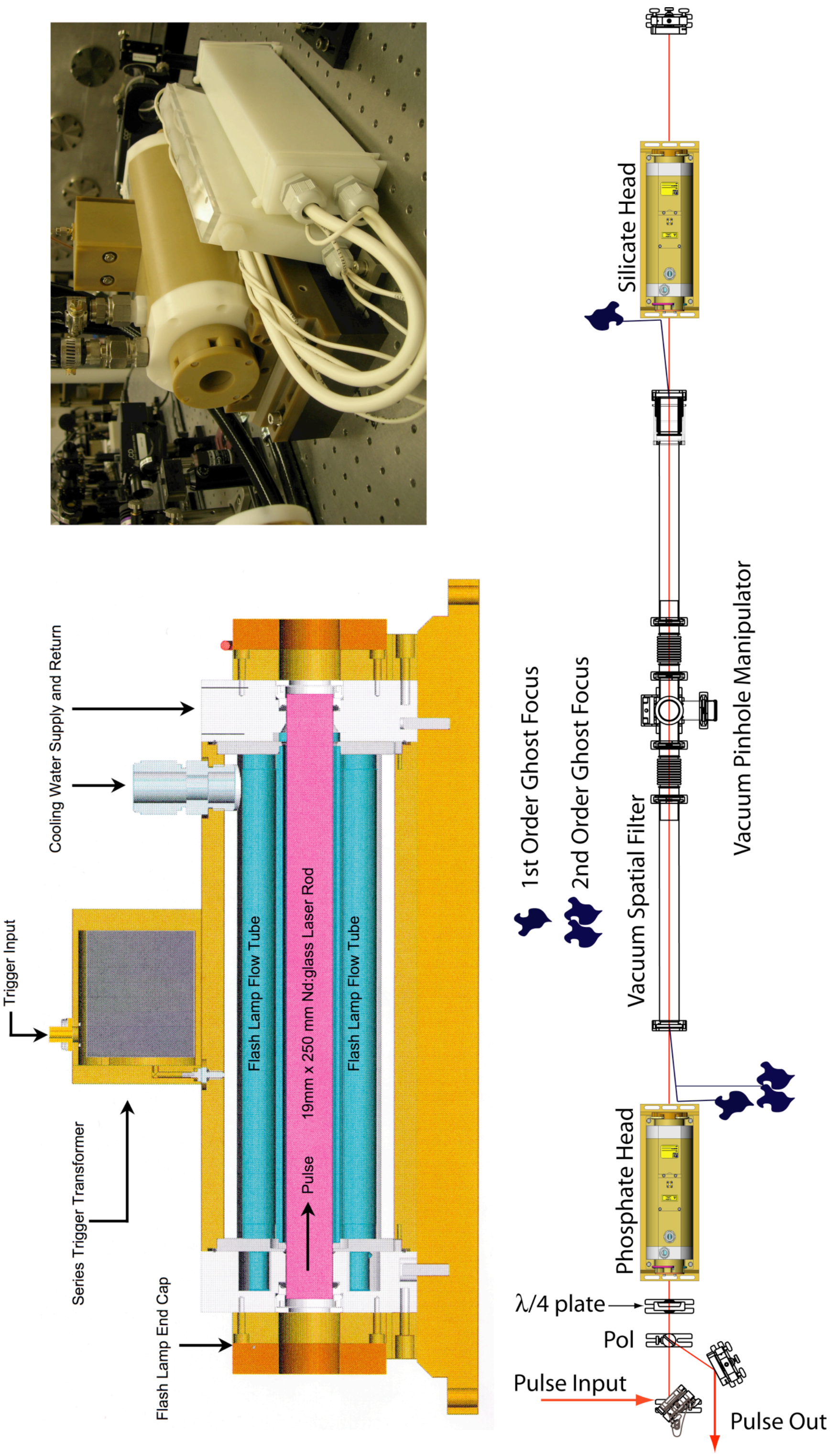

Figure 5.42: Optical schematic of the mixed-glass amplifier.

between (Figure 5.42). They are also double passed for efficient energy extraction. The spatial filter following the OPAs relay images the output of the 4th BBO crystal to the entrance plane of the rod amplifiers. Additionally the polarization is rotated 90° to horizontal by a zero-order half wave plate. The seed pulse enters the amplifier by first passing through a plate polarizer and then a zero-order quarter wave plate to create circular polarization. The pulse first makes a single pass through the phosphate rod. Next it travels through a 1:1 imaging vacuum spatial filter, and then makes the first pass through the silicate rod. A 0° high-reflector is placed after the silicate head to retro-reflect the pulse back through the amplifier. The mirror is positioned 25 cm away from the end of the silicate rod to ensure the pulse does not overlap itself on the return pass. After the second pass through the phosphate rod, the polarization is rotated to the vertical plane by the quarter wave plate. The pulse is ejected from the amplifier by reflecting off the input polarizer.

The vacuum spatial filter between the heads relays the input image from the OPAs, which is before the input polarizer, to the 0° high-reflector after the silicate head. On the return pass it relays the image to a plane after the ejection polarizer. The telescope uses 61 cm focal length lenses (f/# = 12) and a 1.5 mm diameter pinhole placed at the Fourier plane. The large diameter pinhole is used to accommodate the shifting focal position of the telescope caused by the thermal lensing of the two rods. Because the rods are double passed, different materials, and are pumped at different energies, the pinhole cannot be placed in a corrected focal position. Additionally the telescope images through both 25 cm long glass rods. This increases the image and object plane distances from 61 to 69 cm. Therefore the 0° high reflector is positioned 69 cm from the second lens at the image plane.

Because the amplifiers produce a multi-Joule pulse, management of the ghost foci is extremely important. The lenses are mounted with the curved surfaces outside the vacuum, facing towards the glass heads. They are also tilted 3° parallel to each other to deflect the ghost foci off-axis. The telescope creates three critical ghost foci: a first-order back reflection from the first lens by the input pulse (focal length=f/3), a second-order forward reflection from the same lens by the return beam (focal length=f/5), and a first-order back reflection from the second lens by the output beam (focal length=f/3). Both rods are placed 19 cm from each lens to allow the off-axis reflection of the ghost foci to spatially separate and miss the rod. The first-order reflections are dumped on the head housings before they reach focus, and the less critical second-order beam focuses in air outside of the beam path.

A custom designed head was specifically built for the glass rods. It houses eight Xenon flash lamps in radial order around the rod. The lamps and rod are submerged in a water bath that uses multi-pass turbulent flow for active cooling. Both the lamps and the rod incorporate samarium doped flow tubes to absorb ultra-violet radiation from the flash lamps. The flow tubes then fluoresce in the visible spectrum and provide usable radiation in the absorption band of the glass rods. Each head houses a 19 mm diameter by 250 mm long Nd:glass rod. Each rod has 3° parallel-wedged faces to stem off parasitic oscillations.

A custom built pulse-forming network (PFN) is used to pump each head. The PFNs are designed to deliver 3 kJ of energy to the flash lamps. Each PFN consists of a 15 μF capacitor, which can be charged to 20 kV, and an 806 μH coil. The eight lamps are wired in series and form the resistors for the simple L-R-C circuit. Each lamp has a 25 MΩ resistor wired in parallel to act as a voltage divider. These are used to reduce the local potential difference between the terminals and to prevent pre-firing of the circuit. A high-voltage power supply charges to the capacitor to a maximum of 20 kV in approximately 10 seconds. Before the lamps are ionized, they act as a switch that prevents the capacitor from discharging. A series trigger transformer located on each head is used to break down the Xenon in the lamps and dump the capacitor. The circuit generates a peak current of 1400 amps in a 300 μs pulse (Figure 5.43). Figure 5.44 plots the measured fluorescence lifetime of both glasses in the 19 mm heads. Both glasses demonstrate the characteristic ~350 μsec (1/*e*) fluorescence, which are in excellent agreement with the published values [81].

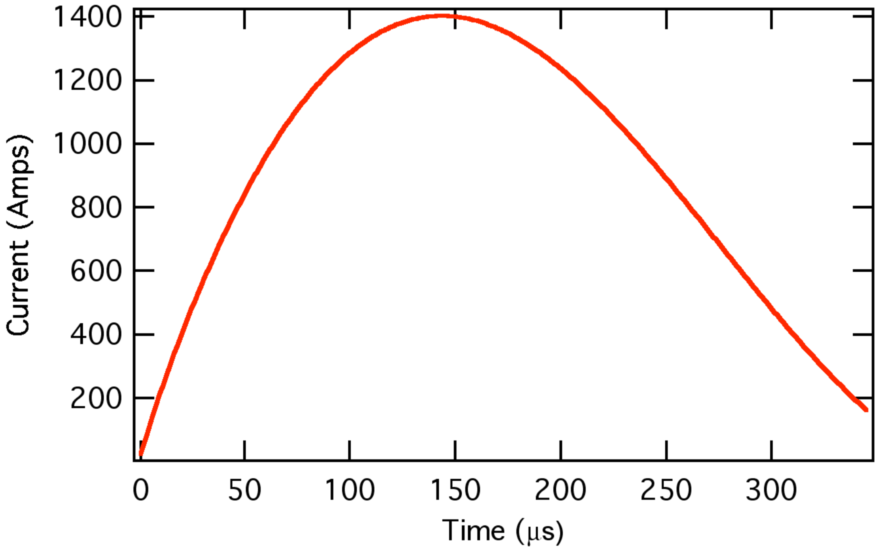

Figure 5.43: Simulation of current versus time from pulse forming network for the 19 mm glass amplifiers.

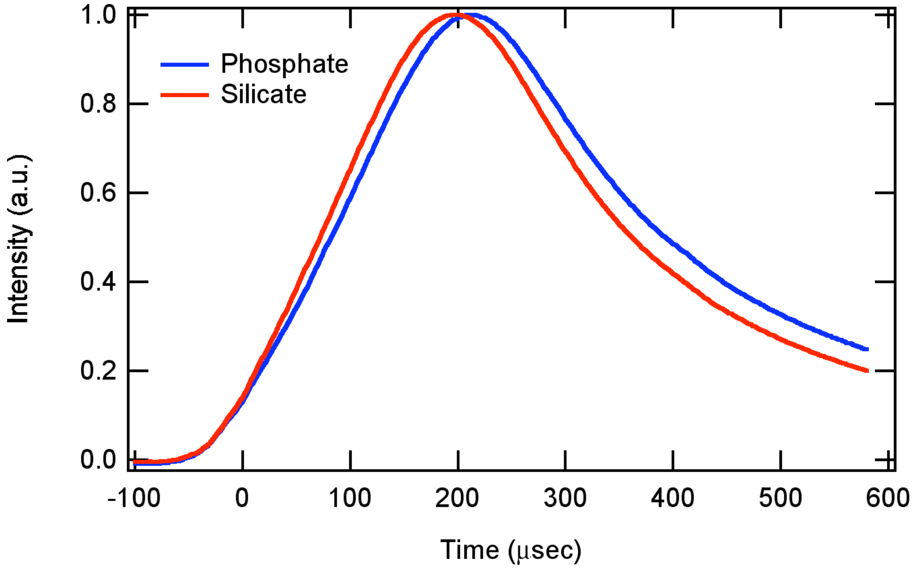

Figure 5.44: Measured fluorescence lifetime from the 19mm Nd:phosphate and Nd:silicate laser rods.

The maximum rep-rate of the glass heads was determined interferometrically. The phosphate head uses APG-1 glass from *Schott Glass Technologies.* APG1 is formulated for high average power, and demonstrates higher thermal conductivity than other Nd:glasses [102]. The LG-680 silicate glass, also from *Schott*, has the longest thermal recovery time [81]; therefore it was used to establish the maximum shot rate. The silicate head was inserted into a Michelson interferometer to measure the wavefront distortions when the head is fired (Figure 5.45). When the head was fired at maximum voltage (20 kV), a peak 2-wave distortion was measured after 30 seconds. An additional 30 seconds was required to return the rod to thermal equilibrium. Therefore the maximum shot rate for the heads is established at 1 shot per minute.

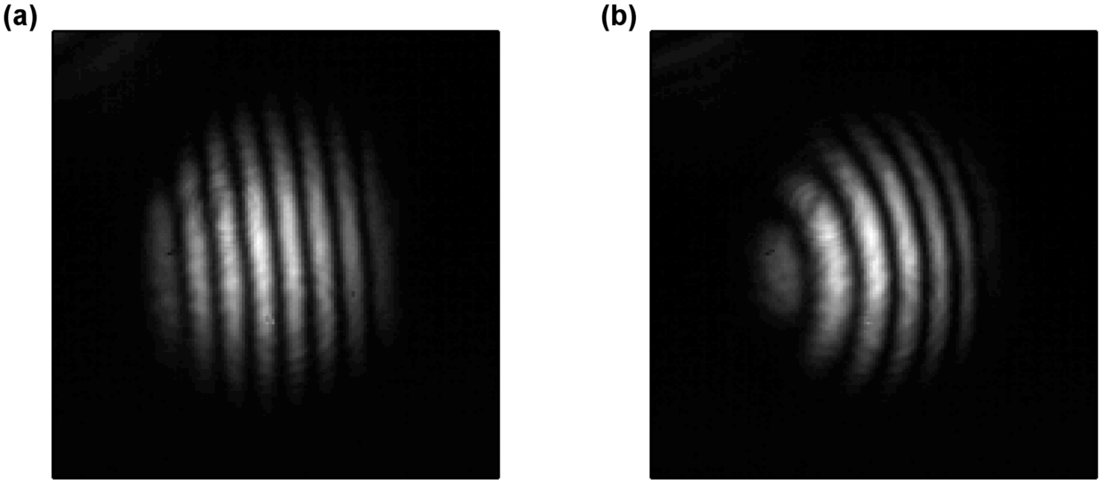

Figure 5.45: Thermal recovery time of Nd:silicate rod fired at 20 kV. The rod takes 1 minute for complete thermal recovery. a) Unpumped rod at t=0 sec. b) Pumped rod at t=30 sec.

The seed mode for the glass amplifier has Gaussian spatial profile (Figure 5.46). It would be more beneficial to use a flattop seed to extract more energy from the amplifier, because the fluence is uniform. However the mode must be spatially filtered following the OPAs to remove modulation and improve the beam quality. The beam is 15 mm ($1/e^2$) in diameter, and has a 66% fill factor in each rod. The round-trip transmission through the amplifier is measured at 80%.

Because the rods are pumped radially, the absorbed energy density is higher at the edges than the center of the rod. Figure 5.47 plots the radial gain profile data for both glasses at two different PFN voltages. At peak voltage, both the phosphate and silicate rod gains have vary by 33% from the center to the wings (G_{center}/G_{wings}). However at the lower PFN voltages, the gain vary less than 25%. Consequently, the radial variance is beneficial when seeding with a Gaussian-profile spatial mode.

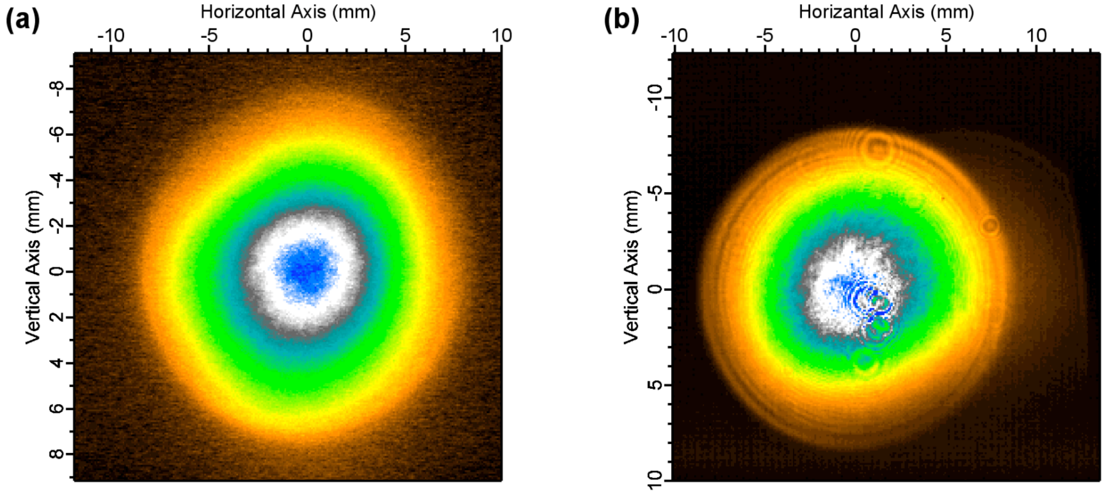

Figure 5.46: Glass amplifier seed mode. The seed is 15 mm ($1/e^2$) in diameter. The amplifier transmission is 80%. a) seed after first pass through glass amplifier. b) ejected seed mode from the glass amplifier. The diffraction rings are from over filling the camera objective.

The double and single pass small-signal gains were measured first by sampling the input and ejected energy. The transmission function was calculated by taking their ratio averaged over 100 shots. The gain was calculated by dividing the amplified beam ratio by the un-amplified transmission ratio. The results for both glasses are shown in Figure 5.48. A spectrally saturated seed from the OPAs was used for the gain measurements. The small signal gain regime was verified by the double-pass gain obeying the square of the single-pass gain values. Further, all curves increase exponentially with PFN voltage, and show no sign of rollover.

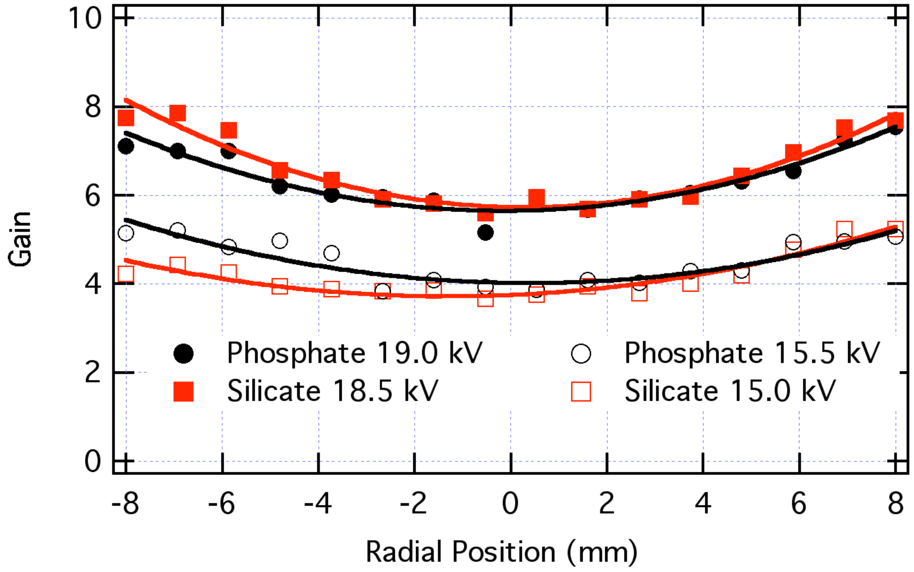

Figure 5.47: Radial gain profile of 19mm glass rods. The markers are data points, and the solid lines are polynomial fits.

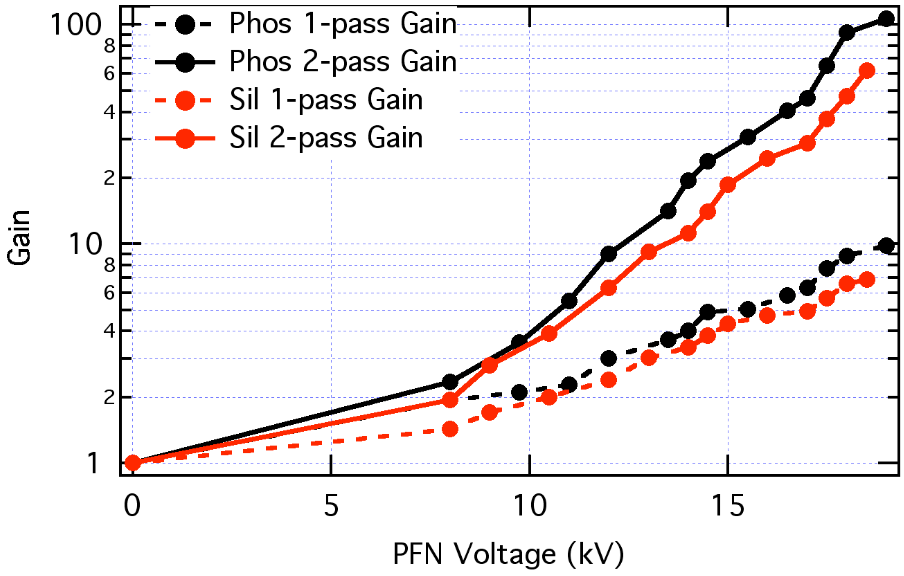

Figure 5.48: Measured single and double-pass small signal gains as a function PFN voltage for the 19 mm Nd:glass heads.

5.4.4 Compressor

Before compression a final vacuum spatial filter resizes the ejected pulse from the glass amplifier. The image plane formed at the output of the amplifier is relayed to inside the vacuum chamber. The final image is formed approximately 75 cm in front of the first grating in the compressor, because spatial constraints prevent the image from being relayed further. The telescope uses a 50 cm primary lens (f/#=10) and a 150 cm secondary lens (f/#=20) to magnify the beam to a diameter of 45 mm ($1/e^2$). A 700 µm pinhole is used to spatially filter the diffraction from the last pass through the phosphate head.

Compression and subsequent transport of the amplified pulse must be done in vacuum to avoid self-phase modulation and B-integral from air. Therefore the 2-grating compressor is housed in custom vacuum tank that accommodates a 5' x 2' optical breadboard. The pulse enters the tank via a fused silica window. The 1740 lines/mm dielectric compressor gratings, manufactured by Lawrence Livermore National Laboratory, are 35 cm wide and 15 cm tall with the rulings parallel to the short axis (Figure 5.49). Both demonstrate >98% diffraction efficiency into the -1 order for s-polarized light at 1057 nm. The s-polarized pulse is incident upon the first grating 4 cm above its centerline. The gratings are rotated to 74.7° to match the stretcher angle. It diffracts away from the first grating at 61° and travels 76 cm to the second grating. The beam then diffracts again from the second grating to a vertical rooftop mirror pair. The rooftop uses two 10x12 cm dielectric mirrors to vertically displace the beam 8 cm down and return the beam for second pass through the grating pair. The pulse exits the compressor 4 cm below the grating center. The measured transmission efficiency is 90%.

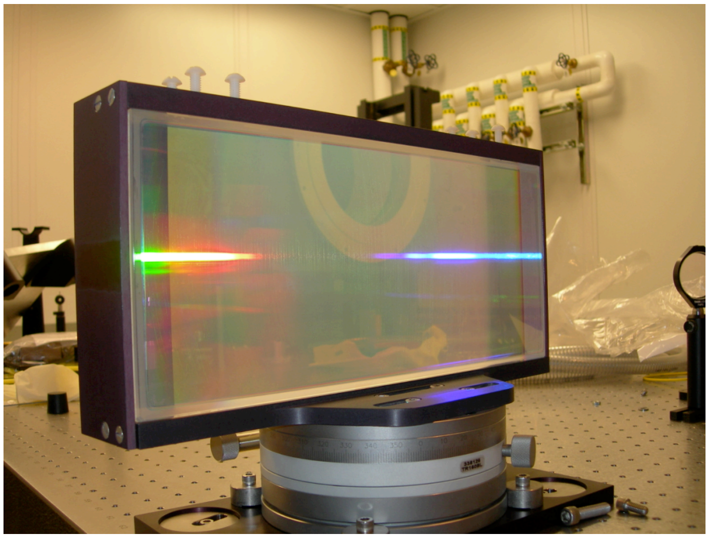

Figure 5.49: Photo of one GHOST dielectric compressor grating. The grating is 35 cm wide by 15 cm tall. The ruling period is 1740 lines/mm.

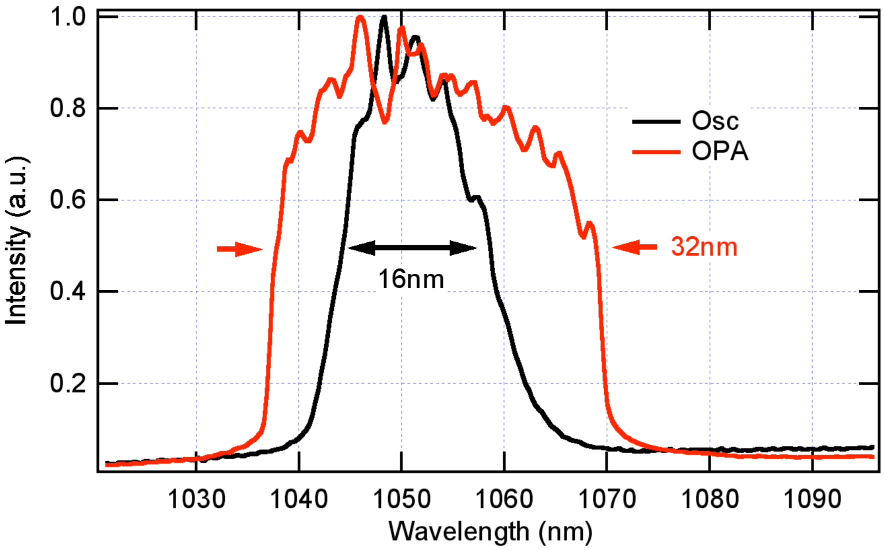

Figure 5.50: OPA amplified seed spectrum measured after the compressor. The pulse is transmitted through the entire laser system, but unamplified by the glass heads.

The compressor is designed to compensate the 63 ps/nm chirp factor of the GHOST stretcher. The 35 cm diameter gratings are oversized for the bandwidth transmitted by the stretcher. As a result, no spectral clipping is observed anywhere in the compressor system (Figure 5.50).

Because of the high groove density and steep angle of incidence, the 1740 lines/mm gratings are extremely subject to compression error if the gratings are not properly aligned. In the double-pass compressor with two gratings, grating parallelism is of extreme importance. Ross et al. showed the recompressed beam will have a pulsefront tilt across the beam caused by nonparallel gratings [24]. The maximum time shift across the beam aperture is given by

$$\delta\tau = \frac{N\lambda L}{c}\tan(\beta)\delta\beta\,. \tag{5.4.1}$$

Here N is the groove density, λ is the central wavelength, L is the length of the grating, β is the diffracted angle, and $\delta\beta$ is the angular deviation between the two compressor gratings. For the GHOST compressor, if the grating parallelism deviates by 26 μrad, the pulsewidth will be broadened by 100 fs. To ensure a high degree of grating parallelism, the compressed pulse was viewed in the far-field using a 2 m focal length lens. Any small error in grating angles will laterally disperse the focused beam.

The *Dispersomatic* simulations in section 5.3.1 indicated the material dispersion of the entire laser could be corrected by increasing the grating angles of the compressor relative to the stretcher by approximately 0.01°. This included 1 meter of BK7 glass to simulate the dispersion of the Nd:glass; however it did not include the nonlinear phase of the OPAs, or the off-axis curved mirror reflection in the stretcher. To facilitate easier pulse compression on GHOST, the stretcher-grating angle was adjusted for 3rd order dispersion correction instead of the compressor gratings. Since the stretcher uses a single grating which is parallel to itself by design, it is more efficient to adjust this angle. In turn, we measured the best pulse compression by decreasing the stretcher angle by 0.25° relative to the compressor.

Figure 5.51 shows a single-shot autocorrelation trace of the amplified OPA spectrum. The pulse is transmitted through the entire laser system to integrate all the material dispersion. The measured pulsewidth of 79.3 fs (FWHM) is found by deconvolving a Gaussian profile. The pulsewidth is 69 fs when using a Sech^2 profile; however neither spectral shape is adequate since the saturated spectrum is highly super-Gaussian. This is confirmed by the expected satellite pulses on the autocorrelation at ± 200 fs. Figure 5.52 plots the same autocorrelation trace with the Fourier-transform of the amplified spectra shown in Figure 5.49. The time-bandwidth product of this pulse is 0.679, and the pulsewidth is within 1 fs of the transform limit for the spectrum.

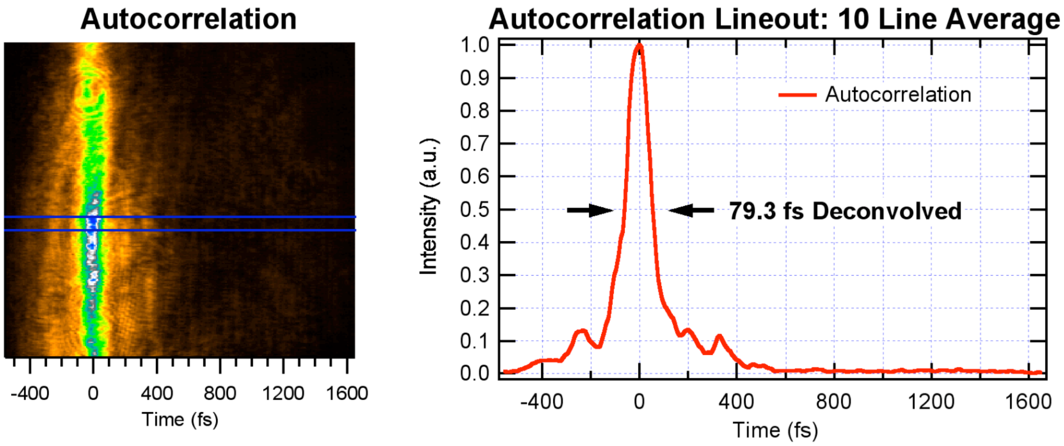

Figure 5.51: Single shot autocorrelation of OPA amplified seed pulse. The pulsewidth is deconvolved from the autocorrelation by assuming a Gaussian-shaped spectrum.

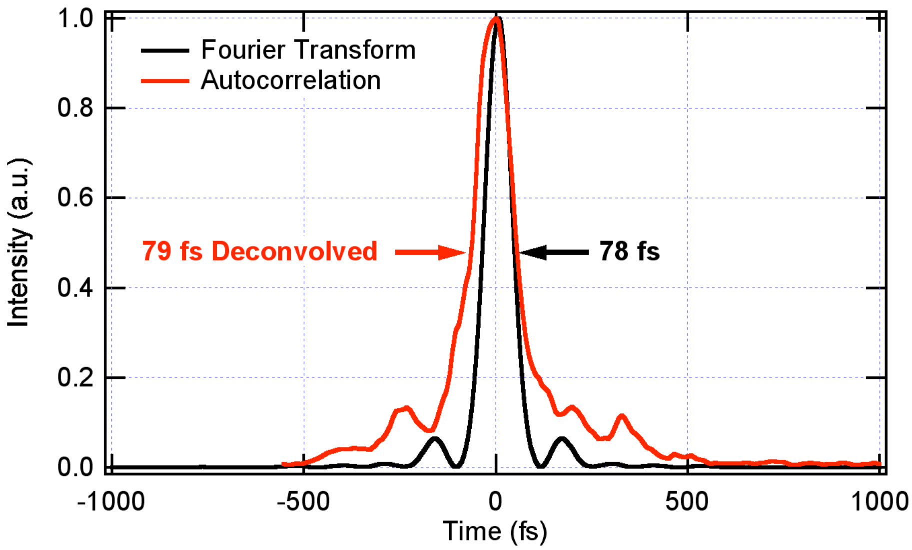

Figure 5.52: Autocorrelation and Fourier transform of OPA amplified seed mode. The autocorrelation is deconvolved assuming a Gaussian profile spectrum.

5.5 Mixed-Glass Amplification

Experiments were performed on the GHOST laser to establish the best gain ratio for mixed-Nd:glass amplifiers in order to produce the broadest amplified spectrum and subsequent shortest compressed pulsewidth. The spectrally saturated seed spectrum from the OPAs was injected into the glass amplifier chain and amplified at various gain ratios. Separate experimental campaigns were run to monitor the amplified spectral bandwidth and the compressed pulse duration at each gain ratio, because equipment limitations prevented simultaneous measurements of both parameters. In each case the total gain was monitored by measuring the amplified energy with a triggered energy meter.

To determine the gain ratio between each glass, high resolution scans of the single and double pass small signal gains were measured in both the phosphate and silicate rods. The spectrally broadened seed with 31 nm of bandwidth (FWHM) was amplified in each rod to determine the broad bandwidth gain factor. Each amplifier was double passed to achieve high gain levels. Thirteen different gain factors were measured in each glass to ensure a high degree of amplification resolution (Figure 5.47). As stated previously, all gain factors are in the small signal regime because of the high saturation fluences of Nd:glasses. The combined calculated gain was determined by multiplying the double-pass gain values for each glass at each PFN setting. The double-pass sequential amplifier geometry of the GHOST laser prevents accurate measurement of the gain per pass in each head during simultaneous operation. To verify the accuracy of this approximation, the amplified energy was measured at every gain ratio perturbation and compared to the calculated gain values.

The first experimental run measured the amplified bandwidth and the total gain as a function of gain ratio. The seed pulse was attenuated to 1 mJ with a neutral density filter before the glass amplifier. The pulse was then amplified at different ratios that netted a constant gain value. The amplified spectrum was monitored by sampling the pulse using an uncoated wedge and a imaging spectrometer. The spectrometer uses a 10 μm slit and a CCD camera with 26 μm pixels to ensure high spectral resolution. The spectra were captured by a triggered frame grabber. The transmitted light through the wedge was then sent to an energy meter to monitor the gain.

The measured amplified spectra for the total gain values of 200 and 260 are contrasted with the simulated values in Figure 5.53. Since saturation is not achieved, the amplifiers exhibit a high degree of shot-to-shot energy jitter. Therefore the amplified spectrum was measured eight times at each gain ratio for statistical purposes. The number of points on each curve was limited by the resolution of the small signal gain values from each glass head. The first item to note is that both measured bandwidth curves are significantly broader than the simulated values. Moreover, the amplified bandwidth increases with increased total gain. The simulated values decrease with increased gain. The increased bandwidth of the measured values could be attributed to a depression at the center of the seed spectrum caused by back-conversion and saturation in the parametric amplifiers. Both the simulated and measured curves demonstrate a bandwidth peak in the gain ratio range of 1 to 10 ($G_{\mathrm{phos}}/G_{\mathrm{sil}}$). Because the total glass gain is relatively small, a broad range of gain ratios spectrally shifts the wavelength center from red to blue while maintaining a similar bandwidth. As to be expected the breadth of the curve peaks diminishes with increased total gain. This is shown more clearly in Figure 5.15, which plots a larger range of simulated amplified bandwidths.

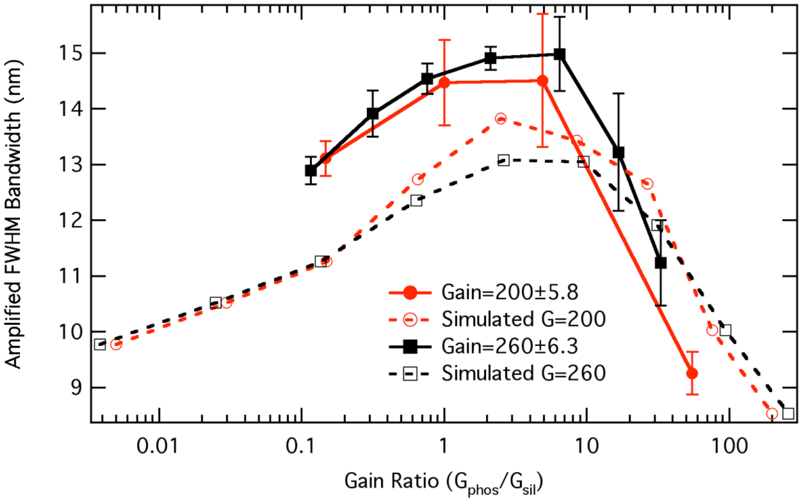

Figure 5.53: Measured and simulated amplified bandwidth with a net gain of 200 and 260 as a function of gain ratio. The measured values are plotted in solid lines, and the simulated values are the dotted lines.

The next experimental run measured the compressed pulsewidth as a function of gain ratio. Using the same experimental setup as the previous data set, a beam splitter was used to monitor simultaneously the amplified energy and to compress the pulse. The low-energy pulses were compressed with the pulse compressor at air, not vacuum. The pulsewidth was measured using a single shot autocorrelator. The autocorrelation was imaged to a CCD camera, and captured with a triggered frame-grabber. The amplified energy was monitored to ensure good experimental agreement with the amplified spectral data. Compressed pulsewidths were measured at every gain ratio perturbation. Figure 5.54 plots the measured and simulated pulsewidths for the same net gains of 200 and 260. Each measured pulsewidth is a single value. The simulated values show very little variance; however a minimum is visible. The measured values are less informative, but they do seem to indicate a minimum occurs in the gain ratio range of 2 to 5 with a minimum pulsewidth of 116 fs. All measured values are at least 10 fs longer than the corresponding simulated values. This could be attributed to self-phase modulation occurring by propagating the compressed pulse approximately 4 meters in air to the autocorrelator. The peak intensities for these pulses exceeded 2 TW in most cases. A further investigation requiring many shots at each point for statistical analysis must be completed to properly ascertain the compressed pulsewidth curves.

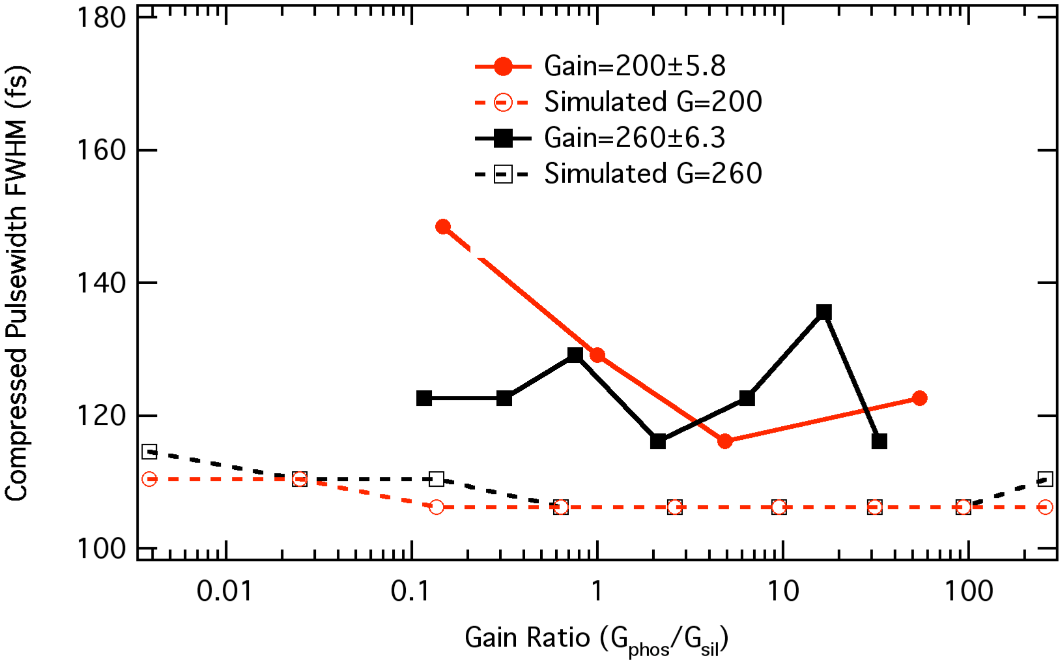

Figure 5.54: Measured and simulated compressed pulsewidth versus gain ratio for gain values of 200 and 260. The measured values are plotted in solid lines, and the calculated values are the dashed lines.

The foremost motivation for the GHOST laser is to examine the operational parameters for the Texas Petawatt laser system. The design specifications for the Petawatt laser call for a minimum gain of 250 from the mixed glass amplifiers. Figure 5.55 summarizes the amplified bandwidths and compressed pulsewidths as a function of gain ratio for a total gain of 260. Both measured and simulated values of the bandwidth indicate that sufficient bandwidth is available for near 100 fs pulsewidths. The preliminary measured compressed pulsewidths clearly show that sub-120 fs are possible. Figure 5.56 plots the corresponding time-bandwidth products for both the measured data and simulations.

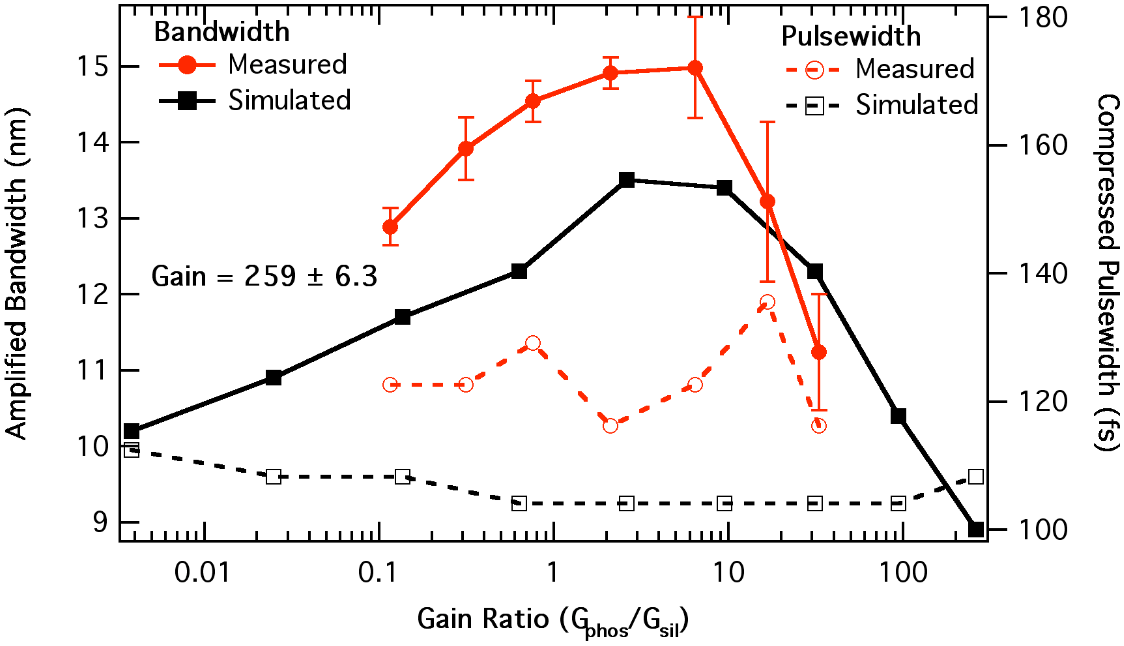

Figure 5.55: Measured and simulated amplified bandwidth and compressed pulse width vs. gain ratio from mixed-glass amplification with a net gain of 259. The pulsewidths and bandwidths at each gain ratio were measured separately.

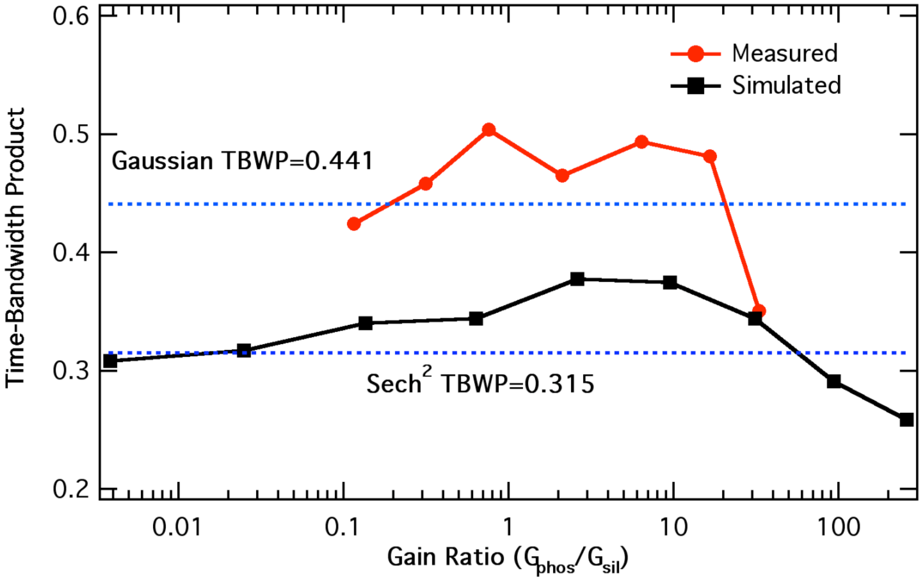

Figure 5.56: Time-bandwidth product of measured and simulated data as function of gain ratio, with net gain of 259.

The shortest duration compressed pulsewidth was measured with a total gain of 283 at a gain ratio of 283 (Figure 5.57). The 109 fs autocorrelation is deconvolved as a Gaussian-profile spectrum. The corresponding time-bandwidth product is 0.430, which is better than the transform limit. When deconvolved as a Sech^2 spectrum, the pulsewidth is 100 fs with a corresponding time-bandwidth product of 0.395. This is 1.25 times larger than the transform limit of 0.315.

This datum is not represented on the prior gain ratio curves, because it did not fall within the specified gain range of $G = 260 \pm 6$. Additionally there were not sufficient similar net gain values at different gain ratios to establish a curve for this point. The asymmetric side pulse on the autocorrelation is attributed to spatial diffraction that occurs from sampling the pulse with small mirrors in the autocorrelator. Further, the autocorrelation is taken at least 8 meters away from the image plane formed before the compressor. The spatial filter pinholes in the last two telescopes are at least 10 times larger than the diffraction limited spot size. They reduce strong diffraction from the rod amplifiers, but they do not fully terminate it. Also the amplified spectrum is taken at the same gain ratio, but it is not the corresponding spectrum to the autocorrelation. These two data points were taken separately. The lineout, which is averaged over 20 lines, is also plotted with the corresponding seed spectrum from the OPAs. The strong depression in the center of the seed spectrum certainly reduces the spectral gain narrowing in the amplifiers by reducing the spectral brightness at the peak of the gain spectrum. Further experiments incorporating an acousto-optic modulator for spectral shaping are slated for the future.

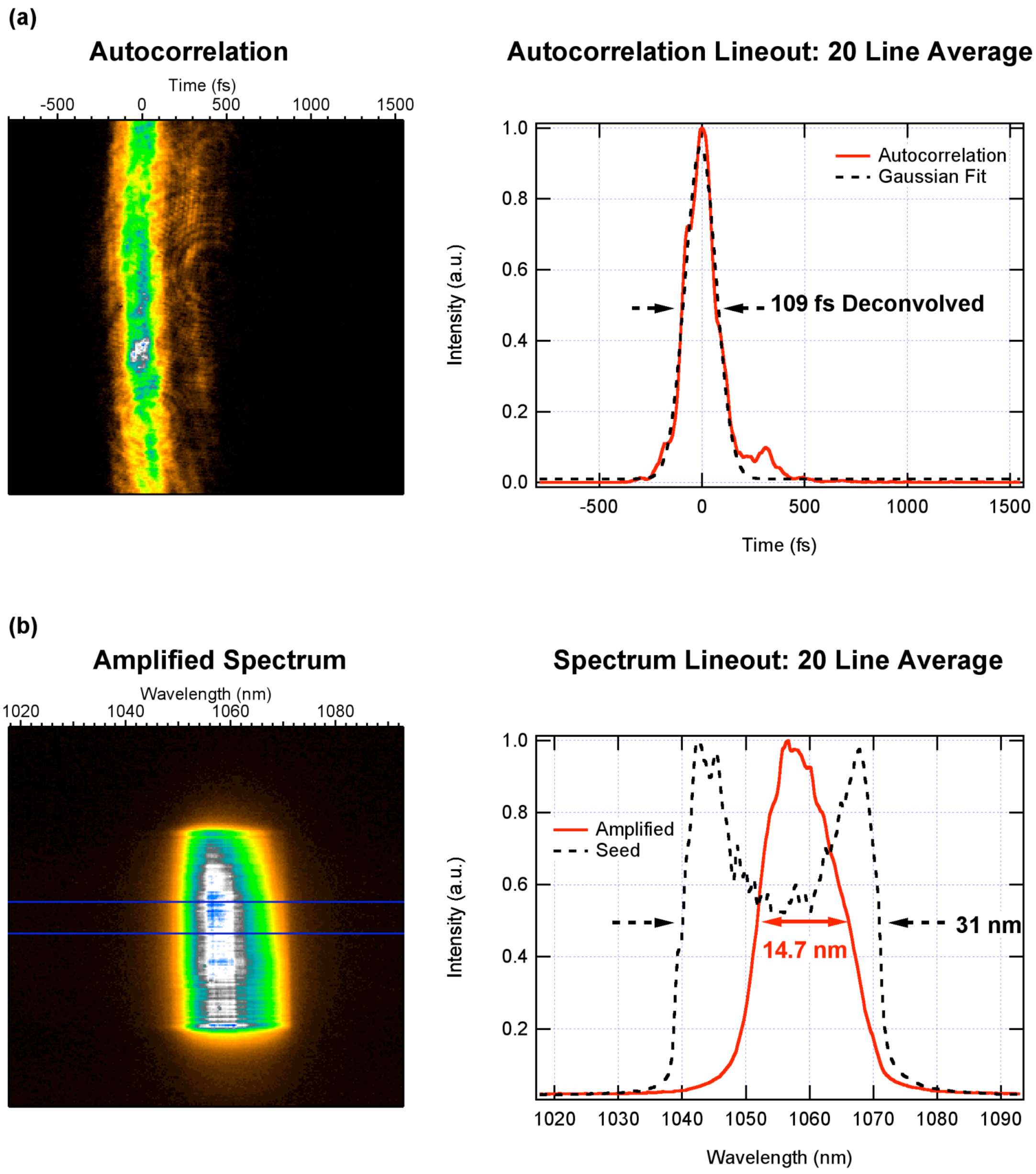

Figure 5.57: Shortest duration pulsewidth for a gain exceeding 250. The calculated gain is 283 with a gain ratio of 3.35:1 (G_{phos}/G_{sil}). a) Autocorrelation and lineout averaged over 20 lines. The pulsewidth is deconvolved by assuming a Gaussian-shaped spectrum. b) Corresponding amplified bandwidth for the same gain ratio. The lineout also plots the seed spectrum into the glass amplifier.

5.6 Summary

In summary the GHOST laser has adequately addressed most of the three questions posed at the beginning of this chapter. The OPAs produce a super-saturated seed spectrum with 31 nm of bandwidth (FWHM) that is amplified to 40 mJ. The pulse also compresses to 79 fs (FWHM), and has a time-bandwidth product of 0.679 when deconvolved as a Gaussian. The mixed-glass amplifiers demonstrate a broad gain ratio range, which varies from 2 to 8 ($G_{\text{phos}}/G_{\text{sil}}$), that produces amplified spectral bandwidths >13.5 nm for gains exceeding 250. Finally seeding the mixed-glass amplifiers with a wavelength center at 1057 nm is sufficient to produce near 100 fs pulsewidths.

Future development on GHOST will determine the energy limit for the glass amplifiers, because the laser is B-integral limited by the nonlinear index of the Nd:glasses. Further experiments will examine closer the compressed pulsewidths as a function of gain ratio. A more rigorous data collection is needed to fully develop these curves. Also investigations using an acousto-optic modulator will be done to examine spectral shaping. Another possibility could be to shift the seed wavelength center to a longer wavelength and re-examine the gain narrowing curves. Preliminary modeling shown in chapter 4 suggests this could significantly improve the compressed pulsewidth.

6 Enhanced Harmonic Generation from Expanding Clusters

Atoms that are illuminated by high-intensity laser radiation with sufficient field strength to ionize, can radiate coherent harmonics of the incident laser frequency. As a result, high harmonic generation (HHG) has produced considerable interest as a possible vehicle for next generation light sources. However advancement of this technology has been primarily limited by low conversion efficiencies below 30 nm ($\leq 10^{-7}$) [1]. Harmonics have been generated from a variety of different media: including molecules [2], gases [1], solids [3], and atomic clusters [4]. Many efforts have sought to improve the overall conversion efficiencies through complex and stringent control of the laser field [5], and by carefully tailoring the interaction media [6]. However atomic clusters provide a unique media for HHG because they demonstrate the combined attributes of solids and gases through long interaction lengths and localized solid densities with high nonlinear susceptibility $\chi^{(n)}$. The following chapter represents an application of a CPA laser system. It also motivates the need for 100 fs laser pulses, like those of GHOST, because of the natural time scale of cluster explosions.

The first demonstration of HHG from clusters showed higher orders could be produced with less saturation than monomer gases [4]; however conversion efficiency and methods to control the process were lacking. Later experiments reported controlled linear absorption resonances ($\chi^{(1)}$) from laser-heated clusters [7, 8], which were interpreted by two different models. In the first case [8], the cluster is treated as a spherical dipole plasma with uniform density, because its diameter is much smaller than the wavelength of the driving laser field [9]. Here the internal electric field of the cluster (E_c) is given by

$$E_c = \frac{3}{|\varepsilon_c + 2|} E_L , \qquad (6.0.1)$$

where E_L is the laser field, and ε_c is the dielectric constant of the cluster described by

$$\varepsilon_c \simeq 1 - \frac{\omega_p^2}{\omega^2} . \qquad (6.0.2)$$

In this case a resonance condition occurs when $\alpha\omega_p = \omega$, where $\alpha = 1/\sqrt{3}$ is a geometric constant produced by the spherical geometry (Figure 6.1). The second model postulated that the cluster expansion is not uniform, thereby producing resonances at the critical density layer ($\omega \simeq \omega_p$) [10].

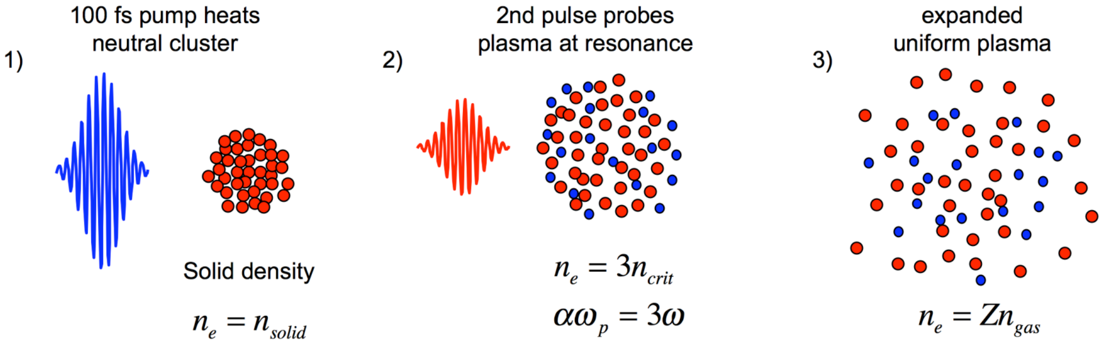

Figure 6.1: 1). A cluster is heated by a short intense pulse and is ionized. 2) A second pulse probes the expanded cluster at a spherical plasma resonance and generates THG. 3). The cluster eventually expands to a uniform plasma.

Subsequent theoretical interpretation of cluster expansion dynamics has suggested that the resonance condition could be extended to high-harmonic generation of odd orders for n=1,3… up to the n^{th} order [11], since the cluster sweeps through many plasma frequencies during the expansion. Further modeling also suggested simultaneous variations of the linear resonant effects could potentially optimize phase matching [12]. However until recently, none of these effects have been demonstrated experimentally. Our efforts have been to measure the dynamics of noble-gas clusters heated by high-intensity laser radiation, using pump-probe experiments to temporally resolve the expansion of the clusters. From these experiments and further analysis we show enhanced third-harmonic generation (THG) from rapidly expanding micro-plasmas of clustered noble gas.

Pump-probe experiments were performed on a pulsed gas jet of argon clusters that was irradiated by intense laser pulses from an ultrafast Ti:sapphire laser. Here a pulsed gas jet is used to form atomic clusters of argon gas. A pump pulse preheats and ionizes the clusters, and then a second pulse is used to probe the plasma at various time delays and produce THG. The laser operated at 10 Hz producing 100 fs pulses at 800 nm with 100 mJ of energy. First a 70/30 beam splitter is used to create two beams for the pump and probe, and an optical delay line was incorporated to time align the two pulses (Figure 6.2). A type I, 1 mm thick KDP crystal, converts the pump beam to the second harmonic at 400 nm, and the unconverted fundamental light is dumped. The energy and polarization of the probe beam is varied using a half-wave plate and thin film polarizer. Each beam is focused individually into the gas jet with a plano-convex lens. The measured focused spot sizes are 40 and 30 μm for the pump and probe respectively. The beams are finally recombined using a dichroic beam splitter and co-propagate into the vacuum chamber.

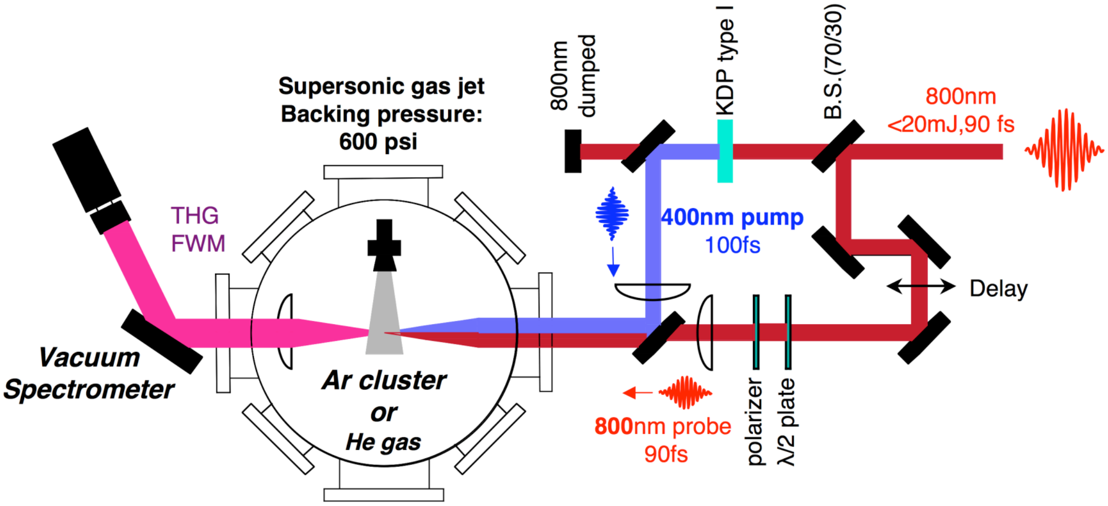

Figure 6.2: Two-color pump probe experimental schematic

The gas jet incorporates a 750 μm aperture with an 11° half angle expansion nozzle. The gas jet is pressurized to 600 psi with Ar gas with an opening time of 2 ms. The average density, which was determined using a Mach-Zehnder interferometer, was measured to be 10^{18} cm^{-3}. Under these conditions, approximately 20% of the emitted gas condenses to clusters, leaving the remainder as monomers [13].

Nonlinear interactions within the gas jet create two sources for radiation at the third harmonic of the probe pulse. In the first case, third harmonic is created directly by the probe through

$$E_{THG}^{3\omega} \propto \chi^{(3)}[E_{probe}^{\omega}]^3, \tag{6.0.3}$$

and is present at all time delays. In the second case, the third harmonic is created by four-wave mixing (FWM) of the pump and probe only during temporal overlap of the two pulses. Here two photons of the pump combine with one photon of the probe by

$$E_{FWM}^{3\omega} \propto \chi^{(3)}[E_{pump}^{2\omega}]^2[E_{probe}^{\omega}]. \tag{6.0.4}$$

In order to spatially separate the two processes, the pump and probe beams were crossed at 2° within the gas jet plume (Figure 6.3). Therefore momentum conservation demands that each of the two signals propagate in different directions, thus allowing the FWM signal to be blocked after the interaction region. The THG signal was collected using and *f*/4 lens and imaged to the entrance slit of a spectrometer for spectral discrimination. The THG pulse intensity was then measured at the output of the spectrometer using a amplified photo-multiplier tube, which incorporated a 266 nm bandpass filter for further wavelength discrimination. Initially the beams were crossed at the center of the gas jet plume where the highest cluster density exists. However strong probe absorption from the long optical path length through the ionized gas squelched the THG at later time delays ($\Delta t \geq 300\,\text{fs}$). Therefore the interaction region was translated to an off-center chord of the plume, approximately 2mm away from the center. Here the interaction length of the beams with the gas jet was approximately 1 mm, which also matched the spatial overlap of the pump and probe beams. Also the earlier quoted average density of 10^{18} cm^{-3} was measured at this location. The probe absorption was measured with an energy meter placed at the throughput of the cluster plume outside of the vacuum tank. For all the experiments the pump intensity was maintained at 10^{15} W/cm^2, which is above the ionization threshold for argon, and the probe intensity was varied from 2×10^{13} to 8×10^{15} W/cm^2.

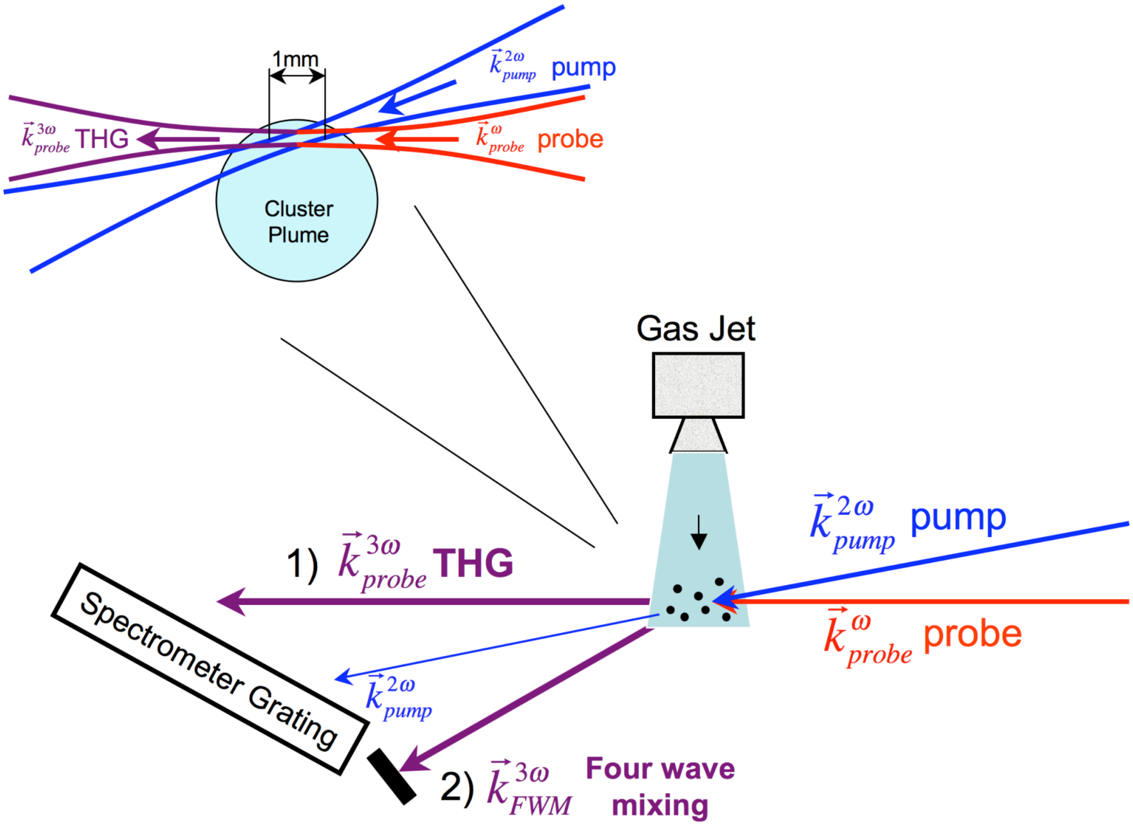

Figure 6.3: Non-collinear pump-probe geometry with momentum conservation. The inset image shows the off-center chord alignment of the pump and probe in the gas jet plume.

Preliminary experiments were performed with the gas jet backed with helium gas at similar average density to establish a baseline from a non-clustering medium. In this case, no linear absorption or THG enhancement was measured at any time delay. However, 3ω created from FWM mixing was detected at times when the pump and probe were temporally overlapped (Figure 6.4) [14]. The enhancement lasts for >200 fs, and is caused by the temporal overlap of the 100 fs (FWHM) pump and probe beams.

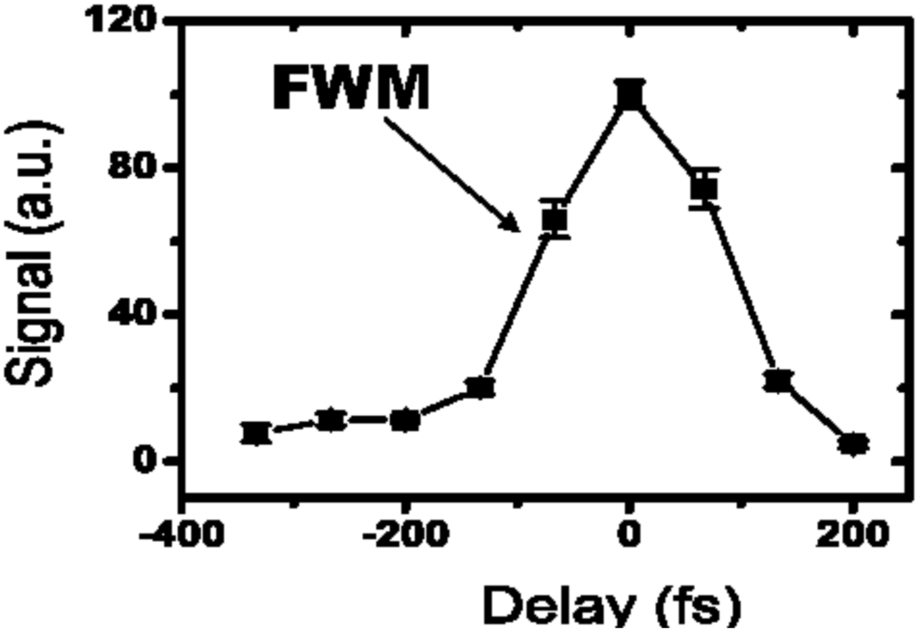

Figure 6.4: 3ω from four-wave mixing (FWM) of pump and probe pulses from He gas with 10^{18} cm^{-3} average density. (image courtesy of B. Shim)

Figure 6.5 [15] shows the time evolution of the probe-generated third harmonic and the probe absorption from laser-heated argon clusters at weak probe intensity (2×10^{13} W/cm^2). The probe and pump polarizations were aligned parallel. The simulated probe absorption (red line) predicts a weak early linear resonance at $\Delta t < 0$ when the pump initially ionizes the plasma. However this is not seen in the measured data, because the signal was either too small to detect and/or the 100 fs probe was unable to resolve the short-duration event. During this time, ionization is occurring on the rising edge of the pump pulse and is rapidly heating the cluster before expansion can occur. The initial ionization rapidly sweeps the plasma frequency (ω_p) through the linear resonance of $\alpha\omega_p = \omega$. At $\Delta t > 400$ fs the clusters show a strong linear resonance that last for 2 to 3 ps, and subsequently decay as the cluster expands and cools. This is in excellent agreement with the simulation, which is based upon the uniform-density model. The THG signal also shows an early time resonance at $\Delta t \sim -100\,\text{fs}$. Again this enhancement occurs at the initial onset of cluster ionization as the plasma frequency sweeps through $\alpha\omega_p = 3\omega$. No THG enhancement is measured at $\Delta t > 0$, because the most of the cluster is not ionized.

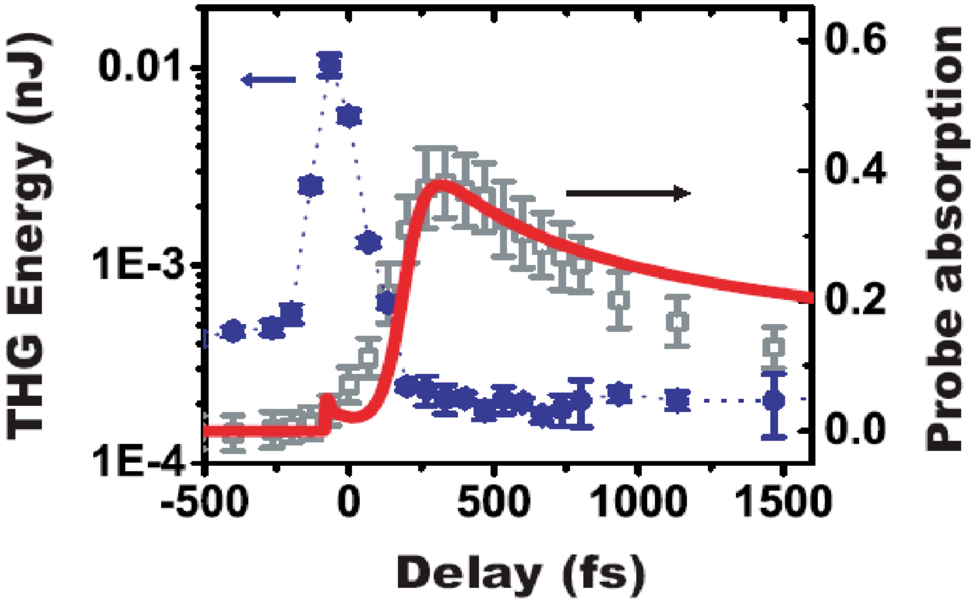

Figure 6.5: THG (filled circles) by and absorption (open squares) of a weak probe ($2\text{x}10^{13}$ W/cm^2), following pump excitation at 10^{15} W/cm^2 with parallel pump and probe polarization. Identical absorption is observed with orthogonal polarizations. Solid curve is calculated from uniform density model; dashed curve connects the THG data points. Each data point represents a 300 shot average. (image courtesy of B. Shim)

Figure 6.6a [15] shows the time-evolutions of the probe THG as a function of probe intensity. First to note is that the enhancement seen at $\Delta t \sim -100\,\mathrm{fs}$ increases as $[I_{probe}]^3$ up to 10^{14} W/cm^2, where it saturates because of probe self-ionization within the cluster (fig. 6.4b). Consequently this intensity is the ionization threshold for argon. As the probe intensity begins to exceed 10^{14} W/cm^2, a delayed time peak ($\Delta t \sim 250\,\mathrm{fs}$) grows rapidly and exceeds the first enhancement by more than five times. This peak scales with the probe intensity (fig. 6.4b) up to where it is equivalent to the pump intensity ($I_{probe} \approx I_{pump} \approx 10^{15}\,\mathrm{W/cm^2}$). Also noted is that the delayed THG enhancement truncates at $\Delta t > 300\,\mathrm{fs}$ as the probe absorption begins to rise. The possibility of the delayed enhancement being caused by pump-induced probe-focusing [16] was eliminated by imaging the probe mode to a CCD camera and monitoring the spot size as a function of temporal delay. The mode size varied less than 10% at any temporal delay. Further, by accounting for increased probe absorption, the probe intensity actually decreased by a factor of two from $0 \leq \Delta t \leq 300$ fs. All of these measurements lead to the conclusion that the measured THG enhancement is caused by either an increase in the third-order nonlinear susceptibility ($\chi^{(3)}$) and/or an increase in the THG coherence length.

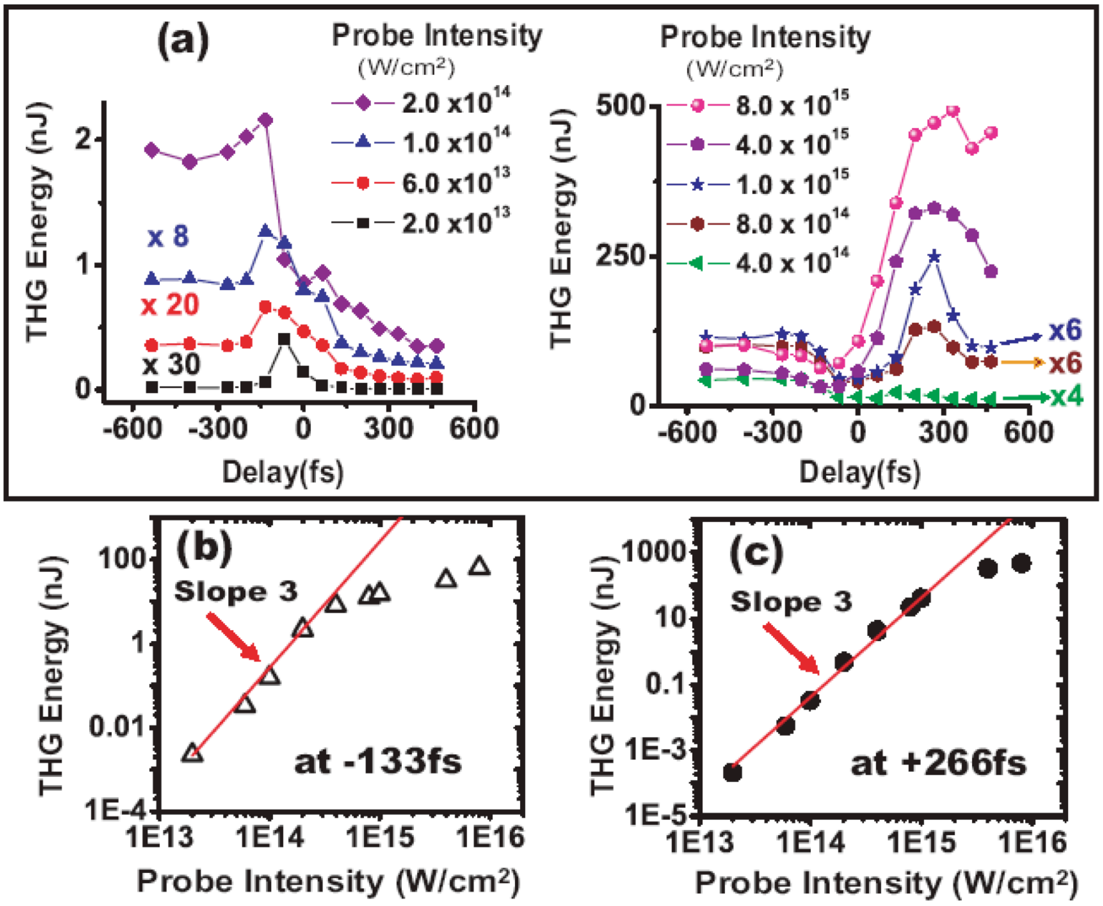

Figure 6.6: (a) Time-dependent, probe THG from clustered Ar jet for pump intensity 10^{15} W/cm^2, for various probe intensities with parallel pump-probe polarizations. Lower panels: I_{probe}-dependence of (b) early THG peak and (c) delayed THG peak, compared to I^3_{probe}. (image courtesy of B. Shim)

When the probe polarization was rotated perpendicular to the pump polarization, we measured a $2\times$ increase in the THG at $\Delta t \sim 300\,\mathrm{fs}$ along with an increase in the enhancement duration (Figure 6.7) [15]. However at $\Delta t < 0$ and $\Delta t \geq 600\,\mathrm{fs}$, the THG enhancement remained isotropic with polarization. At the early time delay during the onset of ionization, the clusters have not yet expanded, and at the later delay, the clusters are expanding to form a uniform plasma.

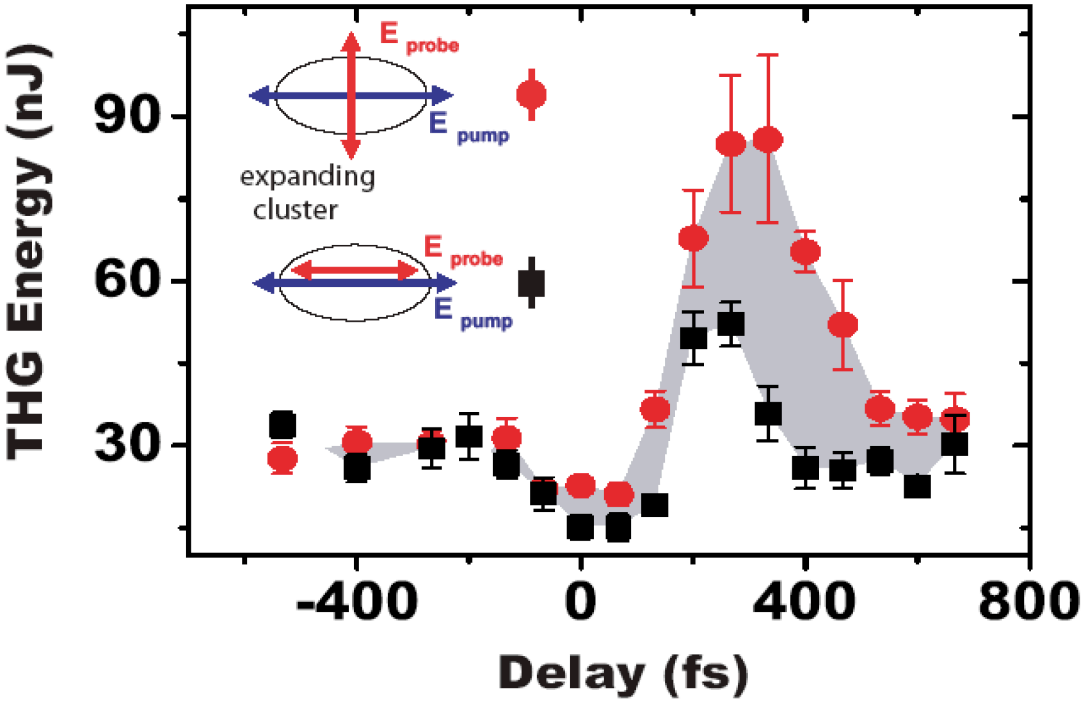

Figure 6.7: Anisotropy of THG from expanding clusters, with pump and probe both at 10^{15} W/cm^2 with parallel (filled squares) or perpendicular (filled circles) polarizations. Each THG data point represents a 100 shot average. Gray shading highlights the region of transient anisotropy. (image courtesy of B. Shim)

Anisotropic $\chi^{(3)}$ responses have been observed previously in unclustered plasmas [17, 18]. Further, anisotropic ion and electron emission from large clusters have also been reported [19, 20] and theoretically simulated [21, 22]. However, to our knowledge, this is the first measurement of harmonic generation anisotropy from hydrodynamically exploding clusters. Kumarappan *et al.* [20], claim the higher polarization pressure from the laser causes the cluster to expand faster in the driving laser polarization direction. Breizman *et al.* [21], suggest that polarization dependent vacuum heating by the pump accompanied by collisional absorption should generate an anisotropic electron pressure that is higher along the axis of the pump field. As a result, ion acceleration driven by this pressure becomes anisotropic, causing the cluster to become ellipsoidal with the major axis along the pump polarization. Therefore the stronger density gradients along the minor axis will cause electrons in the cluster to experience a stronger nonlinear force, thereby generating more third harmonic from the orthogonally polarized probe. This is shown more clearly in the inset of Figure 6.6. This configuration should also be optimum for higher order harmonic generation.

Shim *et al.* [15] simulated the results of these experiments by examining the time evolutions of the complex phase mismatch function ($J_{3\omega}(L)$) and the third order nonlinear susceptibility ($\chi^{(3)}$) using the uniform density model (Figure 6.8). To model the phase mismatch function they examined the refractive indices within the gas jet, which included contributions from the cluster, plus ionized and un-ionized monomers. Their results found $n_{jet}(\omega)$ and $n_{jet}(3\omega)$ initially diverge upon ionization, then partially re-converge at $\Delta t \approx 250$ fs, where the measured delayed THG enhancement occurs. As a result, $J_{3\omega}(L)$ also shows an initial decrease during initial ionization (fig. 6.7a), illustrating that the ionized cluster is less phase-matched than the ionized cluster. However, $J_{3\omega}(L)$ shows a small increase at $\Delta t = 250$ fs where $n_{jet}(\omega)$ and $n_{jet}(3\omega)$ re-converge. This increase in $J_{3\omega}(L)$ contributes to the delayed peak enhancement, but cannot explain by itself the stronger THG for ionized clusters over unionized. Their calculations also indicate that perfect phase matching, *i.e.,* $n_{jet}(\omega) = n_{jet}(3\omega)$, is possible at $\Delta t \approx 250$ fs if the gas jet contains ~80% clusters. Further studies using a cryogenically cooled gas jet could possibly generate these conditions. Their simulation of $\chi^{(3)}$ (fig.

6.7a (solid curve)) also shows a large enhancement occurring at $\Delta t \approx 260\,\text{fs}$, which is almost simultaneous with the increased phase matching. Figure 6.7b plots the simulated time-evolution of the THG as a function of probe intensity, which is in excellent agreement with the measured values of the delayed THG.

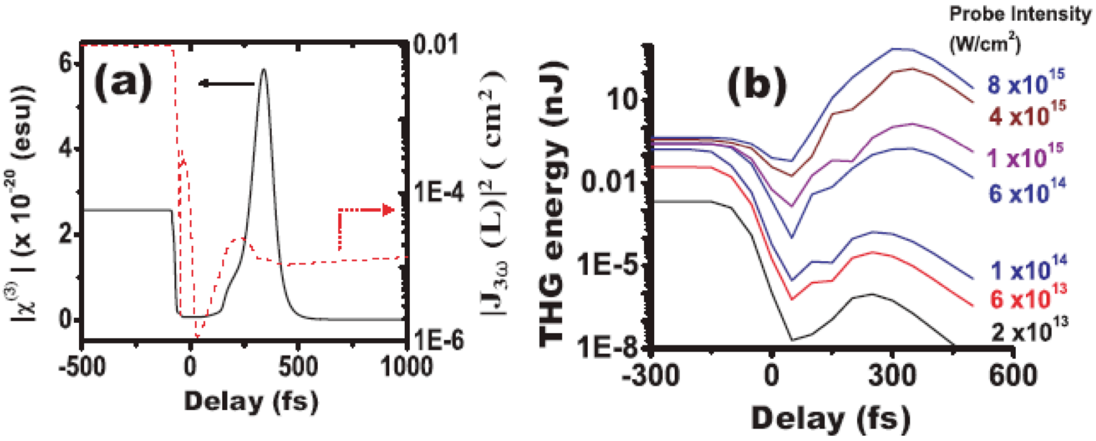

Figure 6.8: Results of calculations for gas jet with 10^{18} cm^{-3} atomic density (85% monomers +15% clusters) following excitation by 10^{15} W/cm^2, 400 nm, 100 fs pump: (a) time-dependent phase-mismatch function $|J_{3\omega}(L)|^2$ (dashed curve) and $|\chi^{(3)}|$ (solid curve); (b) time-dependent THG by 800 nm probe pulses of indicated intensities. (image courtesy of B. Shim)

In conclusion, we have measured delayed enhancement of THG from hydrodynamically expanding, laser-heated noble gas clusters. Our results show THG increases with probe intensity (I_{probe}) without saturation up to the order of the pump intensity at 10^{15} W/cm^2. Further, THG also illustrates the clusters expand anisotropically. Simulations demonstrate an increase in third-order nonlinear susceptibility ($\chi^{(3)}$) and the phase-mismatch function ($J_{3\omega}(L)$) both contribute to the delayed enhancement. These results should scale to higher order harmonic production. Future experiments will examine harmonics for n>3. Here $\chi^{(n)}$ and $J_{n\omega}(L)$ are expected at earlier times, where the probe will experience less absorption. Also fully phased-matched HG may be possible by increasing the cluster/monomer ratio to 0.8 through the application of a cryogenically cooled gas jet.

7 Conclusion

The goal of this thesis has been to investigate both novel and established broad-bandwidth laser media for chirped-pulse amplification. The primary emphasis has been to exploit fully current technologies to produce higher intensities through shorter pulsewidths and stringent spectral management. We have presented two state-of-the-art laser systems that each push the limits of spectral bandwidth for their host laser medium. Further, we have sought to establish new techniques that produce high-energy short pulse lasers with peak intensities that extend well beyond the boundaries of current lasers. Finally, we have measured enhanced harmonic generation from laser-heated clusters. The results of these experiments are scalable to higher order harmonics with possible applications for next generation light sources.

The first laser presented is representative of the most mature form of high-intensity CPA technology today. The THOR laser is Ti:sapphire based laser system that operates at 10 Hz and produces 38 fs pulses with peak intensities up to 18.4 TW. The laser operates near the bandwidth limit of the medium with a 0.49 time-bandwidth product. For this system, we have also presented one and two dimensional energetics simulations that accurately describe the pulse amplification throughout the laser system. While the one-dimensional model accurately simulates the laser energetics, the two-dimensional model more accurately shows the spatio-temporal evolution of the pulse.

The GHOST laser was presented as a proof-of-technology laser for the Texas Petawatt Laser, now being constructed at the University of Texas at Austin. Through the smaller and higher repetition rate GHOST laser, we have been able to accurately establish operation parameters for the Petawatt system. We have shown that broad-bandwidth pulses (>30nm FWHM) can be efficiently amplified at high gains (>10^7) with full spectral saturation in an OPCPA amplifier. Further, optimum gain ratios for mixed-glass amplification have been established through both the laboratory and numerical simulations. The results of which show 2 to 8 times more gain in Nd:phosphate over Nd:silicate will produce the broadest amplified spectra when seeded at 1057 nm with a gain factor of 250 to 300. Most importantly we have demonstrated that ultrashort pulses (≥ 100 fs) can be generated with modest gain from Nd:glass amplifiers.

To further stretch the boundaries of mixed-glass amplification, we have also presented calculations for two novel broad-spectrum laser glasses. If these glasses would become commercially available, implementation of either the Nd:aluminate or the Nd:tantalum/silicate laser glasses in mixed-glass architecture could immediately extend current high-intensity laser systems to the multi-petawatt level with near 100 fs pulsewidths. With further development of current grating and OPCPA technologies, our calculations also suggest a mixed-glass exawatt laser system is possible.

Finally we have demonstrated delayed enhancement of THG from a noble gas jet of hydrodynamically expanding clusters heated by an ultrashort pump pulse. THG polarization dependence shows the clusters expand anisotropically, while I_{probe} shows little saturation up to the pump intensity. Further, modeling shows that the third order nonlinear susceptibility $\chi^{(3)}$ of individual clusters and the coherence length of the clustered plasma optimize nearly simultaneously as the preheated clusters expand. Both contribute to the delayed enhancement.

7.1 Future Work and Experiments

This section is offered as a suggestion for further research and/or provides closing remarks for the various areas investigated within this thesis. Several of the technologies that have been presented are now mature and well established, while others are simply unavailable at present for further analysis. Therefore only a few closing remarks will be offered in these areas. However possibilities for subsequent research on GHOST and harmonic generation are presented.

7.1.1 Ti:sapphire based CPA lasers

As stated previously, Ti:sapphire is the most widely used broad-bandwidth media used in CPA laser design. It has single-handedly ushered in a new era of laser research, and has applications that extend to nearly all regions of contemporary science. The growth and application of this media has been phenomenal. Using the THOR laser as an example, what was state-of-the-art seven years ago, is now commercial and almost commonplace. Similar laser systems are available from several vendors and can be found in physics, chemistry and biology laboratories worldwide. Current and future CPA developments on this material will continue to be twofold: production of rep-rated high-intensity laser systems (>100 TW) entirely comprised of Ti:sapphire [130], or further development of higher average power lasers with more modest energies [131]. In either case, advancement is dependent upon pump laser development.

7.1.2 GHOST and future Experiments

Future development on the GHOST will further analyze operational parameters for the Texas Petawatt Laser. A more detailed investigation of compressed pulsewidth versus gain ratio will be of top priority. While the results shown here clearly indicate sufficient bandwidth for near 100 fs pulsewidths are achievable from mix-glass amplifiers, further analysis on pulse compression is needed. Also since the laser is B-integral limited by the glass amplifiers, the operational energy limit for this system must be determined by comparing the amplified compressed pulsewidth to the total energy extracted from the main amplifiers. As nonlinear effects become prevalent, these effects will immediately be transmitted to the compressed pulsewidth.

Further experimental avenues to be investigated could be to examine spectral shaping for seeding the mixed-glasses. Preliminary simulations shown in chapter 4 suggest that by shifting the seed wavelength center to 1065 nm could substantially improve the compressed pulsewidth. Also spectral shaping of the seed pulse using an acousto-optic modulator might prove valuable; however strong spectral saturation from the parametric amplifiers may limit the enhancements. Even though it is costly and difficult, spectral shaping of the seed could be accomplished in the OPAs by temporal shaping of the pump pulse. Arbitrary waveform generators are routinely used to defeat square-pulse distortion in many high gain pump lasers [27].

7.1.3 Mixed-Glasses

If these novel laser glasses can be manufactured in small batch quantities, immediate applications could develop compact and energetic multi-TW laser systems with direct amplification solely in glass. This would dramatically reduce complexity and cost when compared to similar high-energy, low repetition rate Ti:sapphire systems. The most critical obstacle in developing novel broad-spectrum laser glasses is the inability to have them manufactured. Even though laser glasses are widely used in many large-scale laser facilities, they remain a niche market for most vendors. However petawatt laser facilities are being constructed all over the world, proving an increased interest in Nd:glasses. Even though multi-petawatt lasers (≥2 PW) have yet to be demonstrated, there is already published work considering design and applications of exawatt laser systems [132-134].

7.1.4 Enhanced Harmonic Generation from Laser-Heated Clusters

We are currently exploring the scalability of the delayed THG enhancement to harmonic orders of $n>3$. Here $\chi^{(n)}$ and $J_{n\omega}(L)$ are expected at earlier times, where the probe absorption is weaker. Our simulations also indicate perfect phase matching is possible for a gas jet with ~80% clusters and 20% monomers. Therefore future work will look to produce large-scale clusters (~80 nm) from a cryogenically cooled gas jet by condensing the expanding gas more completely. Even though linear absorption resonances will be stronger and occur earlier for larger scale clusters, the phase matching a nonlinear susceptibility enhancement should also occur before the peak of the probe absorption.

7.2 Conclusions

It seems hardly fathomable that chirped-pulse amplification was first demonstrated a mere two decades ago. Short-pulse, high-intensity lasers and their applications have revolutionized modern physics, chemistry and biology research more than any other technology in the last 20 years. CPA has been arguably the most important technology and application to pulsed lasers since the advent of the Q-switch. One can only postulate where the limits of this technology lie, but the next decade should realize operational multi-petawatt lasers and marked progress towards exawatt intensities.

References

1. T.H. Maiman, "Stimulated optical radiation in ruby," Nature **187**, 493 (1960).

2. R.J. Collins, D.F. Nelson, A.L. Schawlow, W. Bond, C.G.B. Garrett, and W. Kaiser, "Coherence, narrowing, directionality, and relaxation oscillations in the light emission from ruby," Phys. Rev. Lett. **5**, 303-305 (1960).

3. P.A. Franken, A.E. Hill, C.W. Peters, and G. Weinrich, "Generation of optical harmonics," Phys. Rev. Lett. **7**, 118-119 (1961).

4. J.A. Armstrong, N. Bloembergergen, J. Ducuing, and P.S. Pershan, "Interactions between Light Waves in a Nonlinear Dielectric," Phys. Rev. **127**, 1918-1939 (1962).

5. D.A. Kleinman, "Theory of second harmonic generation of light," Phys. Rev. **128**, 1761-1775 (1962).

6. F.J. McClung and R.W. Hellwarth, "Giant optical pulsations from ruby," J. Appl. Phys. **33**, 828-829 (1962).

7. D. Strickland and G. Mourou, "Compression of Amplified Chirped Optical Pulses," Opt. Commun. **55**, 447-449 (1985).

8. P. Maine, D. Strickland, P. Bado, M. Pessot, and G. Mourou, "Generation of Ultrahigh Peak Power Pulses by Chirped Pulse Amplification," IEEE J. Quant. Elec. **24**, 398-403 (1988).

9. F.G. Patterson, R. Gonzales, and M.D. Perry, "Compact 10-Tw, 800-Fs Nd-Glass Laser," Opt. Lett. **16**, 1107-1109 (1991).

10. E.B. Treacy, "Optical Pulse Compression with Diffraction Gratings," IEEE J. Quant. Elec. **QE-5**, 454-458 (1969).

11. P.F. Moulton, "Spectroscopic and Laser Characteristics of Ti-Al2o3," J. Opt. Soc. Am. B **3**, 125-133 (1986).

12. D.E. Spence, P.N. Kean, and W. Sibbett, "60-fsec Pulse Generation from a Self-Mode-Locked Ti:sapphire Laser," Opt. Lett. **16**, (1991).

13. O.E. Martinez, "3000 Times Grating Compressor with Positive Group-Velocity Dispersion - Application to Fiber Compensation in 1.3-1.6 mm Region," IEEE J. Quant. Elect. **23**, 59-64 (1987).

14. C.P.J. Barty, C.L. Gordon, and B.E. Lemoff, "Multiterawatt 30-fs Ti-Sapphire Laser System," Opt. Lett. **19**, 1442-1444 (1994).

15. J.P. Chambaret, C. LeBlanc, G. Cheriaux, P. Curley, G. Darpentigny, P. Rousseau, G. Hamoniaux, A. Antonetti, and F. Salin, "Generation of 25-TW, 32-fs pulses at 10 Hz," Opt. Lett. **21**, 1921-1923 (1996).

16. T. Ditmire, H. Nguyen, and M.D. Perry, "Design and Performance of a Multiterawatt Cr-Lisralf6 Laser System," J. Opt. Soc. Am. B **11**, 580-590 (1994).

17. M.D. Perry and G. Mourou, "Terawatt to Petawatt Subpicosecond Lasers," Science **264**, 917-924 (1994).

18. M.D. Perry, and Shore, B. W., "Petawatt Laser Report," M.D. Perry, ed. (Lawrence Livermore National Laboratory, 1996).

19. J.D. Bonlie, F. Patterson, D. Price, B. White, and P. Springer, "Production of > 10(21) W/cm(2) from a large-aperture Ti:sapphire laser system," Appl. Phys. B-Lasers O **70**, S155-S160 (2000).

20. B.C. Stuart, M.D. Perry, J. Miller, G. Tietbohl, S. Herman, J.A. Britten, C. Brown, D. Pennington, V. Yanovsky, and K. Wharton, "125-TW Ti:sapphire/Nd:glass laser system," Opt. Lett. **22**, 242-244 (1997).

21. C. Rouyer, E. Mazataud, I. Allais, A. Pierre, S. Seznec, C. Sauteret, G. Mourou, and A. Migus, "Generation of 50-Tw Femtosecond Pulses in a Ti-Sapphire/Nd-Glass Chain," Opt. Lett. **18**, 214-216 (1993).

22. N. Blanchot, C. Rouyer, C. Sauteret, and A. Migus, "Amplification of Sub-100-TW Femtosecond Pulses by Shifted Amplifying Nd-Glass Amplifiers - Theory and Experiments," Opt. Lett. **20**, 395-397 (1995).

23. R. Danielius, A. Piskarskas, D. Podenas, and A. Varanavicius, "Broad-Band Nd Glass Regenerative Amplifier with Combined Active Medium," Opt. Commun. **84**, 343-345 (1991).

24. I.N. Ross, M. Trentelman, and C.N. Danson, "Optimization of a chirped-pulse amplification Nd:glass laser," Appl. Opt. **36**, 9348-9358 (1997).

25. I.N. Ross, P. Matousek, M. Towrie, A.J. Langley, and J.L. Collier, "The prospects for ultrashort pulse duration and ultrahigh intensity using optical parametric chirped pulse amplifiers," Opt. Commun. **144**, 125-133 (1997).

26. I. Jovanovic, B.J. Comaskey, C.A. Ebbers, R.A. Bonner, D.M. Pennington, and E.C. Morse, "Optical parametric chirped-pulse amplifier as an alternative to Ti : sapphire regenerative amplifiers," Appl. Opt. **41**, 2923-2929 (2002).

27. E.W. Gaul, T. Ditmire, M. Martinez, S. Douglas, D. Gorski, W. Henderson, G. Hays, A. Erlandson, J.A. Caird, I. Jovanovich, C. Ebbers, and W. Molander, "Design of the Texas Petawatt Laser," in *CLEO/QELS/PHAST 2005*, (Optical Society of America, Washington, D.C., Baltimore, 2005), pp. 100-102.

28. A. McPherson, T.S. Luk, B.D. Thompson, A.B. Borisov, O.B. Shiryaev, X. Chen, K. Boyer, and C.K. Rhodes, "Multiphoton Induced X-Ray-Emission from Kr Clusters on M-Shell (Similar-to-100-Angstrom) and L-Shell (Similar-to-6-Angstrom) Transitions," Phys. Rev. Lett. **72**, 1810-1813 (1994).

29. T. Tajima, Y. Kishimoto, and M.C. Downer, "Optical properties of cluster plasma," Phys. Plasmas **6**, 3759-3764 (1999).

30. J.W.G. Tisch, "Phase-matched high-order harmonic generation in an ionized medium using a buffer gas of exploding atomic clusters," **6204**, (2000).

31. T. Ditmire, J. Zweiback, V.P. Yanovsky, T.E. Cowan, G. Hays, and K.B. Wharton, "Nuclear fusion in gases of deuterium clusters heated with a femtosecond laser," Phys. Plasmas **7**, 1993-1998 (2000).

32. O.F. Hagena and W. Obert, "Cluster Formation in Expanding Supersonic Jets: Effect of Pressure, Temperature, Nozzle Size, and Test Gas," J. Chem Phys. **56**, 1793-1802 (1972).

33. T. Ditmire, R.A. Smith, J.W.G. Tisch, and M.H.R. Hutchinson, "High intensity laser absorption by gases of atomic clusters," Phys. Rev. Lett. **78**, 3121-3124 (1997).

34. T. Ditmire, T. Donnelly, A.M. Rubenchik, R.W. Falcone, and M.D. Perry, "Interaction of intense laser pulses with atomic clusters," Phys. Rev. A **53**, 3379-3402 (1996).

35. J. Zweiback, T. Ditmire, and M.D. Perry, "Femtosecond time-resolved studies of the dynamics of noble-gas cluster explosions," Phys. Rev. A **59**, R3166-R3169 (1999).

36. M. Pessot, P. Maine, and G. Mourou, "1000 Times Expansion Compression of Optical Pulses for Chirped Pulse Amplification," Opt. Commun. **62**, 419-421 (1987).

37. S. Backus, C.G. Durfee, M.M. Murnane, and H.C. Kapteyn, "High power ultrafast lasers," Rev. Sci. Instrum. **69**, 1207-1223 (1998).

38. D.N. Fittinghoff, B.C. Walker, J.A. Squier, C.S. Toth, C. Rose-Petruck, and C.P.J. Barty, "Dispersion considerations in ultrafast CPA systems," IEEE J. Sel. Top. Quant. **4**, 430-440 (1998).

39. J.C. Diels and w. Rudolf, *Ultrashort laser pulse phenomena: fundimentals, techniques, and applications on a femtosecond time scale* (Academic Press, San Diego, CA, 1996).

40. T. Ditmire,"Soft X-ray Generation in Gases with an Ultashort Pulse Laser,"Ph.D. Thesis, University of California Davis, 1996.

41. S.D. Brorson and H.A. Haus, "Diffraction Gratings and Geometrical-Optics," J. Opt. Soc. Am. B-Opt. Phys. **5**, 247-248 (1988).

42. M. Bass, *Handbook of Optics by the Optical Society of America* (McGraw-Hill, New York, 1995).

43. M.C. Gupta, *Handbook of Photonics* (CRC Press, Boca Raton, FL, 1996).

44. R.A. Saroyan, D. Milam, and J.B. Trenholme, "B integrals and Laser Performance Figures," (Lawrence Livermore National Laboratory, Livermore, CA, 1976).

45. R. Adair, L.L. Chase, and S.A. Payne, "Nonlinear Refractive-Index of Optical-Crystals," Phys. Rev. B. **39**, 3337-3350 (1989).

46. M.D. Perry, T. Ditmire, and B.C. Stuart, "Self-Phase Modulation in Chirped-Pulse Amplification," Opt. Lett. **19**, 2149-2151 (1994).

47. P.S. Banks, M.D. Perry, V. Yanovsky, S.N. Fochs, B.C. Stuart, and J. Zweiback, "Novel all-reflective stretcher for chirped-pulse amplification of ultrashort pulses," IEEE J. Quant. Elec. **36**, 268-274 (2000).

48. F. Salin, J. Squier, and G. Mourou, "Large Temporal Stretching of Ultrashort Pulses," Appl. Optics **31**, 1225-1228 (1992).

49. B.E. Lemoff and C.P.J. Barty, "Quintic-Phase-Limited, Spatially Uniform Expansion and Recompression of Ultrashort Optical Pulses," Opt. Lett. **18**, 1651-1653 (1993).

50. D.M. Pennington, C.G. Brown, T.E. Cowan, S.P. Hatchett, E. Henry, S. Herman, M. Kartz, M. Key, J. Koch, A.J. MacKinnon, M.D. Perry, T.W. Phillips, M. Roth, T.C. Sangster, M. Singh, R.A. Snavely, M. Stoyer, B.C. Stuart, and S.C. Wilks, "Petawatt laser system and experiments," IEEE J. Selected Top. in Quant. Elec. **6**, 676-688 (2000).

51. M.D. Perry and B.W. Shore, "Petawatt Laser Report," M.D. Perry, ed. (Lawrence Livermore National Laboratory, 1996).

52. A. Stingl, M. Lenzner, C. Spielmann, F. Krausz, and R. Szipocs, "Sub-10-fs Mirror-Dispersion-Controlled Ti-Sapphire Laser," Opt. Lett. **20**, 602-604 (1995).

53. J.P. Zhou, G. Taft, C.P. Huang, M.M. Murnane, H.C. Kapteyn, and I.P. Christov, "Pulse Evolution in a Broad-Bandwidth Ti-Sapphire Laser," Opt. Lett. **19**, 1149-1151 (1994).

54. M. Aoyama, K. Yamakawa, Y. Akahane, J. Ma, N. Inoue, H. Ueda, and H. Kiriyama, "0.85-PW, 33-fs Ti:sapphire laser," Opt. Lett. **28**, 1594-1596 (2003).

55. R.S. Marjoribanks, F.W. Budnik, L. Zhao, G. Kulcsar, M. Stanier, and J. Mihaychuk, "High-Contrast Terawatt Chirped-Pulse-Amplification Laser That Uses a 1-Ps Nd-Glass Oscillator," Opt. Lett. **18**, 361-363 (1993).

56. F.G. Patterson and M.D. Perry, "Design and Performance of a Multiterawatt, Subpicosecond Neodymium - Glass-Laser," J. Opt. Soc. Am. B **8**, 2384-2391 (1991).

57. Y. Beaudoin, C.Y. Chien, J.S. Coe, J.L. Tapie, and G. Mourou, "Ultrahigh-Contrast Ti-Sapphire Nd-Glass Terawatt Laser System," Opt. Lett. **17**, 865-867 (1992).

58. I. Jovanovic, C.A. Ebbers, and C.P.J. Barty, "Hybrid chirped-pulse amplification," Opt. Lett. **27**, 1622-1624 (2002).

59. R.A.a.B. Baumgartner, R. L., "Optical Parametric Amplification," IEEE J. Quant. Elec. **QE-15**, 432-444 (1979).

60. T. Ditmire, H. Nguyen, and M.D. Perry, "Amplification of Femtosecond Pulses to 1-J in Cr-Lisralf6," Opt. Lett. **20**, 1142-1144 (1995).

61. M. Pessot, J. Squier, P. Bado, G. Mourou, and D.J. Harter, "Chirped Pulse Amplification of 300-Fs Pulses in an Alexandrite Regenerative Amplifier," IEEE J. Quant. Elect. **25**, 61-66 (1989).

62. J. Hein, S. Podleska, M. Siebold, M. Hellwing, R. Bodefeld, R. Sauerbrey, D. Ehrt, and W. Wintzer, "Diode-pumped chirped pulse amplification to the joule level," Appl. Phys. B-Lasers Opt. **79**, 419-422 (2004).

63. W. Koechner, *Solid-State Laser Engineering* (Springer-Verlag, Berlin, 1996).

64. G. Hays, V. Yanovsky, and T. Ditmire, "FALCON: A multi-terrawatt laser-linac facility. ," in *Conference on Lasers and Electro-Optics*, (Optical Society of America, Baltimore, MD, 1999).

65. C.P.J. Barty, T. Guo, C. LeBlanc, F. Raksi, C. RosePetruck, J. Squier, K.R. Wilson, V.V. Yakovlev, and K. Yamakawa, "Generation of 18-fs, multiterawatt pulses by regenerative pulse shaping and chirped-pulse amplification," Opt. Lett. **21**, 668-670 (1996).

66. C.P.J. Barty, G. Korn, F. Raksi, C. RosePetruck, J. Squier, A.C. Tien, K.R. Wilson, V.V. Yakovlev, and K. Yamakawa, "Regenerative pulse shaping and amplification of ultrabroadband optical pulses," Opt. Lett. **21**, 219-221 (1996).

67. C. LeBlanc, P. Curley, and F. Salin, "Gain-narrowing and gain-shifting of ultra-short pulses in Ti:sapphire amplifiers," Opt. Commun. **131**, 391-398 (1996).

68. A. Sullivan, J. Bonlie, D.F. Price, and W.E. White, "1.1-J, 120-fs laser system based on Nd:glass-pumped Ti:sapphire," Opt. Lett. **21**, 603-605 (1996).

69. H. Wang, S. Backus, Z. Chang, R. Wagner, K. Kim, X. Wang, D. Umstadter, T. Lei, M. Murnane, and H. Kapteyn, "Generation of 10-W average-power, 40-TW peak-power, 24-fs pulses from a Ti:sapphire amplifier system," J. Opt. Soc. Am. B **16**, 1790-1794 (1999).

70. A. Sullivan, H. Hamster, H.C. Kapteyn, S. Gordon, W. White, H. Nathel, R.J. Blair, and R.W. Falcone, "Multiterawatt, 100-Fs Laser," Opt. Lett. **16**, 1406-1408 (1991).

71. B.E.A. Saleh and M.C. Teich, *Fundimentals of Photonics* (John Wiley & Sons, Inc., New York 1991).

72. A.E. Siegman, *Lasers* (University Science Books, Sausalito, 1986).

73. P.V. Avizonis and R.L. Grotbeck, "Experimental and Theoretical Ruby Laser Amplifier Dynamics," J. Appl. Phys. **37**, 687 (1966).

74. L.M. Frantz, and Nodvik, J. S., "Theory of Pulse Propagation in a Laser Amplifier," J. Appl. Phys. **34**, 2346-2349 (1963).

75. E.L. Steele and W.C. Davis, "Laser Amplifiers," J. Appl. Phys. **36**, 348-351 (1965).

76. R. Bellman, G. Birnbaum, and W.G. Wagner, "Transmission of Monochromatic Radiation in a Two-Level Material," J. Appl. Phys. **34**, 780-782 (1963).

77. A.E. Siegman and E.A. Sziklas, "Mode Calculations in Unstable Resonators with Flowing Saturable Gain. 1:Hermite-Gaussian Expansion," Appl. Optics **13**, 2775-2792 (1974).

78. A. Brun, P. Georges, G. Lesaux, and F. Salin, "Single-Shot Characterization of Ultrashort Light-Pulses," J. Phys. D - Appl. Phys. **24**, 1225-1233 (1991).

79. J.P. Zhou, C.P. Huang, M.M. Murnane, and H.C. Kapteyn, "Amplification of 26-fs, 2-TW Pulses near the Gain-Narrowing Limit in Ti-Sapphire," Opt. Lett. **20**, 64-66 (1995).

80. J. Collier, C. Hernandez-Gomez, I.N. Ross, P. Matousek, C.N. Danson, and J. Walczak, "Evaluation of an ultrabroadband high-gain amplification technique for chirped pulse amplification facilities," Appl. Opt. **38**, 7486-7493 (1999).

81. S.E. Stokowski, Saroyan, R. A., Weber, M. J., "Laser Glass Nd-doped Glass Spectroscopic and Physical Properties, Rev. 2, vol 1, 2," (Lawrence Livermore National Laboratory, 1981).

82. B.R. Judd, "Optical absoption intensities of rare earth ions," Phys. Rev. B **127**, 750 (1962).

83. G.S. Olfelt, "Intensities of crystal spectra of rare-earth ions," J Chem. Phys. **37**, 511 (1962).

84. O.V. Chekhlov, J.L. Collier, I.N. Ross, P.K. Bates, M. Notley, C. Hernandez-Gomez, W. Shaikh, C.N. Danson, D. Neely, P. Matousek, and S. Hancock, "35 J broadband femtosecond optical parametric chirped pulse amplification system," Opt. Lett. **31**, 3665-3667 (2006).

85. F. Tavella, A. Marcinkevicius, and F. Krausz, "90 mJ parametric chirped pulse amplification of 10 fs pulses," Opt. Express **14**, 12822-12827 (2006).

86. I. Jovanovic, C.G. Brown, C.A. Ebbers, C.P.J. Barty, N. Forget, and C. Le Blanc, "Generation of high-contrast millijoule pulses by optical parametric chirped-pulse amplification in periodically poled KTiOPO4," Opt. Lett. **30**, 1036-1038 (2005).

87. F. Tavella, K. Schmid, N. Ishii, A. Marcinkevicius, L. Veisz, and F. Krausz, "High-dynamic range pulse-contrast measurements of a broadband optical parametric chirped-pulse amplifier," Appl. Phys. B-Lasers Opt. **81**, 753-756 (2005).

88. R.L. Sutherland, *Handbook of Nonlinear Optics* (Marcel Dekker, New York, 1996).

89. T.J. Kessler, J. Bunkenburg, H. Huang, A. Kozlov, and D.D. Meyerhofer, "Demonstration of coherent addition of multiple gratings for high-energy chirped-pulse-amplified lasers," Opt. Lett. **29**, 635-637 (2004).

90. E.W. Gaul, T. Ditmire, M.D. Martinez, S. Douglas, D. Gorski, G.R. Hays, W. Henderson, A. Erlandson, J. Caird, C. Ebbers, I. Jovanovic, and W. Molander, "Design of the Texas Petawatt Laser," in Conference on Lasers and Electro-Optics, (Optical Society of America, Baltimore, MD, 2005).

91. G.H. Miller, E.I. Moses, and C.R. Wuest, "The National Ignition Facility," **43**, 2841-2853 (2004).

92. M.D. Perry, D. Pennington, B.C. Stuart, G. Tietbohl, J.A. Britten, C. Brown, S. Herman, B. Golick, M. Kartz, J. Miller, H.T. Powell, M. Vergino, and V. Yanovsky, "Petawatt laser pulses," Opt. Lett. **24**, 160-162 (1999).

93. H. Yoshida, E. Ishii, R. Kodama, H. Fujita, Y. Kitagawa, Y. Izawa, and T. Yamanaka, "High-power and high-contrast optical parametric chirped pulse amplification in beta-BaB2O4 crystal," Opt. Lett. **28**, 257-259 (2003).

94. I. Jovanovic, C.P.J. Barty, C. Haefner, and B. Wattellier, "Optical switching and contrast enhancement in intense laser systems by cascaded optical parametric amplification," Opt. Lett. **31**, 787-789 (2006).

95. R.W. Boyd, *Nonlinear Optics* (Academic Press, San Diego, 1992).

96. A. Yariv, *Quantum Electronics* (John Wiley & Sons, New York, 1989).

97. Y.R. Shen, *The Principle of Nonlinear Optics* (Wiley, Hoboken, 2003).

98. J.A. Giordmaine, "Mixing of Light Beams in Crystals," **8**, 19 (1962).

99. P.D. Maker, R.W. Terhune, M. Nisenoff, and C.M. Savage, "Effects of Dispersion and Focusing on the Production of Optical Harmonics," **8**, 21 (1962).

100. A.A. Isaev, M.A. Kazaryan, G.G. Petrash, S.G. Rautian, and A.M. Shalagin, "Pulsed emission and evolution of Gaussian-beam in unstable resonator lasers," Sov. J. Quant. Elec. **2**, 1125-1137 (1975).

101. D.J. Armstrong, W.J. Alford, T.D. Raymond, A.V. Smith, and M.S. Bowers, "Parametric amplification and oscillation with walkoff-compensating crystals," J. Opt. Soc. Am. B **14**, 460-474 (1997).

102. S.A. Payne, C.D. Marshall, A. Bayramian, G.D. Wilke, and J.S. Hayden, "LASER PROPERTIES OF A NEW AVERAGE-POWER ND-DOPED PHOSPHATE-GLASS," **61**, 257-266 (1995).

103. Z.H. Chang, A. Rundquist, H.W. Wang, M.M. Murnane, and H.C. Kapteyn, "Generation of coherent soft x rays at 2.7 nm using high harmonics (vol 79, pg 2967, 1997)," Phys. Rev. Lett. **80**, 1795-1795 (1998).

104. B. Dromey, M. Zepf, A. Gopal, K. Lancaster, M.S. Wei, K. Krushelnick, M. Tatarakis, N. Vakakis, S. Moustaizis, R. Kodama, M. Tampo, C. Stoeckl, R. Clarke, H. Habara, D. Neely, S. Karsch, and P. Norreys, "High harmonic generation in the relativistic limit," Nat. Phys. **2**, 456-459 (2006).

105. P. Agostini and L.F. DiMauro, "The physics of attosecond light pulses (vol 67, pg 813, 2004)," Rep. Prog. Phys. **67**, 1563-1563 (2004).

106. A. Rundquist, C.G. Durfee, Z.H. Chang, C. Herne, S. Backus, M.M. Murnane, and H.C. Kapteyn, "Phase-matched generation of coherent soft X-rays," Science **280**, 1412-1415 (1998).

107. T.D. Donnelly, T. Ditmire, K. Neuman, M.D. Perry, and R.W. Falcone, "High-order harmonic generation in atom clusters," Phys. Rev. Lett. **76**, 2472-2475 (1996).

108. M.V. Fomyts'kyi, B.N. Breizman, A.V. Arefiev, and C. Chiu, "Harmonic generation in clusters," Phys. Plasmas **11**, 3349-3359 (2004).

109. S.V. Fomichev, D.F. Zaretsky, D. Bauer, and W. Becker, "Classical molecular-dynamics simulations of laser-irradiated clusters: Nonlinear electron dynamics and resonance-enhanced low-order harmonic generation," Phys. Rev. A **71**, (2005).

110. K.Y. Kim, I. Alexeev, E. Parra, and H.M. Milchberg, "Time-resolved explosion of intense-laser-heated clusters," Phys. Rev. Lett. **90**, - (2003).

111. H.M. Milchberg, S.J. McNaught, and E. Parra, "Plasma hydrodynamics of the intense laser-cluster interaction," Phys. Rev. E **64**, - (2001).

112. V. Kumarappan, M. Krishnamurthy, and D. Mathur, "Two-dimensional effects in the hydrodynamic expansion of xenon clusters under intense laser irradiation," Phys. Rev. A **66**, - (2002).

113. B.N. Breizman, A.V. Arefiev, and M.V. Fomyts'kyi, "Nonlinear physics of laser-irradiated microclusters (vol 12, art no 056706, 2005)," Phys. Plasmas **12**, (2005).

114. F. Dorchies, F. Blasco, T. Caillaud, J. Stevefelt, C. Stenz, A.S. Boldarev, and V.A. Gasilov, "Spatial distribution of cluster size and density in supersonic jets as targets for intense laser pulses," Phys. Rev. A **68**, (2003).

115. I. Alexeev, T.M. Antonsen, K.Y. Kim, and H.M. Milchberg, "Self-focusing of intense laser pulses in a clustered gas," Phys. Rev. Lett. **90**, - (2003).

116. Y. Kornyushin, "Uniform plasma oscillations in ellipsoid of conductive material," **3**, 35-39 (2004).

117. H. Hamster, A. Sullivan, S. Gordon, W. White, and R.W. Falcone, "Subpicosecond, Electromagnetic Pulses from Intense Laser-Plasma Interaction," Phys. Rev. Lett. **71**, 2725-2728 (1993).

118. Y. Fukuda, Y. Kishimoto, T. Masaki, and K. Yamakawa, "Structure and dynamics of cluster plasmas created by ultrashort intense laser fields," Phys. Rev. A **73**, (2006).

119. T.M. Antonsen, T. Taguchi, A. Gupta, J. Palastro, and H.M. Milchberg, "Resonant heating of a cluster plasma by intense laser light," Phys. Plasmas **12**, (2005).

120. H.M. Milchberg, K.Y. Kim, V. Kumarappan, B.D. Layer, and H. Sheng, "Clustered gases as a medium for efficient plasma waveguide generation," Philos. Trans. R. Soc. A-Math. Phys. Eng. Sci. **364**, 647-661 (2006).

121. K.W. Madison, P.K. Patel, D. Price, A. Edens, M. Allen, T.E. Cowan, J. Zweiback, and T. Ditmire, "Fusion neutron and ion emission from deuterium and deuterated methane cluster plasmas," Phys. Plasmas **11**, 270-277 (2004).

122. E. Parra, I. Alexeev, J. Fan, K.Y. Kim, S.J. McNaught, and H.M. Milchberg, "X-ray and extreme ultraviolet emission induced by variable pulse-width irradiation of Ar and Kr clusters and droplets," Phys. Rev. E **62**, R5931-R5934 (2000).

123. Y.R. Shen, *The Principles of Nonlinear Optics* (Wiley, New York, 1984).

124. A. Gupta, T.M. Antonsen, and H.M. Milchberg, "Propagation of intense short laser pulses in a gas of atomic clusters," Phys. Rev. E **70**, (2004).

125. M.V. Ammosov, N.B. Delone, and V.P. Krainov, "Tunnel Ionization of Complex Atoms and Atomic Ions in a Varying Electromagnetic-Field," Zhurnal Eksperimentalnoi Teor. Fiz. **91**, 2008-2013 (1986).

126. E.L. Dawes, "Optical Third-Harmonic Coefficients for the Inert Gases," **169**, 47 (1968).

127. N.E. Andreev, M.E. Veisman, and M.V. Chegotov, "Third-harmonic generation in an ionized gas and its relation to the residual energy of electrons," J. Exp. Theor. Phys. **97**, 554-565 (2003).

128. E. Springate, N. Hay, J.W.G. Tisch, M.B. Mason, T. Ditmire, J.P. Marangos, and M.H.R. Hutchinson, "Enhanced explosion of atomic clusters irradiated by a sequence of two high-intensity laser pulses," Phys. Rev. A **6104**, (2000).

129. T. Taguchi, T.M. Antonsen, and H.M. Milchberg, "Resonant heating of a cluster plasma by intense laser light," Phys. Rev. Lett. **92**, (2004).

130. F. Ple, M. Pittman, G. Jamelot, and J.P. Chambaret, "Design and demonstration of a high-energy booster amplifier for a high-repetition rate petawatt class laser system," **32**, 238-240 (2007).

131. I. Matsushima, H. Yashiro, and T. Tomie, "10 kHz 40W Ti:sapphire regenerative ring amplifier," Opt. Lett. **31**, 2066-2068 (2006).

132. E.I. Moses and C.R. Wuest, "The National Ignition Facility: Status and plans for laser fusion and high-energy-density experimental studies," Fusion Sci. Technol. **43**, 420-427 (2003).

133. T. Tajima and G. Mourou, "Zettawatt-exawatt lasers and their applications in ultrastrong-field physics," Phys. Rev. Spec. Top.-Accel. Beams **5**, (2002).

134. V.M. Malkin, G. Shvets, and N.J. Fisch, "Fast compression of laser beams to highly overcritical powers," Phys. Rev. Lett. **82**, 4448-4451 (1999).

Vita

Gregory Ross Hays was born on May 3, 1972 in Madrid, Spain, the son of William and Rossanna Hays. He graduated from Highland High School in Albuquerque, New Mexico in 1990. He later attended the University of New Mexico in Albuquerque, and graduated in 1995 with a Bachelor of Sciences in Physics. As an undergraduate at New Mexico, he was a cooperative education student at the United States Air Force Phillips Laboratory at Kirtland Air Force Base from 1990 to 1995. Following graduation he was employed at Lightwave Electronics Corporation as a staff engineer in 1995. From December of 1995 to August 2000, he was employed at Lawrence Livermore National Laboratory as mechanical engineering technician. He began his graduate education at the University of Texas at Austin, in Austin, Texas in August 2000.

Permanent address: 3280 Countryside Dr., San Mateo, CA 94403
The author typed this dissertation.